Earthquake nucleation, rupture and slip on rough laboratory faults

CHRISTOPHER WILLIAM ANTHO HARBORD

Earthquake nucleation, rupture and slip on rough laboratory faults

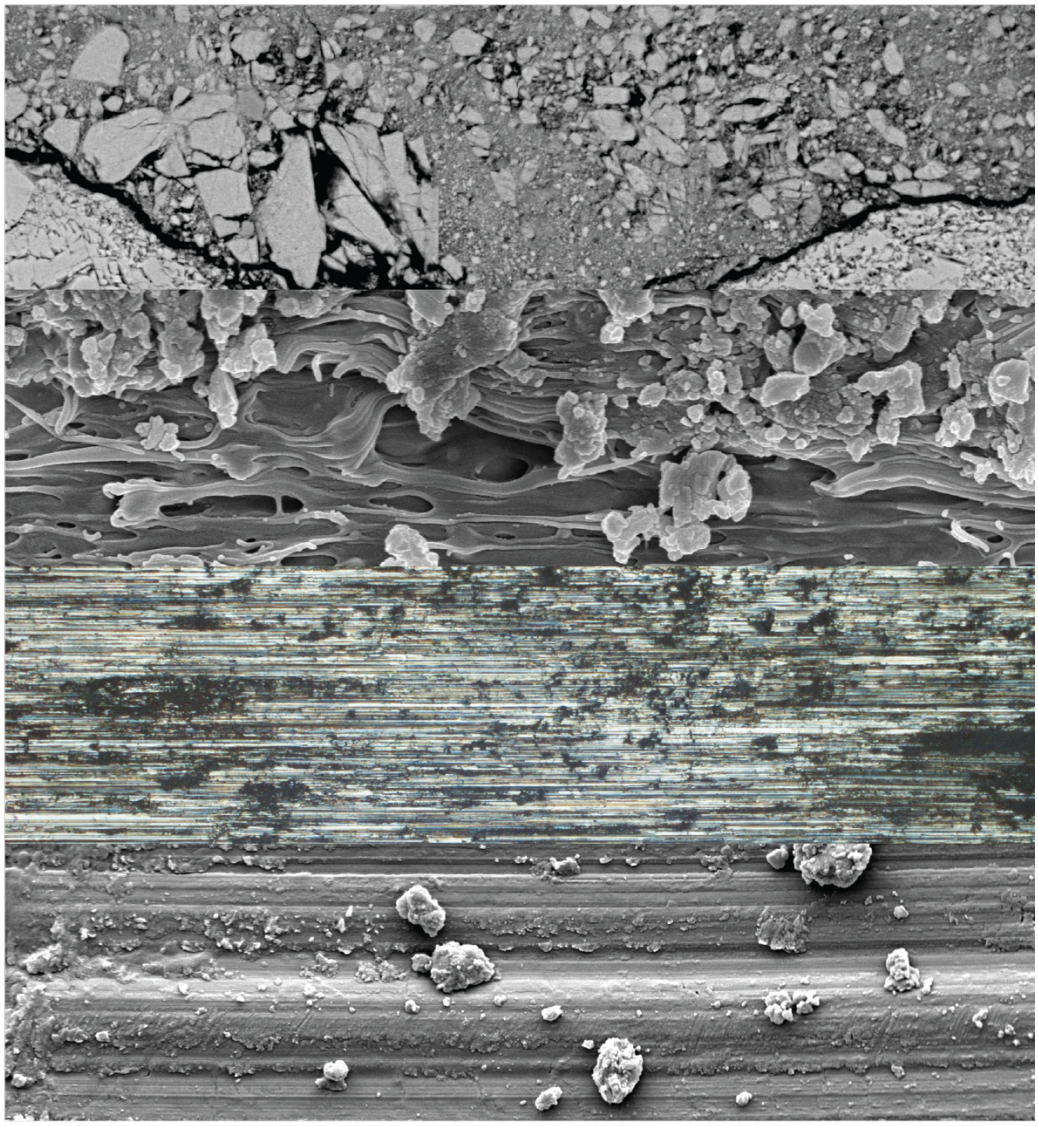

Christopher William Anthony Harbord

A thesis submitted in partial fulfilment of the requirements for the degree of Doctor of Philosophy at Durham University

Department of Earth Sciences

June 2018

Abstract

Fault structural heterogeneity is commonly linked to the nucleation of earthquakes, and once propagating it is used to explain the frictional weakening which drives rupture. However, the current laboratory and modelling perspective of earthquake nucleation processes derives largely from investigations of homogenous materials which neglect many features of natural earthquake faults. This thesis addresses the role of geometric heterogeneity in the nucleation and propagation of earthquake rupture by means of triaxial experiments utilising laboratory simulated faults.

A range of roughness's were applied to rock samples which were deformed at conditions spanning earthquake hypocentral conditions ($30< \sigma \leq 200$ MPa) to investigate the role of geometric heterogeneity (roughness) in earthquake nucleation. The stability and frictional behaviour of rough faults was mapped, revealing a complex interplay between roughness and normal stress conditions. Smooth faults are more unstable at low stress, whilst rough faults are general stable at low stress. Results are found to be in violation of current theories of frictional sliding, with normal stress acting to stabilise slip, and nucleation of rupture occurring in a rate-strengthening regime. A new microphysical model is thus developed, which matches observations, based on the interaction of flaws created by roughness and fracture energy considerations. Significantly this model has definable physical origins which are lacking from current theories of frictional instability.

Elastodynamics of fault slip during nanoearthquake propagation on rough faults is investigated. New experimental techniques are applied to obtain the coupled slip velocity and strength evolution in the nearfield of spontaneous earthquake ruptures. Results are well fit by analytical flash weakening models of high velocity frictional strength. Fracture energy scaling results and self-similarity of individual events supports the application of flash heating theory to explain the weakening expected during small earthquakes ($M<5$). These results are used to suggest that self-similar self-healing slip pulse models are the most appropriate model for use in seismological inversion, crucial for determining earthquake source parameters.

The role of roughness and normal stress on the frictional sliding is revisited using limestone. Experiments are performed on roughened bare surfaces, which were subsequently deformed in a direct shear configuration at a range of normal stress conditions ($30< \sigma \leq 100$ MPa). In all experiments sliding is stable, with the influence of roughness being less pronounced due to the rapid wear of experimental surfaces. Results

show that frictional sliding can either be strongly velocity strengthening and accompanied by plastic deformation processes, or velocity neutral associated to brittle deformation processes depending on initial fault conditions. Result show the first experimental evidence linking the evolution of rate-and-state parameters to frictional wear widely observed on natural faults. It is therefore suggested that wear is a determining factor for the mechanical behaviour of natural faults.

In conclusion results show that the widely observed roughness of natural faults has important implications for the mechanics of faulting and earthquakes, in particular the frictional stability and microstructural evolution. These factors should be taken into greater consideration in future experimental and modelling studies.

Declaration

I declare that this thesis, which I submit for the degree of Doctor of Philosophy at Durham University, is my own work and not substantially the same as any which has previously been submitted at this or any other university. Christopher W.A. Harbord, Department of Earth Sciences, Durham University, June 2018 © The copyright of this thesis rests with the author. No quotation from it should be published without prior written consent and information derived from it should be acknowledged.

“God invented the bulk;
Surfaces were invented by the devil”

-Wolfgang Pauli

Acknowledgements

There are many people to thank, if I forgot you know who you are, my first has to go to my supervisors Stefan Nielsen, Nic De Paola and Bob Holdsworth. Stefan has been the most inspiring supervisor you could imagine, his knowledge, patience, brilliance in tackling problems that on the outset seemed unsolvable never ceases to amaze (as well as the ability to look awake but be half asleep). I have learnt so much from Stefan, including how to be late for meetings…, I know I wouldn't be where I am now, so thanks! Nic has also been brilliant second supervisor, his knowledge is also vast, and his painstaking attention to details has imparted a great deal of rigour into my science. He is always interested to make time to hear about the latest experimental results and discuss science, whilst possessing a great ability to reign in ideas that had wondered down the garden path. Finally, Bob, although we haven't had a great deal of interaction where we have your microstructural knowledge was invaluable (particularly when Stefan fell asleep), adding new context and reality to observations. Also the trips up Assynt were great fun, ahaaaaaa! I hope to continue working with you all in the future to learn more about faulting. A special shout also has to go to Dan Faulkner, who has always up for chats and continued support through the PhD!

Thanks have to given to Ian and Sophie in the thin section lab, their assistance, many times at the 11th hour, has been invaluable and made many things run a great deal smoothly. Also all the folk in the Physics workshop deserve a shout for their patience with sometimes vague instructions and short turnaround times from me!

Considerable thanks also has to go to the rest of the research group. Telemaco has been a great support recently, and shared many stimulating discussions whilst also sharing a healthy scepticism for certain aspects of friction. Giacomo has been brilliant company both in the lab and outside, his nagging over the past years has finally got me into the enlightening world of microstructures. And finally Simon has been a great sounding board and sympathiser for trials and tribulations with strain gauges, whilst also sharing an appreciation for the endless hunt for the often elusive Nielsen! You've all made the research group a vibrant and stimulating environment and I know I will miss it in the future.

Many people in the wider department have made the PhD great fun, there are many people I could name, but in no particular order I would like to thank, Sean (Vic buddy and bestest PhD pal), Erin (party animal…), Emma (writing up pal), Jordan JJJJJJJJ Phethean (did I spell the surname right?), Mathieu (ta mere est une hamster!), Ben (oo nanana), Edward (fellow grumbler), Jamie (some of the best cooking I know), Olly, Mark, Liz, Alex, Sarah, Kate(s), Adam(s), Nuno, Miles, Tom(s), (the worst) Chris and many many more that I have enjoyed the company of… Hopefully we will see each other again! I have to thank my family (+extended family) for all the patience and support they have given, mum, dad, Nick and Johnny, it wouldn't be possible without you, I look forward to celebrating with you all soon. A special shout goes to all of my old Uni mates from Liverpool, see you all soon! Finally a thanks to Mr King (my old old geology teacher) who got me into this all those years ago!

Finally a shout to Alex and Rich for agreeing to examine me, it was a great pleasure and I have taken a lot from the viva, so thanks!

It's been a great ride, so thanks to you all!!!

Symbology

a	Dimensionless rate-and-state parameter
A^*	Creep pre-exponential function, s^{-1} bar^{-n}
A	Nominal contact area, m^2
A_c	Real area of contact
as_n	Nth asperity position, m
b	Dimensionless rate-and-state parameter
C	Dimensionless crack shape factor
C_0	Cohesive strength, Pa
c	Rupture velocity, m/s
D	Grain diameter, m
D_c	Critical slip distance, m
E_H	Frictional work, J/m^2
F	Force, N
F_a	Axial force, N
F_s	Shear force, N
F_n	Normal force, N
f_0	Low velocity coefficient of friction
f_w	High velocity (weakened) coefficient of friction
G	Shear modulus, Pa
GF	Strain gauge factor
H	Hurst exponent
h^*	Rate-and-state nucleation length, m
K_c	Critical stiffness, Pa/m
K_f	Fault stiffness, Pa/m
K_m	Machine stiffness, kN/mm

K_s	Slip weakening stiffness, Pa/m
k	Wavenumber, m^{-1}
k_{min}	Corner wavenumber, m^{-1}
k_0	Reference wavenumber, m^{-1}
L	Fault length, m
L_c	Slip weakening critical nucleation length, m
l_0	Active strain gauge length, m
M	Earthquake magnitude
m	Grain size exponent
n	Stress exponent
P	Signal power, m^3
P_c	Confining pressure, Pa
Q	Wear volume, m^3
R	Gas constant, kcal K/Mol
R_g	Strain gauge resistance, Ohm
r_a	Asperity length, m
r_w	Critical asperity dimension, m
S	Dimensionless stress ratio
T	Temperature, K
T_a	Asperity temperature, K
T_f	Bulk fault temperature, K
T_w	Weakening temperature, K
T_0	Background fault temperature, K
t	Time, s
t_0	Reference time at rupture tip, s
U	Strain energy, J
u	Fault displacement, m

u_c	Stiffness corrected displacement, m
u_{zz}	Crack face closure distance, m
V	Sliding velocity, m/s
V_0	Reference sliding velocity, m/s
V_w	Weakening velocity, m/s
V_{out}	Bridge output voltage, V
V_{in}	Bridge excitation voltage, V
W	Surface width, m
W_G	Fracture energy, J/m^2
W_R	Radiated energy, J/m^2
W_S	Restrengthening work, J/m^2
x	First dimension
y	Second dimension
Z_{rms}	Root mean square elevation, m
z	Third dimension
α	Pre-exponential scaling, m^3
α_{th}	Thermal diffusivity, m^2/s
β	Bridging length scaling factor, m
γ_s	Specific surface energy, J/m^2
$\dot{\gamma}$	Shear strain rate, s^{-1}
Δ	Static strain build-up
δ_c	Slip weakening distance, m
ε_{ij}	2d strain tensor
$\dot{\varepsilon}$	Strain rate, s^{-1}
$\dot{\varepsilon_c}$	Creep compaction strain rate, s^{-1}
$\dot{\varepsilon_g}$	Granular compaction strain rate, s^{-1}
θ	State variable, s

θ_0	Critical state, s
κ	Wear coefficient
λ	Crack length, m
λ_c	Bridging length, m
λ'	Lamé's parameter, Pa
μ	Coefficient of friction
μ_f	Final coefficient of friction
μ_g	Grain boundary coefficient of friction
μ_p	Peak coefficient of friction
μ_r	Weakened (sliding) coefficient of friction
μ_0	Reference coefficient of friction
ξ	Distance from crack centre, m
ϖ	Activation enthalpy, kcal/Mol
$\rho\hat{c}$	Specific heat capacity, J/m^3
ϱ	Granular geometric factor
σ	Normal stress, Pa
σ_c	Indentation hardness, Pa
ς	Grain boundary geometric factor
τ	Shear stress, Pa
τ_c	Asperity shear strength, Pa
τ_p	Peak shear stress, Pa
τ_r	Weakened (sliding) shear stress, Pa
τ_0	Initial shear stress, Pa
$\tilde{\tau}$	Average shear stress, Pa
υ	Poisson ratio
ϕ_{ss}	Steady state fault porosity
ϕ_c	Critical fault porosity

ψ	Granular dilation angle
ω	Frictional work, J/m^2

1 Introduction

Earthquakes continue to be a significant global geo-hazard, representing a major threat to both life and livelihood. Historical catalogues and measurements of earthquakes do not cover a sufficiently long time span to ensure a proper statistical significance of recurrence interval, in particular for mega earthquake cycles which have recurrence times of hundreds of years or more. Therefore, a consistent risk mitigation strategy should be based, at least in part, on the understanding of underlying physical processes involved with the earthquake cycle so as to allow a reliable modelling of the earthquake process. However, many details of the mechanics of earthquakes and faulting remain poorly understood, in spite of recent advances.

One of the principal unknowns of these physical processes is how stresses evolve during earthquake nucleation and propagation. The evolution of stress controls the magnitude, seismic shaking and damage associated with earthquakes (Rice et al., 2005), as well as controlling whether an earthquake is able to nucleate and subsequently propagate (Marone, 1998; Scholz, 1998). Therefore, understanding the dynamics of fault stress and friction behaviour is of paramount importance to furthering any predictive understanding of earthquake likelihood. Unfortunately, due to the fact that these processes occur at several kilometres depth in the Earth, direct in situ observation is often not pragmatic. This has motivated a series of experimental (e.g. Passelegue et al., 2013), seismological (e.g. Nadeau and Johnson, 1998), field (e.g. Chester, Chester and Kronenberg, 2005) and modelling studies (e.g. Andrews, 1976) , with the aim of providing key insights into the mechanical behaviour of earthquake faults.

Field

1.1 Plate tectonics and crustal deformation

Plate tectonics drives stress accumulation in the Earth's lithosphere. This stress build-up causes the lithosphere to deform, and it may, dependant on pressure and temperature conditions deform by the formation of fractures (associated to seismicity) or a shear zone (associated to fault creep). Failure zones within the Earth's crust that allow blocks and tectonic plates to move past each other, resulting in either seismicity or creep. The majority of seismicity occurs at plate boundaries, as highlighted in Figure 1.1.

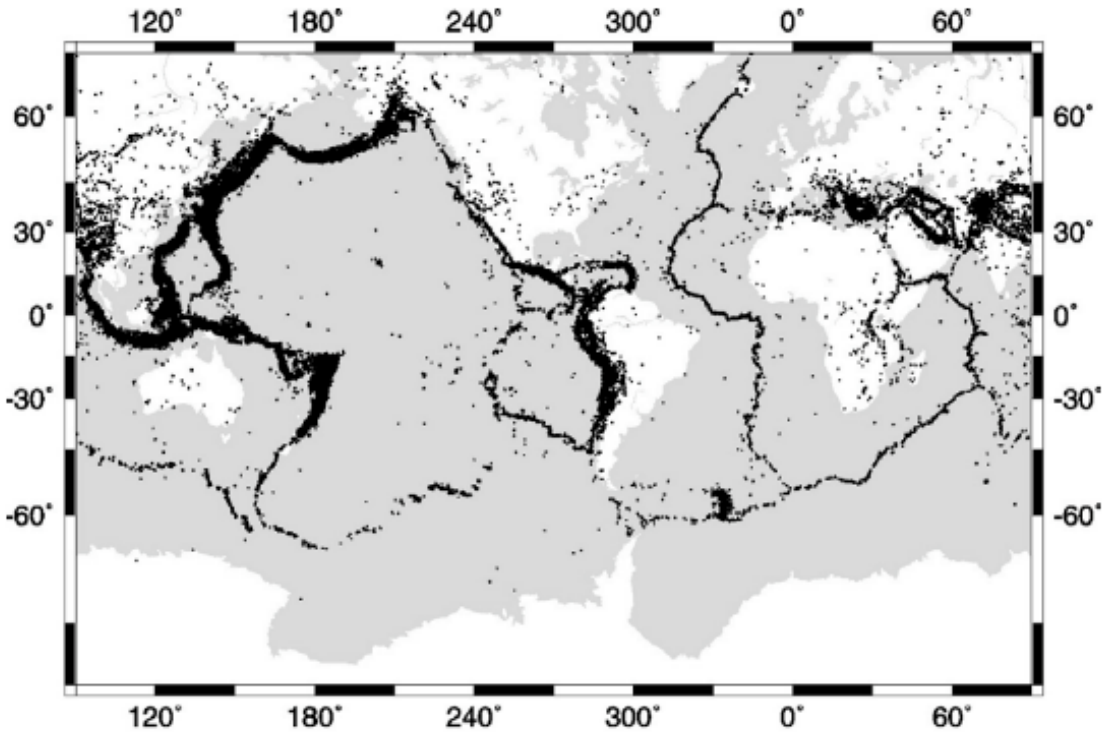

Figure 1.1 Global distribution of seismicity (01/01/1964 to 31/12/1995), 3.1 to 7.3 magnitude earthquakes. Earthquakes mainly occur at tectonic plate boundaries due to stress build-up resulting from the movement of plates, reproduced after Kanamori and Brodsky (2004).

Loading induced by plate tectonics results in mechanical behaviour that can be broadly separated into two components, brittle and ductile behaviour. In the upper crust temperature and pressure conditions are such that rocks deform following linear elasticity (Scholz, 2002; Paterson and Wong, 2005). In this brittle regime rocks fail by coalescence of microcracks, leading to macroscopic failure along a through-going plane i.e. a brittle fault.

During brittle failure stress increases to a well-defined peak strength, which increases with pressure, resulting in a greater accumulation of elastic strain energy with increasing depth. The depth dependence of rock strength is well described by Mohr-Coulomb's criterion (Scholz, 2002):-

$$\tau = C_0 + \mu(\sigma - P_f) \qquad 1.1$$

where τ is the shear stress on the fault in Pa, C_0 is the cohesive strength of the fault in Pa, μ the coefficient of friction, σ the normal stress in Pa and P_f the pore-fluid pressure in

Pa. When considering a pre-existing frictional interface, the cohesion of the surface may be neglected and Amonton's law retrieved ($\mu = \tau/\sigma$), which is assumed for all friction values throughout this thesis. Byerlee (1978) demonstrated that the static frictional strength of rocks is relatively constant for the vast majority of crustal rocks ($\mu = 0.6$ to 0.85), showing a linear dependence on normal stress consistent with Amonton's law. Mohr-Coulomb's law also highlights that the presence of pore-fluid pressure reduces the shear strength of the brittle lithosphere according to Terzaghi's law (Price, 1988).

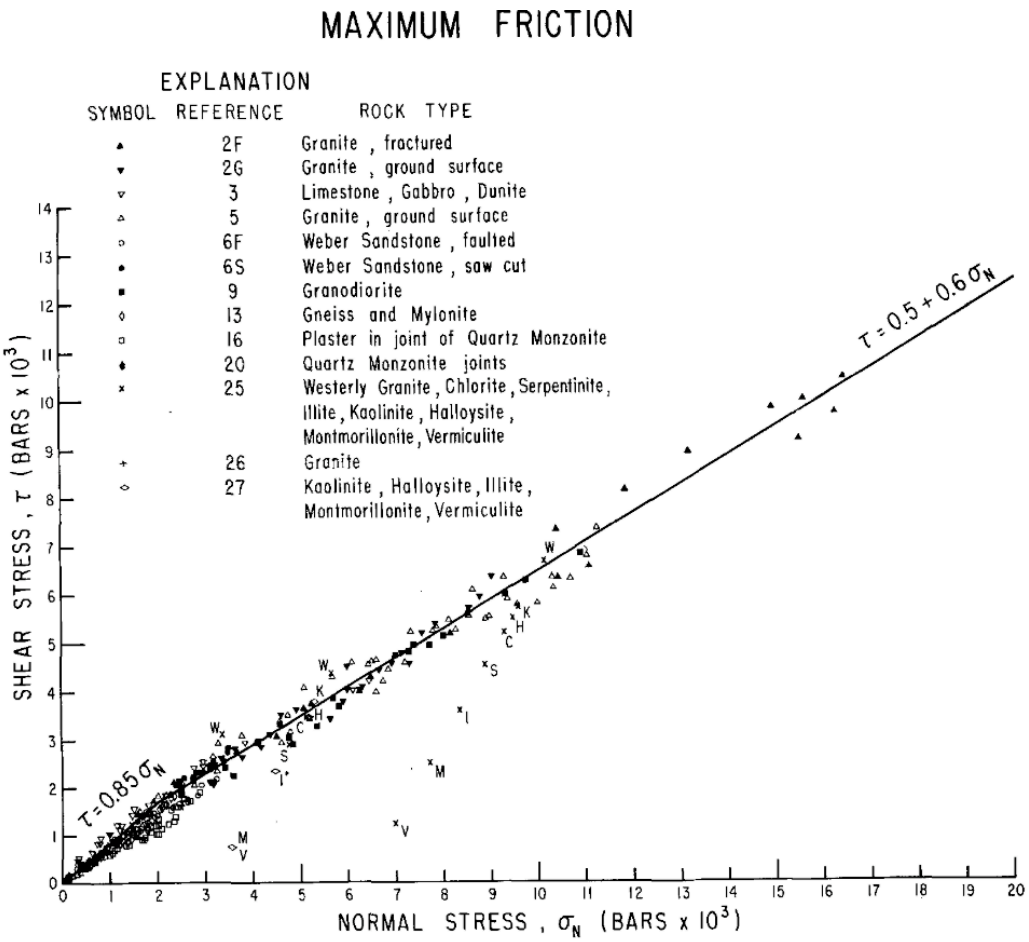

Figure 1.2 Shear stress plotted as a function of normal stress for a wide variety of lithologies. At low stress (< 200 MPa) μ = 0.85, and at high stress (>200 MPa) μ = 0.6. Reproduced after Byerlee (1978).

With increasing depth in the crust, due to conduction of heat from the mantle, the temperature of the lithosphere increases. Increasing temperature and pressure activate plastic deformation mechanisms on the scale of mineral grains, such as dislocation or diffusive mass transfer creep. These deformation mechanisms suppress crack propagation (leading to brittle faults) and deformation is characterised by relatively diffuse deformation zones known as shear zones. Plastic processes lead to a reduction in rock

strength with increasing temperature (Brace and Kohlstedt, 1980), which are captured by Arrhenius laws:

$$\dot{\varepsilon} = A^* D^{-m} e^{-\frac{\varpi}{RT}} \Delta\sigma^n \qquad 1.2$$

where $\dot{\varepsilon}$ is the strain rate of the deforming material in s^{-1}, A^* a pre-exponential function in s^{-1} Pa^{-n}, D the grain size of the rock in m, m the dimensionless grain size exponent of the deformation mechanism (0 to 3), ϖ the activation enthalpy of the deformation mechanism J/Mol, R the gas constant in J K/Mol, T the absolute temperature in K, $\Delta\sigma$ the differential stress in Pa and n the dimensionless stress exponent of the deformation mechanism (typically 1 to 5).

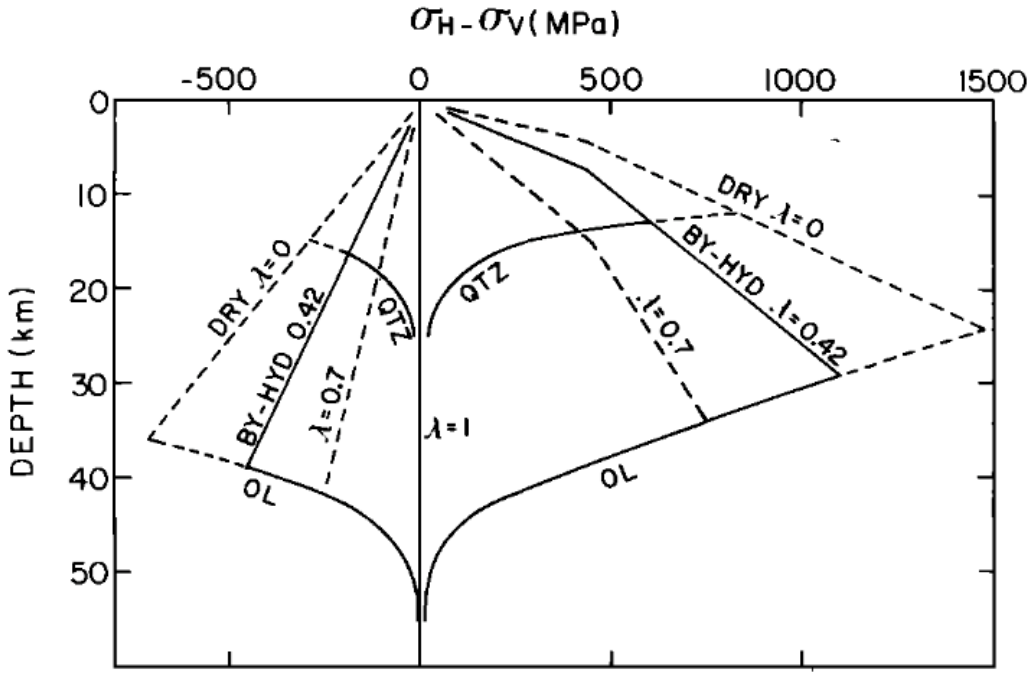

Figure 1.3 Strength determined of the lithosphere as inferred by Brace and Kohlstedt (1980) using expected differential stress predictions. The upper crustal is controlled by brittle deformation and linearly increases with depth, the lower crust is controlled by ductile deformation and strength exponentially decreases with depth. QTZ = quartz rheology, OL = olivine rheology, λ = porefluid pressure factor.

Plastic creep laws show that increasing temperature and decreasing strain rate reduce the strength of rocks (Poirier, 1985; Karato, 2008). These deformation mechanisms lead to a slow and stable release of stress in the lower crust, which is not favourable for the nucleation and propagation of earthquake rupture, suggesting that a depth transition in seismicity occurs in the lithosphere. Water also acts to reduce the activation enthalpy of

deformation mechanisms, and its presence therefore acts to decrease the strength of rocks deforming in a ductile manner (Rutter, 1974). Brace and Kohlstedt (1980) provided an estimate of this transition from brittle to ductile behaviour based on laboratory experiments, which broadly agrees with observations determined from seismological observations (Burov, 2011; Jackson et al., 2008).

1.2 Earthquake nucleation processes

Slow tectonic loading (mm's/yr) builds up elastic strain energy in the rocks surrounding the fault; the sudden failure of the fault abruptly releases the stored energy, resulting in the rapid acceleration of the surrounding rocks during earthquakes (up to m's/s). The acceleration of slip faults resulting in earthquakes is not the only possible outcome; indeed, the stored elastic energy can also be released slowly through aseismic creep (mm's/yr). These two end-member regimes, sometimes referred to as unstable and stable sliding respectively, arise from the intricacies of the fault's friction and structure, its dynamic interaction with the stiffness of the surrounding rocks, and the alteration of energy balance during its evolution.

In early friction experiments it was identified that faults could slide in two manners, analogous to natural fault behaviour (Brace and Byerlee, 1966; Byerlee and Summers, 1976), (a) unstable stick-slip sliding by repeated stress build up (stick) and sudden failure (slip) or (b) stable sliding at a relatively constant stress level. Stick-slip sliding was interpreted to be a laboratory analogue for earthquakes (Brace and Byerlee, 1966), and following this a number of factors, including rock composition (Summers and Byerlee, 1977), fault structure (Byerlee and Summers, 1976; Byerlee et al., 1978) and normal stress (Brace and Byerlee, 1966) were all found to play a role in determining the stability of rock frictional sliding. Following these observations it was identified in experiments that rock friction exhibited dependence on imposed sliding velocity (Dieterich, 1979c). Mathematical descriptions and analysis were subsequently developed (Dieterich, 1979a; Rice and Ruina, 1983; Ruina, 1983; Ranjith and Rice, 1999), that showed that if faults lose strength with increasing sliding velocity (velocity weakening) then acceleration of fault slip may become energetically favourable and result in unstable sliding (Marone, 1998). On the other hand, if fault friction is found to increase in strength with sliding velocity (velocity strengthening), then acceleration is unfavourable and the result is stable aseismic creep (Marone, 1998). This explanation of fault stability, or the lack thereof, can

be framed in the rate-and-state dependent friction laws formalism as will now be discussed.

1.2.1 Rate-and-state dependent friction

Rate-and-state dependent friction (RSF) has well defined empirical principles originally derived from experimental studies (for extensive reviews see Dieterich and Kilgore, 1996, Marone, 1998, and the more recent review by Faulkner et al., 2010). These laws can be formulated as follows:

$$\mu = \mu_0 + a \log\left(\frac{V}{V_0}\right) + b \log\left(\frac{V_0 \theta}{D_c}\right) \qquad 1.3$$

Where V is sliding velocity in m/s, μ is the coefficient of friction defined as $\mu = \frac{\tau}{\sigma}$, where τ is the fault shear stress in Pa and σ is the fault normal stress in Pa, θ is the state variable in s, D_c is a critical slip distance in m, a and b are experimentally derived dimensionless constants (respectively relating to the rate- and to the state- dependence of friction) and μ_0 is the coefficient of friction at a reference velocity V_0 in m/s (Dieterich, 1979c; Marone, 1998; Rice and Ruina, 1983; Ruina, 1983). The frictional response of such a system is shown schematically in figure 1.2.

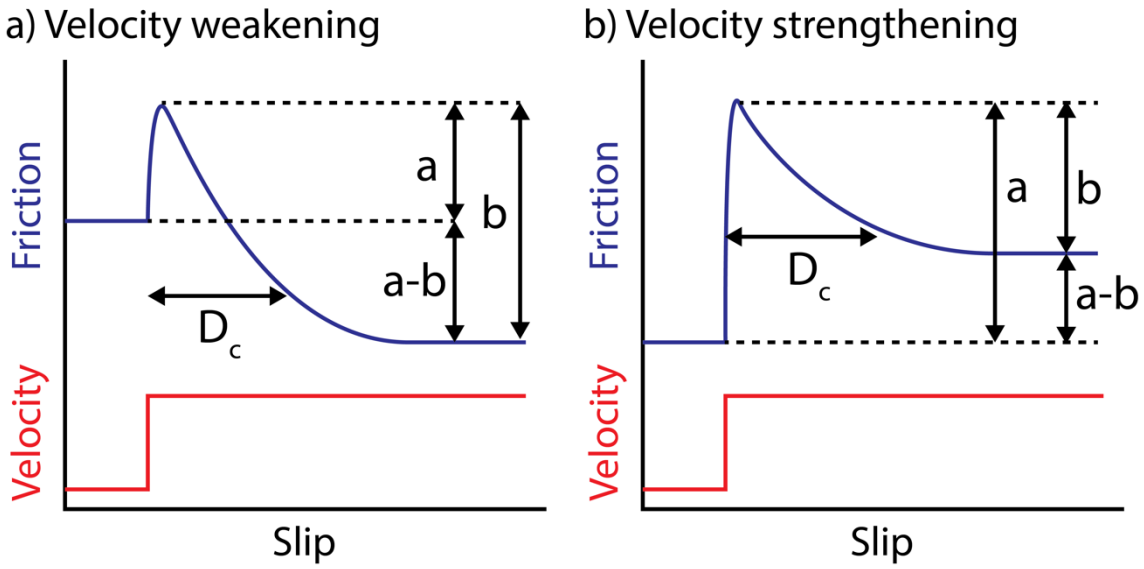

Figure 1.4 Schematic illustration of the frictional response to a step-wise velocity change for a) velocity weakening friction potentially resulting in unstable sliding and b) velocity strengthening friction resulting in stable sliding.

The rate parameter *a* controls the 'direct' frictional change in response to the change in sliding velocity (Dieterich and Kilgore, 1994; Rice et al., 2001). The parameter b, relates to the magnitude of 'delayed' frictional evolution in response to the change in sliding velocity (Faulkner et al., 2010; Ruina, 1983; Marone, 1998; Rice et al., 2001). D_c is often interpreted as the distance at which the population of frictional contacts is renewed during the evolution toward a new steady state upon a change in the sliding velocity (Dieterich and Kilgore, 1996a; Marone, 1998; Marone and Kilgore, 1993). The state variable changes until a new steady state is achieved and is assumed to represent the evolution of the microstructural state of the fault. A plethora of formulations have been suggested to model the evolution of the state variable based on experimental observations and inferences (Ruina, 1983; Dieterich, 1979a; Bhattacharya et al., 2015; Beeler et al., 1994; Nagata et al., 2012). The two most common state evolution laws with respect to time are:

$$\dot{\theta} = 1 - \frac{V\theta}{D_c} \tag{1.4}$$

the classical Dieterich aging law, where $\dot{\theta}$ is the dimensionless first derivative of state with respect to time, and the dominant physical process invoked is time dependent microstructural evolution (Dieterich, 1979a); and

$$\dot{\theta} = -\frac{V\theta}{D_c}\log\frac{V\theta}{D_c} \tag{1.5}$$

or Ruina's slip law, in which the state evolution is assumed to arise from a slip dependent microstructural evolution (Ruina, 1983). Both evolution laws yield differing agreement with the experimental data, the first or the second being more suitable depending on the circumstance (Marone, 1998; Bhattacharya et al., 2015), the formulations (1.4 and 1.5) also yield different earthquake nucleation characteristics in models (Rubin and Ampuero, 2005; Dieterich and Kilgore, 1996b), in addition to the differing physical interpretations.

These friction parameters can be utilised in determining the conditions under which growth of a nucleation patch is possible. If, a-b > 0, friction is velocity strengthening; instability is theoretically impossible regardless of the fault stiffness;

$$K_f = \mathrm{C}\frac{\mathrm{G}}{L}$$

1.6

where C is a dimensionless shape factor, G is the shear stiffness modulus in Pa and L is the length of the fault in m (Rice *et al.*, 1983a; Marone, 1998). The fault will be unconditionally stable, favouring creep behaviour (Scholz, 1998). On the contrary, if a-b < 0 friction is described as velocity weakening, and it becomes energetically favourable for the fault to accelerate. In addition to velocity weakening, for instability to occur, it is required that the critical frictional stiffness $K_c < K_f$, of the fault embedded in an elastic medium, where K_c is defined:

$$K_c = \frac{\sigma(b-a)}{D_c}$$

1.7

In general RSF provides a good description of fault sliding behaviour at low velocity, and has been characterised for a wide range of geological materials (see Marone, 1998, for an extensive review). Results reported are extremely variable and may depend on many conditions including (but certainly not limited to) temperature (Chester and Higgs, 1992; Blanpied et al., 1998; Verberne, Spiers, et al., 2013), composition (Marone, 1998), gouge thickness (Marone and Kilgore, 1993) and surface topography (Marone and Cox, 1994). In general phyllosilicates and carbonates tend to be velocity strengthening (Noda and Shimamoto, 2009; Carpenter et al., 2016), and crystalline silicates tend to be unstable (Leeman et al., 2016; Ikari et al., 2011). Recently RSF has been demonstrated to explain well the onset of instability and the range of friction slip modes in laboratory simulated faults (Leeman et al., 2016; Scuderi et al., 2016) as previously predicted by theoretical analysis (Gu and Wong, 1991b). RSF also provides a rich mathematical framework for modelling the natural seismic cycle, and has been extensively used to make inferences about crustal scale earthquake cycles and earthquake nucleation processes (Noda and Lapusta, 2013; Rice, 1993; Rubin and Ampuero, 2005; Dieterich, 1992). In spite of a plethora of empirical experimental data, the underlying microphysics of rate and state friction are still very poorly understood with little progress towards attaining a sound physical basis since their inception in the 70's. This raises significant questions about the scaling of these parameters, and what effects natural fault heterogeneity cause.

1.2.2 Slip weakening friction

An alternative way to explain the nucleation of earthquake rupture is to consider the energy depletion associated to a slip weakening model of friction. Physical descriptions and formulations are rooted in the original energetic analysis of Griffith (1921), where surface fracture energy is depleted in advancing the crack, while strain energy around the growing crack is released by the loss of strength. Slip weakening friction arises from Griffith's theory and its subsequent extension by Irwin, where a 'cohesive crack tip' is introduced, which accounts for the loss of strength expected at a crack tip (Ida, 1972; Barenblatt, 1962; Irwin, 1957; Palmer and Rice, 1973).

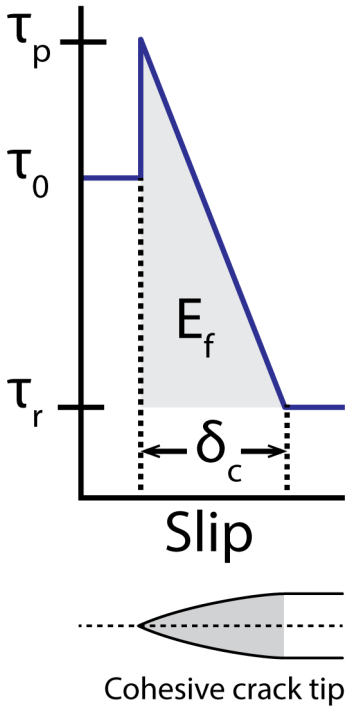

Figure 1.5 The cohesive crack tip model of a growing crack which weakens with respect to slip. τ_0 is the initial shear stress in Pa, τ_p is the peak shear stress in Pa, τ_r is the weakened shear stress in Pa and δ_c is the slip weakening distance in m.

Under slow tectonic loading faults become stressed which may cause the growth of slip surfaces. As these surfaces slip and fail they are expected to lose strength according to a slip weakening stiffness, K_s in Pa/m, dependent on the material properties (Uenishi and Rice, 2003; Palmer and Rice, 1973):

$$K_s = \frac{\sigma(\mu_p - \mu_r)}{\delta_c} \qquad 1.8$$

Where μ_p is the peak friction, μ_r the weakened (sliding) frictional strength, and δ_c a slip weakening distance (m) over which friction drops from μ_p to μ_r. This growth consumes energy by crack growth, but energy is also released from the strain energy release resulting from the slip weakening. At a certain length scale the strain energy release rate is faster than the energy depletion rate and the slipping patch growth may accelerate in an unstable manner (Andrews, 1976; Palmer and Rice, 1973; Uenishi and Rice, 2003; Brantut and Viesca, 2015; Campillo and Ionescu, 1997).

1.3 Earthquake propagation

Once an earthquake has nucleated, the fault slip may rapidly accelerate up to velocities approaching 0.1-10 m s^{-1}, while the earthquake rupture tip propagates as shear fracture at speeds on a similar order as those of elastic waves (km/s). Rapid slip can result in a large transient weakening of the rupturing fault (Di Toro et al., 2011; Passelègue et al., 2016), as will be discussed in the next section.

1.3.1 Theoretical background

Earthquake propagation is the stage of the earthquake cycle that is directly felt and observed through ground shaking as a result of elastic wave propagation. The shaking is a direct consequence of the rapid acceleration of earthquake faults due to the propagation of a shear crack. Most of the theory describing earthquake rupture is therefore rooted in dynamic fracture mechanics, which has been adapted by the introduction of frictional terms (Andrews, 1976; Ida, 1972; Rice, 1980).

Griffith's 1920 paper presents the first theoretical model to describe the phenomenon of failure by crack growth. In the above seminal work, it is considered that cracks are at energetic equilibrium with the surrounding elastic medium. As cracks grow, an energy amount, γ_s (J/m^2), is consumed by the creation of new surfaces. The newly created surface, on the other hand, results in a loss of strength inside the crack which allows strain energy U, to be released from the surrounding medium. At a certain crack length scale L_c, the release of strain energy is faster than the consumption of surface energy and the crack accelerates and propagates at a rapid subsonic velocity. Theoretical calculations of the stress fields surrounding moving Griffith cracks predict rapid accelerations near the crack, due to the large stress concentration around the crack tip (Yoffe, 1951; Kostrov, 1964), thus presenting an early interpretation of the seismic source mechanism.

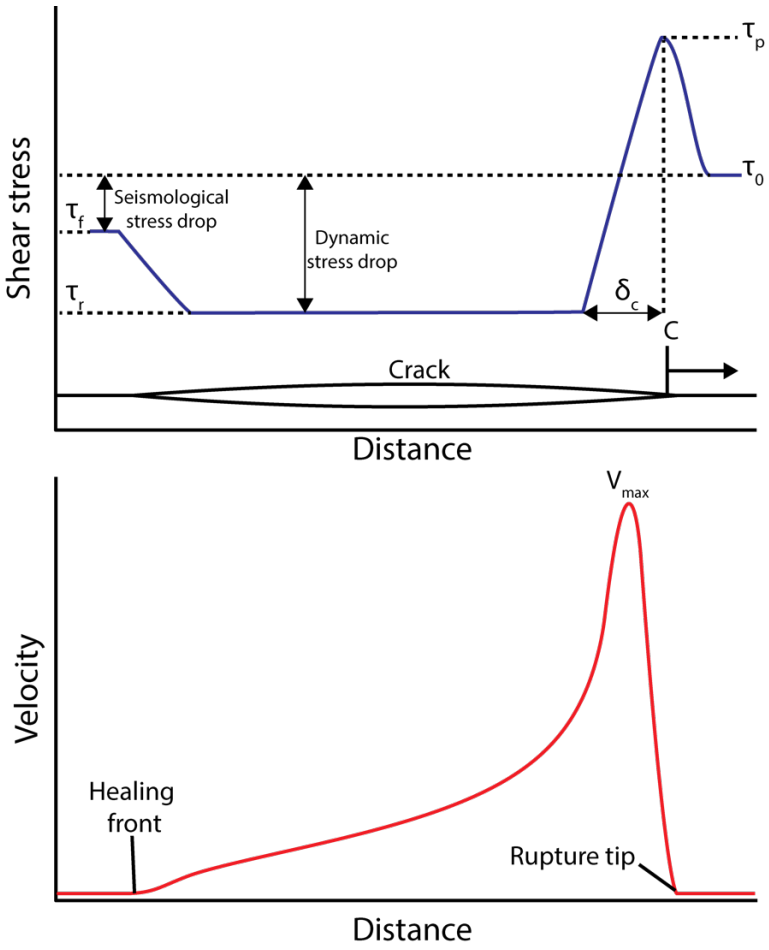

Figure 1.6 Stresses and velocity functions around a self-healing slip-weakening Griffith crack propagating at a constant rupture velocity, $C(x,t)$ (m/s).

In a further development (Barenblatt, 1962) introduced the concept of a cohesive crack tip, to describe the loss of strength expected at a crack tip, with the resulting stress profile following a linear slip weakening form similar to that presented in Figure 1.6. This was then formalised into the problem of earthquake faulting by (Ida, 1972; Palmer and Rice, 1973; Andrews, 1976), by considering that on faults, shear cracks grow with residual internal strength, accompanied by a linear decrease of strength at the crack-tip. These models give a good first order approximation of earthquake rupture, and following this a number of studies, most notably Andrews (1976), implemented these within finite difference models. It was found that ruptures asymptotically approach a limiting final rupture velocity as a function of a number of parameters including, the ratio of rupture length relative to the nucleation dimension, specific surface fracture energy and the stress ratio S, defined as:

$$S = \frac{\tau_p - \tau_0}{\tau_0 - \tau_r},$$

where τ_p is the peak shear stress, τ_0 the intial shear stress, and τ_r the residual or dynamic sliding shear stress, which are represented schematically in Figure 1.6. This highlights many of the links between frictional strength and rupture propagation, which has stimulated a number of experimental studies.

1.3.2 Experimental investigations of dynamic rupture

Experimental developments in the study of dynamic earthquake rupture in crustal rocks have been largely limited by technological advancements, in the face of difficulties arising from the rapid speed of dynamic stress evolution. Early experimental attempts on crustal rocks were made by Johnson and Scholz (1976), who utilised a network of strain gauges positioned close to an unstably sliding fault. They found that faults weakened extremely rapidly (<10 μs) upon arrival of the rupture tip, and inferred, based on a spring slider model, that slip velocity was on the order of m/s's. Further studies aimed at improving the resolution of measurements, finding that the topography of the fault surface played an important role in determining the rupture characteristics (Okubo and Dieterich, 1984; Ohnaka and Shen, 1999) e.g. the weakening time and associated peak velocities.

More recently, dynamic rupture has also been investigated extensively using analogue photo elastic materials, whereby the effects of differing physical conditions on dynamic rupture are analysed (Rubinstein et al., 2004; Xia et al., 2004; Rosakis, et al., 2006; Mello et al., 2010; Nielsen, et al., 2010; Schubnel et al., 2011). Many of these studies explore the effect of loading conditions on rupture speed, a key factor in controlling earthquake damage and ground shaking (Mello et al., 2011). Rupture velocity dependence on S according to the theoretical prediction of Andrews (1976) was confirmed first by Xia et al. (2004) in analogue experiments, and more recently by Passelegue et al. (2013) for crustal rocks.

One key finding is the identification of mode II ruptures exceeding the shear wave velocity (supershear), confirming both theoretical predictions and evidence from natural earthquakes (Bouchon et al., 2001; Dunham and Archuleta, 2004; Andrews, 1976). Numerous analogue experimental studies have confirmed supershear rupture velocities in analogue materials (Mello et al., 2011; Schubnel et al., 2011; Xia et al., 2004) and in westerly granite (V_r > 4km s^{-1}) (Passelègue et al., 2013; Johnson and Scholz, 1976).

1.3.3 High velocity friction

As expected from theoretical and seismological observation, fault slip velocity accelerates rapidly to speeds approaching m's per second. Frictional sliding determines the energetics of rupture propagation, therefore recent experimental work has focused on measuring the frictional strength of faults at seismic slip rates (0.5-4 m s^{-1}). Generally studies from rotary shear experiments have found that friction shows profound weakening at high velocity for nearly all rock types, with rock friction reported to drop from μ=0.3-0.7 to as low as 0.1 or less, in cohesive silicates, carbonates and phyllosilicates (Di Toro *et al.*, 2011, Figure 1.4).

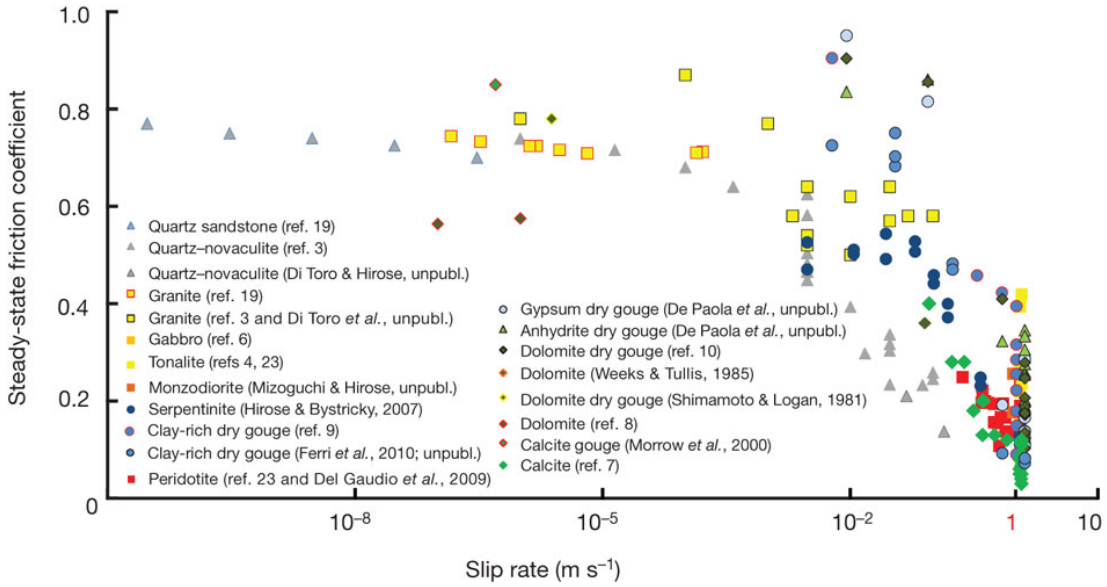

Figure 1.7 Velocity dependence of friction for a range of crustal lithologies at a range of sliding velocities. Faults abruptly weaken at sliding velocities above 1-10 cm/s, demonstrating that faults will be transiently weak during earthquakes. Reproduced from Di Toro et al. (2011).

A variety of processes have been argued to cause the observed weakening as a consequence of frictional heating, including melting (Di Toro et al., 2006; Nielsen 2008, 2010; Goldsby and Tullis, 2011; Niemeijer et al., 2011; Passelègue et al., 2016), thermal pressurisation (Rice 2006; Rempel and Rice 2006; Faulkner et al., 2011; Viesca and Garagash 2015), thermal decomposition (De Paola et al., 2011; Brantut et al., 2010; Han et al., 2007), plastic creep (Smith et al., 2013; De Paola et al., 2015), silica gel lubrication (Di Toro et al., 2004; Goldsby and Tullis, 2011) and powder lubrication (Reches and Lockner, 2010; Han et al., 2010). Typically this weakening occurs in slip distances <1m, often much less, whilst also showing a reduction with increasing normal stress (Di Toro et al., 2011).

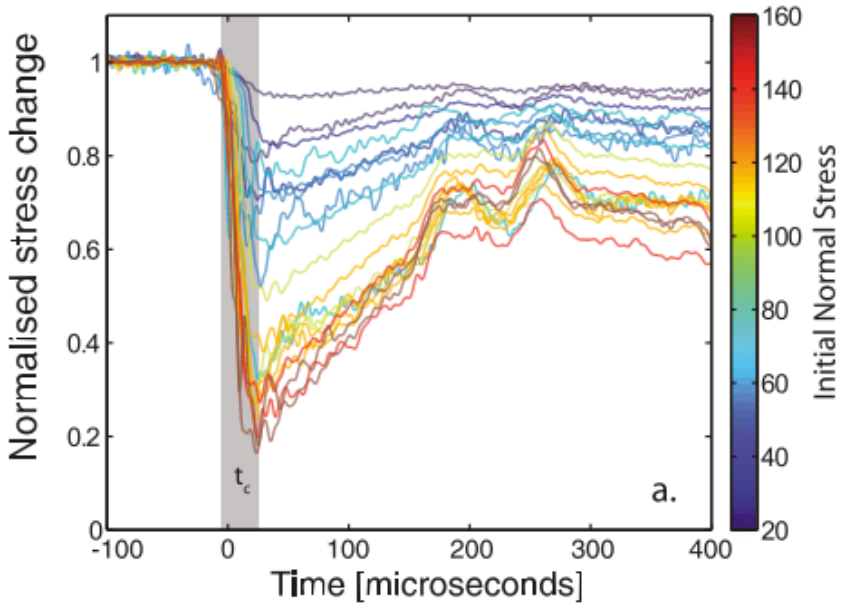

Figure 1.8 Example of recent data obtained by use of measuring strain gauges at high frequency (Passelègue et al., 2016), showing that faults weaken significantly during spontaneous rupture propagation and associated high velocity slip. The data were obtained from diagonally pre-cut cylindrical samples of Westerly granite, subjected to axial load and confinement in a triaxial press. This induced stick-slip instability events equivalent to microearthquakes.

These results highlight that in earthquakes, the dynamic stress drop (during seismically active rupture and slip) is likely to be much larger than the static stress drop (after the end of rupture propagation). However, these experiments have limitations: they are unconfined, are performed under relatively low normal stresses conditions, and are actuated by imposing a non-spontaneous, slip velocity impulse. To overcome this, in a series of recent experiments Passelègue et al. (2016) and also Brantut et al. (2016) were able to position strain gauges on laboratory faults with spontaneously propagating earthquake ruptures at high normal stress conditions (30-200 MPa). The strain gauges were conditioned to record at high frequencies (1 MHz) in order to track the dynamic evolution of shear stress during rupture propagation, as faults slip at m/s's.

Results show that simulated faults in granite weaken significantly during the propagation of dynamic rupture along pre-cut surfaces (Figure 1.8). These results have provided the first experimental verification that crustal rocks at hypocentral conditions, (1) can show substantial and extremely fast dynamic weakening during rupture propagation and (2), can easily transition to super-shear rupture velocity after only a few centimetres of rupture propagation, provided sufficient initial load. These experiments thus provide a route

towards characterising the physical properties of rocks during earthquakes in a more realistic manner than rotary shear experiments.

1.3.4 The earthquake energy balance

As already discussed, earthquake propagation is controlled by a balance between the strain energy release from fault weakening, on the one hand, and the energy required to propagate the earthquake rupture, on the other. Figure 1.9 schematically summarises this balance and is labelled to show the energy source and the different energy sinks that exist during the propagation of rupture.

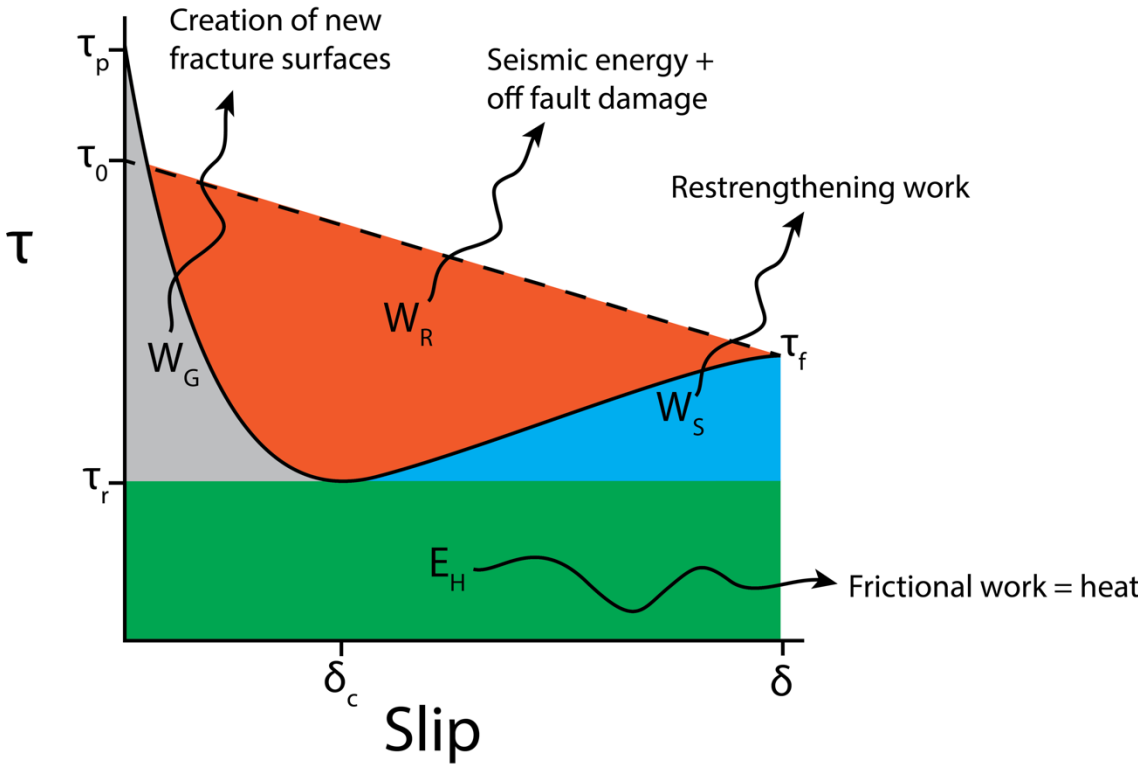

Figure 1.9 Graphical representation of the energy budget of a self-healing slip-pulse earthquake rupture, modified after Kanamori and Brodsky (2004).

The dashed line from τ_0 to τ_f represents the change of potential energy level during the entire rupture, or total energy, which is originating from the elastic strain in the surrounding elastic medium (Kanamori and Anderson, 1975). The solid black curve represents the (expected) frictional strength evolution accounting for a dynamic loss of strength from the peak stress τ_p to the weakened state τ_r over a distance δ_c. After weakening, slip continues until the potential strain energy and strength are at equilibrium and slip ceases (Perrin et al., 1995; Cochard and Madariaga, 1994). This results in a portioning of energy into distinct sinks, W_G represents the fracture energy, which is

consumed by the creation of new fracture surfaces (Abercrombie and Rice, 2005; Ida, 1972; Andrews, 1976; Palmer and Rice, 1973). E_H represents the frictional work, which is largely released as thermal energy and drives weakening processes (Rice, 2006). W_S is the work against strengthening which occurs as the fault decelerates due to co-seismic healing (Tinti, Spudich, et al., 2005). Finally, W_R, which is the difference between the frictional curve and the change in potential strain energy, represents the radiated energy. Radiated energy is dissipated as elastic waves (Brune, 1991) and off fault damage through rock fracture and pulverisation processes (Doan and Gary, 2009; Dor et al., 2006).

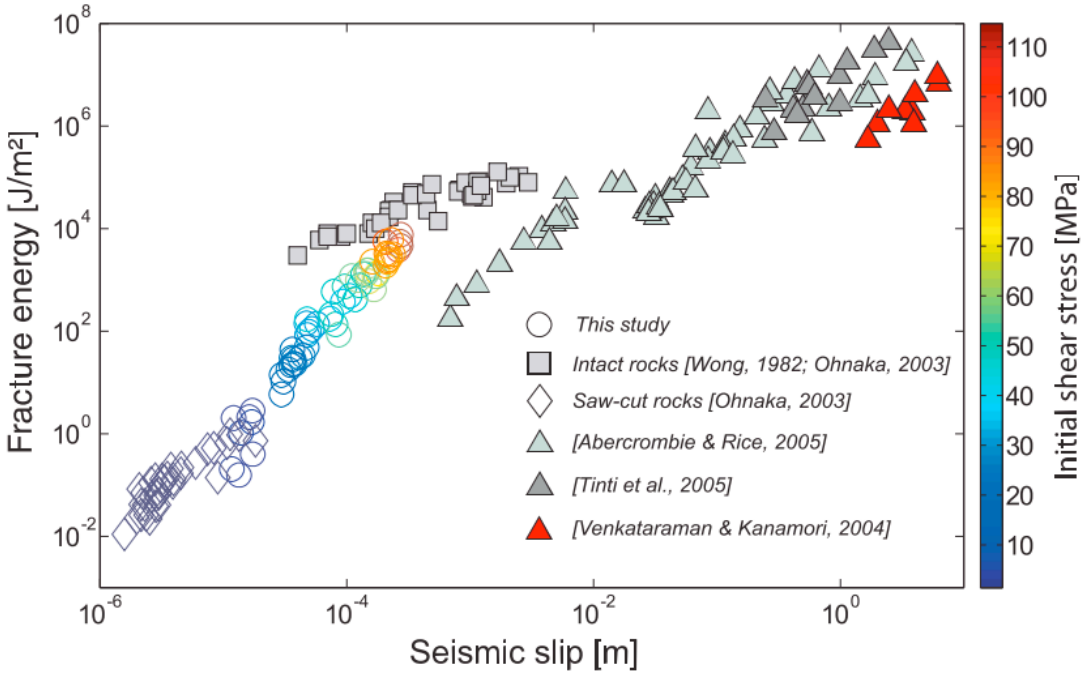

Figure 1.10 Fracture energy scaling relationships reported in previous literature deriving from experimentation and small earthquakes (M < 5.5), reproduced after (Passelègue et al., 2016).

Seismology has provided estimates of the fracture energy depletion during rupture propagation (Abercrombie and Rice, 2005; Tinti, Spudich, et al., 2005; Venkataraman and Kanamori, 2004; Nielsen et al., 2016; Viesca and Garagash, 2015). Fracture energy shows a power-law relationship with total slip, with a typical exponent of ~1.2-1.3 (Nielsen et al., 2016; Viesca and Garagash, 2015) for earthquakes of magnitude (M) less than 5. At M > 5, this scaling is observed to change to values of ~2/3, which is proposed to result from the onset of the increasing influence of either thermal pressurisation processes (Viesca and Garagash, 2015) or off-fault damage (Nielsen et al., 2016). Scaling between laboratory and seismological estimates (M<5) shows similarities with results obtained from intact rock failure (Wong, 1982; Ohnaka, 2003), from stick-slip failure on

a pre-existing interface (Passelègue et al., 2016, see Figure 1.10) and also from high velocity rotary shear experiments (Nielsen et al, 2016) .

Notably, consideration of the earthquake energy balance in Figure 1.9 highlights that seismic wave radiation released by the earthquake is only part of the story. Seismologists only have constraints on the radiated wavefield, the slip and the stress drop, but not on the absolute level of stress during rupture. The detail of frictional evolution, which is critical to determine energy partitioning (Kanamori and Brodsky, 2004), is therefore poorly constrained. Thus, in order to estimate the partitioning of energy during earthquake faulting, seismologist rely on frictional models derived from laboratory experiments and theory, which can provide absolute constraints on key parameters.

1.4 Anatomy of an earthquake

It is important to understand that the nucleation and propagation phases are intrinsically linked. Here I summarise literature observations into a conceptual model of an earthquake; this will provide an introductory framework for concepts used in the forthcoming chapters of the thesis.

Earthquake nucleation and propagation can be divided into a 3-phase physical process. I) the nucleation of a small slipping patch which tends to grow and weaken, sliding at slow sub-seismic velocities (0.001-10mm/s), with a small degree of acceleration (Latour et al., 2013; McLaskey and Kilgore, 2013; McLaskey and Lockner, 2014; Nielsen et al., 2010; Ohnaka and Kuwahara, 1990), until reaching a critical length scale L_c (Andrews, 1976; Passelègue et al., 2013; Rubin and Ampuero, 2005), which in its most general form is defined (Uenishi and Rice, 2003):

$$L_c = CGK^{-1} \qquad 1.10$$

Where C is a dimensionless crack shape factor and K is the previously defined stiffness associated to rate-and-state (K_c, equation 1.7) or slip weakening friction (K_s, equation 1.8) in Pa/m, which scales with the inverse of normal stress.

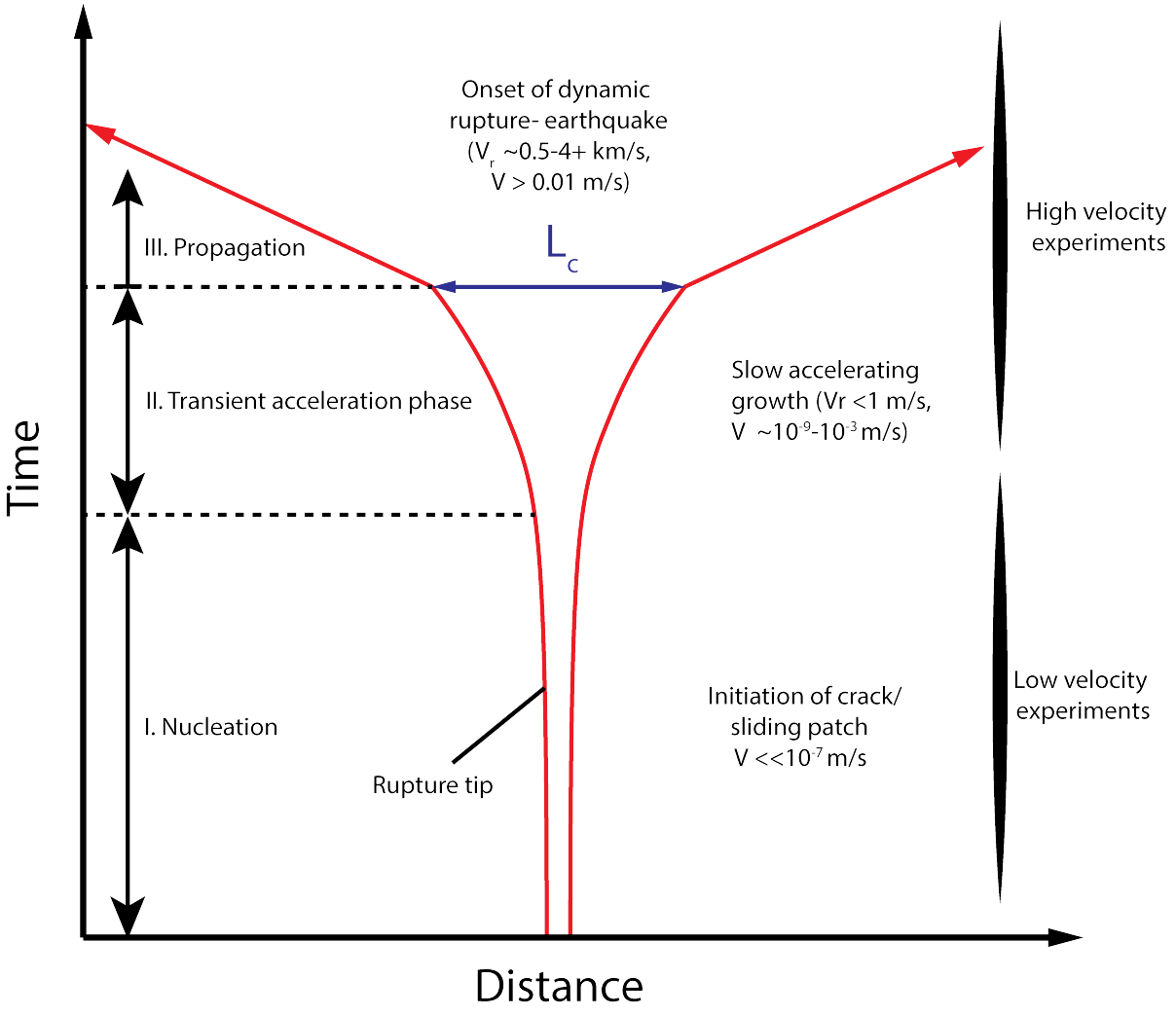

Figure 1.11 Schematic illustration of the spatio-temporal growth of an idealised earthquake. With approximate ranges of experimental validity. Inspired by Latour et al. (2013) and Ohnaka et al. (1999)

In stage (II), once the slipping patch exceeds the length scale defined in equation 1.10, acceleration continues until some limiting velocity (related to elastic waves velocity) is asymptotically approached (Ohnaka and Kuwahara, 1990). (III) Once the rupture velocity reaches a substantial fraction of the shear wave velocity in the medium (typically a few km/s) the earthquake enters the dynamic rupture phase which is characterised by a detectable amount of radiated kinetic energy (Latour et al., 2013; Nielsen and Carlson, 2000; Schubnel et al., 2011; Xia et al., 2004). This phase is the most energetic and therefore damaging stage of the earthquake as a result of the intense ground shaking caused by high frequency seismic radiation. This three-stage model allows to conveniently separate different processes involved in the different earthquake stages.

Field
Field
Field
Field
Field

1.5 The Structure of natural faults

To understand natural faulting processes and to reproduce them adequately in the laboratory environment, it is important to consider the structure of faults from a geological view. The archetype model of crustal fault structure comprises three distinct compartments: the country rock, the damage zone and the fault core, as shown in Figure 1.12 (after Mitchell and Faulkner, 2009; Faulkner et al., 2010).

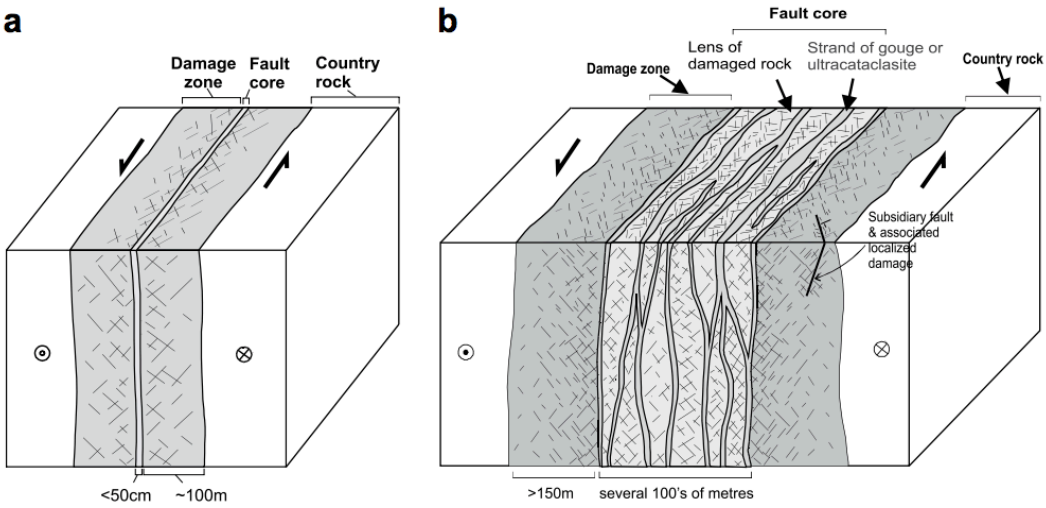

Figure 1.12 Typical structure of crustal faults in quartzo-feldspathic rock (after Mitchell et al., 2009) a) for a single core fault in a mechanically strong protolith, b) a multi core fault in a mechanically weak protolith.

According to this archetype, strain is largely localised to a narrow band of powdered rock within the fault core (typically <<1m), surrounded by a network of fractures comprising the damage zone (typically 10's – 100's m wide), hosted within a protolith of relatively intact rock. Fault cores are typically composed of a mixture of cataclasites, ultracataclasites and gouges, as a result of frictional wear and comminution processes taking place within the fault (Sibson, 1977; Blenkinsop, 1991; Sammis and Ben-Zion, 2008; Chester et al., 2005); within the fault core internal fabrics and structures show linkage, typically defining a through-going slip surface.

The geometry of slip surfaces has been studied fairly extensively across a wide range of scales (e.g. Candela et al., 2012). Recent attention has been devoted to modern scanning techniques that allow the measurement of the topography of faults surfaces on the lab-scale using atomic force microscopy (AFM), white light interferometry (WLI) and stylus profilometry (e.g. Brodsky et al., 2016; Candela and Brodsky, 2016), and up to the field scale using Lidar scanning and photogrammetric techniques (e.g. Bistacchi et al., 2011;

Sagy et al., 2007; Power and Tullis, 1991; Candela et al., 2012). Spectral analysis of fault slip surface measurements yields a consistent self-affine scaling across a wide range of scales (Bistacchi et al., 2011; Brodsky et al., 2016; Candela et al., 2012; Sagy et al., 2007). This power law is defined:-

$$P(k) = \alpha \left(\frac{k}{k_0}\right)^{-1-2H}$$

1.11

where, $P(k)$ is the expected power of the signal in m^3, k is inverse wavelength in m^{-1}, k_0 a reference inverse wavelength in m^{-1}, α a pre-exponential function in m^3 and H is the Hurst exponent. Typically faults occupy a narrow parameter space with H = 0.5-0.7 in a slip parallel direction and H = 0.7-0.9 in a slip perpendicular direction, α is typically between 10^{-7}-10^{-3} m^3 (H = 0.5 is self-similar, H ≠ 0.5 is self-affine). Self-similar surfaces will have the same aspect ratio at every scale of observation, whereas self-affine surfaces show topography that scales with the scale of observation according to the Hurst exponent. For example, surfaces of H > 0.5 will be rough on a small scale but appear smoother on a large scale. These results are consistent over scales ranging from 10^{-4} to 10^5 m (Candela et al., 2012). However, at scales below a cut-off of about 100 μm, the topographic distribution appears to become isotropic (invariant with respect to slip direction). This anisotropy cut-off is interpreted as the minimum scale of grooving, resulting from isotropic plastic flow at asperity tips (Candela and Brodsky, 2016). Mechanically, this cut-off scale has been related to the weakening distance D_c obtained from velocity stepping experiments, suggesting that this cut-off scale is a direct marker of asperity dimension.

Given that roughness dictates the nature of frictional contact in fault zones (Scholz, 1988; Yoshioka and Scholz, 1989; Dieterich and Kilgore, 1994), many authors have argued that it should have a significant influence on the sliding behaviour e.g. (Brodsky et al., 2016; Candela and Brodsky, 2016). Thereafter numerical models show that roughness affects a number of properties such as the static and dynamic strength of faults (Fang and Dunham, 2013), the rupture velocity (Dunham et al., 2003; Dunham and Archuleta, 2004) and nucleation scaling (Tal et al., 2018). In experimental studies, roughness has been little explored, but results suggest that it may affect both nucleation length (Ohnaka and Shen, 1999; Okubo and Dieterich, 1984) and rate-and-state parameters (Marone and Cox, 1994).

1.6 Thesis rationale

Typically, the frictional sliding experiments that are utilised to make inferences about crustal scale faults are performed on a carefully homogenised and sieved layer of gouge (or powdered rock) with constant thickness. However, it transpires from the above literature review that natural faults exhibit a strong inhomogeneity due to structural, geometrical or compositional complexity, which is poorly captured by performing experiments with fault gouge. Thus, a major aim of this thesis is to assess the applicability of current frictional sliding theories on faults with heterogeneous properties. This issue will be explored by conducting experiments on roughened faults, in a more realistic laboratory analogue which allows to consider the interaction of the fault with the protolith material.

Specific questions that will be addressed in this thesis are:

- What is the role of surface roughness and fault structure in the frictional sliding behaviour of rocks?
- More specifically how does roughness influence the stability of faults?
- How does rate-and-state theory apply to heterogeneous faults?
- What role does frictional wear play in the frictional behaviour of faults, how does roughness affect wear and vice-versa?
- What is the dynamic sliding strength of rough faults during spontaneous rupture propagation?

- Is it possible to describe frictional behaviour of rough heterogeneous faults with an appropriate microphysical model?

1.7 Thesis structure

Chapters 3 to 5 of this thesis are the results chapters of this thesis. They are presented as three ‘journal-style’ academic papers or manuscripts, and as such are designed to be standalone. Therefore, there may be some repetition of concepts and motivation in each

chapter introduction. Nonetheless, they contain a through-going theme and are further tied together in the conclusions, chapter 6, at the end of this thesis.

Each results chapter has either been published in, or is intended for submission to, a relevant academic journal within the field of Earth Sciences. These papers are multi-authored and as such my contributions are outlined below:

Chapter 3: Earthquake nucleation on rough faults. This chapter addresses the influence of fault roughness and heterogeneity on the nucleation of earthquake rupture, and also tests the applicability of rate-and-state friction on initially rough surfaces. This chapter has been published in *Geology* in August 2017. As first author of this paper my contributions included, performing friction experiments, design of new experimental techniques, processing and inverse modelling of data, processing of surface topography data, microstructural investigations, development of numerical models in MATLAB and manuscript preparation. Co-authors contributed training, useful discussion and editorial assistance. Concept design and theoretical developments were joint between myself and co-authors. This work also benefitted from reviews by Eric Dunham and two anonymous reviewers.

Chapter 4- Flash weakening during laboratory earthquakes. This chapter addresses the dynamic stress changes encountered during the propagation of earthquake rupture, and by measuring slip velocities in field of spontaneously propagating ruptures, a direct proof of flash heating models is given. This chapter has been submitted to *Nature Geoscience*. As first author of this manuscript my contributions included concept design, development of new experimental techniques, assembly and testing of acquisition systems and experimental components, microstructural investigations, data processing and analysis, MATLAB code development and manuscript preparation. Co-authors contributed training, useful discussion and editorial assistance.

Chapter 5: The influence of normal stress and roughness in limestone faulting. This chapter investigates the effects of roughness and normal stress in limestone faulting, and how wear and microstructural evolution of faults govern the mechanical behaviour of simulated fault zones. This chapter is intended for submission to *Journal of Geophysical Research: Solid Earth. As* first author of this manuscript my contributions included concept development, running friction experiments, data processing and inversions,

microstructural investigations, MATLAB code development and manuscript preparation. Co-authors contributed training, useful discussion and editorial assistance.

1.7.1 Appendices

Appendix I: machine calibrations for the triaxial deformation apparatus

Appendix II: is the published version of chapter 3.

Harbord, C.W.A., Nielsen, S.B., De Paola, N. and Holdsworth R.E. (2017), 'Earthquake Nucleation on Rough Faults', Geology, v. 45(10), p. 931-934, DOI: 10.1130/G39181.1

Appendix III: Is a manuscript which has been accepted for publication pending minor revisions in *Journal of Geophysical Research: Solid Earth* on which I am a co-author (my contribution was to run the triaxial friction experiments at high temperature, assist with microstructural work and manuscript editing)

Tesei, T., Harbord, C.W.A., De Paola, N., Colletini, C. and Viti, C. (In Press), '*Friction of Mineralogically Controlled Serpentinites and Implications for Fault Weakness', Journal of Geophysical Research: Solid Earth.*

Electronic appendix: Contains all inversion modelling results and supplementary microstructural images used to reach the conclusions made in this thesis.

2 Experimental methodology

2.1 Introduction

All experimental work in this thesis was conducted in a high pressure, high temperature triaxial deformation apparatus hosted at the Rock Mechanics Laboratory, Department of Earth Sciences, Durham University. This chapter gives a detailed outline of the triaxial deformation apparatus at Durham University. This is followed by an outline of high frequency strain measurement techniques and an outline of expected sources of error.

2.2 Triaxial deformation apparatus

The basics of the triaxial apparatus are outlined in the following. This is followed by a detailed description of the pressure vessel, sample assemblies, axial loading system, force measurements and servo-control system.

2.2.1 Basic design

The triaxial deformation apparatus used in this work is a high pressure, high temperature deformation rig, capable of applying up to 250 MPa confining pressure (~10 km lithostatic equivalent), 200 MPa pore fluid pressure and temperatures of up to 200°C (Figure 2.1). A differential load of <300 kN can be applied to the sample via a servo controlled electro-mechanical piston (Figure 2.1). Pore-fluid pressure is applied using a servo-controlled pump which can control pore fluid control at the top (upstream) and bottom (downstream) of 20mm diameter samples. As the pore fluid system was not utilised in this thesis it will not be discussed further (for more information see (Mitchell and Faulkner, 2008)).

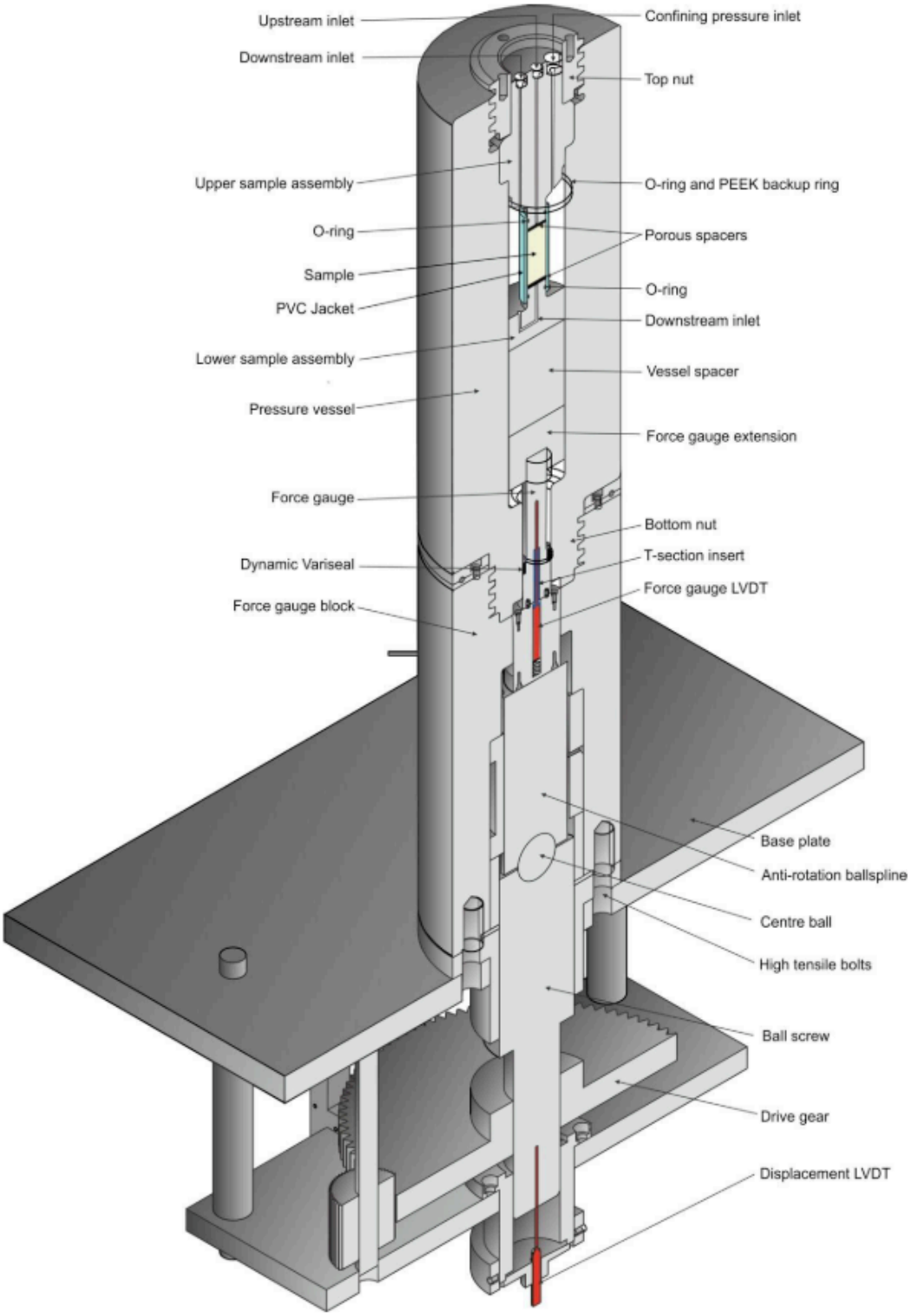

Figure 2.1 Scale drawing the triaxial deformation apparatus used to perform all experiments presented in this thesis. Reproduced after Bedford (2017).

2.2.2 Pressure vessel and standard sample assembly

The cylindrical pressure vessel is made from hot worked tool steel, Jessop Saville H.50 (AISI H.13) (Figure 2.1). It has an outer diameter of 180 mm and an internal bore of 60

mm. The maximum safe working pressure of the vessel is 250 MPa, which has been tested up to 375 MPa, 1.5 times the working pressure, in accordance with the High-Pressure Safety Code. The pressure vessel is mounted at the top of the apparatus, above the axial loading column. Sample assemblies are inserted via a threaded top opening, which is secured using a threaded top nut. The vessel is sealed by a combination of a Viton O-ring and a PEEK delta back-up ring to prevent O-ring extrusion between the sample assembly and the vessel. The standard sample assembly (Figure 2.2) used for the majority of experiments consists of an upper and lower part with an experimental sample sitting in between. It is designed to accommodate cylindrical samples of 20 x 60 mm, of which the majority of samples are of 55-60 mm x 20 mm owing to the use of direct shear configurations.

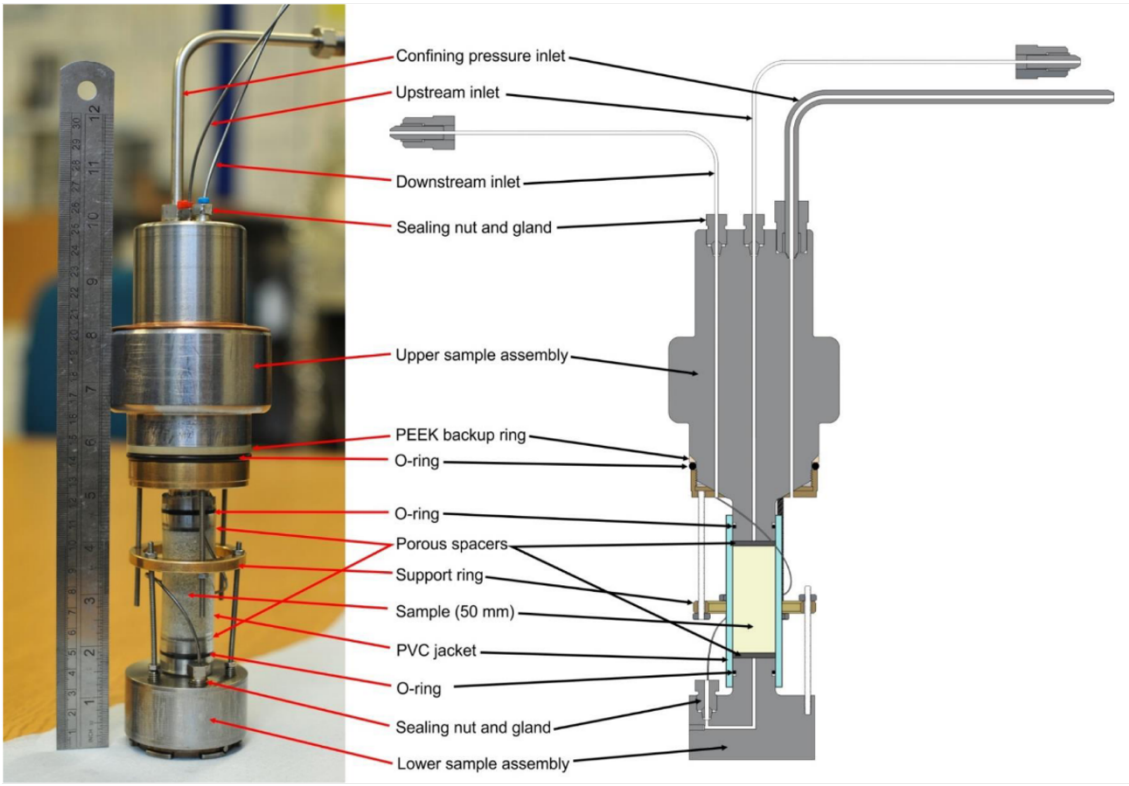

Figure 2.2 Photo and labelled diagram of the standard sample assembly. Reproduced after (Bedford, 2017).

Prior to insertion into the sample assembly, samples are inserted into a PVC jacket lined with Teflon to isolate it from the silicone oil confining medium, with the Teflon lining acting to minimise jacket friction. All jackets used in this thesis are made from PVC tubing, with an inner diameter of 19 mm and outer diameter of 25 mm, for experiments at temperature custom made Viton jackets may be used. The jacket is sealed against O-rings on the upper and lower parts of the sample assembly, and sample spacers of either

17-4 PH or 316 stainless steel are positioned above and below the sample (Figure 2.2). When conducting experiments in a direct shear geometry, a round Teflon shim was placed between the sample and the sample spacers to allow smooth lateral movement of samples (Figure 2.4).

2.2.3 Feedthrough sample assembly

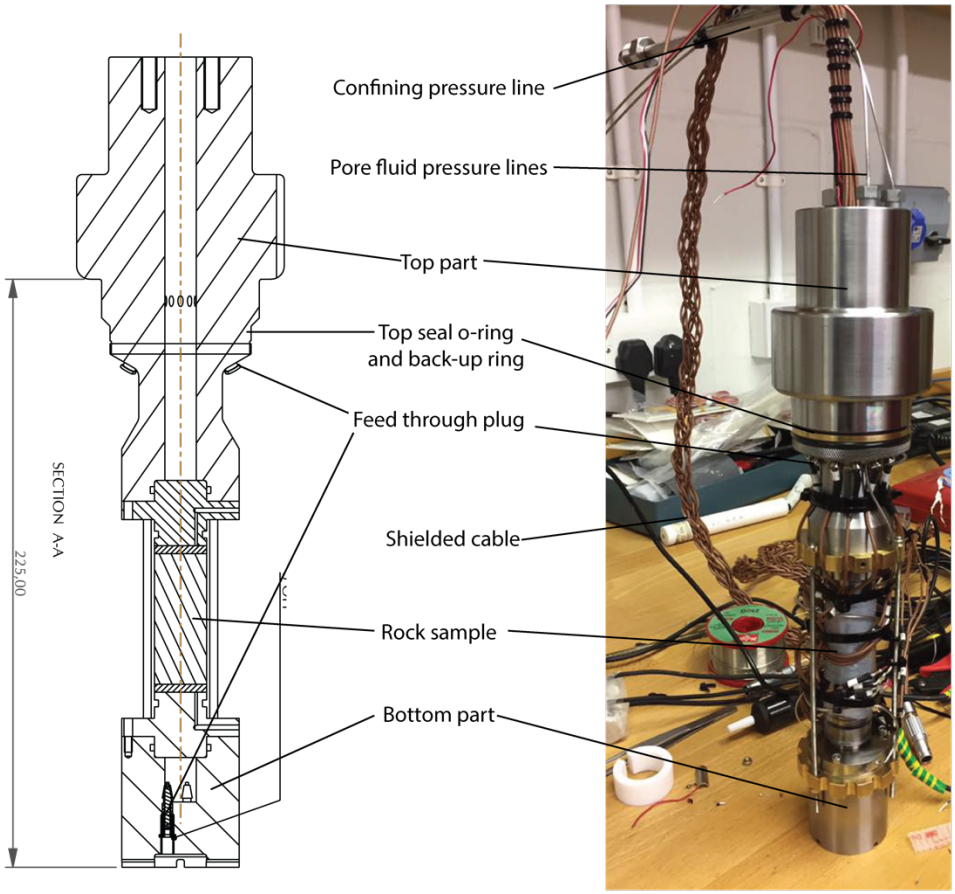

Figure 2.3 Labelled scale drawing and photograph of the feedthrough assembly used to conduct experiments using strain gauges.

To perform experiments with strain gauges installed on the sample, a modified sample assembly is utilised (Figure 2.3). The sample assembly is machined from 17-4 PH steel treated to condition H900. Signals are transmitted into the vessel using 12 narrow bore holes drilled to intersect a wide, long bore hole in the centre of the top part of the sample assembly (Figure 2.3). The narrow bore holes are tapered inwards toward the wide central bore, which provides a sealing surface against the confining pressure. Small silver steel feed through core inserts are encapsulated by PEEK sleeves, providing electrical isolation from the sample assembly. The cores and PEEK sleeves are secured in place on the pressure vessel side using threaded nuts. Shielded cable is soldered onto the cores which

attach to the sample on the pressure vessel side, or on the non-pressured side, run up the central bore of the sample assembly to external amplifiers and data acquisition units. Feedthroughs and LEMO connectors were soldered by the author, and systematically checked to ensure negligible wire resistance indicative of good electric connections.

2.2.4 Direct shear geometries

In this thesis, in order to conduct frictional sliding experiments, adaptations have been made to the experimental configuration. This has led to the development of new sample geometries that have improved the measurement and control of frictional sliding experiments. The first technique utilised was a solid single direct shear that is created by coring down a pre-cut interface, cored parallel to the interface (Figure 2.4a). This results in the creation of two semi-cylinders which are offset using silicon rubber spacers. Utilisation of direct shear techniques offers significant advantages over classical 30° saw cut geometries, as normal stress, shear force and displacement are directly equivalent to confining pressure, force measurements and displacement measurements respectively. It also avoids the need to make complex corrections for surface area changes and stress projections, and experiments can be run to larger displacements at comparable conditions. When jacketing the samples, they were wrapped in a Teflon sheet to reduce the sample friction with the jacket. This technique was successfully utilised for the experiments presented in chapter 3. However due to difficulties in reliable sample preparation and the requirement to use the technique with weaker lithologies, a newer geometry was also developed (Figure 2.4b).

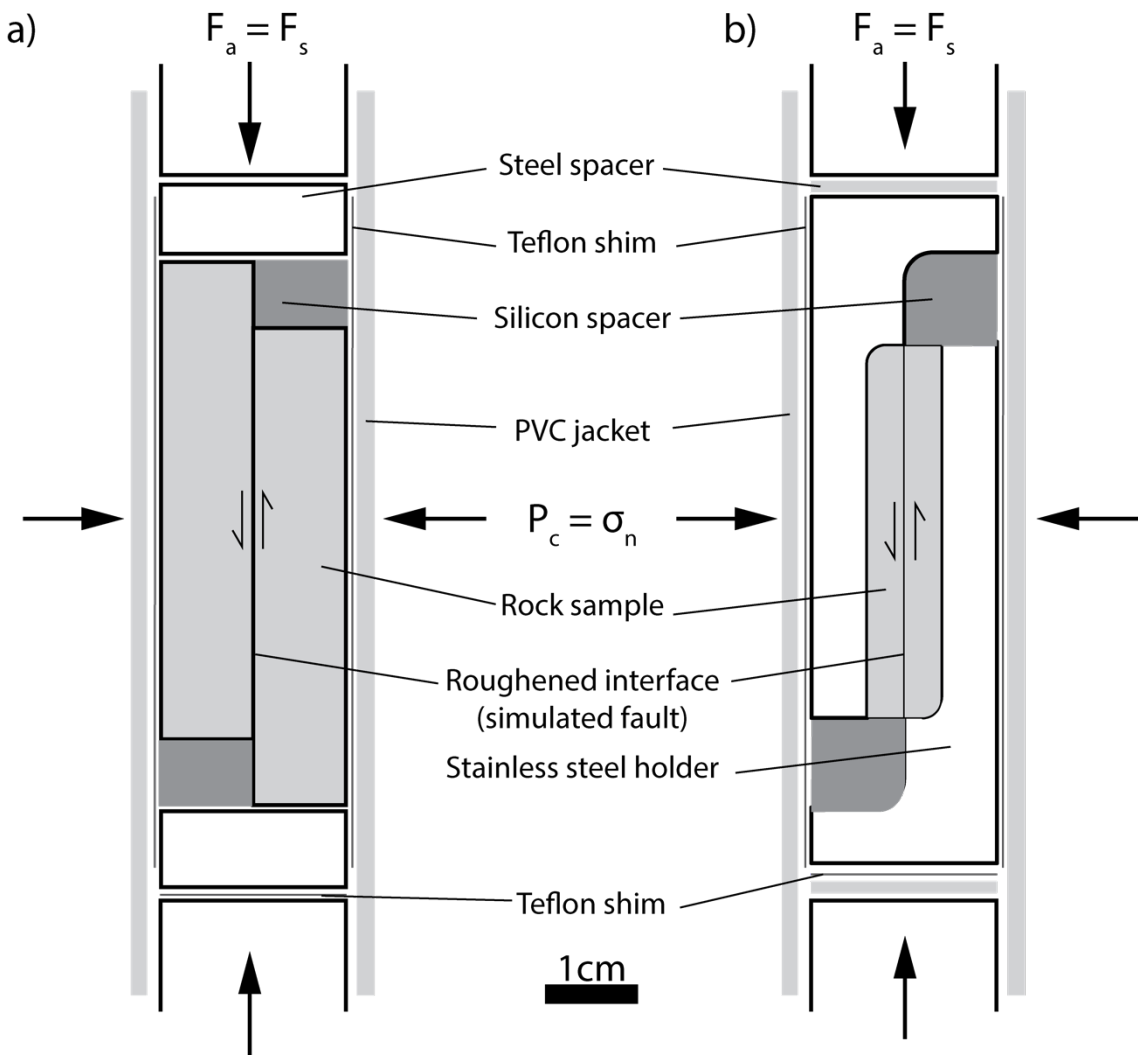

Figure 2.4 Experimental geometries used to conduct experiments presented in this PhD. Configuration a) solid single direct shear was utilised to conduct experiments in chapter 3, and configuration b) slabbed single direct shear to conduct experiments in chapters 4 & 5.

The second configuration retains the direct shear geometry however instead of solid semi-cylinders of rock the new geometry utilises slabs created by thick-sectioning rock (Figure 2.4b). An L-shape block made from stainless steel with a stepped section removed, was used house the blocks, which are glued in place using Loctite 636 superglue. This allows the use of mechanically polished sections which are parallel on the order of better than ±10 μm, with improved consistency in sample preparation. A small chamfer was applied to the loading edge of the sliders to eliminate the stress concentration on the corner of the L-shape. Typically, the samples are made 200-400 μm thicker than the loading ledge to avoid rock on metal sliding due to frictional wear. This assembly allows the use of weak lithologies, such as the limestone (also tested with serpentine and gypsum) used to conduct experiments in chapter 5. It was also developed to approach a 2-d geometry and

allow as close to an in-plane measurement of rupture strain fields for the high frequency measurements presented in chapter 4.

2.2.5 Confining pressure system

The confining medium used for experiments is a low viscosity, 0.01 Pa s silicone oil which enters the pressure vessel through a pipe at the top of the sample assembly (Figure 2.2 and Figure 2.3). Oil is preferentially utilised over water to prevent corrosion and increase the longevity of the pressure vessel. Pressure is increased by an air-driven SC hydraulic pump which can be isolated from the vessel once the desired pressure is reached. Measurements of pressure are by means of an analogue gauge (Figure 2.8) and a RDPE-J type transducer manufactured by Honeywell (Figure 2.7), with measurement accuracy on the order of ~0.01 MPa. Confining pressure can be manually controlled with a Nova Swiss 10cc syringe pump. During introduction of the axial piston to the pressure vessel the syringe pump is retracted due to volume loss inside the pressure vessel. Generally, this results in control better than +/-0.1 MPa.

2.2.6 Axial loading and force gauge block

Axial load is applied using an electro mechanical servo controlled axial piston. This consists of force gauge column that protrudes into the base of the pressure vessel, directly driven by a ball screw actuator from below (Figure 2.1). The pressure vessel is screwed into the force gauge block, which is in turn attached to the base plate of the apparatus using eight M16 high tensile bolts (Figure 2.1 and Figure 2.6). A spacer sits between the pressure vessel and the force gauge block which may be replaced with a cooling plate for high temperature experimentation (Figure 2.1). This creates a thermal block which minimises the effects of elevated temperature on the force gauge measurements. Force gauge sealing is achieved using a dynamic Variseal manufactured by Trelleborg ltd., supported by two PEEK back up rings (Figure 2.5). This prevents leaking of confining oil leaking from the bottom of the vessel. The force is delivered to the sample through a threaded force gauge extension block.

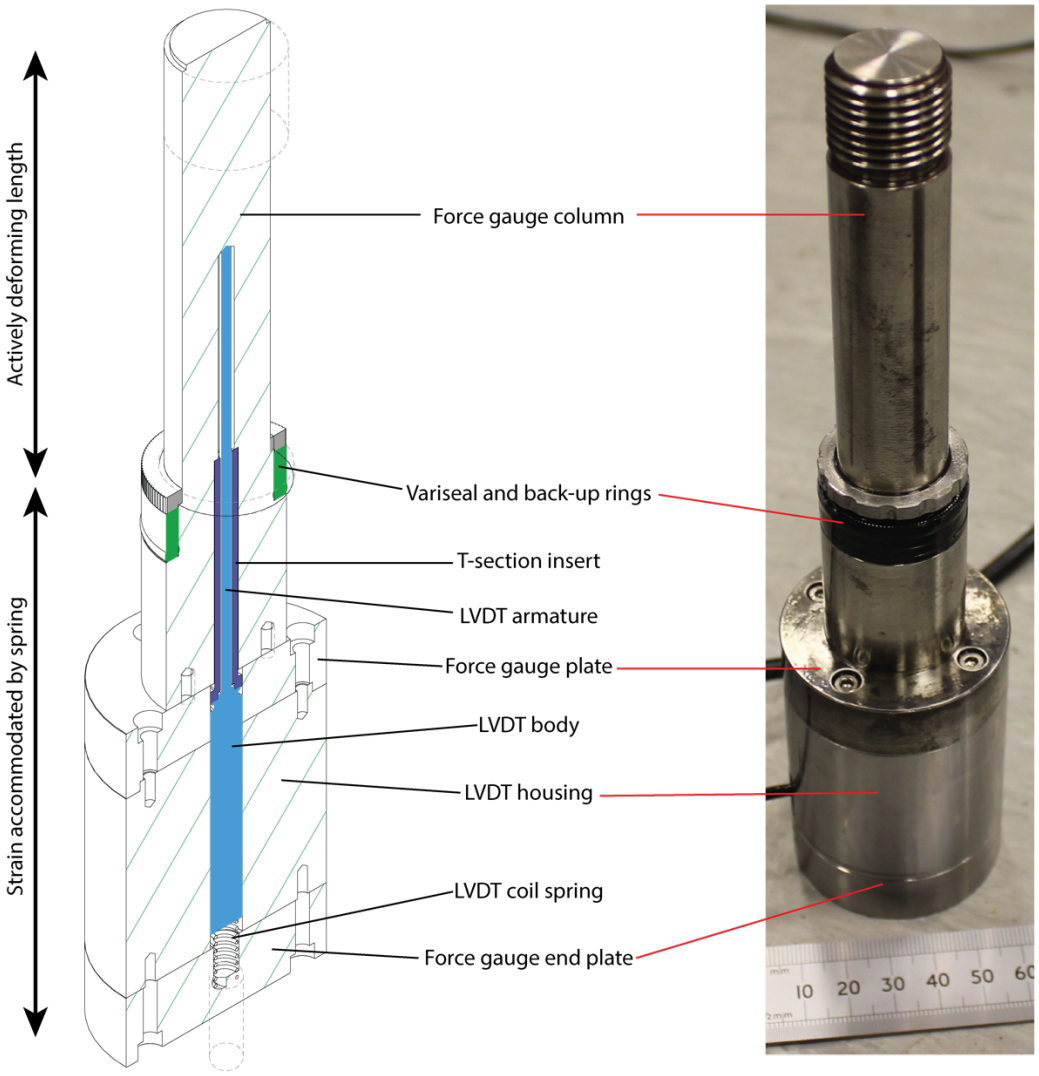

Figure 2.5 Photo and diagram of the force gauge. See text for detail.

As shown in Figure 2.5, force measurements are derived from the measuring the elastic distortion of the force gauge column. A linear variable displacement transducer (LVDT) is located internally within the column which is inserted into a T-section which provides both support and guidance to the LVDT armature. The LVDT insert is pushed against a shoulder within the force gauge housing, above the level of the Variseal. Therefore the actively deforming length of the gauge sits above the seal and no correction for seal friction is therefore necessary (Paterson and Wong, 2005). The force gauge column is made from M300 maraging steel, which has a yield strength of ~2 GPa. The ball screw can support a maximum load of 500 kN, which results from 300 kN at maximum load plus 200 kN acting on the ball screw at 250 MPa. For a 20 mm sample loaded to 300 kN the differential stress on the force gauge would be ~1 GPa, resulting in a safety factor of ~2 at extreme conditions. The overall force gauge resolution is on the order of +/- 10 N.

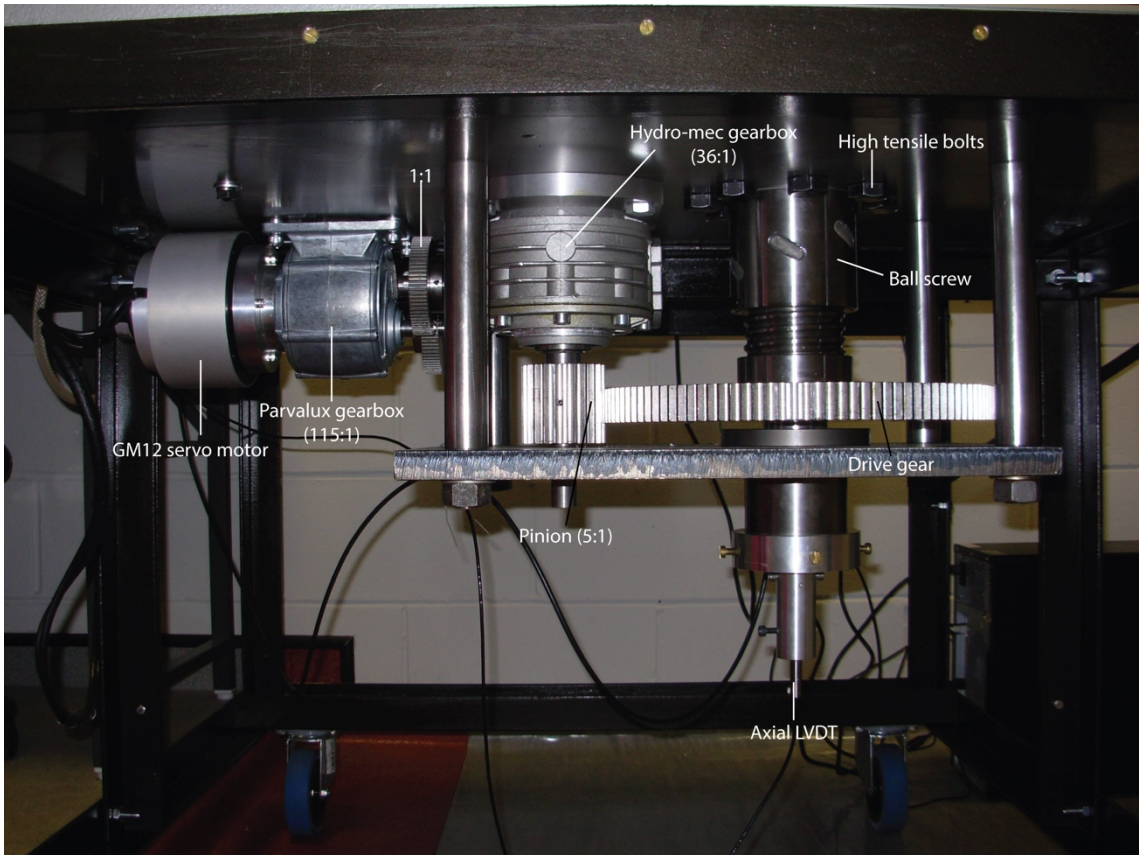

Figure 2.6 Labelled photograph of axial load system. The printed motor works GM12 pancake servo motor drives the gear train, subsequently rotating the ball screw. Axial displacement is measured by an LVDT attached to the base of the loading column. High tensile bolts are utilised to connect the axial loading column to above to the rig base plate.

The force gauge column is positioned above a high torque anti-rotation THK ball spline, which moves along a vertical ball bearing raceway to minimise friction. The base of the spline has a hemispherical geometry which allows coupling to the ball screw (Figure 2.1). The ball ensures that force is transmitted concentrically from the screw to the spline. A helical ball bearing raceway allows the ball screw to rotate with low friction under high loads. The screw is driven by a Printed Motor Works GM12 pancake-type servo motor and gear train (Figure 2.6). The gear train consists of a Parvalux gearbox with a 115:1 ratio connected in series to a Hydro-mec worm gearbox with 36:1 ratio. This finally coupled to the pinion of the main drive gear which has a ratio of 5:1, resulting in a final 20700:1 ratio between the motor and the ball screw (Figure 2.6). The motor has a maximum speed of 3000 rpm, which generates 0.14 rpm at the drive gear. Given that the lead of the ball screw is 10 mm, the maximum loading velocity is therefore 23 μm s^{-1}, however in practise this is ~14 μm/s (see thesis appendix for voltage velocity calibrations.

2.2.7 Data logging & servo-control system

All data is logged using LabView software. This also acts a control interface in conjunction with a series of servo control boxes which convert the DC voltage output from the NI digital input/output interface. A schematic illustration of the pressure circuits and control systems is shown in Figure 2.7.

The control script was written by D. Faulkner (Pers. Comm.) and can be programmed to explore a wide range of experimental conditions. The rig has three LVDT's, which record the position of the pore fluid syringe pump, the axial displacement and the deformation of the force gauge. All LVDT signals are conditioned utilising an RDP 6000 unit, which outputs analogue signals amplified at a bandwidth of 10 KHz. Three Honeywell pressure transducers are utilised to monitor the confining pressure and the up- and down-stream pore fluid pressures. These are also amplified utilising the RDP 6000 amplifier. All output analogue signals are transmitted using coaxial cables which connect into a NI 9215 analogue to digital converter (ADC). The digital signal from the ADC is transmitted to the PC via a USB connection where digital signals are converted from raw voltage into physical values using machine calibrations (Figure 2.8), see appendix for calibrations.

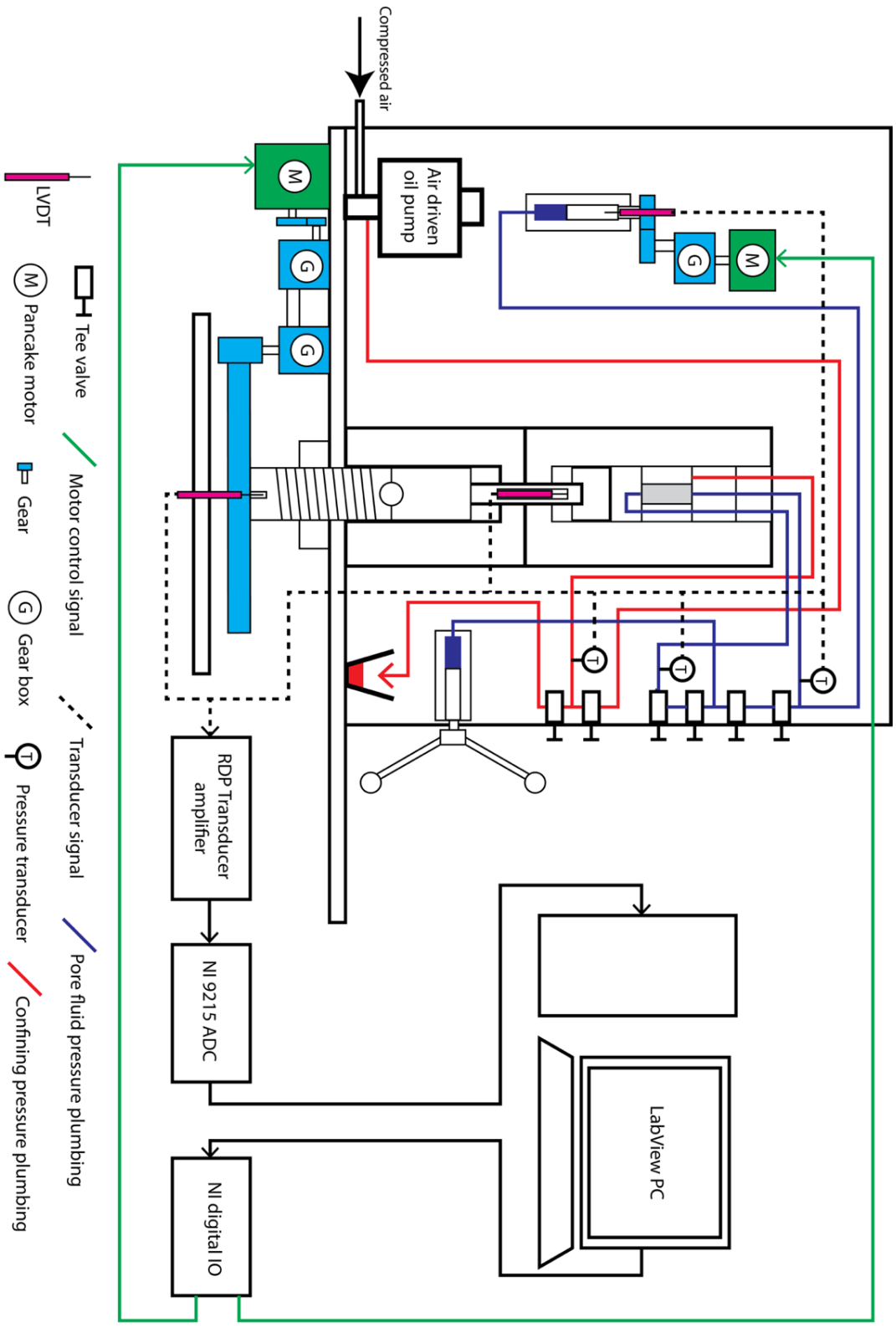

Figure 2.7 Schematic illustration of triaxial deformation apparatus components, data logging and control system utilised for all experiments.

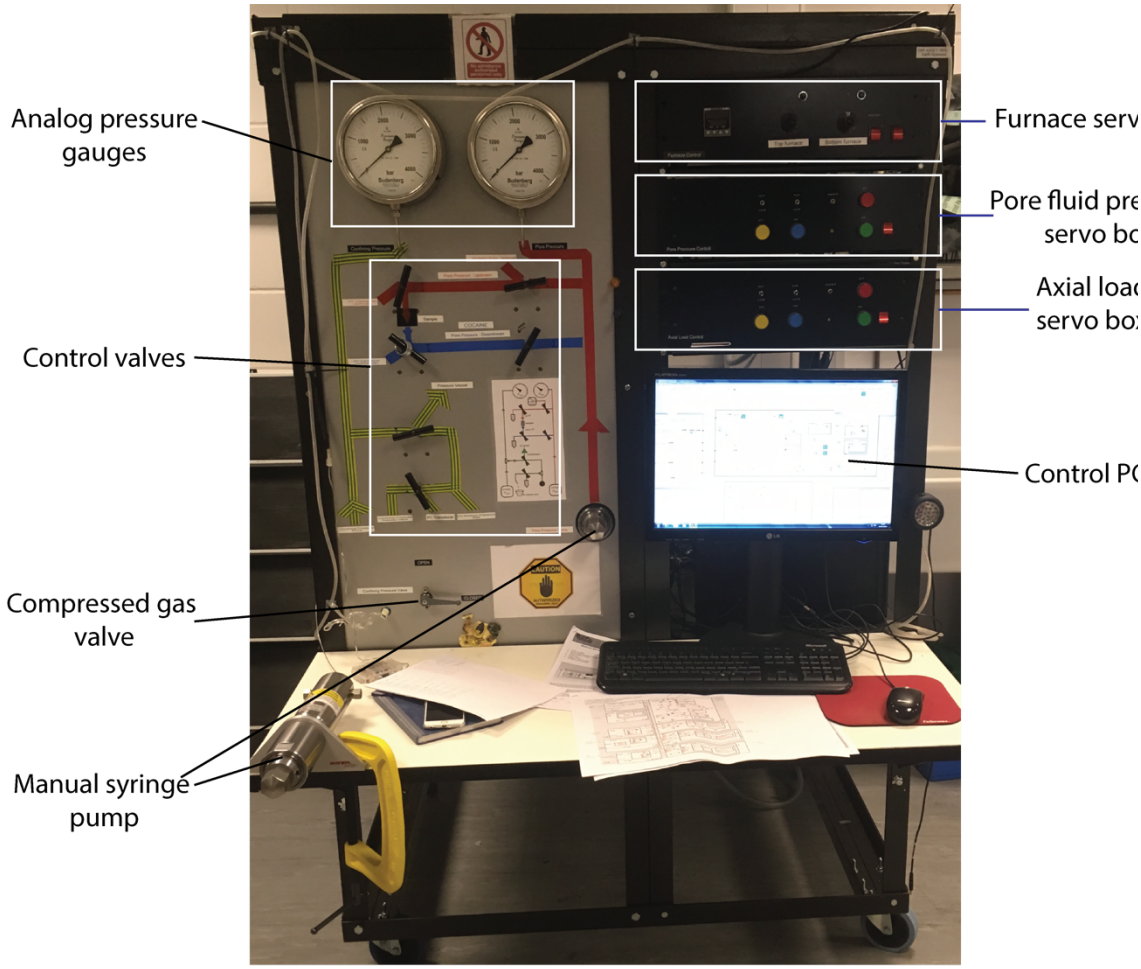

Figure 2.8 Labelled image of the front of the Dutff, showing key components and control systems.

In order to control the servo motors a Proportional Integral Differential (PID) open loop control was utilised for the experiments in chapter 5. PID operates on the principal of matching the control parameter in question, the process variable (PV), to a desired target value, the work set point (WSP), which is generated by the computer. Utilising the error ($e(t) = PV(t) - WSP(t)$), the system applies a series of mathematical operations to calculate the value of output voltage sent to the controlling motor. This is as follows:-

$$u(t) = K_p e(t) + K_i \int_0^t e(\tau)\, d\tau + K_d \frac{d}{dt} e(t) \qquad 2.1$$

Considerable time was devoted to tuning the PID coefficients (K_x) to find the choice of parameters which provided the best combination of fast step changes and stable velocity to provide reliable velocity step measurements.

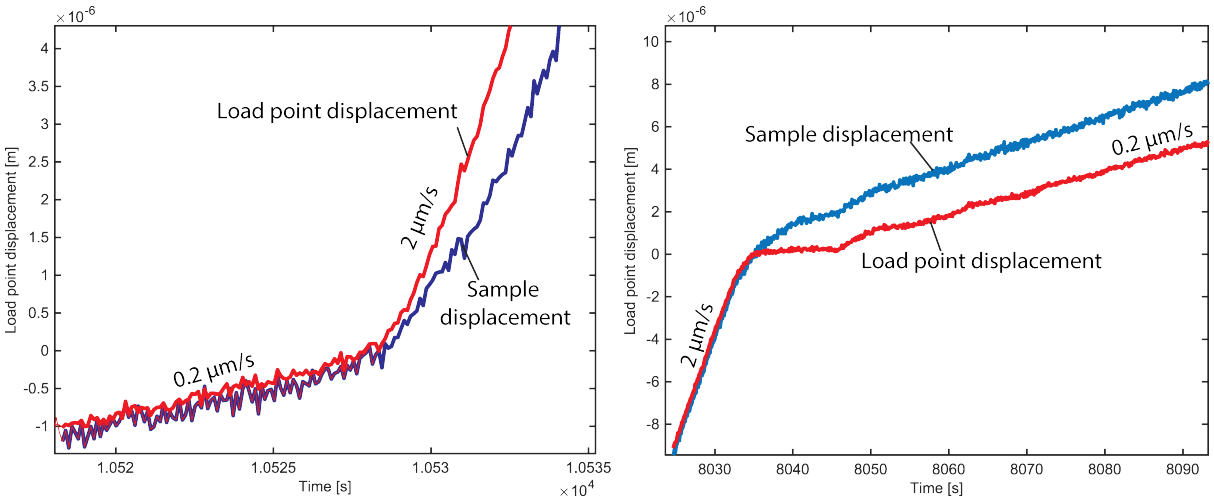

Figure 2.9 Control response of loading system and sample (obtained by removing stiffness) to step-wise change in sliding velocity for an experiment controlled using the PID loop in LabView, a) for a decrease in sliding velocity, b) for a decrease in sliding velocity. Taken from experiment Du206, 05/03/2018.

Generally, the velocity steps produced by the machine in open loop control are reliable during increases in velocity (up-steps) but are not as sharp on step-wise decreases (down-steps) (Figure 2.9). This is likely due to a number of factors, but they are largely due to the machine compliance, electromechanical gear system, and that displacement is measured in the far field. In order to circumvent this problem stepwise changes in input voltage were implemented and used for the experiments in chapter 3. Calibrations of the velocity response are available in the appendix.

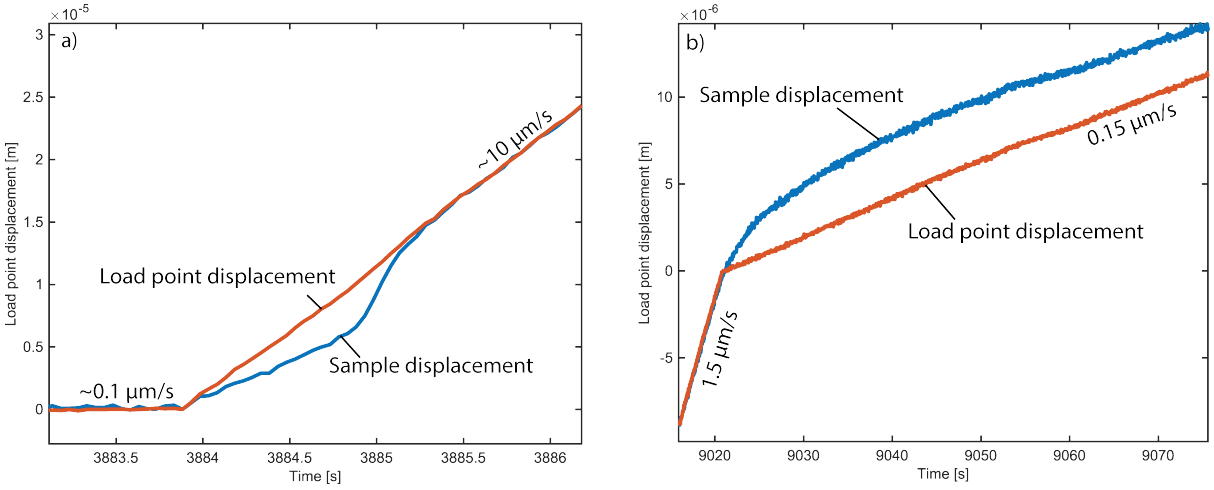

Figure 2.10 Control response of loading system and sample (obtained by removing stiffness) to step-wise change in sliding velocity for an experiment controlled using a constant voltage, a) for a decrease in sliding velocity, b) for a decrease in sliding velocity. Taken from experiment Du49, 06/05/2015.

This gave a much sharper machine velocity response, necessary for reliable RSF characterisation (Figure 2.10). However, this was limited by minor velocity oscillations during steady state velocity, likely due to torque changes induced by the meshing of gears in the drive train. During the course of completing the thesis various adaptations were made to the software. A velocity stepping and slide-hold-slide routine have been developed in order to perform experiments to derive rate- and state- parameters. Adaptations were also made to apply zero offset corrections to the force and confining pressure transducers.

2.2.8 Data processing

All data were post processed in MATLAB using algorithms developed through the course of the PhD. The script frictioncalc2.m was used to import data and calculate the friction coefficients, and imposed load velocity. A second script datasplit2.m, used in conjunction with an excel spreadsheet, is utilised to split experimental data files to isolate individual velocity steps and calculate the average velocity during the step and check its linearity. The velocity step data is then modelled utilising the script FSS 7.0 coded by Hiroyuki Noda (pers. Comm.) (Noda and Shimamoto, 2009). The script utilises a least squares regressive modelling algorithm (Levenberg-Marquardt), with adaptive time stepping. The code can be easily adapted to model the state evolution according to the differing formulations (e.g. aging law, slip law etc.), and also can be used to fit the machine stiffness as a model variable (Noda and Shimamoto, 2009).

2.3 High frequency measurements

2.3.1 Strain gauges

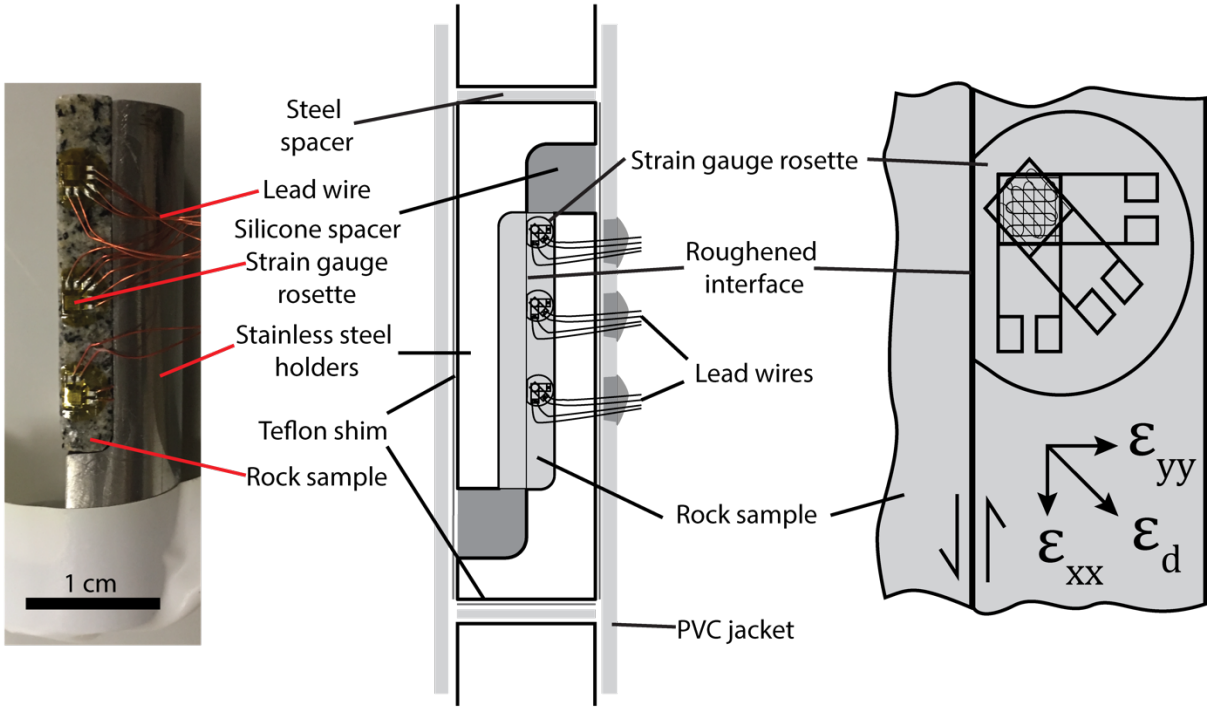

Figure 2.11 Labelled photograph and sketch of positioning and orientation of strain gauges on laboratory faults.

To infer the high frequency strain and stress changes during dynamic rupture propagation a series of strain gauges were affixed to samples (Figure 2.11). The gauges utilised were Micro Measurements G1350 which have a gauge resistance (R_g) of 120 Ohm (±0.6%), an active grid length (l_0) of 1 mm and a gauge factor (GF) of 2.1 ±0.2%[1]. The short patterns are optimal for measurements in regions of steep strain gradients, such as those expected around a propagating rupture tip. The gauge pattern consists of 3 stacked patterns orientated at 45° to each other, allowing measurement of the 3 principal strain components, ε_1, ε_2 and ε_3. To make full advantage of the number of feedthroughs available only 2 patterns were utilised per gauge, and the gauges orientated such that fault parallel strain (ε_{xx}) was directly measured as well as strain at 45° to the fault (ε_d) (Figure 2.11).

[1] Information taken from: http://www.vishaypg.com/docs/11377/G1350.pdf on 06/06/18.

To maximise channel usage gauges were wired in a two-wire quarter bridge configuration which was balanced using an internal resistor within the amplifier, shunt calibration was then utilised prior to sample pressurisation. Gauges were affixed using Loctite 636 glue and lead wires extracted through a small hole punched through the jacket. Once the wire was soldered up to the feedthrough connections the hole was backfilled using Loctite Hysol 9455 flexible epoxy.

Gauge signals were conditioned utilising a strain gauge amplifier, Elsys SGA-2, which has scope for simultaneous amplification of up to 24 channels (Figure 2.12). The amplifier has a bandwidth of 1.5 MHz at a gain of 1 & 10 which reduces to 600 KHz at a gain of 100, the gain error is < ±0.1%. Signals are output at an impedance of 50 Ohm through BNC ports and the gauge excitation voltage can be set to ±2.5 or ±5 V_{dc}.

Raw gauge signals were converted to strain following the formula below:

$$\varepsilon(t) = \frac{-4V_{out}(t)}{G_f\left(V_{in} + 2V_{out}(t)\right)}(1 + \epsilon) \qquad 2.2$$

Where $\varepsilon(t)$ is the time dependant strain, $V_{out}(t)$ the output voltage, V_{in} the voltage applied across the bridge, and ϵ an error term accounting for lead wire resistance which was determined to be ≈0.01. This is subsequently low pass filtered using an 8th order Finite Impulse Response (FIR) filter at 250 KHz in MATLAB, to eliminate high frequency noise. Strain gauge signals were calibrated against the vertical strain imposed on a dummy sample in the triaxial, which also served to confirm the linearity of measurements (R^2 = 0.9997). The calibration was used to apply a correction to the signals during processing. Plots of a calibration are shown in the thesis appendix.

2.3.2 Data logging

To log the high frequency strain signals a combination of techniques were utilised. For the majority of experiments, data were continuously recorded at 10 MHz using 2 Richter units manufactured by ASC Itasca. The Richter ADC system can record data at a maximum rate of 10 MS/s across 4 channels per unit, which are synchronised across up to 6 units in a master-slave configuration recording at 16-bit resolution. Alternatively, a Cecchi system (also manufactured by ASC) was trialled but no results from this method are presented in this thesis. The system acquires data in a triggered mode by utilising a

PAC R6A piezo sensor. The Cecchi system can record data up to 50 MHz, 80 V peak to peak and 128 kilo-samples recorded per channel at a 12-bit resolution. This is also configurable in a master/slave clock synchronisation.

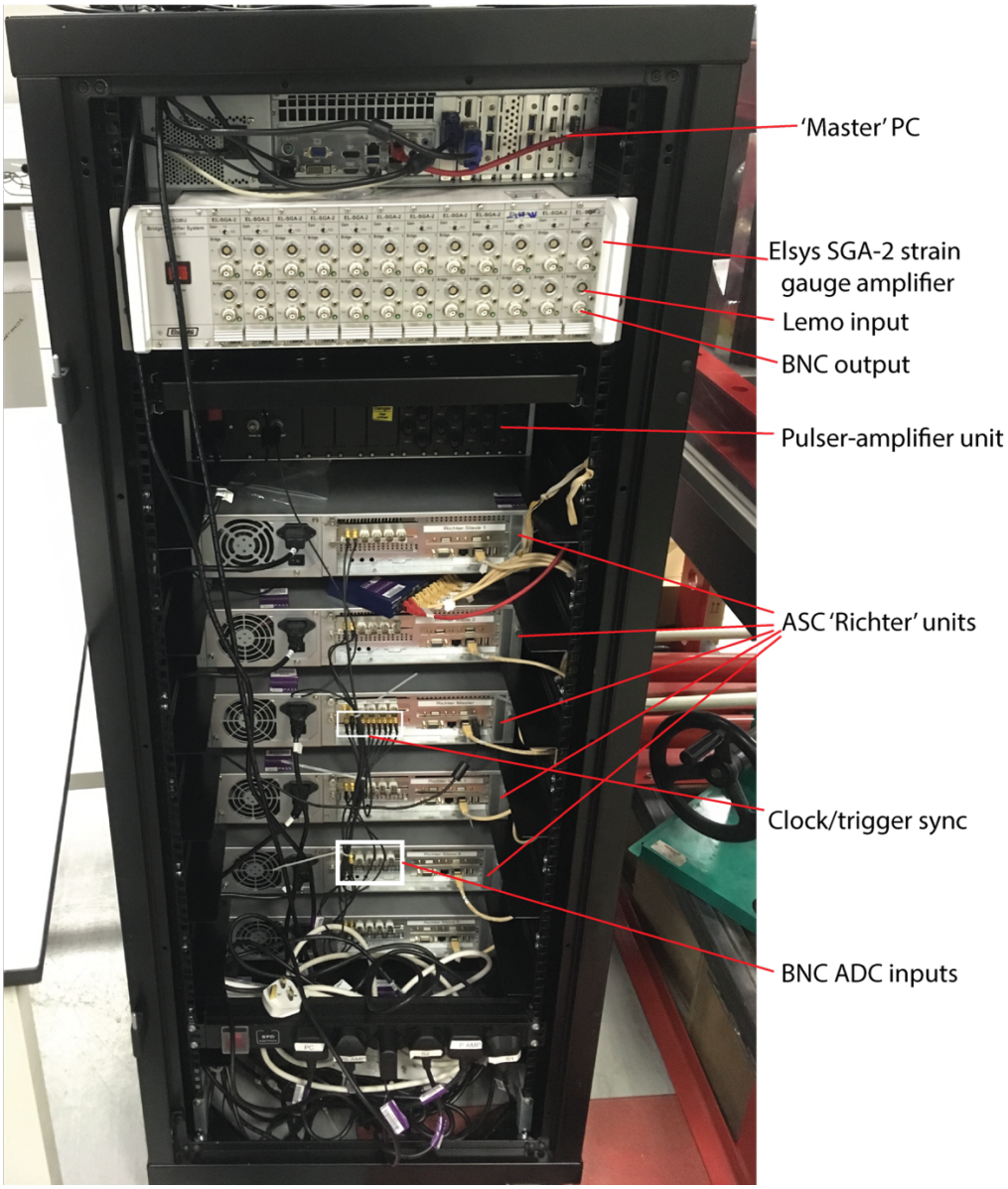

Figure 2.12 Labelled photograph of the high frequency acquisition system used to collect strain gauge data in conjunction with the feedthrough assembly.

2.4 Potential sources of error

All voltages read by the pressure transducers and the distortion of the force gauge measured by the internal LVDT requires calibration against an external pressure gauge and load cell respectively (see appendix for calibrations). The displacement of the axial load column also requires calibration against an external dial gauge. Therefore, unavoidable calibration errors will be introduced into any measurements, but these can

be avoided by careful procedures and repeat calibrations. Electrical noise can also produce an error on the output signals, which is typically low (<0.01 MPa in pressure readings), so its effects are minor. However sometimes noise was induced by the operation of the rotary apparatus in the laboratory, so where possible experiments were not run simultaneously.

Another source of error is induced by diurnal temperature fluctuations in the laboratory, which can result in drift on the pressure vessel as a result of thermal expansions and contractions. However, the majority of experiments were conducted over a period less than 10 hours, therefore these effects were deemed to be minimal. To account for the long-term drift of signals, force values and pressure measurements were zeroed before loading at the hit point (where the loading piston comes into contact with the base of the sample) and pressurisation respectively.

As previously discussed, force measurements are derived from measuring elastic distortion of the force gauge, which should produce a linear force-displacement curve. However, there are several interfaces along the loading column, e.g. between the sample spacer and the bottom of the sample assembly. This results in loading curves that are not perfectly linear during loading of samples, especially when samples are initially loaded and loading interfaces are pushed together. It is therefore salient to isolate machine derived artefacts from real sample deformation.

Finally, errors may be induced by the sample preparation. All samples prepared for chapter 3 of this thesis were cored to 20 mm, ensuring that vertical pre-cuts were orientated parallel to the coring direction better than 0.2° and centred better than 0.05 mm using callipers and printed outlines to position the drill bit. Following this sample ends were ground to a tolerance of < 0.01 mm. Any sample which was deemed not to be up to this standard was discarded. For the slabs samples were mechanically polished using equipment utilised to make thin sections, by continuous rotation during polishing a surface parallelism of < 10 μm was achieved. These preparations are of paramount importance for experiments on roughened interfaces, which often suffer from poor sample preparation resulting in unwanted large topographic features causing heterogeneous stress distributions distinct from grit preparations. These errors are minimised by careful sample preparation.

3 Earthquake nucleation on rough faults[2]

Abstract

Earthquake nucleation is currently explained using rate-and-state stability analysis, which successfully models the behaviour of laboratory simulated faults with carefully prepared gouge layers of constant thickness and homogeneous properties. However, natural faults show roughness, topography, bends, segmentation and inhomogeneity at all scales; the influence of such irregularities on fault slip dynamics, the seismic cycle and earthquake nucleation is little explored. One key question is how roughness, which introduces a strong inhomogeneity in the fault characteristics and stresses, can influence the stability of faults, promoting either unstable seismic behaviour or stable fault creep. This issue is investigated in this chapter based on the results of frictional sliding experiments, conducted on faults with different roughnesses on granite samples at upper crustal conditions (30–200 MPa).

A wide range of behaviours is observed, from stable sliding to stick-slip, depending on the combination of roughness parameters and normal stress. Stick-slip is repeatedly observed under velocity-strengthening friction regimes and increases in normal stress stabilize slip; these features are not fully predicted by current models based on stability analysis. A new instability criterion is derived which matches observations, based on fracture energy considerations and the size of weak patches created by fault roughness.

[2] The results of this chapter have already been published in the peer reviewed Journal *Geology* (Harbord et. al., 2017).

3.1 Introduction

A central question regarding tectonic faults concerns the onset of earthquake-generating stick-slip as opposed to aseismic stable sliding. This problem has been addressed in observational (Dodge et al., 1995; Socquet et al., 2017), theoretical (Rice and Ruina, 1983; Rubin and Ampuero, 2005; Gu and Wong, 1991a; Rice, 1993; Dieterich and Kilgore, 1996b; Uenishi and Rice, 2003) and experimental studies (Leeman et al., 2016; Scuderi et al., 2016) using the predictions of rate-and-state friction law and stability analysis, where instability develops under velocity-weakening friction and low mechanical stiffness (Leeman et al., 2016; Scuderi et al., 2016). However, most experiments have been conducted on homogeneous materials, either generating slip in a constant thickness gouge layers e.g. (Leeman et al., 2016; Scuderi et al., 2016) or on roughened cohesive rock surfaces e.g. (Passelègue et al., 2013; Ohnaka and Shen, 1999). Natural faults, on the other hand, are highly heterogeneous features with variable composition, physical properties and complex slip surface geometries (Bistacchi et al., 2011; Candela et al., 2012; Sagy et al., 2007; Brodsky et al., 2016, 2011).

In this study the effects of heterogeneity due to the roughness of fault surfaces, and its influence on the onset of unstable sliding is investigated. Roughness is observed on faults at all scales (Bistacchi et al., 2011; Brodsky et al., 2016; Sagy et al., 2007; Candela et al., 2012), and plays a key role in fault mechanics by determining the size and distribution of asperities (Dieterich and Kilgore, 1996a, 1994; Scholz, 1988), which control the stress distribution on the fault surface (Persson, 2013; Hansen et al., 2000; Borri-Brunetto et al., 2001; Selvadurai and Glaser, 2017; Stanley and Kato, 1997). (Asperities here are intended as local patches of enhanced contact with higher stress across the sliding surface, essentially due to protruding topography). It is therefore argued that roughness should have significant implications for both the static (Brodsky et al., 2016), and dynamic frictional strength of fault zones (Fang and Dunham, 2013), critical slip distances (Candela and Brodsky, 2016; Ohnaka and Shen, 1999; Okubo and Dieterich, 1984) and nucleation size (Okubo and Dieterich, 1984; Ohnaka and Shen, 1999). To date, however, only a narrow range of conditions haves been investigated experimentally (Marone and Cox, 1994; Okubo and Dieterich, 1984; Ohnaka and Shen, 1999).

Here, results are presented from the first systematic experimental study investigating the occurrence of frictional instability under a range of roughness and normal stress

conditions. It is shown that the combination of these parameters controls the onset of frictional instability of laboratory simulated faults. A microphysical model for observed patterns of behaviour, based on the interaction between maximum weak patch scaling, roughness and normal stress is presented.

3.2 Methods

3.2.1 Experiments

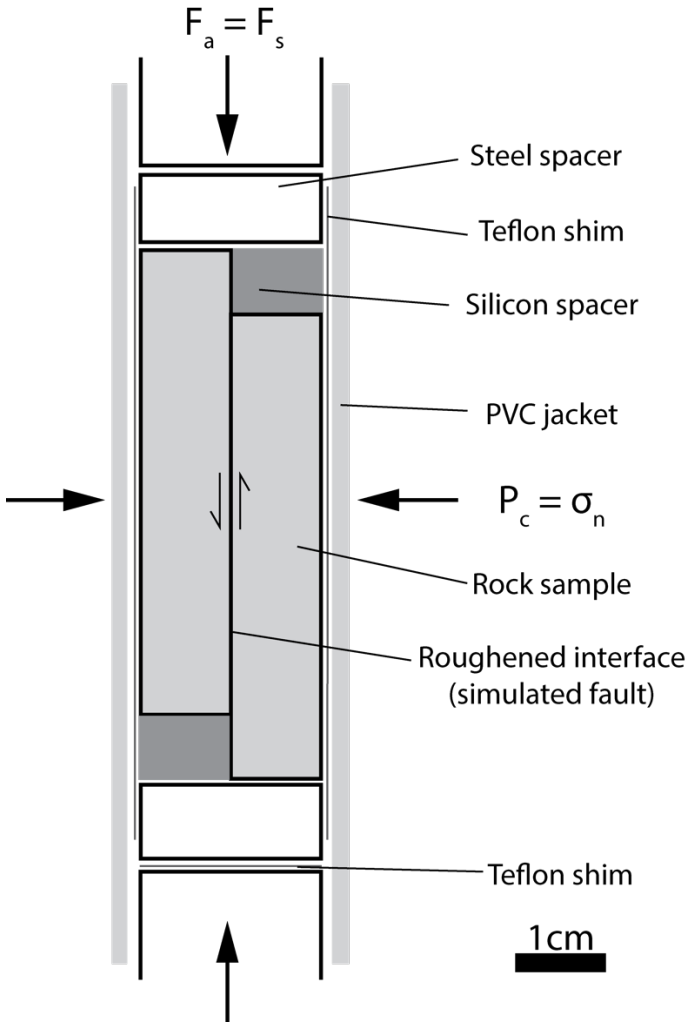

Figure 3.1 Schematic illustration of single direct shear methodology used for the experiments presented in this chapter. The offset between the two half-samples allows to convert the axial force F_a in direct shear. A is the nominal contact area of the sliding surface at any given time, τ and σ_n are the shear and normal stresses on the fault, respectively. P_c is the confining pressure, acting onto the sample through an impermeable jacket of Nalgene PVC. A Teflon shim is added between the sample and the jacket, to reduce friction between the sample and the jacket. See text for further details.

To simulate bare faults with differing initial roughness, axially pre-cut Westerly granite cores are utilised in a direct shear configuration, as is shown in Figure 3.1. This is an adaptation of previous techniques that have already been used to conduct frictional sliding experiments (Samuelson and Spiers, 2012; Leclère et al., 2016), utilising initially bare surfaces here. The fault surfaces are lapped to a fine polish to achieve a nominally flat surface (2.5 μm diamond finish), then they are wet ground with different alumina grits (#60, #100, #220, #320 and #400), to achieve various degrees of roughness depending on the experiment.

During experiments sample blocks are offset using silicon spacers to create a nominal contact area of 800-850 mm^2, which could be deformed to a total of 6 mm displacement, as shown in Figure 3.1. This offset results in a direct shear geometry, where normal stress σ_n is controlled by the confinement pressure ($\sigma_n = P_c$) and shear stress is calculated by dividing the axial load by the nominal area of contact ($\tau = F_a$ /A). Shear stress was calculated as follows:-

$$\tau = \frac{F_a}{W(L + u_c)} \qquad 3.1$$

where τ is the shear stress in Pa, F_a the axial load in kN, W the width of the surface in m, L the initial length of contact in m and u_c the stiffness corrected displacement in m. Here the stiffness corrected displacement is added to account for the increasing surface area during experiments. This configuration presents significant advantages over traditional 30^O sawcut experiments: load point velocity is directly equivalent to the fault velocity, no stress projections are needed, the nominal area of contact changes linearly with cumulative slip, and the normal stress on the fault is not altered by slip.

All experiments were conducted utilising a triaxial deformation apparatus, designed and built by D. Faulkner, as discussed in chapter 2. The apparatus is capable of up to 250 MPa in confinement pressure and 300 KN in axial load, with measurement accuracies of 0.01 MPa for the confining pressure, and an axial force resolution of +/- 10 N.

Experiments were performed by first increasing the confining pressure in the vessel to the target normal stress (30, 100, 150 or 200 MPa), using a compressed air driven pump. Following this the rig was left for 20-30 minutes to allow equilibration of the pressure.

Once a stable target pressure was achieved, the axial forcing piston was driven upwards until it contacted the loading column and the sample assembly, defining an initial "hit-point" for which all force and displacement data is corrected to. After the hit-point was reached, control was switched to a LabView interface and the friction experiment started.

For all experiments closed loop control was utilised. A constant voltage was supplied to the loading system servo motor, resulting in a constant loading velocity which was calibrated a-priori (see appendix) and verified a-posteriori during the experiment. (In case of velocity-stepping experiments a stepwise-constant voltage was supplied). The closed loop was utilised to give sharp step-wise changes in sliding velocity which are required for reliable RSF parameter characterisation. In all experiments an initial run-in period of 1-1.5 mm was utilised to reach initial steady state sliding conditions. Following this a sequence of velocity steps between approximately 0.1, 1 and 10 μm/s were applied to characterise the velocity dependence of friction during stable sliding episodes; during episodes of unstable sliding it was not possible to characterise RSF parameters, however in some cases it was possible to do so right before and after such episodes within the same experiment.

All mechanical data was post-processed in MATLAB. RSF parameters are calculated using FSS7.0 in MATLAB, written by H. Noda (Noda and Shimamoto, 2009) (pers. Comm.), which is based around linear regression techniques (Reinen and Weeks, 1993). All data are fit with a Dieterich's aging law for the state variable evolution (Dieterich, 1979b), where $\dot{\theta} = 1 - \frac{V\theta}{D_c}$.

3.2.2 Surface topography measurements

Surface topography was measured both before and after experiments using a Form Talysurf PGI 1250A stylus profilometry[3] at Durham Precision optics. The stylus profilometer measures topography by moving a spring-loaded armature over the sample surface. The armature has a reflective backing allowing a laser to measure the distance between a reference length and the armature backing. The instrument is capable of 200 mm scan lengths at a sampling interval of 0.125 μm, with a vertical resolution of 0.8 nm

[3]Stylus profilometer specifications obtained from http://www.zimmerman.com.tw/taylor/1250a/pgi1250A.pdf

and RMS noise level of 1 nm. The system utilises a 2μm radius diamond stylus which applies ≈ 1 mN force. For all presented scans a sample spacing of 1 μm was used to perform scans over 30 mm lengths along the slip direction, giving measurements over 5 orders of magnitude. All scans were run parallel to the slip direction.

Once the scans were complete all data was imported into MATLAB as a 2D matrix, the first column defining a 1D coordinate position along the fault slip direction (X) and the second column defining the elevation (Z) perpendicular to slip direction. Surface statistics were processed using routines developed by A. Corredatti (pers. Comm.). Any small overall trend in the profilometry was removed by subtracting the mean plane from the data (i.e., by setting the z axis parallel to the smallest surface eigenvector with the MATLAB function detrend.m). Once corrected, the 2-d data was converted into a 1D vector of z. Following this, data were interpolated to re-establish a regular spacing of the data points, with an interpolation distance (dx) of twice the average spacing of the original points (Candela et al., 2012) to avoid aliasing.

A taper in the form of a cosine function was applied to the outermost 1% of the surface measurement, this avoids the FFT becoming a function of the initial data point. The final profiles were analysed using FFT (the script psd_stylus.m was used, an adaption of the original code supplied by A. Corredatti) to calculate the signal power within the inverse wavelength range $(L/2)^{-1} < k < (2dx)^{-1}$, where L is the total scan length in m and k the inverse wavelength in m^{-1}. Multiple spectra were then averaged at each inverse wavelength. All data show a log-log-linear spectrum above a clear corner inverse wavelength, k_{min}. The corner inverse wavelength varies with surface roughness (defined in terms of Z_{rms}, see below), and was selected by taking a trend through two linear slopes of the spectrum. All statistics quoted are derived from the high inverse wavelength linear portion of the spectra, which is characterised by the following power law:

$$P(k) = \alpha \left(\frac{k}{k_0}\right)^{-1-2H} \qquad 3.2$$

Where P(k) is the average topography of the surface at inverse wavelength k, normalised by a reference inverse wavelength k_0 (here 1 m^{-1}), α is a constant prefactor (m^3) and H is the dimensionless Hurst exponent. As documented in a number of previous studies (Brodsky et al., 2011, 2016; Candela et al., 2012; Bistacchi et al., 2011), 3.2 is a

representative distribution for the topography of natural fault surfaces, where *H* in the range 0.6-0.8 is generally observed (*H* = 0.5 describes self-similar surfaces and equates to distributions generated by random Brownian motion, while H > 0.5 surfaces display self-affine scaling).

The root mean square roughness (Z_{rms}) of the surfaces was evaluated by numerical integration of the surface spectra, where Z_{rms} in m is given by:

$$Z_{rms} = \int_0^{1/k_{min}} P(k)dk \qquad 3.3$$

Where k_{min} is the corner inverse wavelength in m^{-1}. Using equation 3.2 for *P(k)* in equation 3.3 yields an analytical expression for Z_{rms} as a function of α and H, by:-

$$Z_{rms}|_0^{1/k_{min}} = \sqrt{\frac{\alpha k_0}{2H}}\left(\frac{k_{min}}{k_0}\right)^{-H} \qquad 3.4$$

Hereafter, the initial surface topography is quantified utilising Z_{rms}, as it provides a single combined parameter for the roughness statistics. In some cases, a trial of white light interferometry was performed, with data collected using a New View 7300. However, it was found to be difficult to measure the surface at DPO and so only a few measurements were made, the results are not reported in the surface statistics, but are used for making some of the contact models.

3.2.3 Elastic contact modelling

3.2.3.1 2D modelling

In order to investigate the nature of frictional contact in this chapter a series of modelling techniques were applied to the topographic data collected using the stylus profilometer and white light interferometry. The first method was based on the 1D crack face closure equation. Displacements along the length of a crack, $u_{zz}(\xi)$, are given by

$$u_{zz}(\xi) = \frac{(\upsilon + 1)\sigma}{4\mu'}\sqrt{\lambda^2 - \xi^2}$$

3.5

Where υ is the Poisson ratio, σ the far field normal stress (Pa), μ′ the shear modulus in (Pa), λ the length of the crack (m) and ξ the distance from the centre of the crack (m) (Jaeger et al., 2009). By rearranging equation 3.5 and substituting $u_{zz}(\xi) = Z$ it is possible to solve for the closure stress, σ_s, required to bring to closure each point of non-contact in the elevation vector. Following this, the minimum value of stress required for a single additional closure is found, with the corresponding position taken to represent a new asperity, a_n. The minimum closure stress is then added to the far field normal stress, and also used to calculate a modified topography between asperities. The length of each crack is defined as the distance between two consecutive asperities i.e.

$$\lambda_n = as_{n+1} - as_n$$

3.6

Where λ_n is the length of the nth crack in m, and as_n the nth asperity position. If asperities are positioned next to each other then they are considered to be part of the same asperity. Models are conditionally looped until the required range of stresses are spanned. At each value of stress, a counting algorithm is used to calculate the length of asperities. To qualify model validity, the results were checked by calculating the effective normal stress supported by the asperities $\sigma_c = \frac{F_n}{A_c}$ (where A_c is the real contact area across all asperities) yielding values of 5-10 GPa. These values are compatible with the indentation strength of the minerals found in Westerly granite (σ_c = 10, 8 and 0.8 GPa for quartz, feldspar and mica respectively (Broz et al., 2006)). The code *elasticclosure.m* used to implement these equations is available in the thesis appendix.

3.2.3.2 3D elastic modelling

In order to model surface contact in 3D, an implementation of Stanley and Kato's FFT algorithm was used (Stanley and Kato, 1997; Hansen et al., 2000), which solves for contact normal stress in an elastic half space. The surface is pressed against a mathematical plane of infinite hardness, which is expected to give the same modelling result as two contacting surfaces with similar topography statistics (Borri-Brunetto et al., 2001) because the resulting opening will have the same properties as the topography of a single surface.

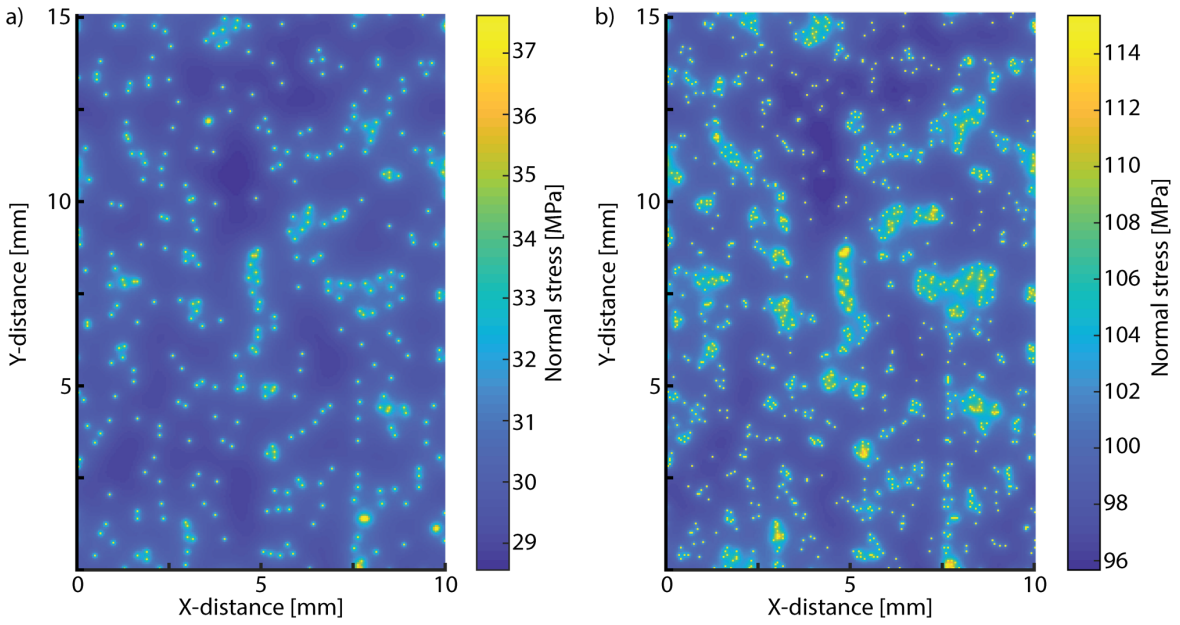

Figure 3.2 Snapshot of stress map obtained by implementation of the Stanley-Kato algorithm using the topography obtained from post-experimental measurements of experiment Du52b (Z_{rms} = 8 µm @ 100 MPa). Inset a) shows the results from loading a surface to 30 MPa, and inset b) from loading the surface to 100 MPa. Data taken from WLI measurements.

The initial condition is set by assuming that only the highest 3 points are in contact. Thereafter, the following procedure is iterated: (1) An infinitesimal force increase is imposed at the sites of the contact asperities. (2) The array of forces corresponding to step 1 is transformed to the Fourier domain and multiplied by a Green's function kernel. (3) The inverse Fourier transform of the multiplication from step 2 yields the deformation of the topography due to the forces' array. Steps (1-3) are repeated until a new point on the surface reaches zero elevation, at which point a new asperity contact is formed. (4) Steps (1-3) are resumed with four contact asperities, then five, and so forth until the net force across all created asperities matches the normal force across the sample. These models were utilised to generate the asperity maps presented in Figure 3.12. Snapshots of the modelling are shown in Figure 3.2 which are generated using the FFT procedure defined above.

3.3 Results

3.3.1 Surface topography statistics

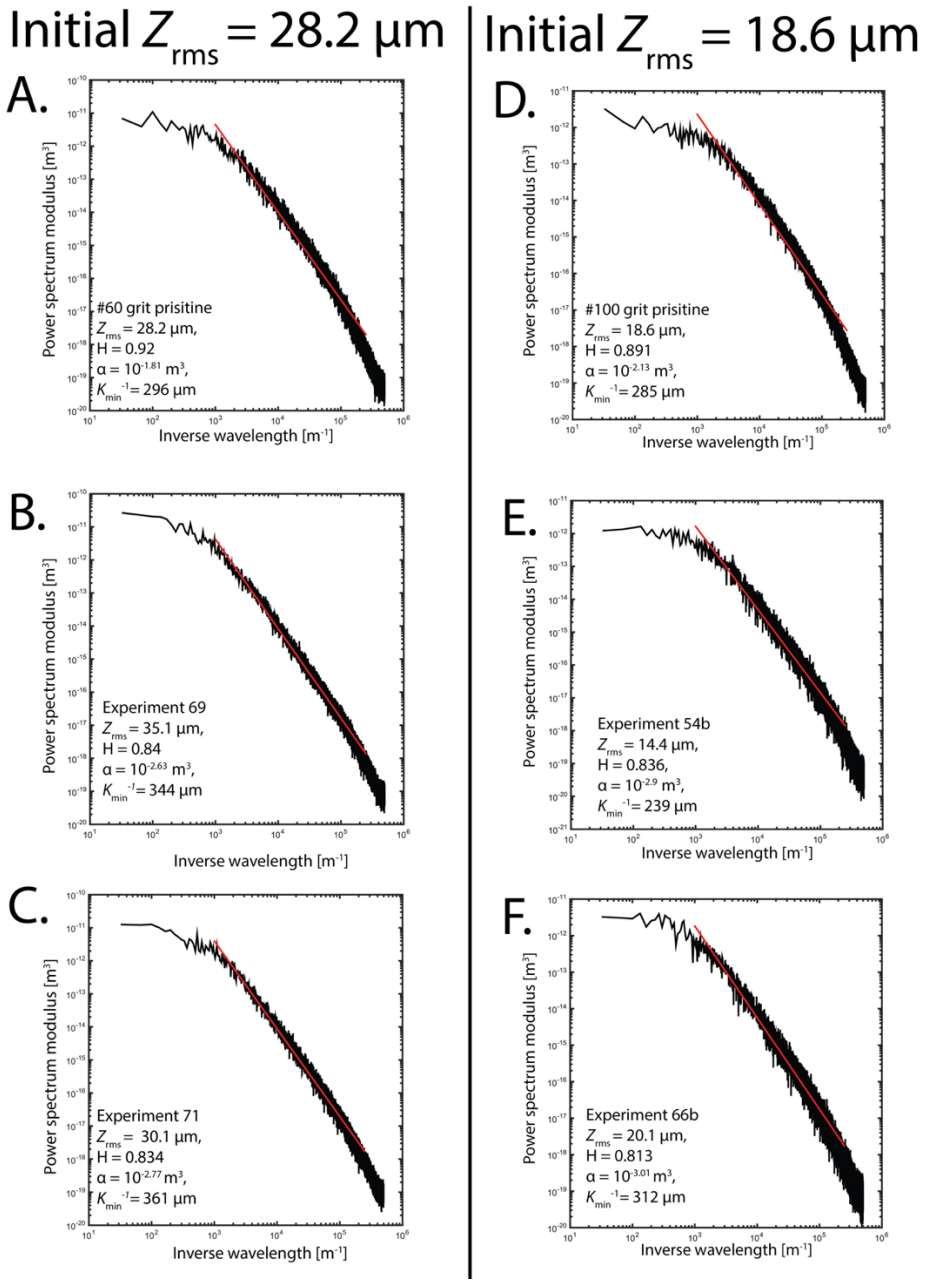

Figure 3.3 Power spectral density plots obtain from stylus profilometry of sample surfaces prepared with #60 and #100 grit. A) and B) represent pristine surface measurements of #60 and #100 grit respectively. B) and C) are from #60 faults deformed at 100 and 200 MPa normal stress, and E) and F) are from #100 faults deformed at 100 and 200 MPa normal stress.

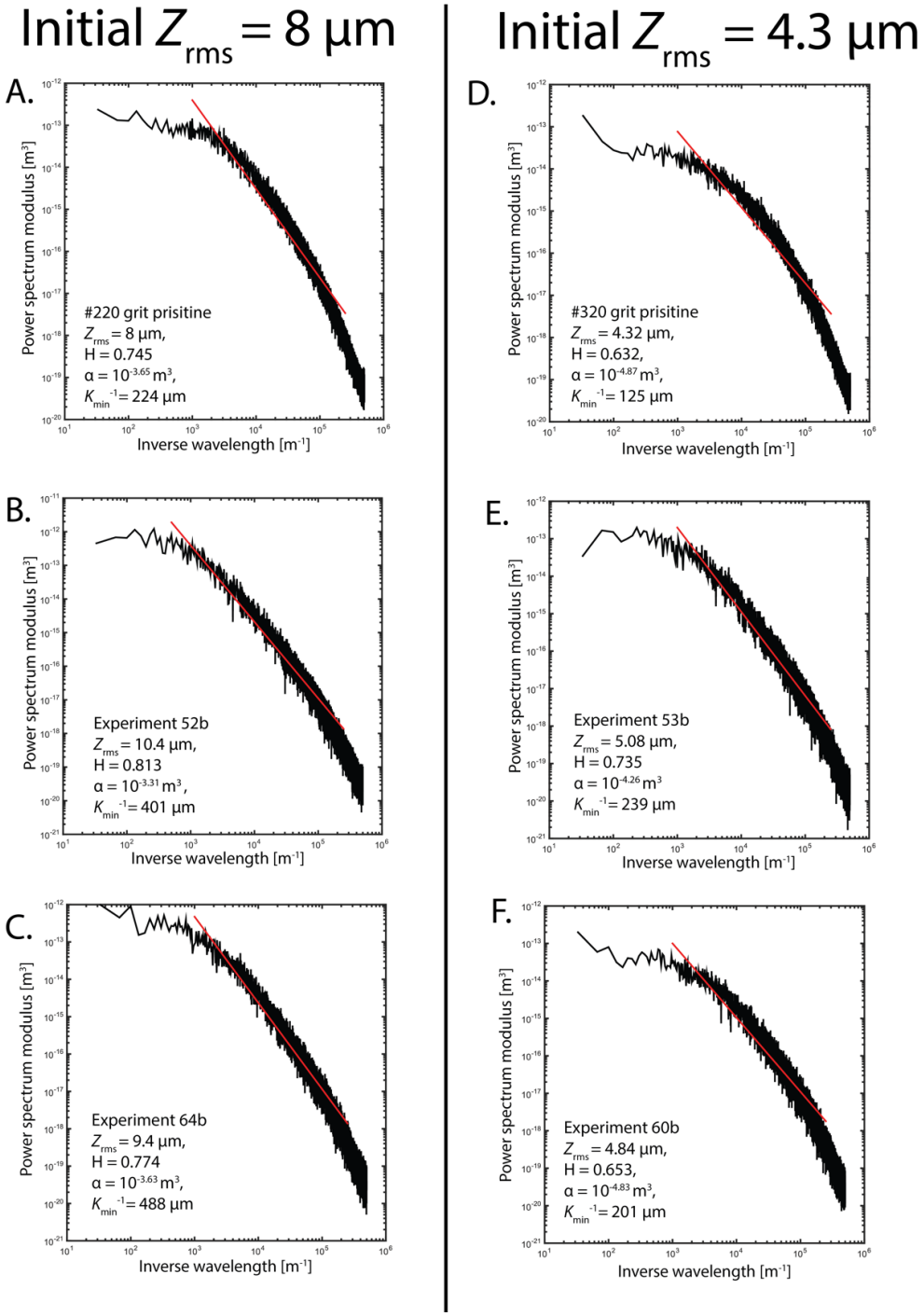

Figure 3.4 Power spectral density plots obtain from stylus profilometry of sample surfaces prepared with #220 and #320 grit. A) and B) represent pristine surface measurements of #220 and #320 grit respectively. B) and C) are from #220 faults deformed at 100 and 200 MPa normal stress, and E) and F) are from #320 faults deformed at 100 and 200 MPa normal stress.

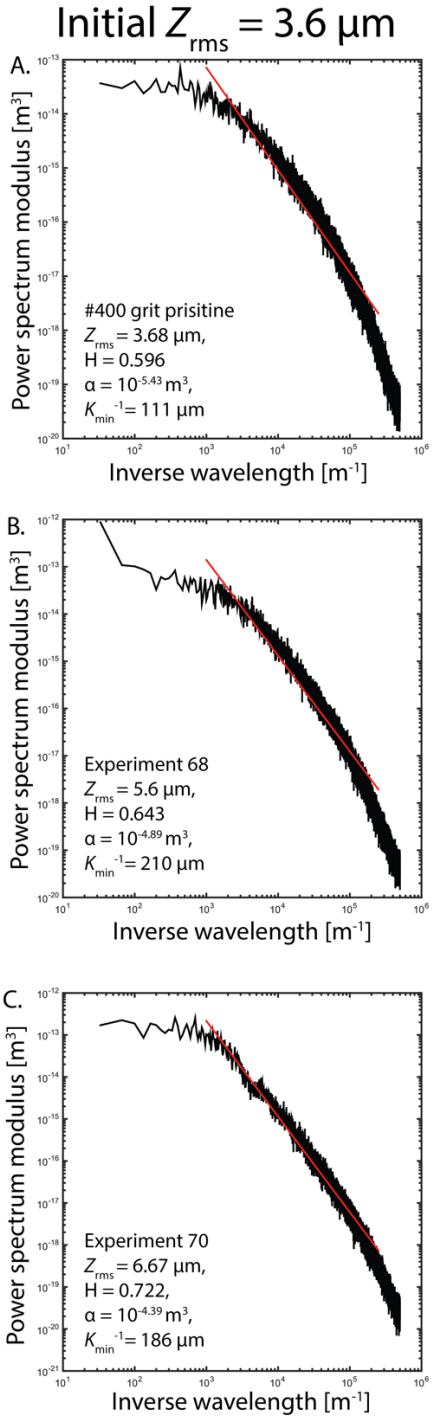

Figure 3.5 Power spectral density plots obtain from stylus profilometry of sample surfaces prepared with #400 grit. A) represents pristine surface measurements of #400 surfaces, B) and C) are from #400 faults deformed at 100 and 200 MPa normal stress.

3.3.2 Mechanical data

Experiment	Z_{rms} [μm]	H	α	K_{min}^{-1}	α	Behaviour	*a-b* range
49a	3.6	0.6	$10^{-5.4}$	111	30	M. Stable	[-0.0044, -0.003]
49b	3.6	0.6	$10^{-5.4}$	111	100	Unstable	[n/a]
52a	8	0.74	$10^{-3.6}$	181	30	Stable	[-0.004, -0.0006]
52b	8	0.74	$10^{-3.6}$	181	100	M. Stable	[-0.0034, -0.0001]
53a	4.3	0.63	$10^{-4.9}$	125	30	M. Stable	[-0.0036, -0.0013]
53b	4.3	0.63	$10^{-4.9}$	125	100	Unstable	[n/a]
54a	18.6	0.89	$10^{-2.1}$	285	30	Stable	[-0.0005, +0.0014]
54b	18.6	0.89	$10^{-2.1}$	285	100	Stable	[+0.00014, +0.0028]
56a	28.2	0.92	$10^{-1.8}$	296	30	Stable	[-0.00025, +0.001]
56b	28.2	0.92	$10^{-1.8}$	296	100	Stable	[+0.0013, +0.0035]
57a	3.6	0.6	$10^{-5.4}$	111	150	Unstable	[n/a]
57b	3.6	0.6	$10^{-5.4}$	111	200	M. Stable	[n/a]
60a	4.3	0.63	$10^{-4.9}$	125	150	Unstable	[n/a]
60b	4.3	0.63	$10^{-4.9}$	125	200	M. Stable	[+0.0032, +0.0053]
64a	8	0.74	$10^{-3.6}$	181	150	M. Stable	[-0.0011, +0.0037]
64b	8	0.74	$10^{-3.6}$	181	200	M. Stable	[+0.0013, +0.0032]
66a	18.6	0.89	$10^{-2.1}$	285	150	M. Stable	[+0.0015, +0.004]
66b	18.6	0.89	$10^{-2.1}$	285	175	Stable	[+0.0018, +0.0065]
67a	28.2	0.92	$10^{-1.8}$	296	150	M. Stable	[+0.0016, +0.0045]
67b	28.2	0.92	$10^{-1.8}$	296	200	Unstable	[n/a]
68	3.6	0.6	$10^{-5.4}$	111	200	Stable	[+0.00083, +0.002]
69	28.2	0.92	$10^{-1.8}$	296	200	Unstable	[n/a]
70	3.6	0.6	$10^{-5.4}$	111	100	Unstable	[n/a]
71	28.2	0.92	$10^{-1.8}$	296	100	Stable	[+0.0011, +0.0042]

Table 3.1 Experiments presented in this chapter

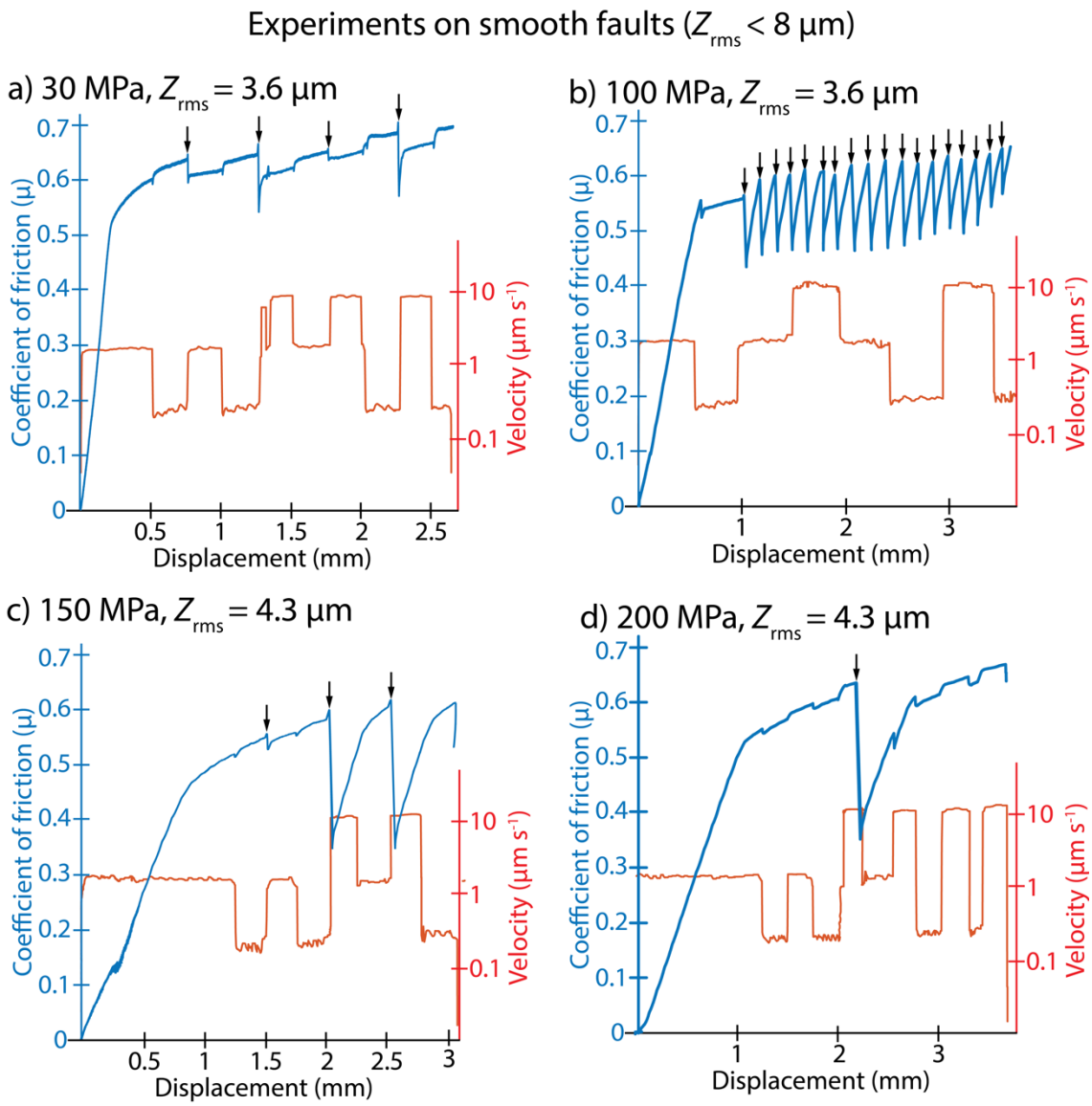

Figure 3.6 Experiments conducted on smooth faults prepared with #320 and #400 grit at a range of normal stress conditions. Black arrows show fast stick-slip events.

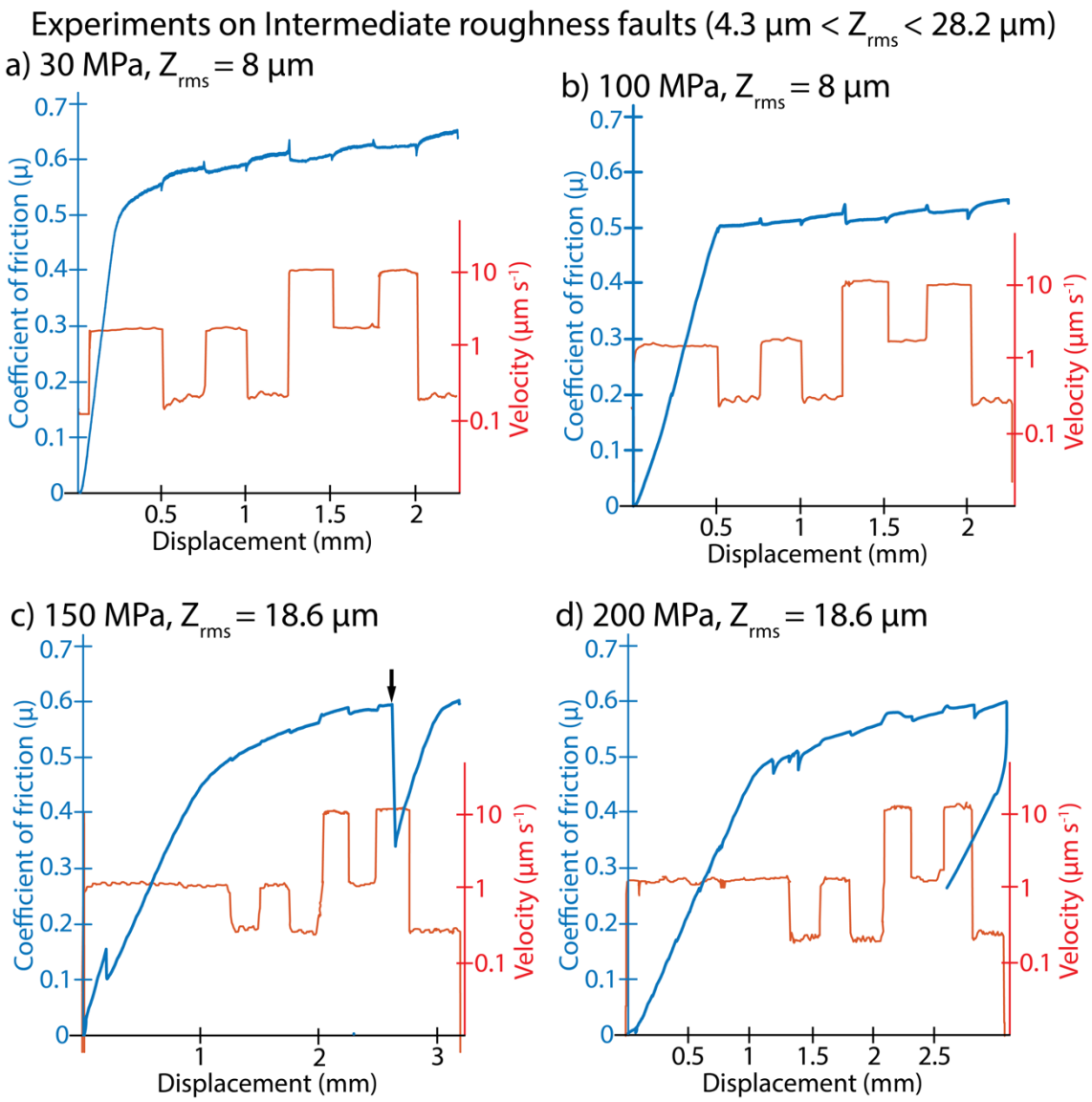

Figure 3.7 Experiments conducted on faults prepared with #100 or #220 grit, deformed at a range of normal stress conditions. Black arrows show fast stick-slip events.

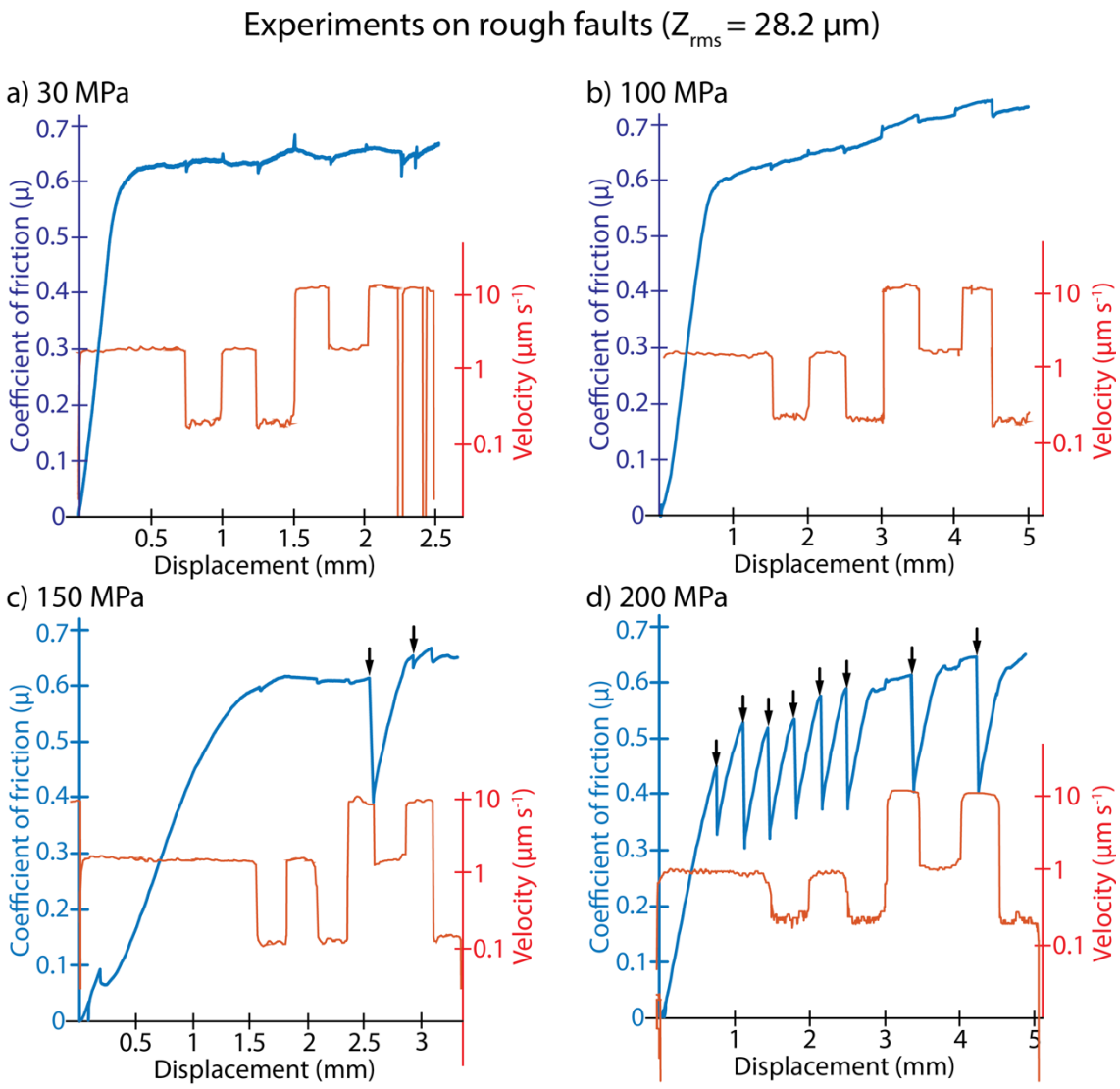

Figure 3.8 Experiments conducted on faults prepared with #60 grit deformed at a range of normal stress conditions. Black arrows show fast stick-slip events.

All experiments show an initial elastic loading followed by frictional roll-over where the contacting surfaces begin to slide (see Figure 3.6-Figure 3.9). Once past this initial stage, the frictional strength remains relatively constant and a steady-state is reached (typically requiring a displacement of 0.75–1.5 mm). The full spectrum of frictional sliding behaviours is observed, from stable sliding to seismic stick-slip, across the range of experimental conditions. In several experiments, it was possible to determine the rate-and-state friction parameters a, b by modelling the frictional data to load-point velocity stepping during stable sliding episodes as shown in Figure 3.6-Figure 3.8. Figure 3.9 shows examples of typical slip dynamics observed in different experiments.

At lower normal stress (σ = 30 MPa), rougher faults (Z_{rms} >8 µm) are observed to slide stably with velocity-neutral friction (Figure 3.9a and Figure 3.8a). Marginal instability is

confined to the smoothest faults (Z_{rms} <4.3 μm), manifested by fast stress drops during step-wise velocity increases as is shown in Figure 3.6a and Figure 3.9b.

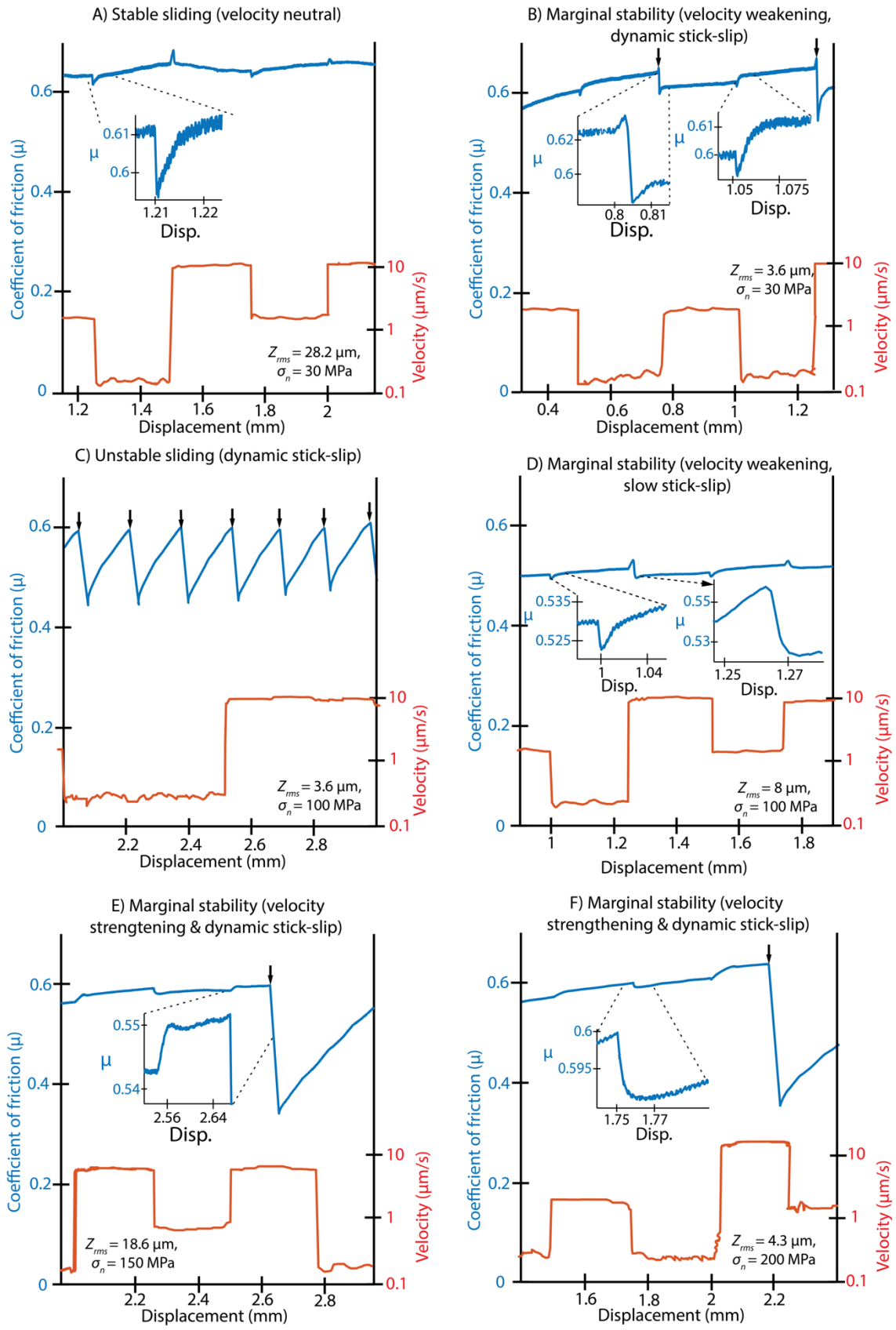

Figure 3.9 Summary of the range of frictional sliding behaviours observed during experiments at a range of roughness and normal stress conditions.

When normal stress is increased to 100 MPa, smooth faults ($Z_{rms} \leq 4.3$ μm) are observed to become fully unstable with repetitive fast stick-slip instabilities (Figure 3.6 b-c Figure 3.9c). This behaviour is confirmed by observations of frictional melting in scanning electron microscopy (SEM) imaging of slip surfaces (Figure 3.10c). Intermediate roughness surfaces (Z_{rms} = 8 μm) show marginal stability with velocity-weakening to neutral friction accompanied by slow stress drops upon increases in velocity (Figure 3.7b-c and Figure 3.9d). Rougher faults ($Z_{rms} \geq 18.4$ μm), are stable throughout the course of experimentation with velocity-strengthening friction (Figure 3.8b), and abundant cataclasis is observed in SEM imaging (Figure 3.10d).

For $\sigma > 100$ MPa sliding shows a wider spectrum of behaviours, with some unexpected results. At 150 MPa smooth faults ($Z_{rms} \leq 4.3$ μm) remain unstable with repetitive fast stick-slip cycles. Surprisingly, however, all rougher faults ($Z_{rms} > 4.3$ μm) are marginally stable, with evidence of fast stress drops nucleating spontaneously (without a velocity kick) or upon step-wise velocity increases, in spite of velocity-strengthening friction measurements (Figure 3.7c, Figure 3.8c, Figure 3.9e) , with evidence of frictional melt in SEM images (Figure 3.10a). Surprisingly increasing the normal stress to 200 MPa results in the smoothest faults (Z_{rms} = 4.3 μm) becoming marginally stable (Figure 3.6d Figure 3.9f). Similar behaviour is also observed on intermediate roughness faults ($4.3 < Z_{rms} <$ 28.2 μm) which are stable with velocity-neutral to -strengthening friction (Figure 3.7d). Unexpectedly, given the consistently velocity-strengthening friction at lower normal stresses, the roughest fault (Z_{rms} = 28.2 μm) is unstable with repetitive dynamic stick-slip (Figure 3.8d).

3.4 Discussion

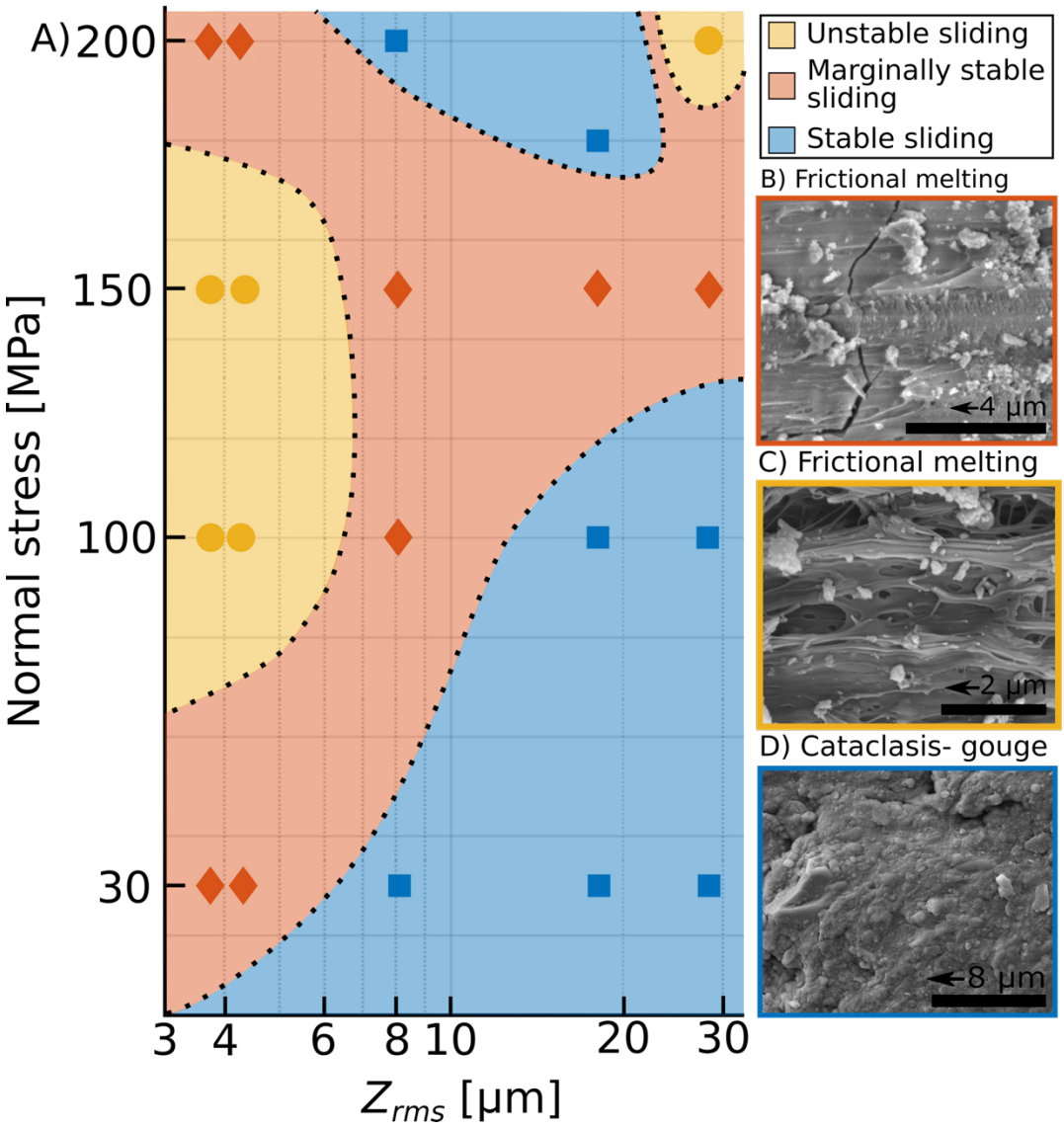

Figure 3.10 A) approximate stability map resulting from the range of experimental conditions investigated, each point corresponds to an individual experiment, which in some cases were repeated (see Table 3.1). B-D) represent insets of microstructural images taken from samples deformed in differing sliding regimes. Arrows denote the sliding direction of the overlying fault block.

The complex variety of slip behaviours observed is summarized in Figure 3.10, where points correspond to various experimental conditions (Z_{rms}, σ), which allow approximate definition of differing frictional domains. Two characteristic trends emerge in the data (Figure 3.10a): First, there is a transition from stable to unstable and marginally stable slip as normal stress is increased, in accordance with the predictions of rate and state (Marone, 1998; Rice and Ruina, 1983), with the transition at increasingly higher normal stress as faults become rougher. Secondly, with further normal stress increase up to 200

MPa, instability is suppressed on all but the roughest faults which becomes unstable (Figure 3.10a). The occurrence of spontaneous rupture nucleation in a velocity strengthening regime for several experiments and the second trend of the stabilizing effect of normal stress are not predicted using a standard stability analysis (Marone, 1998; Rice and Ruina, 1983).

3.4.1 Natural fault structure

Results are now discussed in light of rupture stability criteria with the development of a theoretical model based on roughness-induced weak fault patches. To frame the following discussion consideration of surface roughness statistics must be given. Studies of natural fault surfaces show that faults have a characteristic self-affine roughness, described by a power density spectrum (equation 3.2). Results suggest that this is true over 9-orders of magnitude (from 10^{-4} to 10^{5} m) with $\alpha = 10^{-3}$-10^{-1} m^3 and H=0.6-0.8 (Bistacchi et al., 2011; Candela et al., 2012). At shorter length scales of <1–50 μm, this scaling diminishes and becomes isotropic as a result of plastic yielding at asperity contacts (Candela and Brodsky, 2016). From stylus profilometry measurements of pre- and post-experimental surfaces a corner frequency, k_{min}, is identified using Fourier analysis (Figure 3.3 to 3.5), above which surfaces obey self-affine scaling.

3.4.2 Stability criteria

The onset of rupture propagation can be interpreted either: (a) in the context of rate- and state-dependent friction (Marone, 1998; Rice and Ruina, 1983) when stable sliding initiating at a point can spread out with an accelerating velocity when the sliding patch reaches a critical size or (b) as the consequence of stress concentration around a weak patch, which may propagate unstably according to fracture energy considerations, originally developed in fracture mechanics (Barenblatt, 1962; Griffith, 1921) which have been adapted to the problem of shear cracks and earthquake faulting (Andrews, 1976; Ida, 1972).

According to criterion (a), stability is controlled by the ratio of the mechanical stiffness K_f to the frictional stiffness K_c, defined as:

$$K_c = \frac{\sigma(b-a)}{D_c}$$

3.7

where σ is the normal stress in Pa, a and b are rate- and state-friction dimensionless parameters and D_c is the critical slip distance in m. When the stiffness criterion K_f/K_c <1 is satisfied, instability can develop, otherwise sliding is conditionally stable (Marone, 1998; Rice and Ruina, 1983; Rubin and Ampuero, 2005; Gu and Wong, 1991b). In the case of tectonic faults embedded in an elastic medium, K_f represents the stiffness of the fault and can be expressed as $K_f = C\frac{G}{L}$, where G is the shear modulus in Pa, L the linear fault dimension in m and C is a dimensionless crack shape factor. The stiffness criterion (equation 3.7) allows the definition of a minimum dimension h^*:

$$h^* \approx \frac{CGD_c}{\sigma(b-a)}$$

3.8

of a slip patch required for instability to develop. Rate- and state-friction laws and Equation 3.8 provide effective tools to model slip during the earthquake cycle. The stiffness criterion has been successfully used to explain the spectrum of fault slip behaviours observed across relative homogeneous sliding interfaces such as gouge dominated faults (Leeman et al., 2016; Scuderi et al., 2016).

On the other hand, stability criterion (b) based on fracture energy, surmises the presence of a pre-existing flaw or weak patch of finite size. Material flaws are inherent in Griffith's original crack theory (Griffith, 1921), and in the case of tectonic faults they may be equated to an elastic bridge between asperities (Figure 3.12a-b). For earthquake nucleation, instability arises when the growth of the weak patch is energetically favourable. This requires that the strain energy release from the surrounding elastic medium exceeds that of the residual fault strength, which includes fracture energy, allowing slip to accelerate. In problems of shear crack propagation, fracture energy is often equated to the frictional work dissipated during the loss of strength, according to a model of slip weakening, over a characteristic distance, δ_c (Andrews, 1976; Ida, 1972).

Criterion (b) allows the definition of a critical length, $L_c = CG\delta_c\frac{\tau_p-\tau_r}{(\tau_0-\tau_r)^2}$, at which a shear crack undergoes unstable dynamic failure (Andrews, 1976), where τ_0 is the static shear stress on the fault, $\tau_p = \mu_p\sigma$ is the peak shear stress in Pa, μ_p the peak friction coefficient and $\tau_r = \mu_r\sigma$ is the shear stress after weakening where μ_r is the sliding (or

weak) friction coefficient. To enhance similarity with h^*(Eq. 3.8), a lower bound length estimate for L_c may be derived, assuming that the stress state on the fault is close to the peak stress during experiments (i.e., $\tau_0 \approx \tau_p$), yielding:

$$L_c \approx \frac{CG\delta_c}{\sigma(\mu_p - \mu_r)} \quad 3.9$$

Though the critical patch length h* and L_c share some scaling similarities, they may differ by orders of magnitude: a-b is typically small (< -0.005) while expected values of $\mu_p - \mu_r$ can be quite large. Here frictional strength at asperities equates to $\mu_p - \mu_r$, and within elastic bridges or zones of reduced asperity density it equates to μ_r. Estimates $\mu_p - \mu_r = 0.2$ are adopted, as suggested by the observations of (Selvadurai and Glaser, 2017) on rough surfaces, which show that stress fluctuations can be as much as 40% of the peak stress at asperities.

Estimates of the nucleation size for experiments showing stick-slip instability at moderate normal stress using Eq. 3.8 for a fault of Z_{rms} = 3.6 μm ($C = 7\pi/24$, a-b = -0.003, D_c = 5 μm, G = 50 GPa, Z_{rms} = 3.6 μm, σ = 100 MPa) yield h* ≈1m, 2 orders of magnitude larger than the size of samples utilized. Following the slip weakening limit derived in Rubin and Ampuero (2005) and Uenishi *et al.* (2003), if the rate parameter a is neglected, it is found that h_b^* ≈0.3 m (a = 0.005), which is still an order of magnitude larger than the size of the sample. Calculating the nucleation length using equation 3.9, values for L_c = 1.25-3.75 cm (with G = 50 GPa, σ = 100 MPa, $\mu_p - \mu_r$= 0.2 and δ_c = 5 – 15 μm). Values of L_c obtained are also in agreement with other studies that posit that the nucleation length should be smaller than the sample length (L_0 = 4 cm), for lab stick-slip occurrence (Ohnaka and Shen, 1999; Okubo and Dieterich, 1984; Passelègue et al., 2013). The values estimated here for δ_c = 0.05 k_{min}^{-1} (Ohnaka and Shen, 1999) are consistent with previous estimates using high frequency strain gauges (Okubo and Dieterich, 1984) and also those predicted by numerical modelling of elastic surface closure (see Figure 3.11). This is in contrast to values of D_c obtained during velocity steps, which do not show a systematic dependence on roughness. The onset of instability observed at higher normal stress for increasing roughness is in accord with $\delta_c \propto k_{min}^{-1}$.

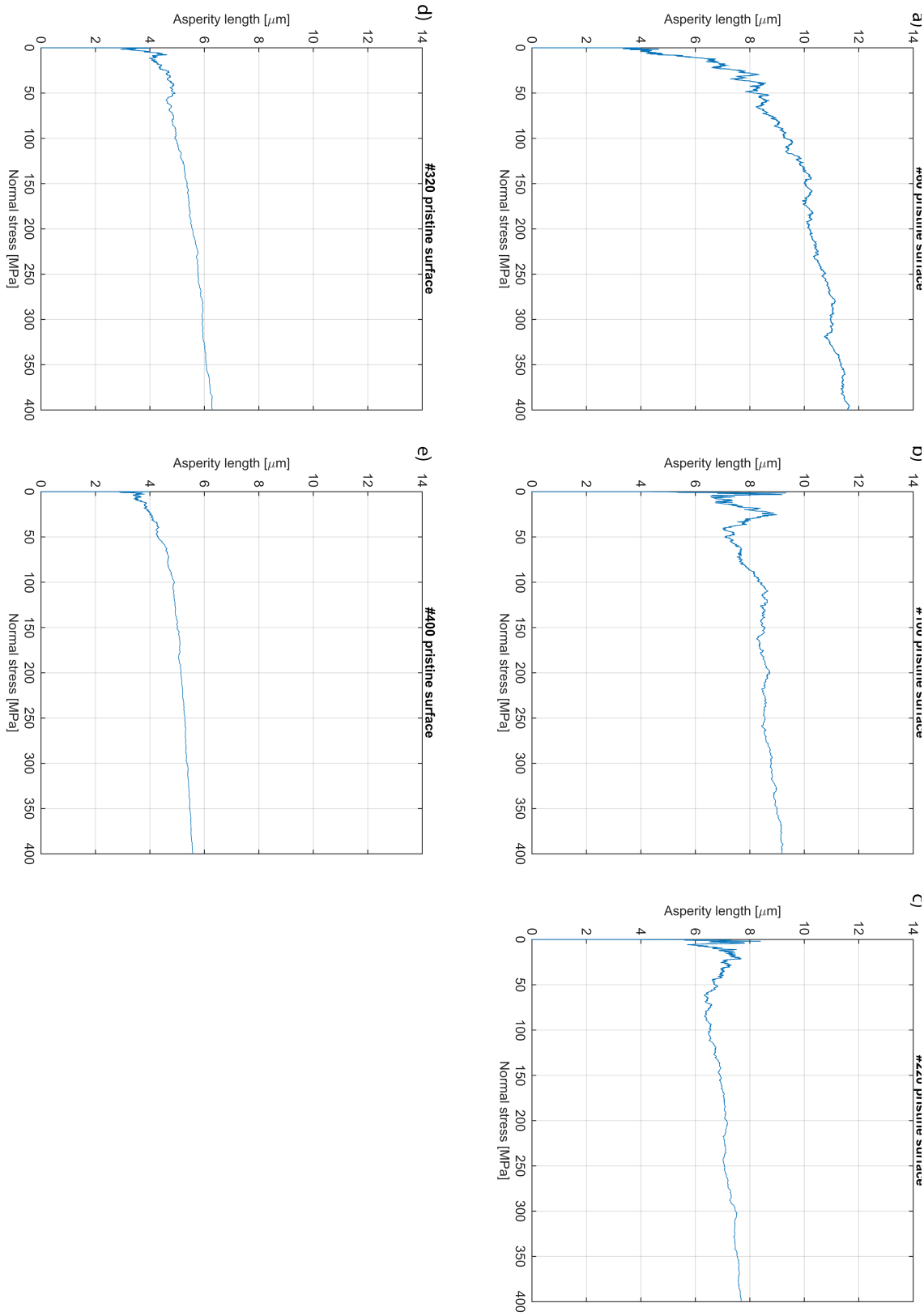

Figure 3.11 Asperity length models obtained by solving the 1D crack closure equation (Equation 3.5). Insets show modelled lengths as a function of normal stress a) for a #60 surface (Z_{rms} = 28.2 µm), b) for a #100 surface (Z_{rms} = 18.6), c) for a #220 surface (Z_{rms} = 8 µm), d) for a #320 surface (Z_{rms} = 4.3) and e) for a #400 surface (Z_{rms} = 3.6 µm).

While a stability criterion based on fracture energy (e.g., Equation 3.9) can explain the onset of stick-slip during our experiments at low/moderate normal stresses (30–150 MPa), the surprising observation that slip instability is suppressed at higher normal stress indicates the presence of some limiting process (Figure 3.10a). As discussed below, this behaviour could be explained by considering the microphysical properties of contact asperity distribution in relation to fault zone roughness, and the associated stress heterogeneity (Scholz, 1988).

3.4.3 A new microphysical model for earthquake nucleation

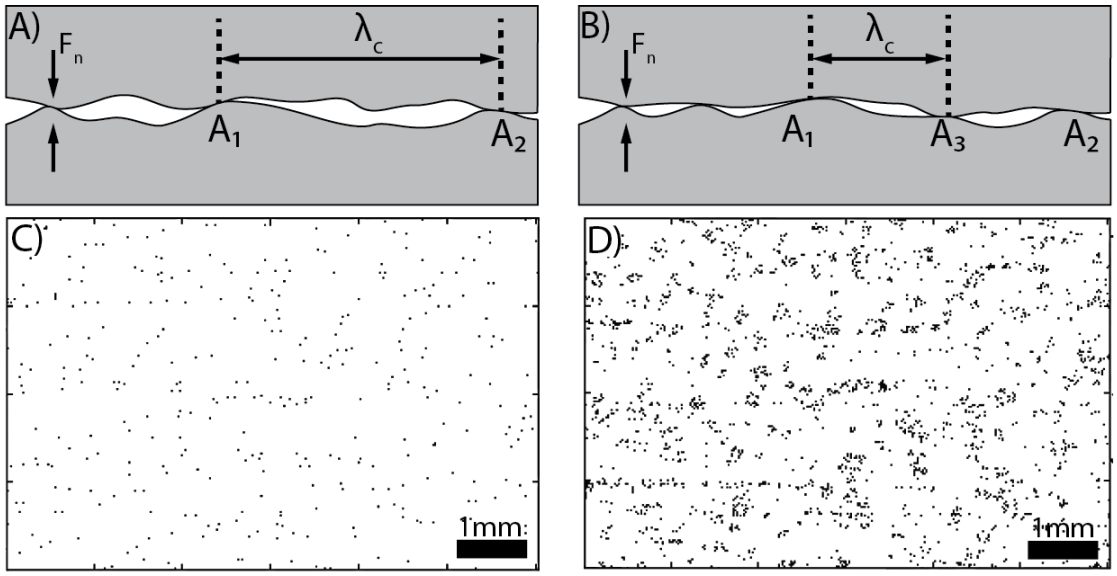

Figure 3.12 Illustration of the changing nature of frictional contact as a function of normal stress. A) and B) represent schematic cross sections through 2 rough surfaces in contact, highlighting that as normal stress increases more asperities are produced, reducing the open crack size. C) and D) show results from a 2d numerical simulation of frictional contact expected on a #220 fault at 30 MPa (C) and at 200 MPa (D).

Previous studies imaged the distribution of frictional contacts with increasing normal stress and varying surface roughness in transparent materials (Dieterich and Kilgore, 1994, 1996a). With increasing normal stress, contact asperities increase in number and also grow as is shown in Figure 3.12. Theory indicates that stress and asperity sizes will follow a power law distribution for a self-affine surface under load (Scholz, 1988). The asperity bridging length, λ_c, which is the maximum supportable elastic length or bridge between asperities, is also shown to decrease as $\lambda_c \propto \lambda_n^{-2}$ for a self-similar surface. A generalization of this result to any self-affine surface is considered with $0 < H < 1$ as

$$\lambda_c = \beta \left(\frac{E}{\sigma}\right)^{\frac{1}{1-H}}$$

3.10

Where $\beta = \left(\sqrt{\frac{\alpha {k_0}^{1+2H}}{2H}}\right)^{\frac{1}{1-H}}$ is a scaling factor in m and E the Young's modulus in Pa. From measurements of experimental fault surfaces, the Hurst exponent is typically 0.6–0.9 above K_{min}, yielding $\lambda_c \propto \sigma^{-2.5} - \sigma^{-10}$. In comparison, Equation 3.10 gives $L_c \propto \sigma^{-1}$, demonstrating that as normal stress increases, the bridging length will decrease at a faster rate than that of the nucleation length (Figure 3.13a). In extreme cases, bridges of length scale λ_c may represent voids, as is shown in Figure 3.12, but more generally zones of reduced normal stress, or weak patches of low stiffness, filled with under-compacted gouge. These weak zones can act as stress concentrators and initiate rupture, provided that $L_c < \lambda_c$ and $L_c < L_0$ as is shown in Figure 3.13. However with increasing normal stress, the bridges will gradually be closed and the maximum open patch will decrease until $\lambda_c < L_c$, and rupture nucleation is no longer possible in accordance with our experimental observations (Figure 3.6-Figure 3.9 and Figure 3.10). In general, instability leading to rupture nucleation in the experiments presented in this chapter is only observed when the nucleation length L_c satisfies the condition $\lambda_c > L_c$ and $L_0 > L_c$. Conversely the conditions $L_c > L_0$ at lower normal stress, and $L_c > \lambda_c$ at higher normal stress, lead to stable sliding (Figure 3.13).

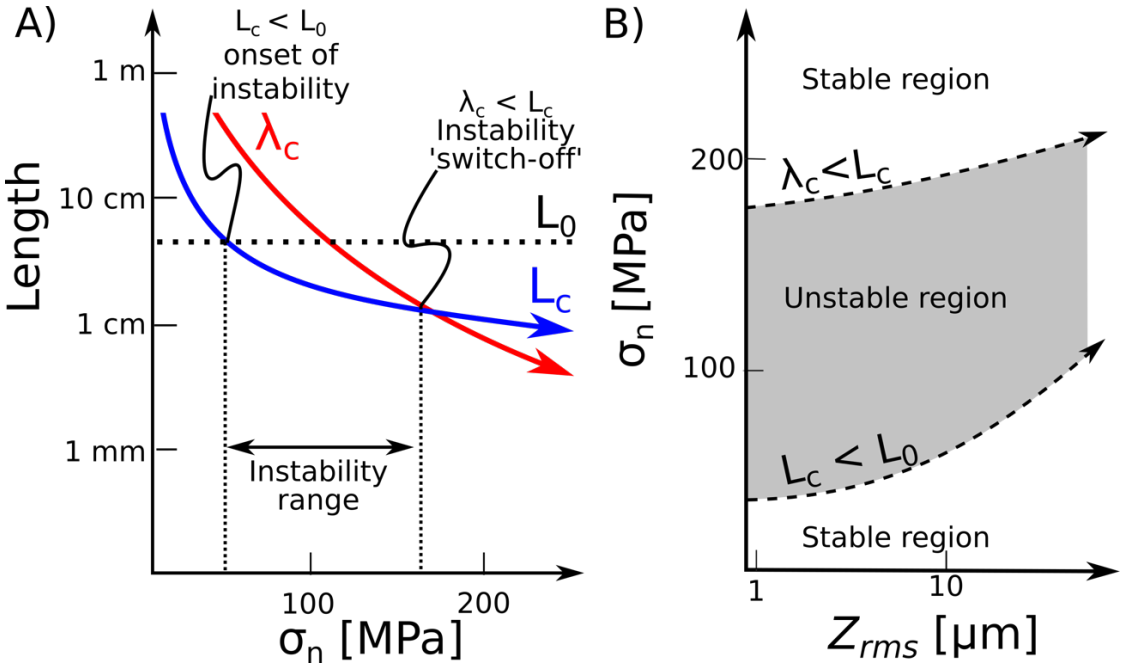

Figure 3.13 Schematic illustration of dimensional argument (a) proposed to explain the resulting frictional stability pattern (b) observed in experiments and theory.

3.5 Conclusions

The findings of this chapter have implications for the larger scale behaviour of natural fault zones. In principle, the model shown in Figure 3.13 suggests the transition from seismic to aseismic faulting may be controlled by the stabilizing influence of increasing normal stress upon asperities, in addition to currently accepted temperature-induced rheological changes (Scholz, 1998). Equations 3.9 and 3.10 may be used in future to estimate seismicity transition when constraints on nucleation parameters are improved. In addition to this, our results qualitatively support observations of subduction zone seismicity, where rough sea floor topography is observed to be related to creeping behaviour, and smooth sea floor topography to seismicity and large earthquake nucleation (Wang and Bilek, 2014).

Presented results highlight the key role of fault heterogeneity in earthquake nucleation. On larger scales such heterogeneity includes fault jogs, compositional contrasts, fluid injection in addition to fault roughness as suggested herein. These results complement rate-and-state friction stability analysis, providing a physical framework to include the complexity of roughness in earthquake nucleation models.

3.6 Supplementary material: Generalisation of λ_c

Scholz (1988) showed that the maximum bridge that remains open between asperities scales inversely to the square of normal stress, λ,

$$\lambda_c = \chi \left(\frac{E}{\sigma}\right)^2$$

3.11

Where E is the Young's modulus in Pa, and χ is a length constant derived from fault scaling statistics.

The root mean square of surface elevation for a power spectrum $P(k)$ is

$$Z_{rms} = \sqrt{\int_{k_{min}}^{k_{max}} P(k)dk}$$

3.12

The root mean square is a generalised mean, such that at a given inverse wavelength $k = k_{min}$, it will equate to the average elevation of the surface, integrating all the topography over the range $\frac{2\pi}{k_{max}}$ to $\frac{2\pi}{k_{min}}$. Hence

$$Z^2(k) = \int_{k}^{k_{max}} P(k)dk$$

3.13

And for a self-affine distribution with Hurst exponent H, using the power spectrum $P(k) = \alpha \left(\frac{k}{k_0}\right)^{-1-2H}$, where k_0 is a reference inverse wavelength, gives

$$Z^2(k) = -\frac{k}{k_0}^{-2H} \left[\frac{k}{k_0}^{-2H}\right]_k^{k_{max}}$$

$$-\frac{\alpha k_0}{2H}\left[\left(\frac{k_{max}}{k_0}\right)^{-2H} - \left(\frac{k}{k_0}\right)^{-2H}\right]$$

3.14

Since $k_{max} \gg k$ and $H > 0$ then the part with k_{max} may be neglected, after taking the square root:

$$Z(k) = \sqrt{\frac{\alpha k_0}{2H}}\left(\frac{k}{k_0}\right)^{-H}$$

$$= \sqrt{\frac{\alpha k_0}{2H}}\left(\frac{2\pi}{\lambda k_0}\right)^{-H}$$

3.15

Note that $Z_0 = \sqrt{\frac{\alpha k_0}{2H}}$ has length dimensions, and corresponds to the elevation of the surface at the reference wavelength, $\lambda_0 = \frac{2\pi}{k_0}$. The aspect ratio $\frac{Z}{\lambda}$ of a bridge will control the closure stress, σ, so

$$\sigma = E\frac{Z}{\lambda}$$

3.16

And substituting 3.15 into 3.16 yields,

$$\sigma = \frac{E}{\lambda}\sqrt{\frac{\alpha k_0}{2H}}\left(\frac{2\pi}{\lambda k_0}\right)^{-H}$$

$$= E\sqrt{\frac{\alpha k_0}{2H}}\left(\frac{k_0}{2\pi}\right)^{H}\lambda^{H-1}$$

3.17

Finally, the maximum bridging length $\lambda_c$is

$$\lambda_c = \beta\left(\frac{E}{\sigma}\right)^{\frac{1}{1-H}}$$

3.18

With

$$\beta = \left[(2\pi)^{-H}\sqrt{\frac{\alpha k_0^{1+2H}}{2H}}\right]^{\frac{1}{H-1}}$$

3.19

Where β is a constant of length dimensions. The above equation is equivalent to the case of Brownian surface derived previously (Scholz, 1988), by setting H = 0.5.

4 Flash weakening during laboratory earthquakes[4]

Abstract

The dynamic evolution of fault strength during earthquakes cannot be solely determined by seismological studies. However, dynamic fault strength is a key ingredient to model rupture and to estimate key seismic source parameters (e.g. dynamic stress drop and strength recovery, slip pulse velocity function, fracture energy). Hence results from theoretical predictions and laboratory friction experiments are being widely used to represent dynamic weakening in models and earthquake source studies, in addition to indirect estimates from natural earthquake data. High velocity experiments (HVE) conducted within the range of seismic slip conditions (slip velocity ≈1 m/s, normal stress ≥ 10 MPa), show a dramatic strength reduction. It has been proposed that such dynamic weakening is caused by thermally-activated processes (e.g., flash heating, melting, pressurization) triggered by frictional heating of the slip zone. However, HVE experiments are mostly conducted by imposing the slip velocity, therefore lack specific aspects related to spontaneous rupture propagation. The results reported in this chapter, detail the slip function and the frictional evolution measured at high frequency directly on a simulated fault surface, during spontaneous dynamic rupture propagation in a rock. Under conditions representative of nanoearthquakes at crustal depths, it is shown that slip can accelerate up to ~0.6 m/s within tens of microseconds, concomitant with large dynamic stress drops due to the dramatic weakening of the sliding interface. The weakening phase of the friction is compatible with a flash heating model, and accurately matches independent predictions based on thermal and mechanical rock parameters. The recovery phase of friction, however, is too gradual to be accounted for by the flash heating model alone. It is also found that the slip velocity pulse shares similarities with the Yoffe function for a propagating shear rupture, legitimizing its use as a source function in models. These results open a window on to previously inaccessible aspects of earthquake source dynamics under crustal conditions.

[4] The contents of this chapter have been submitted to *Nature Geoscience*

4.1 Introduction

Earthquakes are a manifestation of rapid frictional slip, driven by a dramatic release of the strain energy stored around a fault. Rupture propagation is controlled by the balance between dissipated energy which resists rupture propagation (e.g. fracture energy, frictional work, kinetic energy radiation), and the work of elastic energy which promotes fracture propagation and is made available by the stress drop in the sliding parts of the fault (e.g. dynamic weakening). A vast effort has been undertaken to understand the dynamics of earthquake slip in theory (Andrews, 1976; Heaton, 1990; Rice, 2006; Cochard and Rice, 1997; Nielsen and Madariaga, 2003; Richards, 1973; Viesca and Garagash, 2015), seismological observations (Abercrombie and Rice, 2005; Lay et al., 2005), field studies (Di Toro et al., 2005; Chester et al., 2005) and laboratory experiments (Passelègue et al., 2013, 2016; Leeman et al., 2016; McLaskey and Lockner, 2014; Ohnaka and Shen, 1999; Okubo and Dieterich, 1984; Johnson and Scholz, 1976; Nielsen et al., 2010; Goldsby and Tullis, 2011; Di Toro et al., 2011).

Seismological studies are hampered by the difficulty to estimate key seismic source parameters e.g. dynamic stress drop, finite fault slip and fracture energy (Abercrombie and Rice, 2005; Venkataraman and Kanamori, 2004). Therefore, some major breakthroughs in understanding earthquake propagation mechanics have come from laboratory studies (e.g. Di Toro et al., 2011; Passelègue et al., 2016; Brantut et al., 2016; Passelègue et al., 2013). In particular fault strength evolution predicted by theoretical constitutive laws of dynamic weakening mechanisms (e.g. flash heating) are often used to model earthquake rupture, and to estimate these key seismic source parameters. Furthermore, several assumptions about source functions (e.g. self-healing slip-pulse vs. crack like rupture) are currently utilised to invert seismograms and model crustal earthquakes (Tinti, Fukuyama, et al., 2005; Nielsen and Madariaga, 2003; Cochard and Rice, 1997) which are strongly dependent on the nature of the frictional law utilised (Beeler and Tullis, 1996; Cochard and Madariaga, 1996). The lack of experimental observations from spontaneously propagating laboratory earthquakes prevents the validation of theoretical constitutive laws describing frictional strength evolution (e.g. flash heating) and of their predictions about source parameters. This calls into question the applicability and choice of models used to infer earthquake slip and strength evolution, which are elastodynamically coupled.

Since the identification of stick-slip as a laboratory analogue for earthquakes (Brace and Byerlee, 1966) numerous studies have aimed to study the dynamic properties of spontaneous dynamic rupture propagation using high frequency strain measurements (Brantut et al., 2016; Passelègue et al., 2016; Ohnaka and Shen, 1999; Okubo and Dieterich, 1984; Johnson and Scholz, 1976). Early studies established that faults can weaken rapidly (<10 μs) during the passage of earthquake rupture (Johnson and Scholz, 1976; Okubo and Dieterich, 1984). Recently, technological advancements have verified that fault frictional drop is significant (to almost zero strength) during the passage of a dynamic rupture (Brantut et al., 2016; Passelègue et al., 2016), in agreement with experiments conducted under imposed high slip velocity (Di Toro et al., 2011). In terms of the earthquake energy balance these results suggest that frictional energy dissipation can be relatively low, and other energy sinks (seismic wave radiation and off-fault damage) may become significant during earthquakes (Nielsen et al., 2016). In spite of these advances, studies are restricted by the lack of an accurate measurement of slip velocity and its interplay with dynamic weakening during rupture propagation, which allow more definitive constraints on the nature of dynamic friction.

Here the results from high frequency strain measurements, recorded during experimental simulations of spontaneous dynamic rupture in crustal rocks, are presented. Simultaneous measurements of slip and shear stress evolution at a single point are measured during spontaneous rupture events. During a typical laboratory earthquake, faults accelerate up to 0.6 m s^{-1} over a weakening distance of 5-25 μm. A series of stick-slip events, with variable duration and magnitude show a self-similar behaviour and scaling between shear stress drop and peak velocity. Furthermore, the observed velocity dependence of friction is well predicted by flash heating during the weakening phase of ruptures.

These results are significant for the current understanding of frictional dynamic weakening, confirming that frictional work can be very low when seismic slip rates are attained. These results also shed light on the earthquake energy balance, and on the mechanism of crustal micro-earthquakes where very large (GPa) stress drops are observed (Nadeau and Johnson, 1998). The strong velocity weakening observed at seismic slip rates, even at extremely small amounts of slip (10's of μm), supports the hypothesis of self-healing slip pulses (Heaton, 1990; Beeler and Tullis, 1996; Nielsen and Madariaga, 2003; Cochard and Madariaga, 1994).

4.2 Methods

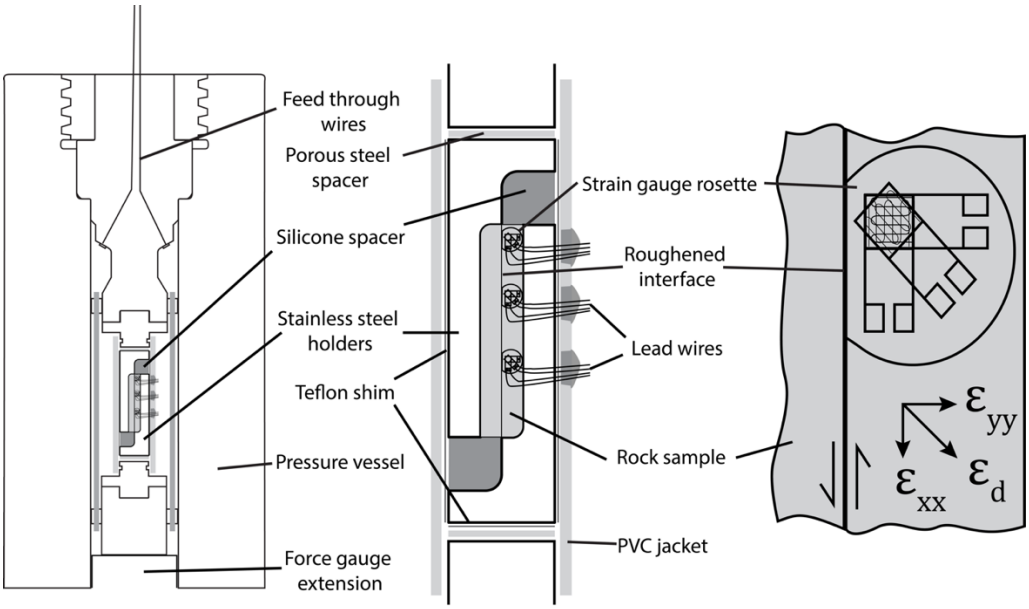

Figure 4.1 Schematic illustration of experimental set-up. The slabbed geometry allows measurement of strain close to in-plane conditions, whilst also maintaining a constant normal stress during sliding events. Small gauges are utilised which can be positioned extremely close to fault surfaces, providing a near field measurement of dynamic strain, which is crucial for obtaining accurate slip records.

Laboratory earthquakes were induced on laboratory simulated faults in Westerly Granite (Rhode Island, USA). Samples were prepared by creating polished rock slabs (20x30x4.4mm) and gluing them into a set of L-shaped steel sliders (316 stainless or 17-4 PH H900 steel). The holders are offset using silicone rubber spacers resulting in a single direct shear configuration (Figure 4.1). Surfaces were ground to a final finish on a water wet polishing plate with #600 alumina grit promote instability (Harbord et al., 2017). Two to three strain gauge rosettes were glued approximately 1 mm from the fault surface, at 6mm intervals along the fault surface. The proximity of the gauge patterns to the fault plane allows the measurement of rupture strain in the near field, limiting the signal convolution resulting from measurements made in the far-field as was the case in Passelègue *et al.* (2016) and Brantut *et al.* (2016). For each rosette, gauge patterns were positioned to measure strain fault-parallel (ε_{xx}), fault perpendicular (ε_{yy}) and at 45 degrees (ε_d). Shear stress was calculated

$$\sigma_{xy} = 4G\varepsilon_d - 2G\varepsilon_{xx}\left(1 - \frac{\lambda}{\lambda + 2G}\right)$$

4.1

where G is the shear modulus in Pa (= 60 GPa), and λ is Lame's parameter in Pa (=), see appendix for derivation. Measurements of $\frac{\partial \sigma_{yy}}{\partial t} \approx 0$, as expected for a planar fault in a homogeneous medium. As suggested previously (Rubino et al., 2017; Svetlizky and Fineberg, 2014) slip velocity can be estimated from the fault parallel strain and the rupture velocity. Given that the fault parallel strain is:

$$\varepsilon_{xx} = \frac{\partial u_x}{\partial x}$$

4.2

and assuming that rupture can be approximated by a steady-state slip pulse propagating at constant velocity c in the positive x direction such that

$u_x = f(x - ct)$, it can be written that,

$$\frac{\partial u_x}{\partial t} = -c\, f'(x - ct) = -c\, \frac{\partial u_x}{\partial x}.$$

4.3

The off-fault particle velocity is therefore:-

$$v_x(x,t) = -c\, \varepsilon_{xx}(x,t)$$

4.4

Because of symmetry in simulated faults and the proximity of the sensor to the fault surface, slip velocity is assimilated to $V \approx 2v_x$. To obtain zero velocity at rupture cessation a linear correction, $corr = -\frac{\Delta}{\delta t}$, was applied following the observation of a static strain build up, Δ (see appendix for proof). Strain gauge signals were conditioned using an Elsys SGA2 1.5 MHz strain gauge amplifier in a quarter bridge configuration, and over-sampled at 10 MHz in continuous acquisition.

Load point velocity was driven at 0.5-5μms^{-1}, resulting in a sequence of fast stick-slip events. To estimate rupture velocity, c, the travel time between two gauges is utilised,

yielding an apparent velocity. All strain gauge signals were post processed using a FIR low pass filter at 250 KHz in MATLAB to eliminate high frequency noise and smooth the data. Strain values were calculated using equations for quarter bridge configurations, with compensation made for the lead wire resistance.

$$\varepsilon(t) = \frac{-4V_{out}(t)}{G_f\left(V_{in} + 2V_{out}(t)\right)}(1+\epsilon) \qquad 4.5$$

Where V_{out} is the recorded voltage, V_{in} the voltage applied across the bridge, G_f the gauge factor and ϵ and error factor accounting for the lead wire resistance (=0.01). Due to spatially variable shear stress on the fault, the shear stress was normalised by the peak stress preceding each stick-slip event and multiplied by the bulk coefficient of friction to obtain a value of scaled friction to allow comparison across events.

4.3 Results

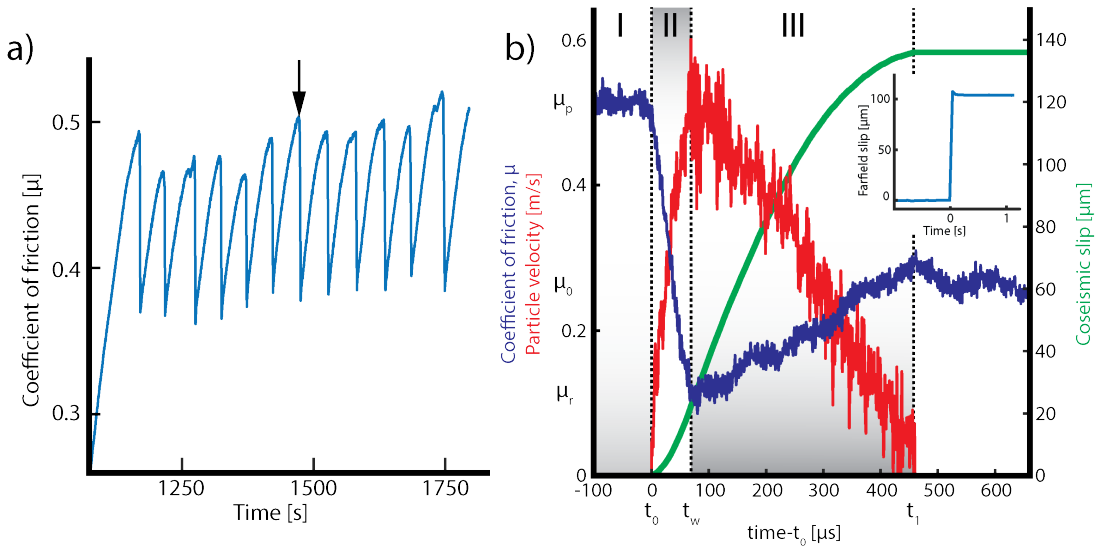

Figure 4.2 Mechanical data recorded at a) low frequency and b) high frequency during experiment Du160. In a) recordings from the force gauge show a typical sequence of stick-slip events as a function of time. In b) the high frequency recordings from strain gauges is shown, showing detail of shear stress, velocity and cumulative slip plotted as a function of time. Recordings are for event 28 of Du160 at 75 MPa normal stress. The inset in b) shows the retrieved LVDT stiffness corrected slip record which shows reasonable agreement with the integrated slip record obtained from strain gauges.

All high frequency recordings of stick-slip events (typically 30-40 per experiment) were examined before events with clear strain signals were selected for further data analysis.

Therefore, the results presented in Table 4.1, and subsequently in this chapter are a small fraction of those recorded.

Experiment	Event	Normal stress	V_r (m/s)
Du157	15	75 MPa	1100
Du157	34	75 MPa	1000
Du159	18	80 MPa	2500
Du159	29	100 MPa	2190
Du159	30	100 MPa	2560
Du160	9	58 MPa	2166
Du160	21	73 MPa	1460
Du160	27	75 MPa	1797
Du160	28	76 MPa	1800

Table 4.1 Individual stick-slip events presented in this thesis chapter.

An example of a typical series of stick-slip events recorded at low frequency is plotted in Figure 4.2a, with faults typically failing at $\mu = 0.5$, with a typical friction drop of $\Delta\mu = 0.15$. In Figure 4.2b, the high frequency recording corresponding to the labelled event in Figure 4.2a is shown, which is representative of a typical stick-slip event. Typical events are characterized by three stages, (I) transient rise to the peak stress τ_p, associated with a stress concentration around the rupture tip, immediately preceding rupture passage which arrives at time t_0 (Figure 4.2b). Due its rapid decay (in $r^{-1/2}$) with distance r from the tip, such rise is not observed systematically in these experiments, and was not observed in previous studies (Passelègue et al., 2016; Brantut et al., 2016). (II) Rapid weakening to dynamic stress τ_r and concomitant acceleration of slip which reaches peak weakening at time t_w. (III) Gradual re-strengthening to a static friction level μ_0 and particle deceleration. In Figure 4.2b, slip velocity is plotted as a function of time. Initial slip reaches peak velocity (V_{max}~0.55 m s^{-1}) in about 50 μs, resulting in accelerations of the order of 1.1×10^4 m s^{-2} ($\approx$1000 g). The peak velocity also corresponds to the lowest friction, in this case $\mu_r = 0.12$. Following the attainment of peak velocity, the fault decelerates almost linearly in time to reach zero in about ~350 μs, while sliding friction recovers from $\mu = 0.12$ to $\mu = 0.3$ and rupture arrests at time t_1.

Frictional relation to slip velocity is highlighted in Figure 4.3a, showing weakening during the acceleration and modest recovery with deceleration. Integrating velocity in time to obtain coseismic slip yields an estimate of weakening distance, which varies between a few μm, up to ≈25 μm for the events reported in Figure 4.3b. Of note is that

the weakening depends primarily on peak velocity rather than slip amount, and therefore shows a predominantly velocity-weakening behaviour for granite under these conditions. However, during the recovery phase, the restrengthening is modest and shows a non-bijective relation to velocity.

Comparison of differing events at a range of conditions reveals a fairly fixed, albeit extremely rapid, weakening rate with events sliding at different final levels of shear stress. This results in the weakening distance scaling with the dynamic stress drop.

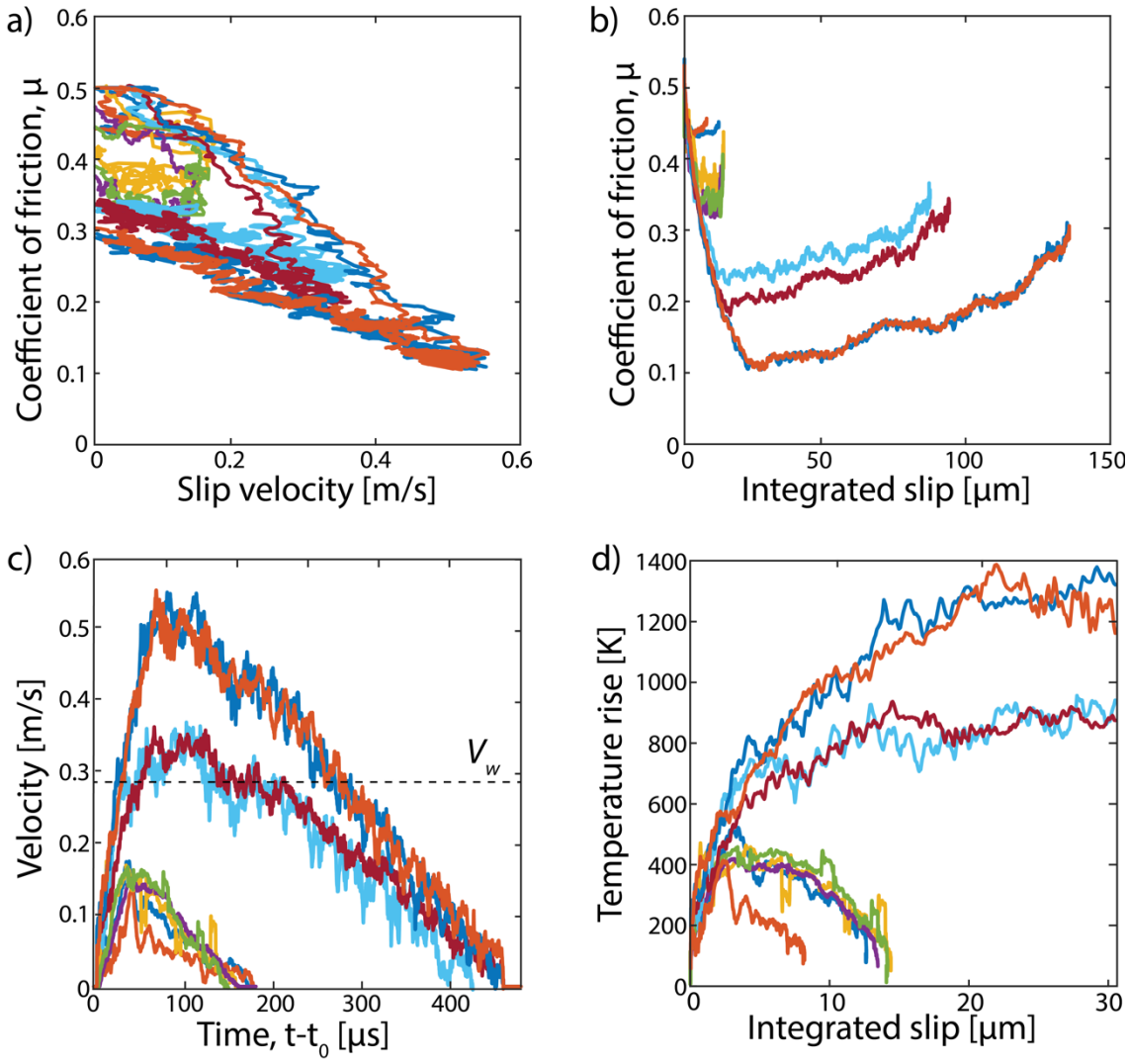

Figure 4.3 Compilation of key physical parameters during stick-slip events. A) Friction plotted as a function of instantaneous particle velocity, B) friction plotted as a function of slip, C) time-velocity functions and D) modelled temperature rise during the weakening phase of ruptures on asperities.

As is shown in Figure 4.3c all events accelerate to differing peak velocities V_{max} = 0.15-0.55 m/s, within a timescale of 30-50 μs, with resulting accelerations of between 5000-10000 m/s^2 (500-1000 G). During this acceleration friction is observed to weaken to

values between μ_r = 0.12-0.45, resulting in a dynamic friction drop of μ_p-μ_r = 0.05-0.38, over a weakening distance, δ_c = 1-23 μm (weakening rate 16,000 - 50,000 m^{-1}).

Thermal rise calculations during weakening, plotted in Figure 4.3d, were determined following an asperity scale model (Proctor et al., 2014). The background temperature rise of the fault surface, T_f is given by:-

$$T_f = T_0 + \int_0^t \frac{\tau(t')V(t')}{\rho\hat{c}} \frac{1}{\sqrt{4\pi\alpha_{th}(t-t')}} dt'$$

Where T_0 is the ambient temperature in K, $\tau(t')$ the time dependant shear stress, $V(t')$ the time dependant velocity, $\rho\hat{c}$ the specific heat capacity in J/m^3 and α_{th} the thermal diffusivity in m^2/s. To model the asperity temperature rise, a model considering flash heating theory was also applied, with the asperity temperature, T_{asp}, given by:-

$$T_a = T_f + \frac{\tau_c}{\rho\hat{c}}\left(\frac{Vr_a}{\pi\alpha_{th}}\right)^{\frac{1}{2}}$$

where τ_c the contact shear strength in Pa, defined as $\tau_c = f_0\sigma_c$, where f_0 is the static coefficient of friction, σ_c the indentation strength in Pa and r_a the mean asperity dimension. This model assumes asperities lose contact after a distance greater than the contact diameter, having a lifetime equal to $\frac{r_a}{V}$. Asperity size r_a is defined as 2.5 μm based on numerical modelling which is discussed in further detail later on in the chapter. The parameters τ_c = 5 GPa (f_0 = 0.5 and σ_c = 10 GPa), α_{th} = 1.25x10^{-6} m^2/s, $\rho\hat{c}$ = 2.16x10^6 and T_0 = 298 K were all used to compute the thermal models.

Thermal modelling indicates that the temperature rise reached at asperities (T_a) ranges from ~500 K, up to 1250 K. For westerly granite the weakening temperature (T_w) is commonly estimated to be 1000°C. Slip surfaces that reach temperatures above T_w are expected to show large stress drops which is observed to be the case in Figure 4.3. This observation is also confirmed by SEM imaging of experimental slip surfaces which show abundant evidence of frictional melting (Figure 4.4a and b).

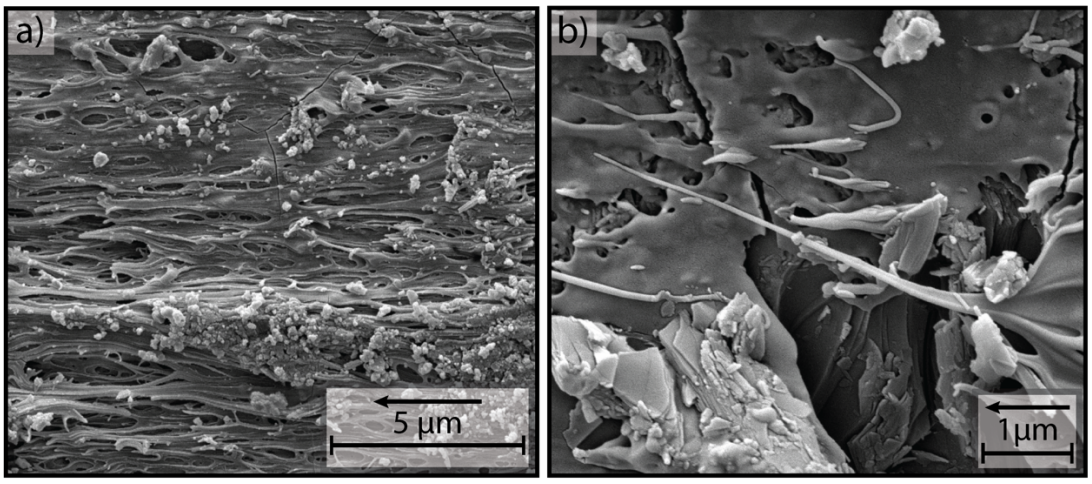

Figure 4.4 Evidence of frictional melting observed in SEM imaging of slip surfaces. A) Typical psuedotachylyte microstructure comprised of thin strands of melt with high porosity b) melting associated to a biotite grain, with necked melt strands.

In Figure 4.7 the coefficient of friction recorded during the weakening phase ($t_0 - t_w$) is plotted as function of velocity from t_0 to t_w, showing a critical velocity ($V_0 \approx 0.15$ m/s), above which strong frictional weakening is observed. Points are coloured using the integrated slip, highlighting that weakening scales with accumulated slip. This strongly suggests that weakening occurs through thermally activated weakening mechanisms.

As friction is obtained as a function of slip it is possible to compute the breakdown energy consumed during rupture propagation (Tinti, Spudich, et al., 2005),

$$W_b = \int_{t_0}^{t_w} (\tau(t) - \tau_r) V(t) dt \qquad 4.6$$

Values obtained through numerical integration of friction curves yield estimates on the order of 4 to 208 $Jm^{-2,}$ scaling with total coseismic fault slip. Values obtained are on a similar order to those obtained at comparable conditions, and demonstrate a similar scaling to previous experimental work (Passelègue et al., 2016; Ohnaka, 2003). These results are plotted in Figure 4.9 as a function of total coseismic slip, alongside data from seismological estimates.

4.4 Discussion

4.4.1 Flash heating processes

In order to investigate the microphysical basis for the observed velocity dependence of friction at fast slip rates, results are now considered in relation to a model of flash heating. Heating and melting of asperities is a currently favoured model to explain the high velocity weakening of dry frictional interfaces at high velocity conditions (Beeler et al., 2008; Goldsby and Tullis, 2011; Passelègue et al., 2016). Flash heating provides a theoretical estimate of the velocity dependence of friction, and assumes that during an asperity contact lifetime, defined:

$$\theta = \frac{r_a}{V} \tag{4.7}$$

where θ is the contact lifetime in s and V is the sliding velocity, all dissipated frictional energy goes into producing heat. If the temperature exceeds the melting temperature of the rock, T_m, then the contact is assumed to weaken to a dynamic strength, f_w. Weakening can only occur if the contact lifetime exceeds the weakening lifetime, θ_0, which allows definition of a critical velocity, V_w, above which asperities will be in a state of incipient weakening.

$$V_{\mathrm{w}} = \frac{\pi\alpha}{r_a}\left[\frac{\rho\hat{c}\left(T_b - T_f\right)}{\tau_c}\right]^2 \tag{4.8}$$

This may be rewritten to obtain a critical asperity dimension, r_w, for a given velocity:-

$$r_{\mathrm{w}} = \frac{\pi\alpha}{V}\left[\frac{\rho\hat{c}\left(T_b - T_f\right)}{\tau_c}\right]^2 \tag{4.9}$$

When $V > V_w$, for a fixed asperity dimension strength is expected to reduce from f_0 to f_w, and the overall strength of the fault as a function of velocity is therefore:-

$$f = (f_0 - f_w)\frac{V_{\mathrm{w}}}{V} + f_w$$

4.10

This provides a strength estimate for a fault with fixed asperity dimension (Beeler et al., 2008; Rice, 2006; Rempel and Weaver, 2008). However given that the majority of fault surfaces demonstrate self-affine scaling both in the laboratory and nature (Candela et al., 2012), asperity lengths are likely distributed around a mean value (Scholz, 1988; Yoshioka and Scholz, 1989; Dieterich and Kilgore, 1994). This means that during weakening, for a given velocity, asperities of dimension $r_a > r_w$ are expected to be weak during their lifetime. Those that are smaller are expected to be at their static strength. Given that the overall strength of the fault is given by the integrated strength of asperities, and that during the lifetime of an asperity some of it may be weak, then the overall strength of the fault is:-

$$f_{ss} = f_0 \int_0^{r_0} P(r_a) dr_a + \int_{r_0}^{\infty} \left[(f_0 - f_w) \frac{r_a}{r_w} + f_w \right] P(r_a) dr_a$$

4.11

Where f_{ss} is the bulk steady state friction coefficient, f_0 the initial unweakened friction coefficient, f_w the weakened friction coefficient, d the asperity dimension, r_w the critical asperity dimension in m and $P(r_a)$ the asperity probability density function.

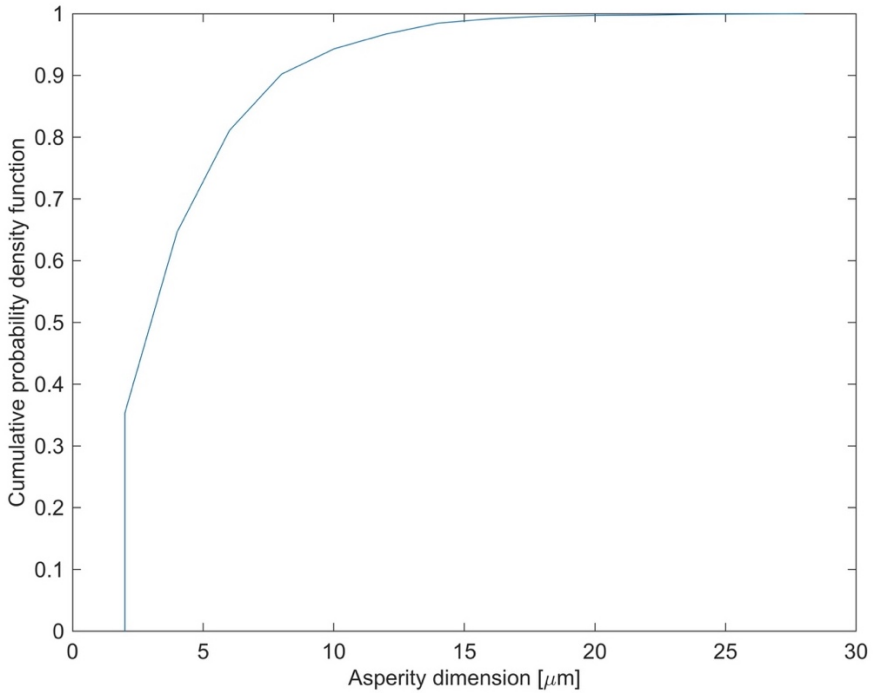

Figure 4.5 Cumulative density function of asperity dimension from numerical modelling of surface contact.

Using the integrated strength relationship and the models of elastic contact developed in chapter 3, it is possible to apply this model to WLI and stylus profilometer scans obtained from post-experimental scans. By calculation of the asperity density function using the code elasticflash2.m and applying equation 4.11, the expected strength of the fault was computed from post-experiment topographic measurements. Results from this modelling are shown in 4.5, and Figure 4.6 shows the strength relation predicted by the 1-d elastic modelling code.

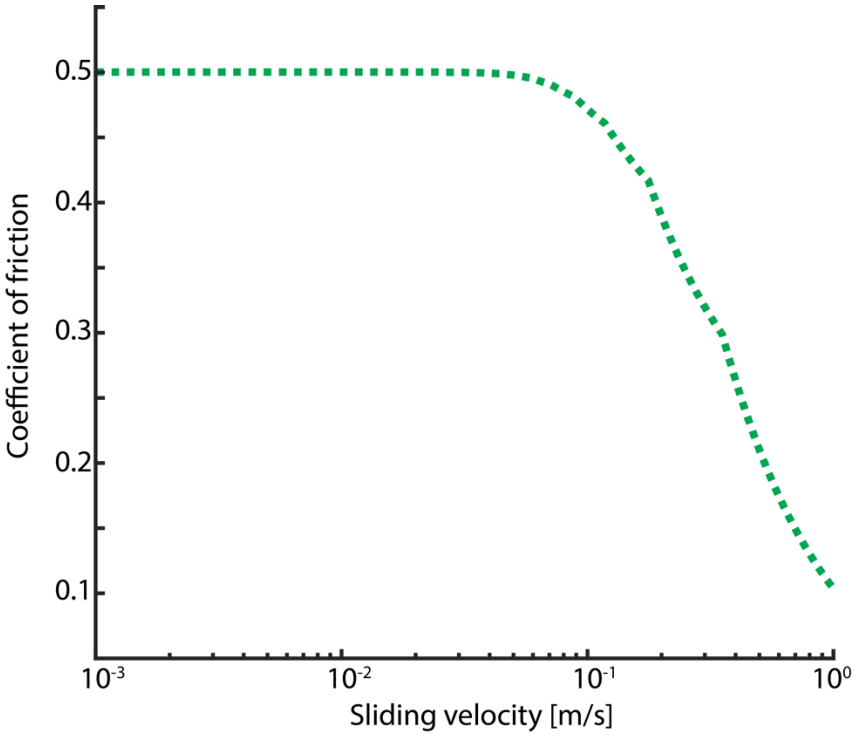

Figure 4.6 Predicted velocity dependent strength at high sliding velocity deriving from numerical model of surface contact.

Alternatively substituting in the frictional strength for a log-normal population of asperities is given by:-

$$f = f_w + \frac{f_0 - f_w}{1 + \frac{V}{V_w}\left\{1 - exp\left[-\left(\frac{V}{V_w}\right)^2\right]\right\}}$$

4.12

Here the expected strength following independently derived thermal parameters is modelled following (Goldsby and Tullis, 2011), for the asperity dimension a value of r_a = 2.5μm, which is a best estimate derived from 1-d numerical modelling of rough surface contact (Harbord *et al.*, 2017, and chapter 3 of this thesis).

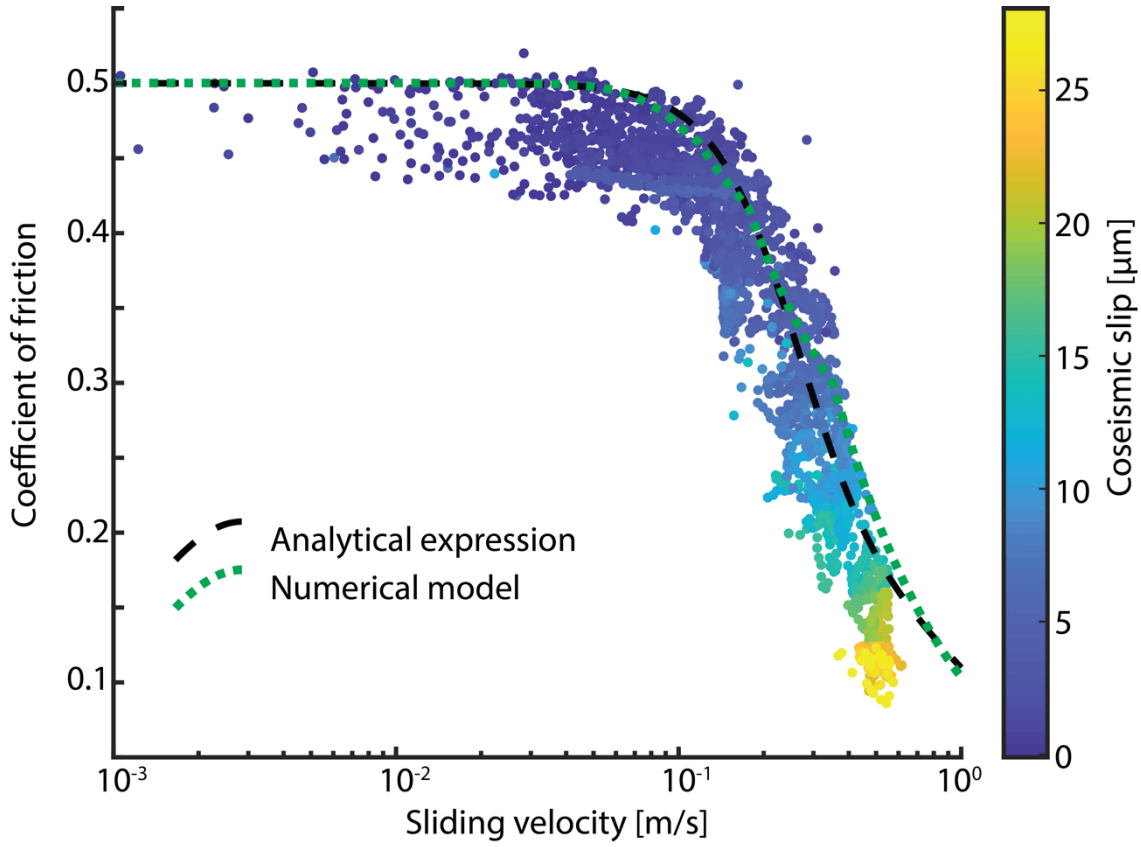

Figure 4.7 Comparison of mechanical data with flash heating theory during weakening phase of stick-slip events. Points are coloured according to the cumulative slip, with increasing slip correlating with increased dynamic weakening. The analytical solution (equation 4.12) is the black dashed curve, and the numerical solution (solved using equation 4.11) is the green dashed curve.

Comparison of the predicted frictional strength deriving from a distributed asperity contact dimension shows excellent agreement with experimental results during the weakening phase of STE. This suggests, in agreement with studies conducted at imposed conditions (Goldsby *et al.*, 2011), that flash heating provides an accurate physical description of fault friction under dry high velocity sliding conditions.

This result is supported by the microstructural evidence of melting (Figure 4.4), consistent with experiments run at similar conditions (e.g. Passelègue *et al.*, 2016; Hayward *et al.*, 2016). This suggests that flash heating captures the fundamental physics governing the velocity dependence of high velocity slip during spontaneous laboratory earthquakes.

4.4.2 Relationship to high velocity experiments

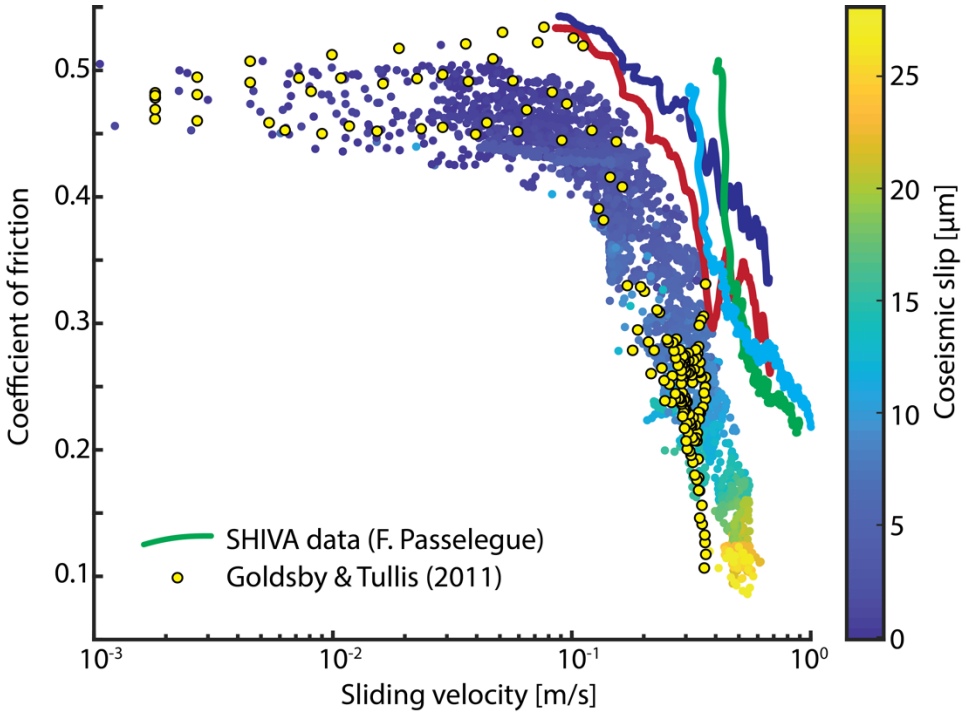

Figure 4.8 Comparison of strain gauge data with high velocity friction data. Note that the data deriving from (Goldsby and Tullis, 2011) has been rescaled to fit $f_0 = 0.5$ to allow a closer comparison of the datasets.

In order to place the experiments presented in the context of previous studies, results from imposed high velocity experiments conducted using initially bare surfaces of westerly granite are compared to high frequency data in Figure 4.8. Data from Goldsby and Tullis (2011) shows a good agreement with the high frequency strain gauge data presented in this thesis chapter, although there is some divergence in strength observed at high velocity. This may be a result of the fact that the data obtained by Goldsby and Tullis (2011) derives from steady state sliding velocities, where weakening may be more efficient as a result of the background temperature rise, whereas these results are obtained during spontaneous rupture propagation. The data obtained from F. Passelegue (unpublished, Pers. Comm.), shows a similar form in weakening behaviour, however it is shifted to higher velocity. In this case differences may result from the differing normal stress conditions 75-100 MPa for results in this chapter vs. 25 MPa for the high velocity experiments.

4.4.3 Scaling of laboratory earthquakes

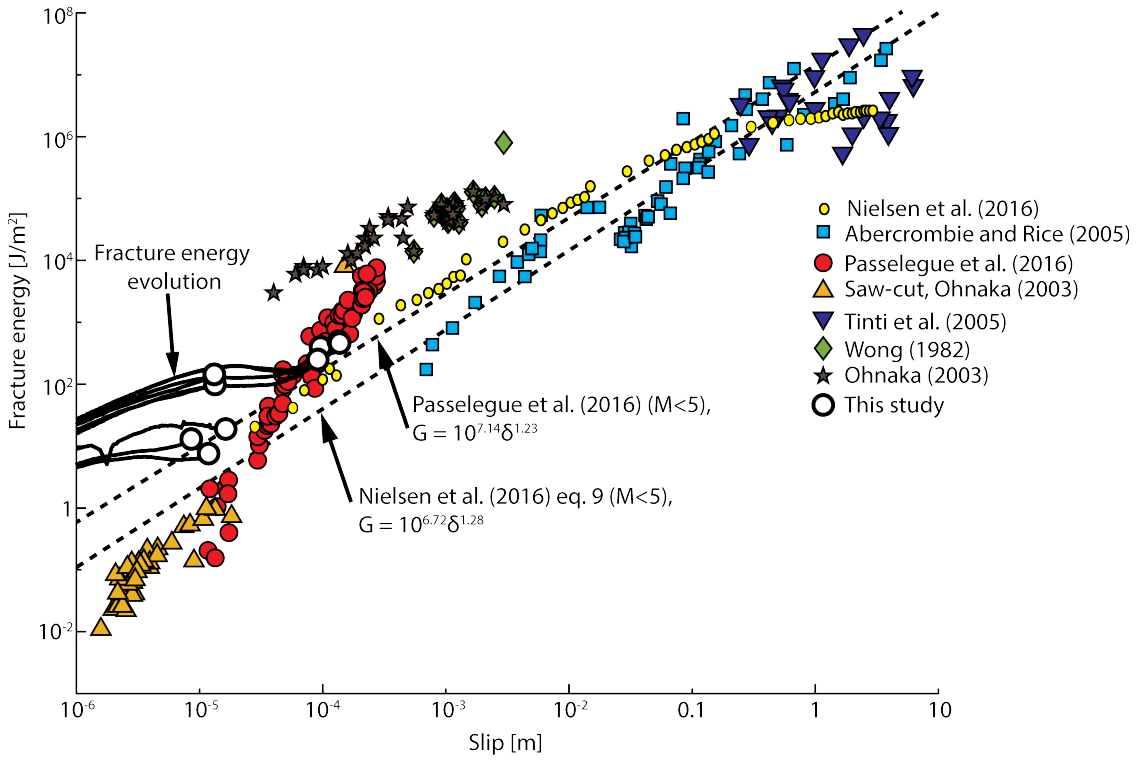

Figure 4.9 Comparison of fracture energy estimated from strain gauge data as a function of total slip against previous literature data.

In order to investigate the scaling of the ruptures presented in this chapter, in Figure 4.9 fracture energy is plotted as a function of total slip. The data presented in this thesis chapter are shown as black circles with a white infill, the rest of the data derive from a review of previous literature (Nielsen et al., 2016; Abercrombie and Rice, 2005; Passelègue et al., 2016; Ohnaka, 2003; Tinti, Spudich, et al., 2005; Wong, 1982). The dashed lines show best fits of the literature reviewed by Passelègue *et al.* (2016), and the second estimate derives from Nielsen *et al.* (2016). The results from this study agree well with this scaling relationship for earthquakes of M<5, therefore hinting at a self-similar scaling.

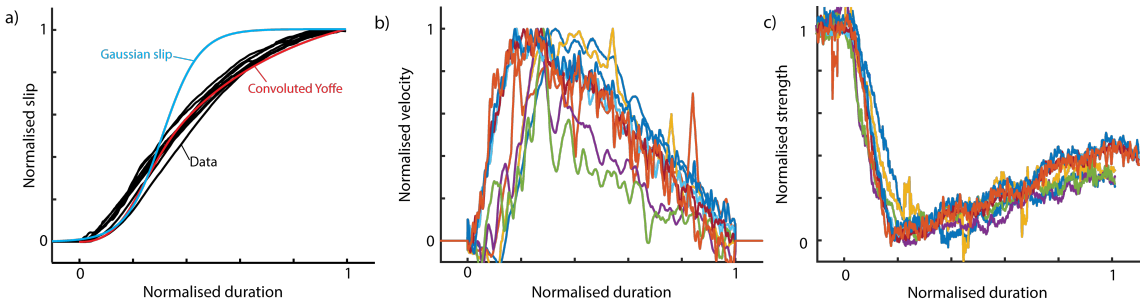

Figure 4.10 Self-similarity of individual laboratory earthquakes identified by normalisation of a) slip, b) velocity and c) strength with respect to normalised duration. The convoluted Yoffe function was computed following Tinti et al. (2005)

In order to investigate the origins of the fracture energy scaling presented in Figure 4.9, normalised slip (Figure 4.10a), normalised velocity (Figure 4.10b) and normalised stress drop (Figure 4.10c) are plotted as a function of normalised event duration. The slip functions in Figure 4.10 a) show a very close collapse to a single function, demonstrating similarities to a convoluted Yoffe function computed after Tinti *et al.* (2005). For reference a gaussian slip profile is also plotted. The velocity function in Figure 4.10 b) also shows a close collapse of data, although the collapse is limited by the high frequency noise originating from data sampling. Finally, in Figure 4.10 c) the normalised stress shows a near perfect collapse, some events also demonstrate a record of peak stress preceding rupture arrival indicated by a peak in strength >1 before weakening onset. These results therefore directly support the speculated self-similarity of earthquake source mechanisms, and point towards the use of self-healing slip-pulse models e.g. (Nielsen and Madariaga, 2003; Heaton, 1990) in kinematic source models.

4.5 Conclusions

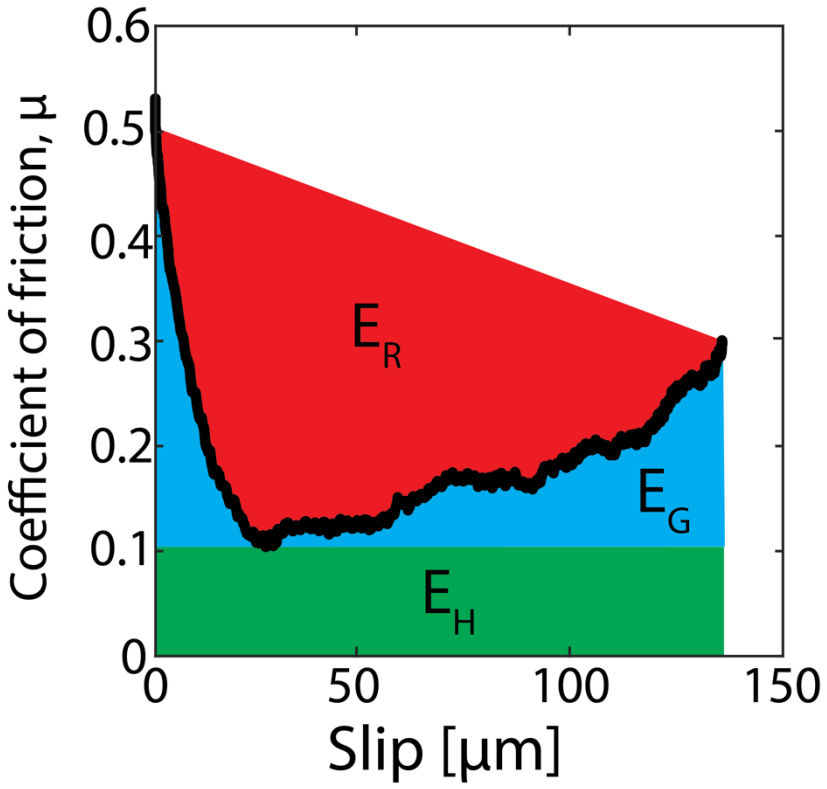

Figure 4.11 Towards quantifying the earthquake energy balance in the lab. Schematic infill of portioning of energy sinks during experiment Du160, event 28 at 76 MPa. E_R is the radiated energy as seismic waves and off-fault damage, E_G the fracture energy dissipated as new surface creation and E_H the frictional energy dissipation as heat.

Results presented here have significant implications for the mechanics of natural earthquakes. Flash heating has been postulated to play a key role in the initial weakening stages of earthquake rupture (Rice, 2006; Brantut and Viesca, 2017), and it is likely to be an important weakening mechanism for small slip earthquakes (Nadeau and Johnson, 1998). This is supported by the energy scaling that is observed in the results presented in this chapter with M<5 earthquakes. For larger earthquakes flash heating may be active during the initial phases of slip, before other mechanisms e.g. thermal pressurization (Viesca and Garagash, 2015) or off-fault damage (Nielsen et al., 2016), take precedence as indicated by breakdowns in energy scaling. Additionally, in agreement with analogue experiments (Rubino et al., 2017), presented friction-velocity relationships show that commonly used slip weakening formulations (e.g. Andrews, 1976) are not able to accurately capture the nature of dynamic frictional sliding. It is also salient to note that the non-bijective nature of the dynamic friction suggests that flash heating describes well the weakening but cannot explain restrengthening. This suggests that more work is required understand the nature of dynamic friction under conditions of spontaneous

rupture. Looking forward, as is shown in Figure 4.11, these results directly open up pathways to provide a complete constraint on the earthquake energy balance. They may also permit the investigation of the nature of dynamic weakening at a range of hypocentral conditions previously inaccessible by experiment.

4.6 Appendix

4.6.1 Thermal parameters

τ_c	α	$\rho\hat{c}$	T_b	T_f
5 GPa (0.5*10 GPa)	$1.25\text{x}10^{-6}$ m^2/s	$2.16\text{x}10^6$ J/m^3	1293 k	298 k
(Goldsby and Tullis, 2011)	(Beeler et al., 2008)	(Beeler et al., 2008)	(Beeler et al., 2008)	(Beeler et al., 2008)

4.6.2 Steady-state propagating perturbation

For a wave, rupture or other strain-inducing perturbation which is propagating, considering a reasonable approximation that: (1) the propagation along direction x is at a constant velocity c, and (2) the perturbation is steady-state (no change in form or amplitude with time), then the particle motion in any direction *i* at *x* can be written as a function of $(x - ct)$ alone (for propagation in the positive x direction) such that:

$$u_i(x,t) = u_i(x - ct, 0) = u_i(x - ct) \tag{4.13}$$

Therefore, the derivatives in time and space become:

$$\partial_t u_i(x,t) = -c\, u'(x - ct) = -c\partial_x u_i(x,t) \tag{4.14}$$

And, given $\varepsilon_{xx} = \partial_x u_x$, the strain velocity equivalence can be written

$$\partial_t u_x(x,t) = -c\varepsilon_{xx}(x,t)$$

$$v_x(x,t) = -c\varepsilon_{xx}(x,t)$$

4.15

4.6.3 Fault and rupture symmetries

If a fault is embedded in an homogeneous medium and is reasonably straight to preserve symmetry, assuming a fault of normal y and slip in direction x. In the vicinity of the fault the displacement u_x equates to half the slip Δu across the fault therefore,

$$u_x(x, y \to 0^+) = \frac{1}{2}\Delta u$$

$$v_x(x, y \to 0^+) = \frac{1}{2}\Delta v$$

4.16

Then according to equation 4.15,

$$\Delta v = 2c\varepsilon_{xx}$$

4.17

Therefore measurements of strain parallel to the fault will give a measurement directly proportional to slip and the proportional to slip and the proportionality factor is the apparent propagation velocity c in direction x. Note that slip direction need not be necessarily along x (if not Δv from equation 4.17 will be the slip velocity projected along x), or that propagation of rupture is not in direction x (if not, then c would be the effective velocity projected in direction x).

Symmetry allows to predict that the fault normal stress $\sigma_{yy} = 0$ (where σ_{yy} is not the absolute stress level, but the rupture induced variation alone). Therefore, isotropic elasticity,

$$\sigma_{ij} = \lambda\delta_{ij}\varepsilon_{kk} + 2G\varepsilon_{ij}$$

4.18

With summation over repeated indexes; therefore, it can be written (assuming 2D elasticity for simplicity):

$$\sigma_{yy} = \lambda\left(\varepsilon_{xx} + \varepsilon_{yy}\right) + 2G\varepsilon_{yy} = 0$$

$$\sigma_{xy} = 2G\varepsilon_{xy}$$

4.19

Assuming that ε_{yy} is not measured directly, it can be deduced from ε_{xx} alone given the equality in equation 4.19

$$\varepsilon_{yy} = -\frac{\lambda}{\lambda + 2G}\varepsilon_{xx}$$

4.20

Furthermore, measuring strain at the diagonal, ε_d along direction *x'* at π/2 from the fault, and using strain rotation with $\cos\frac{\pi}{2} = \sin\frac{\pi}{2} = \frac{\sqrt{2}}{2}$ it may be written:

$$\varepsilon_d =$$

$$\varepsilon_{x'x'} = \varepsilon_{xx}\cos^2\theta + \varepsilon_{yy}\sin^2\theta + \varepsilon_{xy}\sin\theta\cos\theta$$

$$= \frac{1}{2}(\varepsilon_{xx} + \varepsilon_{yy} + \varepsilon_{xy})$$

4.21

Replacing the value of ε_{yy} according to equation 4.19 and solving for ε_{xy}

$$\varepsilon_{xy} = 2\varepsilon_d - \varepsilon_{xx}\left(1 - \frac{\lambda}{\lambda - 2G}\right)$$

4.22

And the shear stress is

$$\sigma_{xy} = 4G\varepsilon_d - 2G\varepsilon_{xx}\left(1 - \frac{\lambda}{\lambda - 2G}\right)$$

4.23

4.6.4 Approximations in non-steady-state cases

In cases where the steady-state is effective then strain ε_{xx} before and after passage of the perturbation will be equal, and eq. (5) will produce a velocity correctly going to zero again at the end of the slip locally on the fault. In cases where steady-state ceases to be a good approximation, it is expected that $\varepsilon_{xx}^{init} - \varepsilon_{xx}^{final} = \Delta \neq 0$, the difference being due to a residual static gradient in slip along the fault. However ε_{xx} may be corrected by de-trending the transient signal with more or less sophisticated algorithms.

In the ignorance of the exact deviation from steady-state, a linear, increasing de-trend

of slope $-\frac{\Delta}{\delta t}$, where δt is the slip pulse duration, may be applied from the beginning to the end of the slip pulse. It can be shown in a few theoretical rupture pulse examples that such correction generally results in a satisfactory approximation of the actual slip velocity, although such demonstration obviously lacks in generality. One example of non-steady-state slip is the self-healing, self-similar pulse with propagating edge at velocity c and healing edge at velocity c_h. In this case the slip velocity has the form,

$$\Delta v = \alpha \, Re \left\{ \frac{\sqrt{c_h - \frac{t}{x}}}{\sqrt{\frac{t}{x} - c}} \right\}$$

which is self-similar (Nielsen and Madariaga, 2003). Comparison of the *v* derived using ε_{xx} and the actual one is shown in Figure 4.12a, and the result of *v* after linear de-trending of Δ is compared in Figure 4.12b.

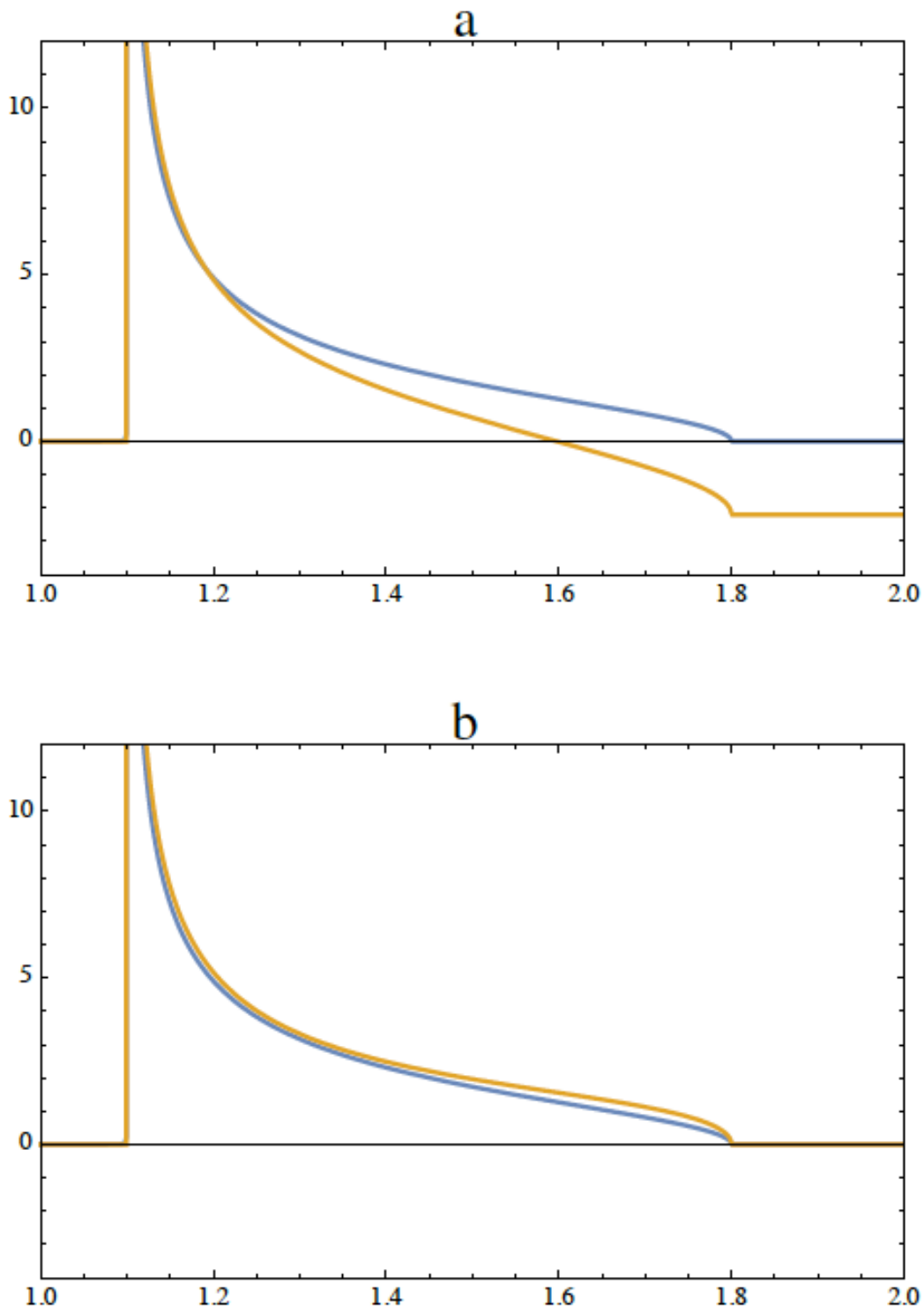

Figure 4.12 Slip velocity (a, blue) for a self-healing slip-pulse and the slip velocity retrieved from strain ε_{xx} with no detrending (a, orange) and after detrending (b, orange). In this example rupture velocity is 95% and healing velocity is 55% of the shear wave speed. Vertical axis is velocity and is arbitrary in units.

5 The effects of roughness and normal stress in the deformation of limestone faults

Abstract

Roughness of fault surfaces is an important physical characteristic of natural faults which influences the nucleation phase of earthquakes. Here, results are presented from a set of experiments that investigate the role of roughness (roughened with #60, #220, #400 and P1000 grit), and normal stress (30, 50 and 100 MPa) on frictional sliding of initially bare limestone surfaces. Frictional behaviour shows a non-trivial dependence on the normal stress and roughness, with frictional wear playing a key role in controlling the mechanical response to the imposed sliding velocity. Two regimes of frictional sliding are observed I) velocity-strengthening friction with negative *b*-values associated to pervasive formation of fault mirrors, and II) velocity neutral friction with a reduced prevalence of fault mirrors and a dominance of high porosity gouge. Regime I) sliding is observed at lower normal stress and smoother initial fault conditions, whereas regime II) is observed at high normal stress and is generally restricted to the initially rough faults (#60 grit). Sliding in regime I is interpreted to originate from semi-brittle or plastic deformation mechanisms. Sliding in regime II is dominated by brittle deformation processes with cataclastic flow and brittle grain size reduction observed. Frictional behaviour in regime II is similar to that of experiments with simulated gouge. Velocity dependence of friction is intrinsically linked to wear and the overall microstructural state of the fault, indicating that the frictional behaviour of fault zones is controlled by roughness in a complex manner.

5.1 Introduction

Limestone rocks represent a major rock type in the brittle crust, which are predominantly comprised of calcium carbonate ($CaCO_3$), and is found in a variety of tectonic settings (Nichols, 2009). Often, they form as bioclastic deposits or as biochemical precipitates in marine or lacustrine settings. The largest deposits form as platform carbonates and pelagic muds at the edges of continental shelf's. After diagenesis and uplift in the orogenic cycle, limestone bodies frequently become the protolith for many faults found in rifts and the fold-and-thrust belts of orogens e.g. the Italian Apennines (Bullock et al., 2014; Tesei et al., 2013; Collettini et al., 2003; Alvarez et al., 1978), the Zagros (Sharland et al., 2004) and the gulf of Corinth (Goldsworthy et al., 2002). Therefore earthquakes are commonly hosted within limestone terranes, such as the recent Norcia-Amatrice earthquake sequence (Tinti et al., 2016), highlighting the importance of understanding the mechanics of carbonate faulting.

As earthquakes are the result of frictional failure in tectonic faults, it is important to investigate the frictional behaviour of limestones to better understand seismogenesis in such lithologies. At room temperature conditions, limestone gouges can generally either exhibit stable velocity strengthening friction (Carpenter et al., 2016; Verberne, Spiers, et al., 2013), or in some cases unstable velocity weakening friction (Carpenter et al., 2014; Tesei et al., 2014). In Carpenter et al. (2016) it was observed that low normal stress conditions are dominated by brittle sliding behaviour, but with increasing normal stress a transition to ductile sliding behaviour at slower velocities (<10 μm/s) was observed. However, gouge sliding is observed to transition to unstable sliding at temperatures above 100°C, which has been linked to the increasing efficiency of plastic diffusive mass transfer processes (Verberne, de Bresser, et al., 2013; Verberne, Spiers, et al., 2013).

Experimental studies of carbonate friction, using initially bare surfaces are limited at low imposed sliding velocity (<1 mm/s), but indicate non-trivial sliding behaviour with observations of negative rate and state *b*-values for dolomite (Weeks and Tullis, 1985). In other studies it was found that reactivated limestone fault surfaces exhibit velocity neutral to weakening friction, with rapid healing rates (Carpenter et al., 2014). More recently Sagy, et al., (2017) and Tesei et al. (2017) demonstrated that bare limestone surfaces can be very strong (μ = 0.8-0.9) and smooth surfaces exhibit apparent negligible frictional healing at low sliding velocities (<1 mm/s). At the microscale, sliding was

accompanied by pervasive wear and the formation of fault mirror surfaces (Tesei et al., 2017).

Limestone fault surfaces obey power law scaling similar to faults in other lithologies, typically with a Hurst exponent H = 0.7 (Candela et al., 2012; Brodsky et al., 2011). Often slip on limestone-bearing faults forms highly polished mirror slip surfaces, which are formed of well packed nanometric grains. These have in the past been interpreted to be seismic slip indicators (Siman-Tov et al., 2013), as they are observed to form during high velocity experimentation (>1 mm/s) (Fondriest et al., 2013; De Paola et al., 2015; Siman-Tov et al., 2015). Recently, however, observations of fault mirrors forming during low velocity experiments (<1 mm/s) has called these inferences into question (Tesei et al., 2017; Verberne et al., 2014; Verberne, Spiers, et al., 2013).

In chapter 3 and (Harbord et al., 2017) it was identified that the combination of normal stress and roughness plays a fundamental role in the frictional sliding behaviour of initially bare Westerly granite faults. Therefore, in order to extend this study and test the general applicability of these results, further investigation of the effects of roughness and normal stress is warranted for a different lithology, in this case limestone. In the case of limestone it is expected that surfaces will wear at a faster rate, which may act to suppress the instability mechanisms developed in chapter 3 and Harbord et al. (2017). Gouge formation is expected to smooth out stress fields, which is hinted at by previous observations of gouge build-up suppressing instability (Byerlee and Summers, 1976).

5.2 Methods and materials

5.2.1 Experimental materials

To simulate initially bare rough faults in limestone, undeformed samples of the Scaglia Rossa unit were selected from a suite of samples collected from the Appenine region of Central Italy (Bullock et al., 2014). The Scaglia Rossa is part of a Jurassic to Oligocene carbonate succession in the Umbria-Marche Appenines (Collettini et al., 2003; Alvarez et al., 1978). The basal part of this formation consists of interbedded pale grey-red, micritic limestones, with regular marl interbeds up to several cm's thickness. For this study, the micritic beds were selected due to their relatively high purity (~95% $CaCO_3$), fine and uniform grain size (1-3 μm), low porosity (<5%) internal anisotropy (Bullock et

al., 2014). This helps to separate the relative influences of composition and initial rock fabric on both the wear and roughness evolution during friction experiments.

5.2.2 Deformation apparatus

All experiments were conducted in the Durham University triaxial apparatus with fluid flow (DUTFF) in the Rock Mechanics laboratory at Durham University (see chapter 2). The apparatus is capable of applying confining pressures of <250 MPa, porefluid pressure of <200MPa and axial load of <300 kN. Axial load is driven by a servo controlled electromechanical ball screw system which can operate at velocities between 0.01-24 μm/s in velocity control. The machine has a stiffness of K_m = 180 kN/mm when tested with a steel calibration dummy. All data was logged at a sampling frequency of 10 Hz.

Samples were prepared for experiments by cutting intact slabs of Scaglia Rossa limestone (4.4x30x20 mm) using thin sectioning equipment in the Thin Sectioning Laboratory at Durham University. To ensure surface parallelism, the experimental surfaces were mechanically polished to a finish of 2.5 μm. During the polishing process samples were constantly rotated to avoid preferential alignment of polishing grooves and surface aberrations. Following this, surfaces were wet ground using alumina grit of #60, #220, #400 on a polishing plate or P1000 SiC grit paper to create varying degrees of initial surface roughness. A small chamfer was made on the loaded edge of the sample to match the chamfered geometry of the sample sliders (Figure 5.1). Samples were glued into the sample sliders utilising Loctite 636 super glue, and sample edges were hand ground to match the width and length of the sample holder. To ensure pristine sample surfaces, samples were cleaned in an ultrasonic bath, dried and blasted with compressed air, both after surface roughness application and after the final shaping of samples. SEM imaging of prepared samples revealed this to be an effective technique to remove preparation debris (see chapter 5 appendix).

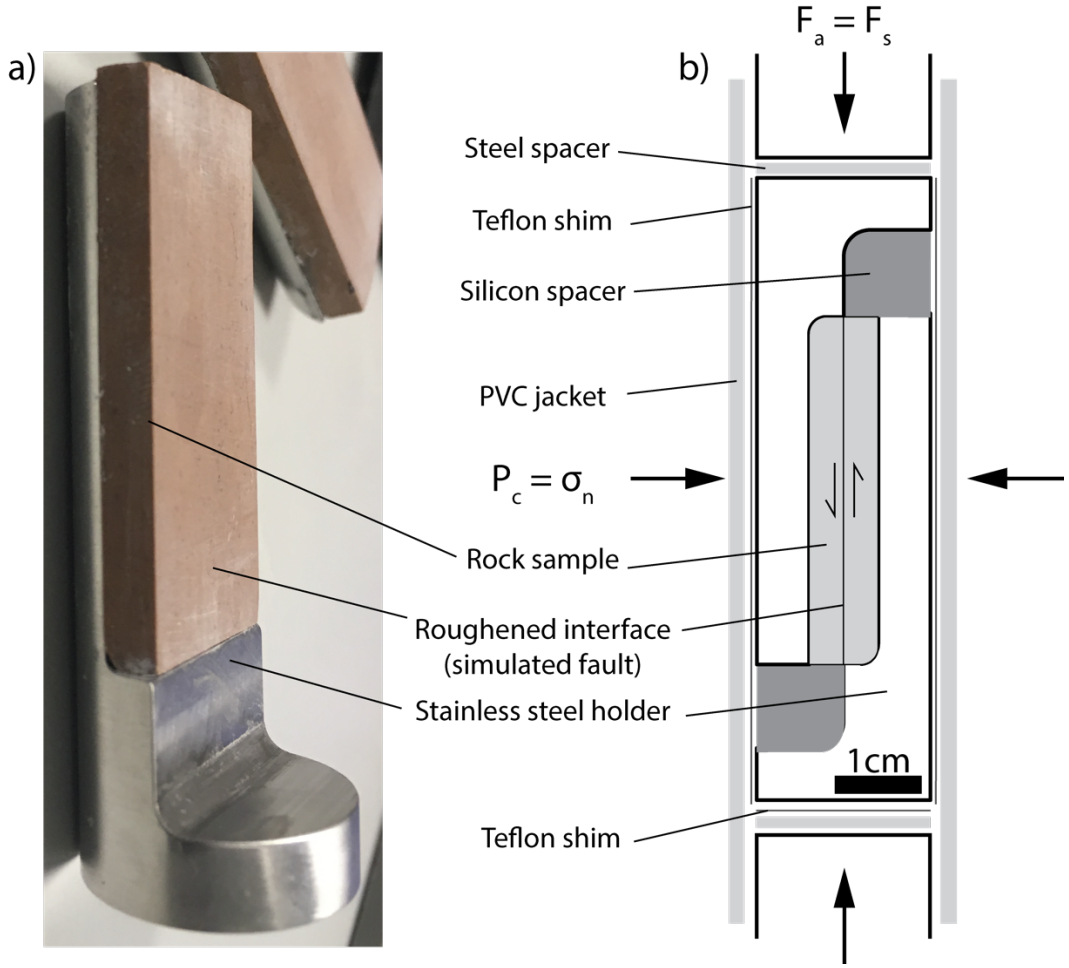

Figure 5.1 Overview of experimental technique, a) photograph of sample blocks before experiment, b) schematic of experimental set-up drawn to scale. The configuration used means that normal stress is kept constant, shear force is equivalent to the axial load, displacement measurements are the same and surface area changes are linear. It also allows solid blocks to be deformed in direct shear at higher normal stresses than normally possible using biaxial apparatus.

Following roughening, the mounted samples and the silicone spacers were wrapped together in a Teflon sleeve and inserted into a softened PVC sample jacket, before mounting into the standard sample assembly (Figure 5.1). A Teflon shim was added to reduce the contribution of jacket friction to axial force measurements. A small amount of cellotape was used to secure the Teflon shim around samples and keep the blocks together when jacketing the blocks.

In the single direct shear configuration, the normal stress is directly equivalent to the confining pressure, and the shear load and cumulative slip equal to the axial load and axial displacement respectively. This presents a significant advantage over more traditional 30° saw cut experiments as (1) shear force and normal stress are directly measured rather than being derived through stress projections; (II) non-trivial changes in

contact area due to the elliptical geometry of saw cuts are avoided; (III) no change in normal stress occurs due to slip of the fault surface.

5.2.3 Rate- and state-inversions

Following experimentation, all data was post-processed in MATLAB with shear stress calculations accounting for a linear loss of surface area according to:-

$$\tau = \frac{F_a}{W(L - u_c)} \tag{5.1}$$

Where τ is the shear stress in Pa, F_a the axial load in N, W and L the initial width and length of the samples block in m and u_c the stiffness corrected displacement on the fault in m, where $u_c = u - k_m F_a$ where u is the LVDT displacement in m and K_m the machine stiffness (=180 kN/mm).

All velocity step data was fit according to rate and state laws of frictional sliding, which provide an estimate of fault sliding stability (Marone, 1998). These are defined as,

$$\mu_{ss} = \mu_0 + a \ln \frac{V_1}{V_0} + b \ln \frac{V_1 \theta}{D_c} \tag{5.2}$$

Where μ_{ss} is the steady state friction coefficient at the new velocity V_1 in m/s, μ_0 the steady state frictional strength at the previous sliding velocity, V_0, in m/s, a the dimensionless direct rate parameter, b the dimensionless rate parameter, θ the state variable in seconds and D_c the critical slip distance in m. These parameters are schematically shown on a upstep in Figure 5.2.

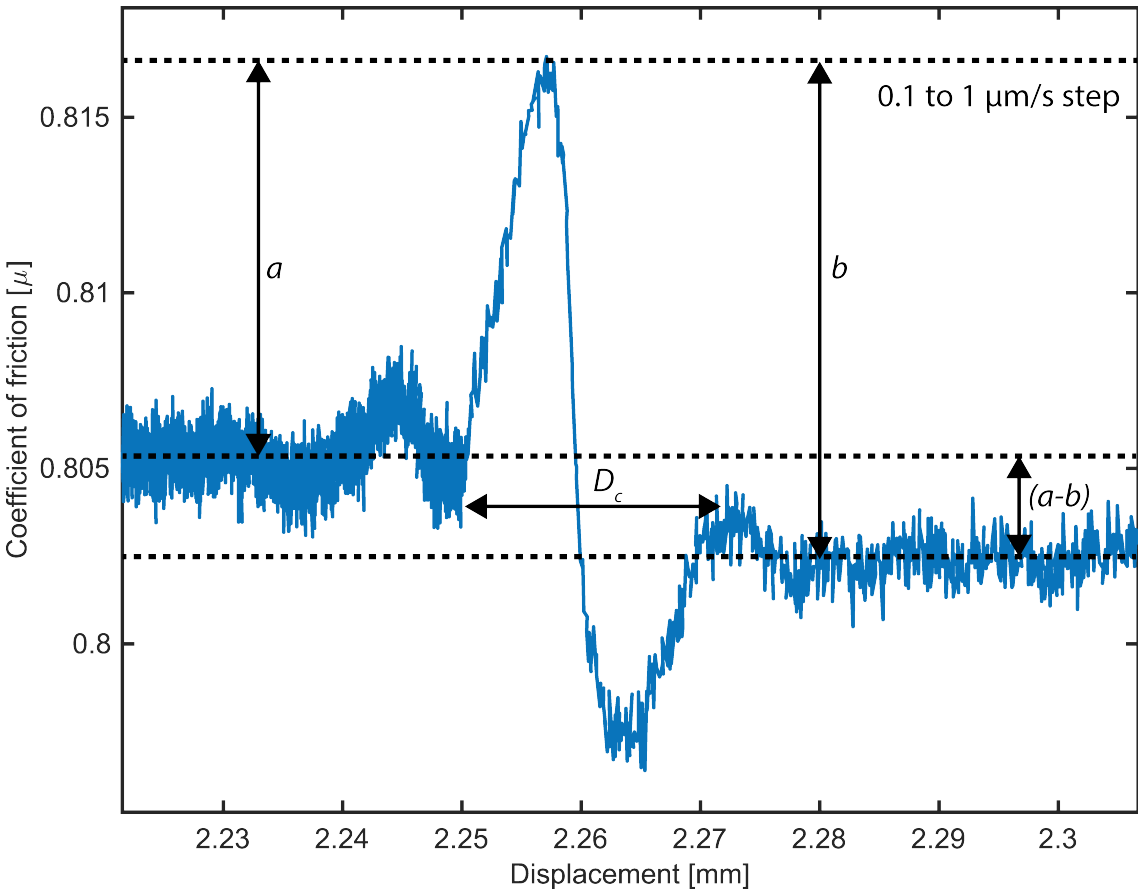

Figure 5.2 Example of a velocity step with the friction constitutive parameters a, b, a-b and D_c schematically labelled for a velocity weakening up-step. Data is sampled at 10 Hz.

Following calculation of frictional strength, data was split to perform inversions and obtain the parameters *a*, *b* and D_c using FSS 7.0 (H. Noda pers. Comm.). FSS 7.0 employs a least squares regression method (Reinen and Weeks, 1993) and uses a Levenberg Marquardt algorithm for fitting the frictional evolution. All data inversions are available in an electronic appendix on a disc provided with the thesis in the folder 'Chapter 5'. For more details of the code see Noda and Shimamoto (2009). Initial guesses are provided by the user, and multiple starts are often required to avoid issues of multiple minima. Following experimental tests of state evolution laws (Bhattacharya et al., 2015), and trial modelling of velocity steps with the different state evolution laws (Dieterich's aging law and Ruina's slip law, see appendix), data were fit with the slip law formulation (Ruina, 1983):-

$$\dot{\theta} = -\frac{V_1\theta}{D_c}\ln\frac{V_1\theta}{D_c} \qquad 5.3$$

Where $\dot{\theta}$ is the evolution of the state variable with respect to time. All inversion results are available as an electronic appendix.

5.2.4 Microstructural analysis

After each experiment the limestone blocks were removed from sample holders by applying a small amount of heat to the base of the metal blocks to decompose the superglue. Following removal of blocks, selected samples were left to air cool before being prepared for scanning electron microscopy (SEM). For secondary electron (SE) microstructural investigations of experimental surfaces, samples were sputter coated using a 30 nm Au coating. For cross sectional analysis, samples were vacuum impregnated using epoxy and then cut and polished parallel to the slip direction. Following this, samples were mounted on stubs using silver paint and then sputter coated with a 30 nm C coat and imaged using back-scattered electrons (BSE). All images were acquired using a Hitachi SU-70 field emission SEM. For SE images an accelerating voltage of 5 kV was used at a typical working distance of 7-8 mm. For BSE images an accelerating voltage of 12 kV was used, at a typical working distance of 14 mm. In addition, the majority of samples were imaged using a Nikon Eclipse LV100POL reflected light microscope in plain polarised light (PPL), and cross polarised light (XPL). For reference, a summary of all microstructural investigations is provided in table 5.1.

5.3 Mechanical and microstructural results

5.3.1 Mechanical data

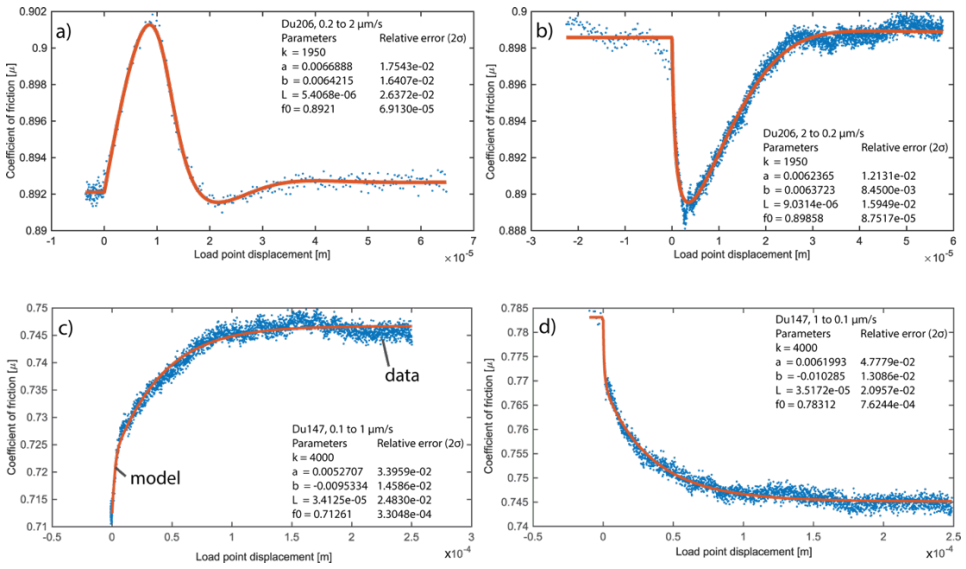

Figure 5.3 Examples of the frictional response to stepwise changes in sliding velocity and inversion model results obtained using FSS 7.0, blue points are measured data and red the modelled frictional response. Upsteps are shown in a) for 0.2 to 2 µm/s with a positive value of the parameter b, c) for 0.1 to 1 µm/s for an experiment with a negative value of b. Downsteps are shown in b) showing positive values of the parameter b for a step from 2 to 0.2 µm/s and d) negative values of b for a step from 1 to 0.1 µm/s.

In total 20 experiments are presented, and demonstrate that in the majority of cases frictional sliding on initially bare limestone surfaces is velocity strengthening, with *a-b* values ranging from velocity weakening (-0.005) to very strongly velocity strengthening (+0.02) (Figure 5.3). This strong velocity strengthening is largely a result of the consistently observed negative b-values obtained during the majority of velocity steps (Figure 5.3c and d). It is also found that the critical slip distance is large (10- 100 µm) relative to similar experimental tests conducted utilising calcite fault gouges at comparable conditions (Figure 5.3). These are both unusual observations, particularly negative b values which are often observed at high homologous temperature conditions (Shimamoto, 1986; Blanpied et al., 1998), or for experiments conducted using clays (Ikari et al., 2009; Logan and Rauenzahn, 1987).

During experimentation frictional, wear is likely to be an important factor influencing the microstructure of the sample as a function of slip and normal stress, and therefore the subsequent mechanical behaviour (Wang and Scholz, 1994; Scholz and Engelder, 1976; Boneh et al., 2013; Beeler et al., 1996). Wear volume is proportional to the mechanical

work dissipated on the surface (Archard, 1959; Queener et al., 1965; Boneh and Reches, 2018), which is captured on a first order by Archard's law:-

$$Q = K\frac{\mu\sigma Au}{\sigma_c}$$

Where Q is the wear volume in m^3, κ the dimensionless wear coefficient, μ the coefficient of friction, σ the normal stress in Pa, A the fault surface area in m^2, u the cumulative fault slip in m and σ_c the indentation strength. This highlights that, frictional wear is directly proportional to the product of the slip averaged shear stress and the cumulative slip. Therefore, to test whether frictional parameters scale with wear, all frictional parameters are plotted as a function of frictional work, $\omega = \mu\sigma\delta$, in units of J/m^2, as well as displacement. ω also provides a single parameter to combine results from a range of normal stresses and displacements, allowing compilation and comparison of results.

Experiment	Grit	σ_n	Velocity history	Microstructures
Du126	#60	30 MPa	1|0.1|1|0.1|1|0.1|1|0.1|1|0.1|1|0.1|1|0.1|1|10	
Du131*	#60	30 MPa	1	SEM, optical
Du140	#60	30 MPa	1|0.1|1|0.1|1|0.1|0.01|0.1|SHS	SEM, optical, X-section
Du127	#220	30 MPa	1|0.1|1|0.1|1|0.1|1|0.1|1|0.1|1|10|1|0.1|1|0.1|0.01	SEM, optical
Du125	#400	30 MPa	1|0.1|1|0.1|1|0.1|1|0.1|1|0.1|1|0.1|1|0.1|1	SEM, optical, X-section
Du130*	#400	30 MPa	1	SEM, optical
Du147	P1000	30 MPa	1|0.1|1|0.1|1|0.1|1|0.1|1|0.1|1|0.1|1|0.1|1|SHS	SEM, optical, X-section
Du133	#60	50 MPa	1|0.1|1|0.1|1|0.1|1|0.1|1|0.1|1|0.1|1|0.1|1	Optical
Du205	#60	50 MPa	2|0.2|2|0.2|2|0.2|2|0.2|2|0.2|2|0.2	
Du134	#220	50 MPa	1|0.1|1|0.1|1|0.1|1|0.1|1|0.1|1|0.1|1|0.1|1	Optical
Du132	#400	50 MPa	1|0.1|1|0.1|1|0.1|1|0.1|1|0.1|1|0.1|1|0.1|1|0.1|0.01|0.1|1	Optical
Du153	#400	50 MPa	1|0.1|1|0.1|1|0.1|1|0.1|1|SHS	Optical
Du154	#400	50 MPa	1|0.02|0.2|0.02|0.2|2|0.2|0.02|2|SHS	
Du202	#400	50 MPa	0.02|0.01	Optical
Du148	P1000	50 MPa	1|0.1|1|0.1|1|0.1|1|0.1|0.2|2|0.2|2|0.2|2|0.2|2	Optical
Du188**	#60	100 MPa	2|0.2|2|0.2|2|0.2|0.02|0.2|2|SHS	Optical, X-section
Du178**	#220	100 MPa	2|0.2|2|0.2|2|0.2|2|0.2|2|0.2|0.02|0.2|2	Optical
Du189**	#400	100 MPa	2|0.2|2|0.2|2|0.2|0.02|0.2|2	Optical, X-section
Du206**	P1000	100 MPa	2|0.2|2|0.2|2|0.2|2|0.2|2|0.2	
Du211**	P1000	100 MPa	2|0.2|2|0.2|2|0.2|2|0.2|2|0.2	Optical
			*Stopped at 1mm displacement	**Conducted in 17-4 PH sliders

Table 5.1 Summary of experimental conditions and microstructural images presented in this thesis chapter.

All experiments show initial elastic loading characterised by a linear portion of the curves in presented data (Figure 5.4-5.7). After elastic loading, a yielding of the fault occurs as the surfaces begin to slide at a typical strength of $\mu = 0.65$-0.8, within the expected range of strengths for carbonate built rocks (Byerlee, 1978). After the attainment of steady state

strength at constant loading velocity, a series of velocity steps results in changes to strength, allowing characterisation of the rate-and-state parameters. Results are discussed first as a function of roughness and normal stress, and then brought together for comparison.

5.3.1.1 #60 data

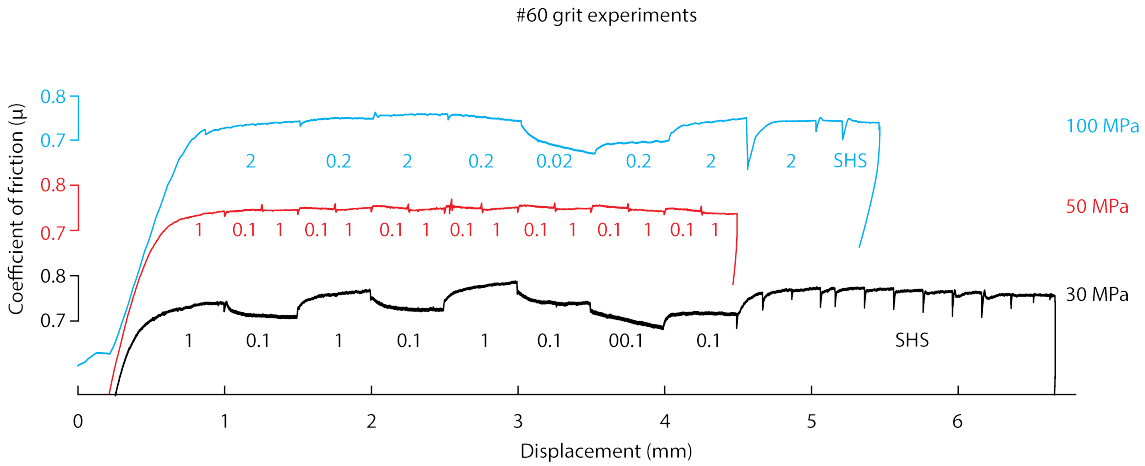

Figure 5.4 Friction plotted as a function of displacement for experiments conducted utilising #60 grit roughened limestone at a range of normal stresses indicated to the right of the curves. The sliding velocity for each step is indicated below the curves in units of μm/s, SHS = slide hold slides.

At all normal stresses the frictional strength of #60 grit surfaces shows a relatively consistent frictional strength of $\mu = 0.75$ at a velocity of 1-2 μms^{-1}, suggesting frictional strength is independent of normal stress. However, velocity dependence of friction and velocity step responses show a clear dependence on normal stress.

At 30 MPa the frictional response shows a strong dependence on sliding velocity with a-b = +0.008 to +0.029. All velocity steps result in negative b-values in the range -0.015 to -0.005 (Figure 5.9a), which always results in velocity strengthening behaviour. As a function of displacement, a-b values show a weak decrease with increasing displacement, approaching a steady state value of around +0.02 (Figure 5.4 and Figure 5.8a). Increases in normal stress to 50 MPa results in a clear transition of frictional velocity dependence to velocity neutral/weakening behaviour, accompanied by the disappearance of negative b-values, which increase to +0.005 to +0.01 (Figure 5.9a). Values of a-b range from -0.0025 to +0.0003, with values showing an initial reduction with displacement before reaching a steady state at a-$b \approx$ -0.002 (Figure 5.8a). This observation was confirmed by a repeat run at the same conditions (Du205).

Finally, when normal stress is increased to 100 MPa, velocity dependence of friction becomes velocity neutral with *a-b* values of -0.003 to +0.016 (Figure 5.4 and Figure 5.8a). Data shows an increase in *a-b* values with displacement (Figure 5.8a). Towards the end of the experiment a step down from 0.2 µm/s to 0.02 µm/s was applied and is characterised by negative *b*-value and velocity strengthening friction (Figure 5.8a and Figure 5.9a). Following this period of slow velocity (0.02 µm/s), subsequent steps up to 0.2 and 2 µm/s also give negative *b*-values (Figure 5.9a), and velocity strengthening friction (Figure 5.8a). This indicates that there is a strong memory effect in the sliding behaviour with respect to previous velocity history.

5.3.1.2 #220 data

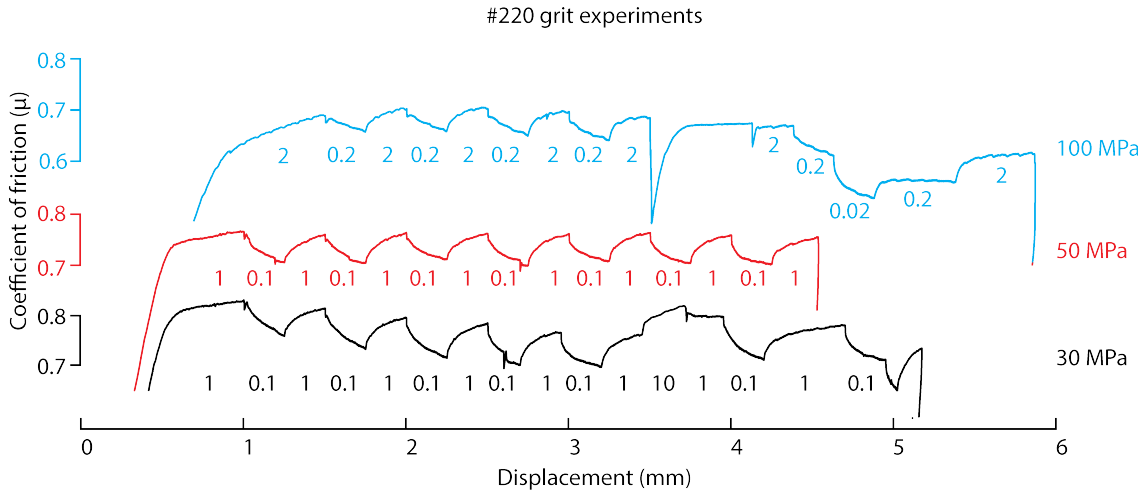

Figure 5.5 Friction plotted as a function of displacement for experiments conducted utilising #220 grit roughened limestone at a range of normal stresses. The red curve is for the experiment run at 30 MPa normal stress, green for 50 MPa and blue for 100 MPa. The velocity for each step is shown in units of µm/s.

Experiments conducted with #220 grit are shown in Figure 5.5. Frictional strength shows a decrease with increasing normal stress, with µ = 0.8 at 30 MPa, decreasing to µ = 0.7 at 100 MPa, for a velocity of 1-2 μms^{-1}. Velocity dependence of friction is less dependent on normal stress changes however.

At 30 MPa *a-b* values range between +0.01 to +0.024, and demonstrate strong velocity strengthening behaviour (Figure 5.5). Values of *a-b* remain fairly constant throughout the duration of the experiment, at around +0.024 (Figure 5.8c). Negative *b*-values are observed throughout the duration of the experiment, showing an increase from initial values of -0.035 to -0.013 to values of ≈-0.01 with increasing displacement (Figure 5.9c). Increasing the normal stress to 50 MPa results in an increase in *a-b* values, with modelled

values ranging between +0.0235 to +0.0273 (Figure 5.8c). However, with increasing displacement, *a-b* values show a continued decrease throughout the experiment from around +0.027 to +0.024, consistent with final values obtained at 30 MPa (Figure 5.8c). All *b*-values are negative, but once again show a trend of increasing as a function of displacement, from -0.022 to -0.017 (Figure 5.9c). Sliding at the highest normal stress (100 MPa), results in a reduction of *a-b* values, which range between +0.012 to +0.02 (Figure 5.8c). These *a-b* values remain fairly constant throughout the duration of the slip at around +0.018. Once again negative *b* values are observed throughout the duration of experiment (Figure 5.9c), with values remaining fairly constant with increasing displacement.

5.3.1.3 #400 data

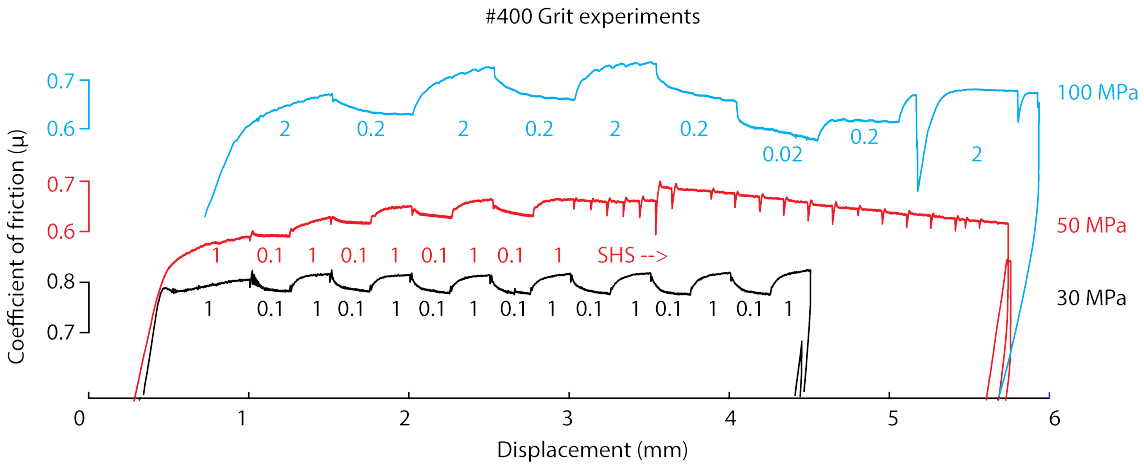

Figure 5.6 Friction plotted as a function of displacement for experiments conducted utilising #400 grit roughened limestone at a range of normal stresses indicated to the right of the curves. The velocity for each step is shown below each curve in units of μm/s.

For smoother faults of a #400 grit preparation, strength is fairly constant across the range of normal stresses with strength between μ = 0.65-0.72, at a sliding velocity of 1-2 μms^{-1} (Figure 5.6). At the same time, absolute strength is strongly dependant on sliding velocity, and shows some changes with increasing normal stress at low sliding velocities. At 30 MPa, velocity stepping results in *a-b* values that range between +0.016 to +0.023 (Figure 5.8e). These values of *a-b* are observed to show a slight increase throughout the experiment duration to a value around +0.02, indicating velocity strengthening behaviour. Negative *b*-values are also observed at the end of the experiment, with modelled values reducing from +0.005 to -0.01 (Figure 5.9e). At 50 MPa normal stress there is a reduction in *a-b* values (Figure 5.6), with modelled values between +0.06- +0.012, with little change as a function of displacement (Figure 5.8e). Initial b-values are positive (b = 0 to

+0.005) but reduce to negative values with increasing displacement (b = -0.01 to 0) (Figure 5.9e). At 100 MPa the value of *a-b* shows a marginal increase to values between +0.01 to +0.02, with a slight increase as a function of displacement (Figure 5.8e). All modelled *b*-values are negative, and remain relatively constant as a function of displacement, ranging between -0.014 to -0.007 (Figure 5.9e).

5.3.1.4 P1000 data

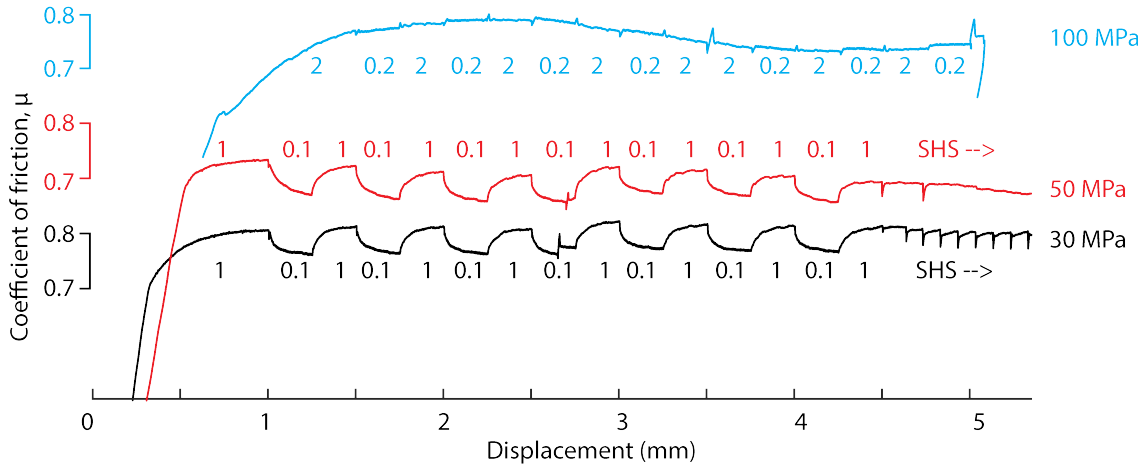

Figure 5.7 Friction plotted as a function of displacement for experiments conducted utilising P1000 roughened limestone at a range of normal stresses indicated to the right of the curves. The velocity for each step is shown below each curve in units of μm/s, SHS = slide hold slides.

For the smoothest faults prepared with p1000 grit paper, frictional strength is observed to show a marginal decrease with normal stress increase, with μ = 0.8 at 30 MPa, to μ = 0.74 at 50 MPa (Figure 5.7). At 30 MPa *a-b* values are velocity strengthening and are observed to increase as a function of increasing displacement from ~+0.015 to +0.018 (Figure 5.8g). All modelled *b* values are negative and show a decreasing trend with increasing displacement, from initial values around -0.011 decreasing to -0.013 at 4.5 mm displacement (Figure 5.9g). Increases in normal stress to 50 MPa results in a slight increase of *a-b* values, which range between +0.015 to +0.0225 (Figure 5.8g). Values of *a-b* are also observed to decrease from +0.0225 to +0.015 with increasing displacement (Figure 5.8g), in contrast to the lower normal stress experiment. Throughout the experiment *b* values are negative and show an increase from -0.014 to -0.007 with increasing displacement (Figure 5.9g). Increasing the normal stress to 100 MPa results in an abrupt change in the frictional rate dependence (Figure 5.7), which becomes velocity neutral with *a-b* between -0.0034 to +0.0004 (Figure 5.8g). This shows a slight decrease at the start of the experiment before reaching a steady value of around -0.002. Associated

b-values are positive with modelled values between +0.005-+0.01 (Figure 5.9g). The overall strength also shows a period of slip weakening from 2-3.5 mm displacement, possibly indicative of a microstructural evolution of the sample surface (Figure 5.7). Repeats of this test confirmed this change in behaviour (Du211), suggesting that it is a real effect.

5.3.2 Evolution of *a-b* and *b*-values with frictional work

In order to investigate trends across the range of normal stresses and displacements, modelled friction parameters are plotted as a function of frictional work (Jm^{-2}) (Figure 5.8 b, d, f and h, and Figure 5.9b, d, f and h). In general, the behaviour and trends in data are somewhat variable, and show a complicated pattern. However, there are indications in the data that a steady state in *a-b* and *b*-values is attained towards the end of experiments for both of the intermediate roughness faults (#220 & #400 grit), resulting in *a-b* values close to +0.019 and $b \approx -0.01$.

For the roughest initial surface preparation (#60 grit) *a-b* values are positive (= 0- +0.03), and b-values are negative (≈-0.015 to -0.005) at low levels of mechanical work ($\omega < 50$ kJ/m^2). However, with increasing mechanical work (+normal stress) *a-b* values show a reduction to velocity neutral behaviour (a-b = -0.003- + 0.01) accompanied by an abrupt transition to positive *b*-values (≈ +0.01).

For the intermediate rough surface preparation (#220 grit) at low levels of mechanical work ($\omega < 100$ kJ/m^2) *a-b* values are large (*a-b* = +0.02-+0.04) and are accompanied by negative b-values (≈-0.025 to –0.015). However, with increasing levels of mechanical work above 100 kJ/m^2, values of *a-b* reduce with increasing work reaching a fairly steady value around +0.017-+0.02. Reducing a-b values are accompanied by *b*-values which show a gradual increase to a final value of around $b \approx -0.01$.

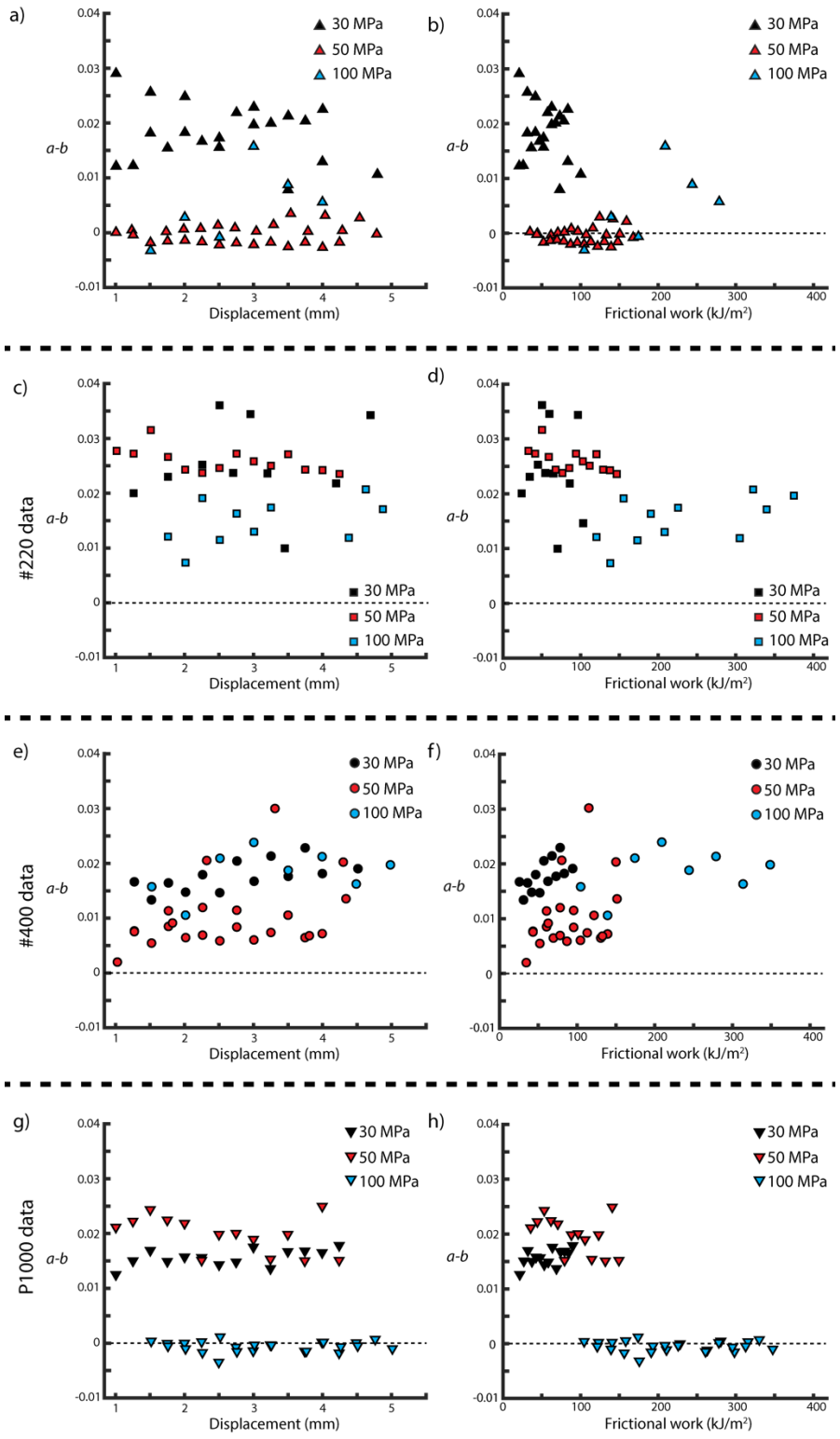

Figure 5.8 Frictional rate dependence plotted as a function of displacement on the left-hand side, and frictional work on the right-hand side. All points are coloured according to the normal stress.

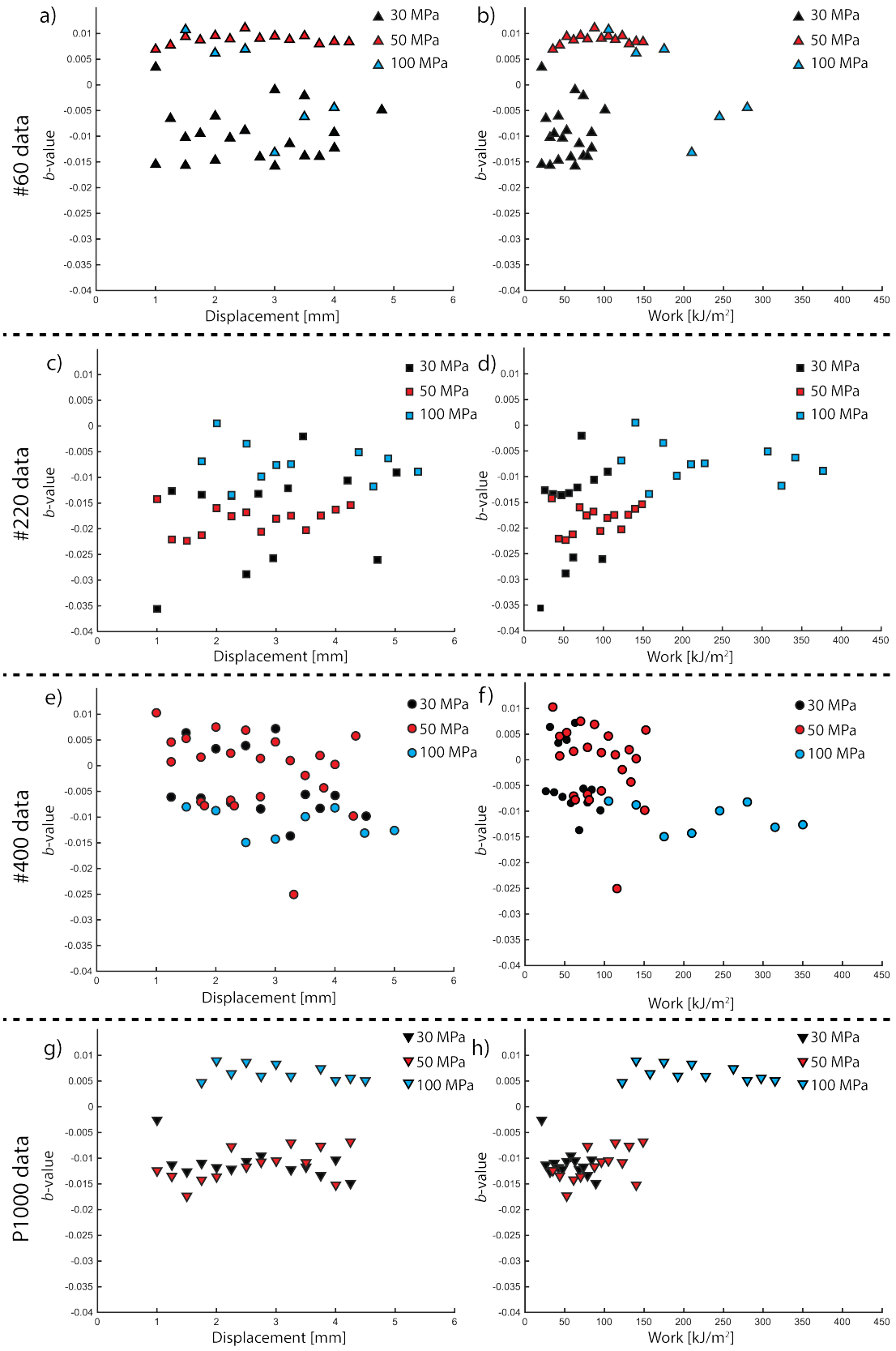

Figure 5.9 Plots of b-value for differing roughness as a function of displacement and frictional work. See text for details.

Intermediate smooth samples (#400 grit) are characterised by relatively small but positive values of *a-b* (+0.005-+0.015) at low values of mechanical work (ω < 50 kJ/m^2). These

are accompanied by a range of b-values between -0.005 to +0.005. However, with increasing values of work ($50 < \omega < 100$ kJ/m^2) the range of *a-b* values is observed to increase towards a value of +0.018-+0.022. This increase in a-b values is accompanied by a decrease in b-values towards values of $b \approx -0.01$, indicating that #220 and #400 faults show very similar behaviour at high levels of frictional work.

Finally, for the smoothest samples tested (P1000) values of *a-b* are quite large and velocity strengthening (*a-b* = +0.015- +0.024) at low values of mechanical work ($\omega <$ 100 kJ/m^2). These values show little change with increasing work in this range and are also notably similar to a-b values obtained for the intermediate roughness samples (#220 and #400 grit preparation). Modelled *b*-values also show little trend at low work, with values clustering around $b \approx -0.012$. However, above a work of $\omega > 100$ kJ/m^2, *a-b* values abruptly switch to velocity neutral to weakening behaviour (*a-b* = -0.004-0). This switch in *a-b* is accompanied by a switch to positive *b*-values of value around +0.007.

5.3.3 Evolution of the critical slip distance

Plotting the critical slip distance D_c, as a function of displacement reveals that data is fairly scattered (Figure 5.10a). Some data shows evidence of decreasing D_c with slip, whilst other data shows an increasing trend with slip. In general, there is no particular trend to remark on. However, when plotted as a function of frictional work, D_c shows a decrease with increasing work (Figure 5.10b). A lower bound is observed on the length scale of ≈5 µm at all levels of frictional work, however the upper limit to D_c is observed to decrease with increasing work. At $\omega < 50$ kJ/m^2 the upper bound is roughly on the order of 120 µm, decreasing to ≈100 µm at $\omega = 100$ kJ/m^2 and reducing to a value of ≈40 µm at the highest levels of frictional work ($\omega > 250$ kJ/m^2).

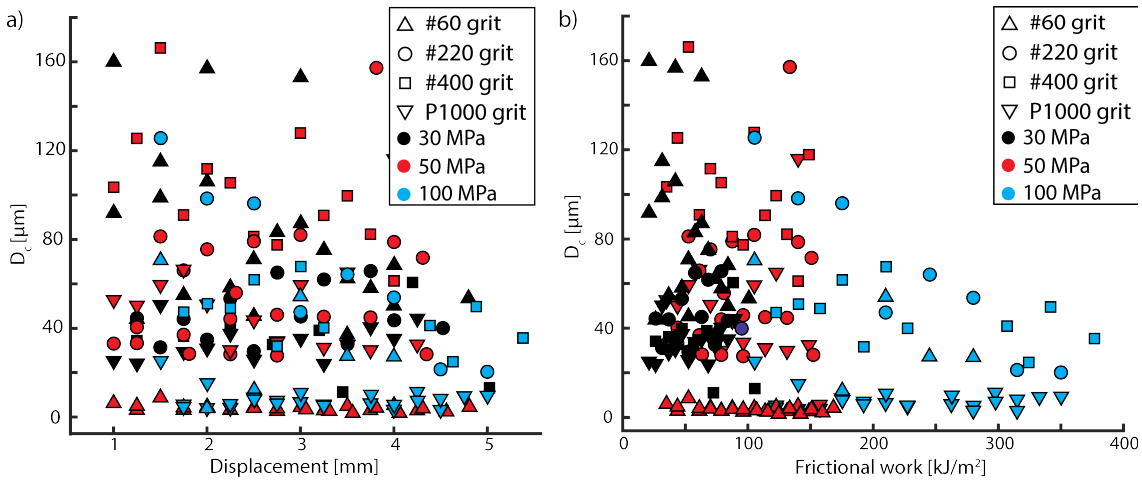

Figure 5.10 Evolution of the critical slip distance with a) displacement and b) frictional work.

5.3.4 Microstructures

In order to gain an insight into the deformation mechanisms and microstructural evolution controlling the evolution of frictional parameters SEM imaging of both sample surfaces and cross-sections were prepared. The aim was to compare the influence of initial roughness on microstructural development, in addition to the effects of displacement which was constrained by stopping experiments Du130 (#400 at 30 MPa) & Du131 (#60 at 30 MPa) at 1 mm displacement. Throughout this section reference will be made to shear orientations, such as R-, P-, Y- and B-shears, therefore to guide the reader shear orientations are illustrated in Figure 5.11.

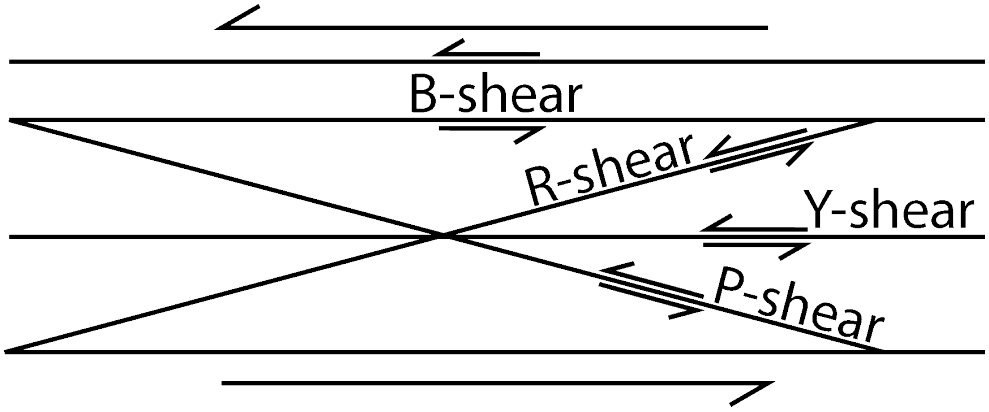

Figure 5.11 Common orientations of shear microstructures developed in the images presented in this chapter, modified after Logan et al. (1992).

5.3.4.1 Surface microstructures

The results of surface investigations are now reported in the following section as a function of each roughness which has undergone detailed study. Due to the relative similarities of #220 surfaces with #400 surfaces, imaging results from #220 surfaces are omitted to the appendix of this chapter.

5.3.4.1.1 Samples initially roughened with #60 grit

In Figure 5.12 and in Figure 5.17a and c, example images of surface microstructures developed at 30 MPa are shown. Figure 5.17a and Figure 5.12 a-d shows representative microstructures of the features developed during the initial deformation, with samples retrieved after 1 mm of total slip. Optical reflecting microscopy in PPL reveals surfaces

that are decorated with a mixture of loose high porosity gouge material which are identified as white patches (Figure 5.17a and Figure 5.12a), and indurated gouge, which appears as transparent patches. In a places the indurated gouge shows rare reflective streaks, identified in XPL, which are interpreted to represent fault mirror surfaces (Figure 5.17c). In between the gouge patches the bare wall rock is still visible, as is highlighted in Figure 5.12a.

In SEM images, gouge patches are easily identifiable by their striations which form parallel to slip (Figure 5.12b). Gouge patches typically form on a length scale of 200-500 μm, and are clearly separated by bare wall rock, which is uncoated by gouge material (Figure 5.12b). Smaller scale observations show that the centre of gouge patches are comprised of nanometric particles of 100-200 nm diameter (Figure 5.12d). The rims of gouge patches are comprised of relatively larger angular particles of 1-3 μm grain size, which loosely fill the gaps between the striated patches (Figure 5.12c). All striated surfaces are observed to intersect scallop shaped fractures which appear to dip antithetically to slip (Figure 5.12d), possibly suggesting that they may be R shears.

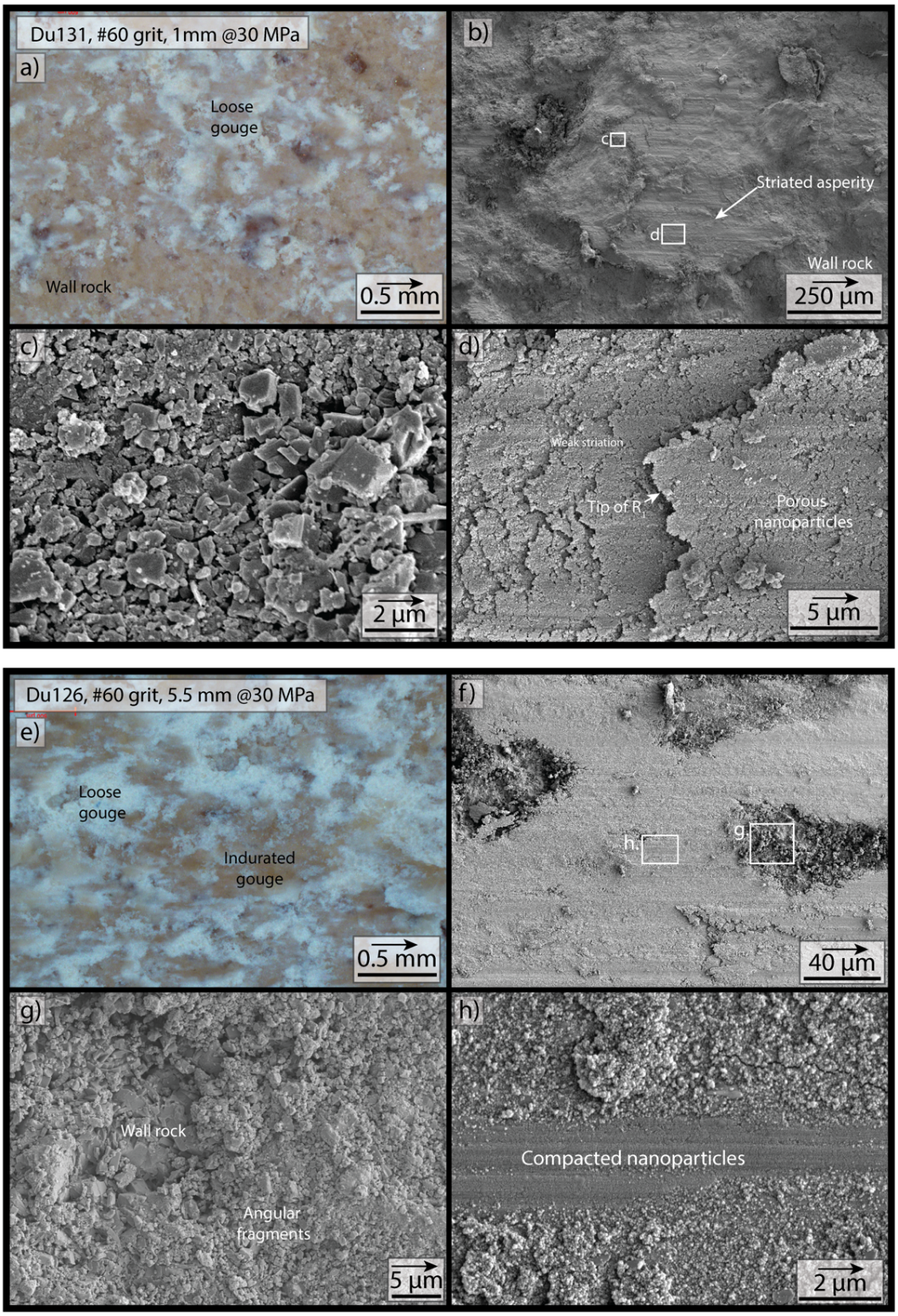

Figure 5.12 Evolution of surface microstructure with displacement for initially rough surfaces prepared with #60 grit. Arrows denote sliding direction of overlying block. a) and e) are reflected light images, and b)-d) and g)-h) are taken in secondary electron mode. In a) and e) white patches are formed by high porosity unconsolidated gouge comprised of angular particles as is shown in c) and g). Darker translucent patches are formed by nanometric grains as is shown in d) and h), in places the nanoparticles are compacted and form streaky mirrors as in h).

In Figure 5.12e-h typical surface microstructures from #60 samples sheared to 5.5 mm displacement at 30 MPa are shown. Surfaces show a significant microstructural evolution in comparison to the initial surface microstructures presented in Figure 5.12a-d. In reflected light microscopy (Figure 5.12e) samples are comprised of a mixture of loose gouge (light colour), and more indurated material which shows the development of streaky mirrors in XPL (Figure 5.17c). On a smaller scale, surfaces show a near total filling of the volume between striated patches (Figure 5.12 e-f), being largely covered in weakly striated particle sheets (Figure 5.12f) of nanometric dimension (d ≈100-200 nm, Figure 5.12h). In places the wall rock is still visible through gaps in the nanoparticle sheets, which are largely filled with angular material of 1-4 μm grain size (Figure 5.12g). In many locations within the nanogouge, 2-4 μm wide streaks of relative porosity reduction are observed, which are interpreted to represent fault mirrors (Figure 5.12h). This is also identified by shiny streaks in optical reflected microscopy as is shown in Figure 5.17c, XPL.

Figure 5.17f shows typical surface microstructures observed on #60 faults at 50 MPa after 5 mm displacement. The PPL image shows that surfaces are predominately made up of white gouge material, with a reduction in indurated gouge patches relative to 30 MPa surfaces. In XPL images fault mirrors are rare (Figure 5.17f), and form very narrow streaks, but are nowhere near as pervasive as those formed at 30 MPa on #60 faults (Figure 5.17c). At 100 MPa the #60 fault surface microstructures (Figure 5.17i) are visually similar in PPL to those observed at 50 MPa (Figure 5.17f), with a dominance of loose white gouge material relative to indurated gouge patches. In XPL, fault mirrors formed at 100 MPa (Figure 5.17i), show more widespread development than at 50 MPa (Figure 5.17f), however they are not as well-developed than those formed at 30 MPa (Figure 5.17c), suggesting that normal stress inhibits their formation.

5.3.4.1.2 Samples initially roughened with #400 grit

In Figure 5.17 b, d, g and j, and in Figure 5.13 images from post experimental samples initially roughened with #400 grit are presented. Figure 5.17b and Figure 5.13a show reflected light images taken from #400 grit samples deformed at 30 MPa, and deformed to a displacement of 1 mm. The PPL reflected light images of these surfaces (Figure 5.13a and Figure 5.17b), reveal that the size of loose gouge material (white patches) are smaller and less abundant than those formed on #60 samples deformed at the same conditions

(Figure 5.17a). In the XPL image (Figure 5.17b), small patchy fault mirrors are observed, which are not clearly observed on #60 faults at the same conditions (Figure 5.17a).

In the SEM (Figure 5.13b), sample surfaces are decorated with 50-200 μm long striated gouge patches, that are separated by patches of angular fragments (Figure 5.13b). Higher magnification images reveal that striated patches are comprised of sub-micron grains (d ≈ 100-200 nm), of a fairly uniform size (Figure 5.13c). These patches show bands of well packed grains, interspersed with bands of more poorly packed grains, that are intersected by poorly formed scallop shaped cracks (Figure 5.13c). Angular fragments found around striated patches have a larger grain size of 1-4 μm, similar to that of the protolith (Figure 5.13d). Angular fragments are often coated or dispersed with minor volumes of finer sub-micron size particles that comprise the striated patches. In general, the gouge patches developing on #400 surfaces at these conditions (30 MPa and 1 mm displacement), show comparatively lower porosity than #60 surfaces at the same conditions (Figure 5.12c and d).

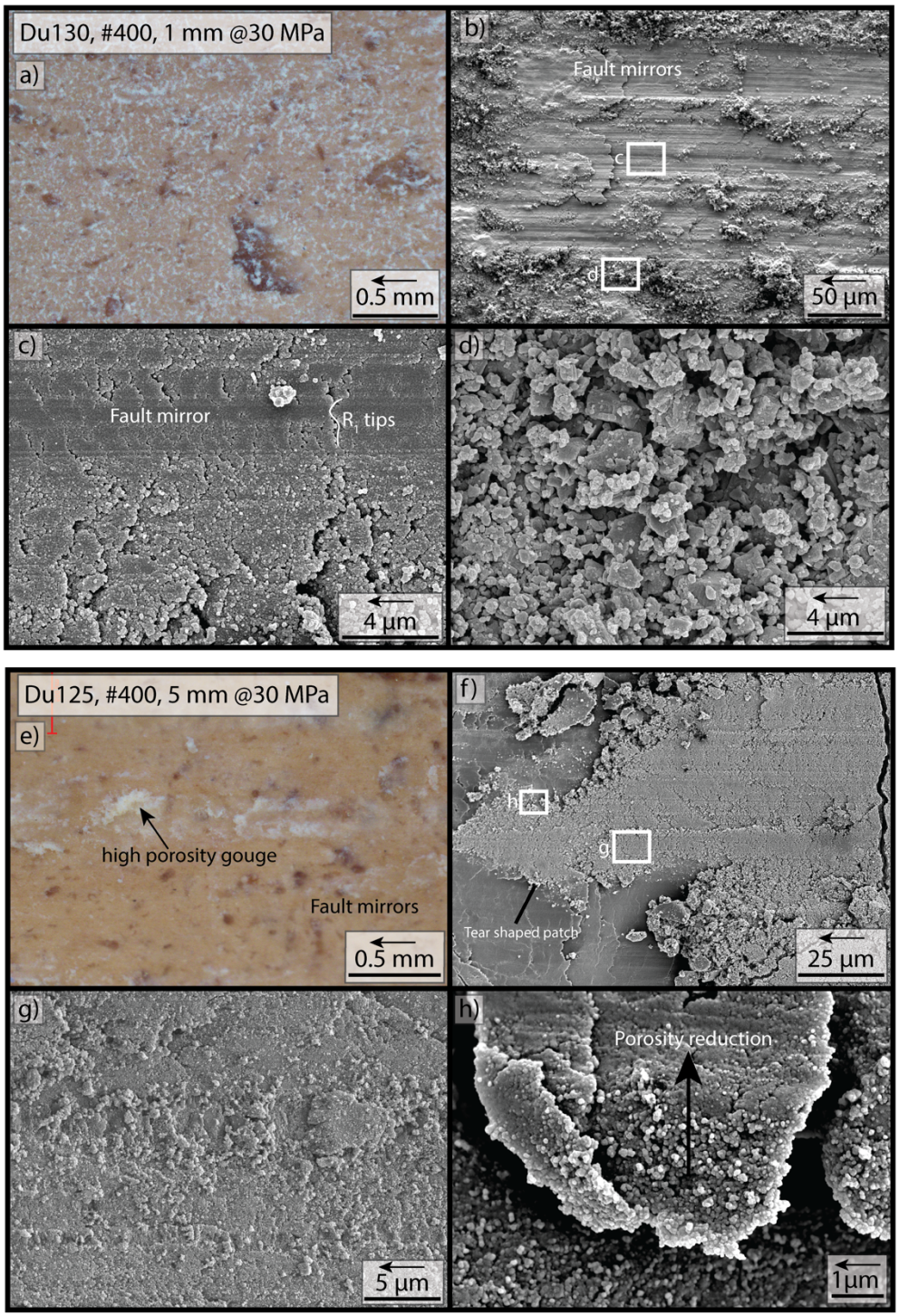

Figure 5.13 Evolution of surface microstructure with increasing displacement for initially smooth samples roughened with #400 grit. Arrow denotes sliding direction of overlying block. A) and e) are reflected light images, and b)-d) and g)-h) are taken in secondary electron mode. All images taken from a sinistral shear sense (i.e. overlying block to the left). In a) and e) reflected light pictures reveal a low proportion of loose gouge material relative to #60 surfaces, and surfaces are largely dominated by mirror surfaces e.g. b), c) and f). Mirrors are an early microstructural development in these samples, b) and c) show they are extensively developed after 1 mm displacement. High porosity gouges in g) form 'tear' shaped patches at 5 mm displacement as is shown in f).

For #400 faults, deformed to 5 mm displacement, reflected light images (Figure 5.17d and Figure 5.13e) show that surfaces are largely comprised of transparent gouge material, with only a minor proportion of loose white gouge material. XPL images (Figure 5.17d) reveal that surfaces an abundance of streaky mirrors, that are aligned parallel to slip. These mirrors are longer and narrower, in comparison to those found on #60 faults at the same experimental conditions. In SEM images (Figure 5.13f-h), fault surfaces are almost entirely comprised of nanometric particles, with a typical grain size of 120-170 nm. Within the surface gouge layer, relatively low porosity mirrors of striated nanoparticles are interrupted by relatively higher porosity regions (Figure 5.13f). These higher porosity patches are comprised of weakly striated nanoparticles of similar grain size to low porosity regions (Figure 5.13g), and they show a gradational loss of porosity into the surrounding low porosity material (Figure 5.13h). The patch of higher porosity material intersects scallop shaped fractures (Figure 5.13g), likely representing the tops of R shears.

Reflected light images from 50 MPa experiments (Figure 5.17g), show that in PPL fault surfaces are very similar to those formed at 30 MPa (Figure 5.17d and Figure 5.13e), being comprised of transparent gouge patches interrupted by minor loose gouge patches. In XPL (Figure 5.17g), however, reflected light images reveal that fault mirrors are pervasively developed, and cover a higher proportion of the fault surfaces than at 30 MPa (Figure 5.17d, XPL). Reflected light images of the surface formed at 100 MPa (Figure 5.17j), shows a similar microstructure to those observed at lower normal stress conditions (Figure 5.17d and g). In XPL images (Figure 5.17j), surfaces are almost entirely comprised of fault mirrors, with a few unreflective patches corresponding to lose gouge material. These observations suggest, that in the case of #400 faults, normal stress increases promote mirror formation.

5.3.4.1.3 Samples initially roughened with P1000 grit paper

No systematic investigation of P1000 surface microstructures has been conducted using the SEM, however reflected light images have been taken and are now discussed. In Figure 5.17e, h and k, reflected light images of surface initially roughened with P1000 grit paper are presented. Low normal stress samples (30 MPa, Figure 5.17e), shows that in PPL surfaces appear to bare, but are in actual fact coated by a transparent gouge layer. On these surfaces there appears to be no loose white gouge material, which is observed on other faults deformed to the same normal stress and displacement conditions (30 MPa, 5 mm displacement). However, in XPL (Figure 5.17e), nearly all of the surface is

reflective, indicating that mirrors dominate the fault surface. At 50 MPa (Figure 5.17h), surface microstructures are virtually indistinguishable from surfaces formed at 30 MPa normal stress, with pervasively developed mirror surfaces. However, at 100 MPa a dramatic transition in surface microstructure is observed in Figure 5.17h. Surfaces show the development of long (3-5mm), 0.5-1 mm wide grooves of loose white gouge, sharing some similarities to #60 faults at comparable conditions (Figure 5.17i). In XPL (Figure 5.17k) the grooves show no reflectivity, but they are surrounded by reflective fault mirrors, which appear to be cross cut by the grooves. These observations therefore suggest that on P1000 faults, mirror formation is suppressed by normal stress increases.

5.3.4.2 Cross sectional images

5.3.4.2.1 Samples initially roughened with #60 grit

In cross sections through #60 samples deformed at 30 MPa to 5 mm displacement, samples show an infilling of topography by material comprised of angular fragments (Figure 5.14a). Large angular particles (d ≈10-20 μm) are supported by a finer grained matrix, with grains ranging from 1-2 μm particles down to grains of unresolvable size that are most probably nanoparticles identified in SE imaging of surfaces (Figure 5.12g). The total recovered thickness is on the order of 20-30 μm, and samples show little internal structure suggestive of a chaotic cataclastic flow of material. The sharp flat termination of the top surface is probably representative of the striated patches observed in surface images (e.g. Figure 5.12f).

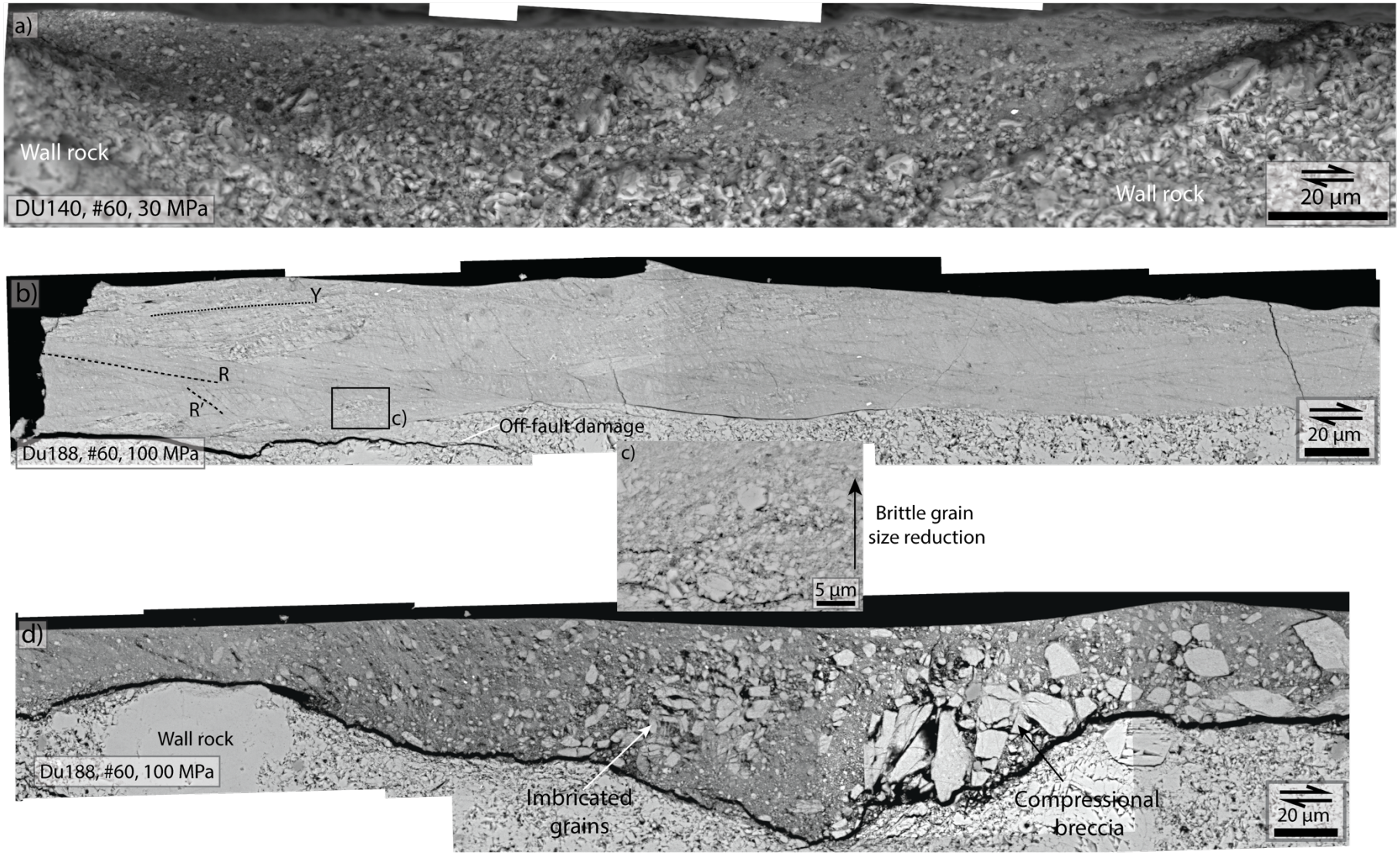
a)
Wall rock
DU140, #60, 30 MPa
Wall rock
20 µm
b)
Y
R
R'
c)
Off-fault damage
Du188, #60, 100 MPa
20 µm
c)
Brittle grain
size reduction
5 µm
d)
Wall rock
Du188, #60, 100 MPa
Imbricated
grains
Compressional
breccia
20 µm

Figure 5.14 (Previous page) BSE cross sectional images through gouge layers developed on faults initially roughened with #60 grit and deformed at 30 MPa (a) and 100 MPa normal stress (b, c and d). At low normal stress (30 MPa, a), large angular grains are observed to mix with finer gouges which range from micro- to nano-metric sizes. The abundance of randomly orientated angular grains is indicative of cataclastic flow. Inset b) shows the Internal microstructure of the PSZ for sample Du188 deformed at 100 MPa showing internal mixing of the gouge layers and incipient R shears interlinking with Y-shears at the left-hand margin of the image. C) shows a zoom of the gouge layer close to the wall rock boundary and shows angular grains with fine into the PSZ zone. d) Image of a compressional jog in sample Du188 with brecciated fragments imbricating within a finer matrix of gouge particles.

In Figure 5.14 b) and c) example cross sections through #60 faults deformed at 100 MPa are shown. Cross sections through these samples show an internal ordering of the microstructure (Figure 5.14b), with complex networks of P and R shears. Off fault damage is abundant, with evidence of carving out of the wall rock, and Riedel shears that extend out from the slip zone into the wall rock (Figure 5.14b). At a smaller scale the gouge layer shows a brittle grain size reduction, with angular fragments that fine into the slip zone (Figure 5.14c). In many other regions wall rock topography infilled by immature cataclasites (Figure 5.14d), which show an abundance of large angular fragments of large grain size (10-20 μm) supported by a fine matrix of small angular clasts (1-4 μm) and ultrafine particles of unresolvable size that probably represent nanoparticles. In Figure 5.14d the large grains are imbricated in a compressional jog, with grains showing clear mode I fracture, indicative of brittle comminution. The total recovered thickness of the slip zone is on the order of 50-100 μm.

5.3.4.2.2 Samples initially roughened with #400 grit

A representative cross section taken through sample Du125 (30 MPa) is shown in Figure 5.15a. The sections show an internally ordered asymmetric fault microstructure, with development of R- and a B-shears, which are interlinked. The B-shear is comprised of very low porosity nanometric scale material, and has wavy boundaries, indicating that the R- and B-shears were likely active at the same time. Many of the R_1 shears cross the entire width of the gouge layer, suggesting that stress transmission is still occurring across the width of the fault (Figure 5.15a). Close inspection of the gouge layer shows a fining of material from the wall rock towards the low porosity band of nanoparticles (Figure 5.15a).

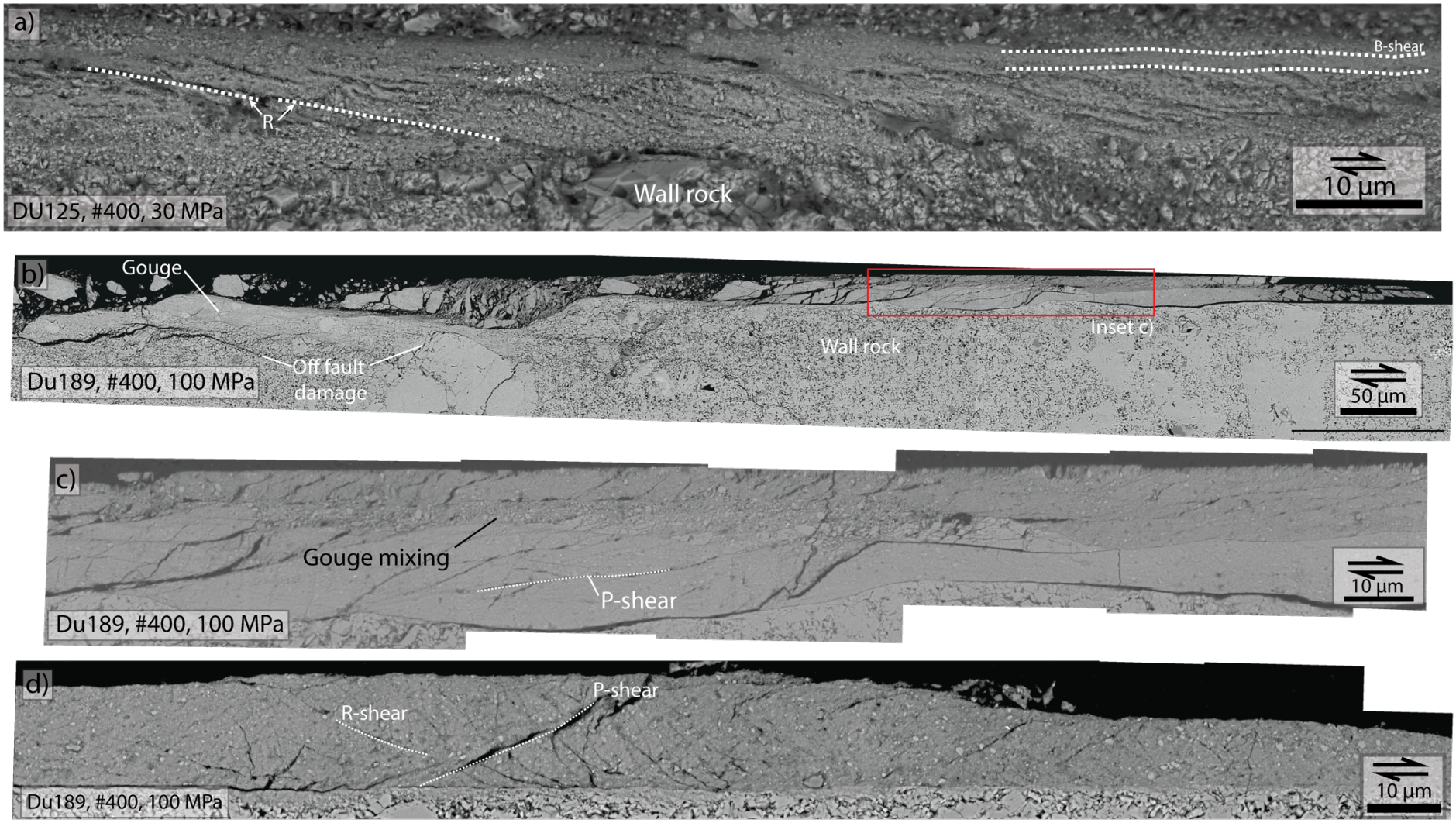
a)
B-shear
R1
Wall rock
10 µm
DU125, #400, 30 MPa
b)
Gouge
Inset c)
Wall rock
Off fault damage
Du189, #400, 100 MPa
50 µm
c)
Gouge mixing
P-shear
10 µm
Du189, #400, 100 MPa
d)
P-shear
R-shear
10 µm
Du189, #400, 100 MPa

Figure 5.15 (Previous page) Representative cross sections through samples initially roughened with #400 grit and deformed at 30 MPa (a) and 100 MPa (b-d) to a displacement of 5 mm. A full thickness cross section through sample Du125 at 30 MPa is shown in a. The gouge layer shows asymmetry with a band of low porosity material comprised of nanoparticles forming in a B-shear with associated R shears which traverse the full PSZ thickness. In b) a large area BSE image of microstructures developing at 100 MPa is shown. In places gouge is adhered to the wall rock, showing the propagation of R_1 fractures from the gouge layer into the wall rock and compression of gouge in jogs. Inset c) zoomed BSE image showing evidence of gouge mixing and abundant p-shears that form in response to the local wall rock topography. d) BSE image of the PSZ for experiment Du189 (#400 grit), showing some internal microstructure consisting of P- and R_1 shears forming along slip at an incidence of 45°. The bounding Y-shear is interpreted to represent a mirror surface.

Cross sections taken through a sample initially roughened with #400 grit deformed at 100 MPa also shows development of an internal structure within the slip zone (Figure 5.15b-d). On a large scale the wall-rock gouge boundary has a stepped geometry (Figure 5.15b), with gouge pockets forming in regions of low topography or dilation jogs. At a smaller scale (Figure 5.15c), within compressional jogs, P-shears are observed which result from interactions of the gouge layer with the topography. Some of the P-shears are intersected by bands of relatively higher porosity material sandwiched between low porosity regions in an orientation parallel to the slip zone boundaries (Figure 5.15a and b). In inset Figure 5.15c these bands of material are observed to thin and grade out along the slip direction, either seemingly assimilating or grading into low porosity regions.

In Figure 5.15c) and d), the boundary between the gouge layer and the wall rock is sharp, being characterised by a transition from intact wall rock to a well packed layer of ultrafine grain size (<0.5 μm, not resolvable), with some larger fragments (1-2 μm) (Figure 5.15c and d). These fragments may be relics representative of the early stages of deformation, similar to the grains shown in Figure 5.13 d). Internally there is an abundance of conjugate shear band pairs which form at ≈30-45° to the imposed slip direction, and at 90-120° to each other (Figure 5.15d). In general, the recovered thickness of deformed material for the #400 sample is on the order of 10-20 μm (Figure 5.15a-c), which is relatively thinner than that of #60 sample cross sections in Figure 5.14.

5.3.4.2.3 Samples initially roughened with P1000 grit paper

Example cross sections through P1000 faults deformed at 30 MPa are presented in Figure 5.16. Samples show an infilling of wall rock topography by gouge, which is comprised largely of sub-micron grains, and is truncated by a sharp flat surface. In Figure 5.16a, wall rock topography is infilled by differing generations of gouges which are bounded by discrete surfaces that separate individual gouge volumes. Each individual volume thins along slip and forms a total width of 5-10 μm, suggestive of a progressive infilling and smearing with slip. In other areas compacted nanogouge (d <1 μm) is found stacked against a topographic high (Figure 5.16b), which is cracked underneath. The crack beneath the grain suggests that the grain is being plucked from the wall rock, and will become part of the gouge layer, acting as an effective asperity. Along slip of the grain, an abundance of angular gouge of grain size 1-2 μm is observed, which is relatively less compacted than the nanogouge (Figure 5.16b). This may indicate a region of relative tension in comparison to the gouge up slip of the grain.

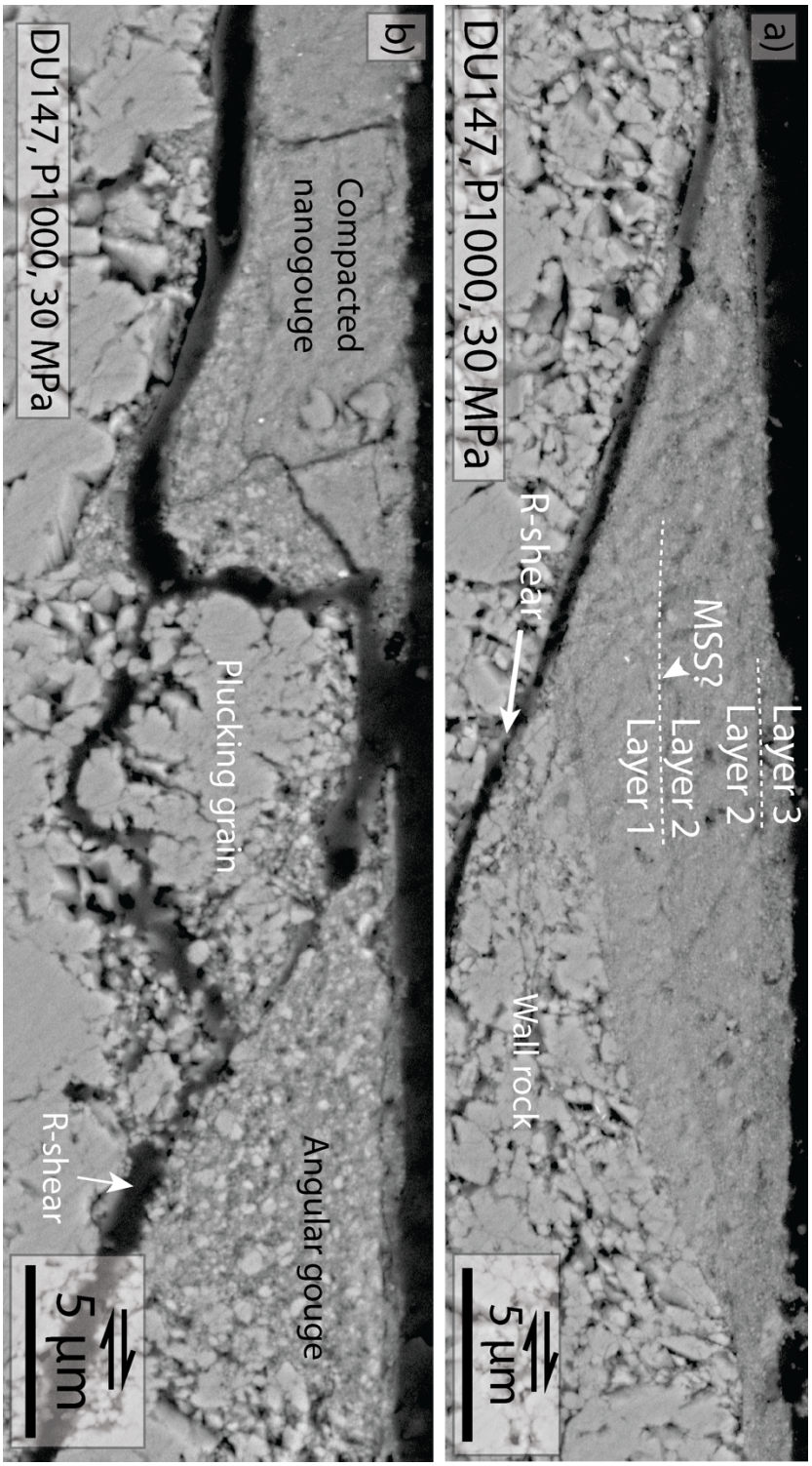

Figure 5.16 Cross sections taken through samples initially roughened with P1000 grit. In a) a R-shear extending out of the PSZ in which discrete gouge layering is observed, infilling layers are separated by sharp boundaries, possible indicative of gouge smearing through progressive slip accumulation. B) piling of low porosity fine grained material up slip of a grain which is being plucked from the wall rock, with a region of angular gouge preserved along slip.

5.3.4.3 Summary and comparison of microstructures

In summary, a wide range of microstructures are observed, with many faults exhibiting evidence of cataclastic features and frictional wear. In Figure 5.17 a compilation of reflected light images of surface microstructures is presented. Each image corresponds to the normal stress conditions and displacement conditions on the left of the matrix, and initial roughness conditions across the top axes. PPL and XPL images are also presented to highlight the relative abundance of loose gouge material (white patches) and the abundance of fault mirrors (reflective in XPL). Examining these images together allows the definition of faults which fall under regime I, dominated by fault mirrors; or regime II, dominated by loose gouge material. For #60 faults, the experiment at 30 MPa shows a significant build-up of white gouge material, but in XPL it is clear that mirrors have extensively developed (Figure 5.17c), and therefore the fault is categorised as regime I. However, faults at higher normal stress (50 MPa and 100 MPa), show poor development of fault mirrors and may be categorised as being gouge dominated (regime II). Images of #220 faults in the appendix (Figure 5.25) all show well developed mirrors and a lack of loose surface gouge, categorising them as regime I.

In Figure 5.17, all #400 faults are dominated by fault mirrors across the range of normal stress conditions (Figure 5.17b, d, g and j), categorising them as regime I. Finally, for P1000 faults, both the 30 and 50 MPa experiments are dominated by mirrors (Figure 5.17e and h), and therefore fall under regime I. The appearance of white gouge grooves at 100 MPa however categorises this fault as regime II.

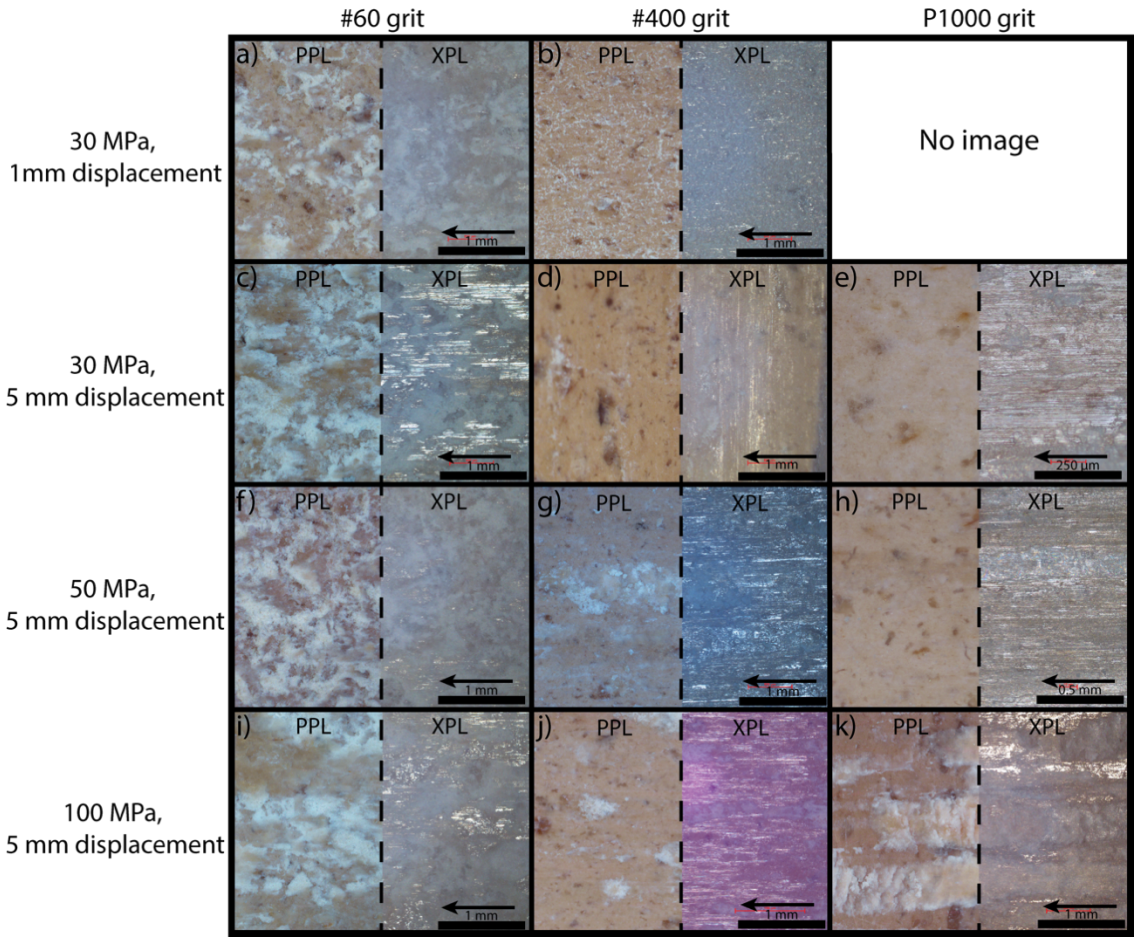

Figure 5.17 Compilation of reflected light images of post experimental fault surfaces taken from faults at roughness and normal stress conditions indicated to the top and left of the grid respectively. Arrows above scale bars denote the shear sense of the overlying block. PPL = plain polarised light and XPL = cross polarised light. For #60 faults (a, c, f and i) a reduction of mirror prevalence is generally observed with increasing normal stress, as highlighted by XPL images. Relative to indurated material (semi-transparent), more loose gouge (white material) is observed at higher normal stresses. For #400 faults (b, d, g and j), the development of fault mirrors correlates well with increases in normal stress, with proportionally more observed at higher normal stress. Also notable is the increased prevalence of fault mirrors, and lack of loose gouge material developing on #400 surfaces in comparison to #60 faults at comparable conditions. For P1000 surfaces (e, h and k), at low normal stress conditions (e and h) faults are almost entirely comprised of fault mirrors, with almost no loose gouge material observed. However, surface microstructures at 100 MPa are markedly different (k), with clear development of wear tracks filled with loose gouge, which are surrounded by mirrors of lower topography.

5.4 Discussion

5.4.1 Deformation regimes

In the microstructural data it was possible to define two microstructural regimes based on surface observations, regime I, characterised by fault mirror formation, and regime II,

characterised by loose gouge development. In order to test links between the microstructural state of experimental faults and the mechanical data, mechanical and microstructural characteristics of each regime will now be considered.

5.4.1.1 Deformation in regime I

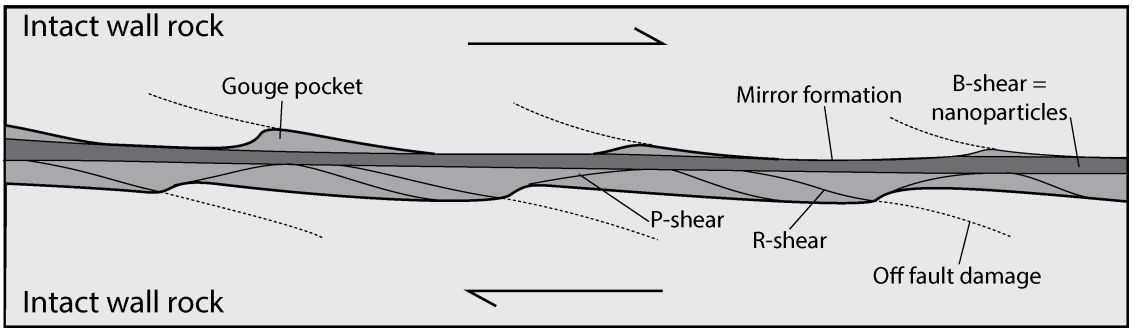

Figure 5.18 Schematic illustration of fault microstructure formed during regime I sliding. The grayscale of the gouge layer indicates the relative porosity of layers, with darker having lower porosity. Mirrors form at the boundary between the wall-rock and the bounding Y-shear, and possibly on the lower contact with the gouge layer below. It is anticipated that the B-shear, which is comprised of low porosity nanoparticles, deforms as a volume in similarity to Pozzi et al. (2018), as suggested by the cross section in Figure 5.15a. R-shears extend out of the slip zone resulting in off-fault damage.

The rate dependence of all faults that are identified as being dominated by mirrors (regime I), have been compiled and plotted as a function of displacement (Figure 5.19a) and frictional work (Figure 5.19b). Mirror dominated faults are characterised by strong velocity strengthening, with *a-b* converging to values of +0.02 with increasing frictional work (Figure 5.19b). This trend is also observed in *b*-values, with values of *b* converging to -0.01 with frictional work (Figure 5.19f). The critical slip distance, D_c, is also large, but shows a significant reduction with increasing frictional work for regime I faults (from ≈ 120 to 40 μm, Figure 5.19d). In previous work negative *b* values have been associated to a semi-brittle flow (Shimamoto, 1986), and have been observed in calcite gouge at similar deformation conditions to those in this chapter (Carpenter et al., 2016; Verberne, Spiers, et al., 2013).

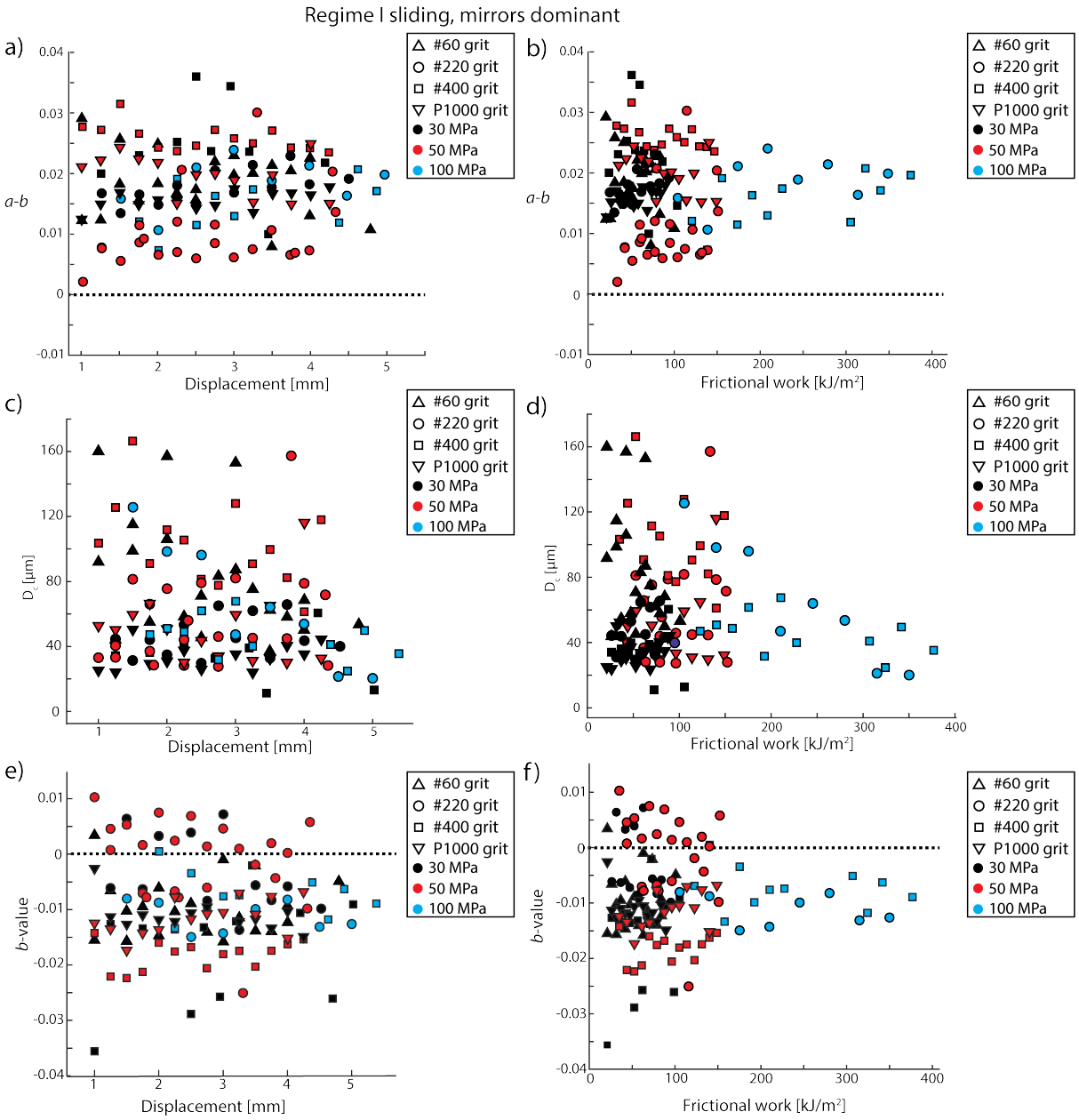

Figure 5.19 Mechanical characterisitics of faults dominated by fault mirror formation deforming in regime I. a) and b) are a reproduction of Figure 5.8 combining data from all experiments where mirrors dominate the final microstructural state of the fault as shown in c)-f). A) Shows a-b plotted as a function of displacement, revealing little dependance on cumulative slip alone, however in b) convergance of a-b values with frictional work is observed. This convergance suggests that frictional wear is important in determining the mechanical response of faults in regime I. In c) and d) D_c is plotted as a function of displacement and frictional work respectively. D_c shows little dependance of displacement, but shows a clear trend for a reduction and convergance with frictional work. In e) b-values are plotted as a function displacement, and show a weak convergance, however plotting b-values as a function of frictional work in f) shows a clear convergance to a value of b ≈ -0.01.

Many experimental studies have shown that the deformation of calcite at conditions comparable to those of these experiments occurs through a range of plastic and brittle

deformation mechanisms, which include, pressure solution (Verberne et al., 2014; Verberne, Spiers, et al., 2013; Carpenter et al., 2016; Chen and Spiers, 2016), intracrystalline plasticity (Fredrich et al., 1989; Schubnel et al., 2006) and frictional sliding (Carpenter et al., 2016; Tesei et al., 2017). In particular Carpenter *et al.* (2016) showed that at comparable deformation conditions to experiments present in this chapter, a transition from positive to negative values of b is observed with increases in normal stress from 20 to 100 MPa, with the negative values being observed only at low velocity ($V < 10$ μm/s). These are interpreted to be representative of a transition between brittle to semi brittle behaviour, in similarities to previous suggestions from experiments in halite gouges (Noda and Shimamoto, 2010; Shimamoto, 1986; Bos et al., 2000).

Under regime I, the prevalence of fault mirrors and low porosity gouge comprised of nanometric particles shares many similarities to microstructures observed in natural faults and high velocity experimentation (Pozzi et al., 2018; De Paola et al., 2015; Siman-Tov et al., 2015; Fondriest et al., 2013; Smith et al., 2013; Siman-Tov et al., 2013). Recently it has been shown in high velocity friction experiments (>1mm/s), that the formation of mirrors and nanometric particles is associated to diffusive creep mechanisms (Pozzi et al., 2018; De Paola et al., 2015). Microstructures developed in #400 faults, sliding under regime II at 30 MPa (Figure 5.15a), and 100 MPa (Figure 5.15d), share many similarities with those that are developed in higher velocity experiments. In particular, the presence of a low porosity band comprised of nanoparticles is reminiscent of stage III microstructures documented in Pozzi et al. (2018). In these experiments diffusive mechanisms are enhanced by shear heating and an extremely small grain size, which gives rise to low frictional strength. Here a temperature rise is not expected due to the slow sliding velocities, which would limit the activity of diffusive mechanisms. However the strain rate in these experiments is considerably lower, up to 5-7 times smaller, which when combined with the very small grain size (100-200 nm), may be slow enough to allow diffusive creep mechanisms to occur.

Under regime I, an important observation is made about the dependence of rate-and-state parameters with frictional work. In Figure 5.19a, *a-b* is plotted for all of these faults as a function of displacement, and shows no systematic trend. However, when plotted data as function of frictional work (Figure 5.19b), a clear convergence of *a-b* values with increasing frictional work emerges, to a value between +0.018-+0.02. The same is true of plotting D_c (Figure 5.19d) and *b*-values (Figure 5.19f) as function of frictional work,

which both show a relative convergence to a common value ($D_c \approx 40$ μm and $b \approx -0.01$). This therefore demonstrates that rate-and-state parameters evolve with frictional wear under regime I deformation, this is a key observation of this chapter. It is well established that frictional strength is related to wear processes (Archard, 1953; Queener et al., 1965; Power et al., 1988; Wang and Scholz, 1994), however a convergence of rate-and-state friction parameters with wear has not previously been observed or suggested. These data therefore suggest that rate-and-state friction is intrinsically linked to frictional wear processes, which are widely observed on natural faults (Brodsky et al., 2016; Sagy and Brodsky, 2009; Kirkpatrick and Brodsky, 2014).

5.4.2 Deformation in regime II

In Figure 5.21 the velocity dependence of friction (a-b) for all faults categorised microstructurally as regime II are compiled. In Figure 5.21a, a-b is plotted as a function of displacement, and in Figure 5.21b a-b is plotted as a function of frictional work. These plots show that in regime II, a-b values are typically velocity weakening to velocity strengthening ($-0.005 < a\text{-}b < +0.005$), which is markedly different from regime I a-b values (Figure 5.19). Little evolution of a-b is observed as a function of slip or frictional work. The insensitivity to displacement or work suggests that wear may be fast in this regime and therefore a coarse band of angular gouge is developed early during sliding. Additionally, all faults deforming in this regime show positive values of b (Figure 5.21e and f), which show a slight decrease with frictional work. Values of D_c are small, typically between 5-10 μm (Figure 5.21c and d) but show little dependence on displacement (Figure 5.21c), or frictional work (Figure 5.21d) in direct contrast to what is observed for regime I.

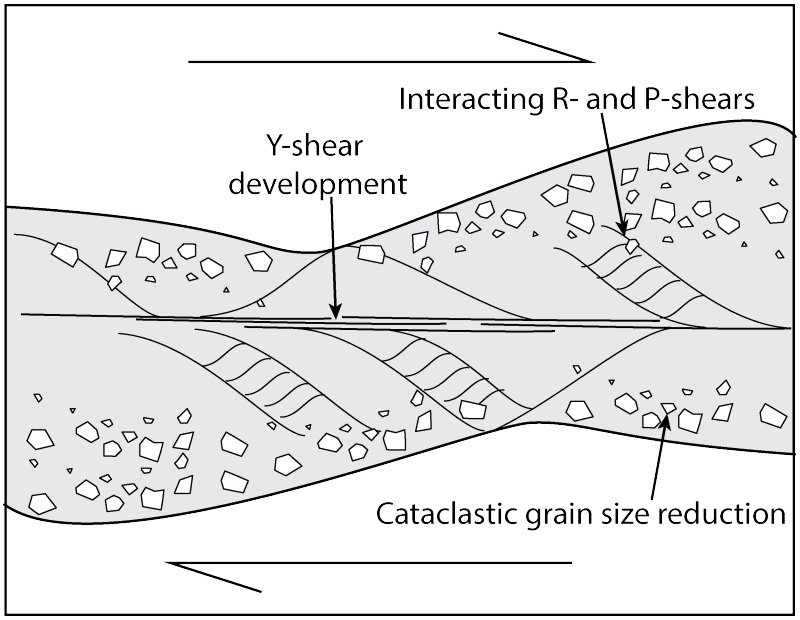

Figure 5.20 Deformation features of regime II schematically summarised in a cartoon cross section. In this regime the prevalence of brittle deformation leads to cataclastic flow, with evidence for brittle grain size reduction, interaction of R- and P-shears, and initial development of Y-shears. Slip localised within the gouge layer in similarity to experiments conducted on simulated gouge.

Microstructural observations on these surfaces show a greater predominance of looser, higher porosity gouge formation in reflected light microscopy (Figure 5.17f, i and k). In cross sections at high normal stress there is evidence for brittle cataclastic deformation with an abundance of large angular fragments within the gouge layer (Figure 5.14c). The #60 fault cross section at 100 MPa is also notable by the lack of continuous low porosity nanoparticle bands which are observed in regime I. Instead it is dominated by thick gouge layers with complex networks of R-shears and an abundance of angular fragments. An idealised cartoon section through a fault deforming in regime II is shown in Figure 5.20.

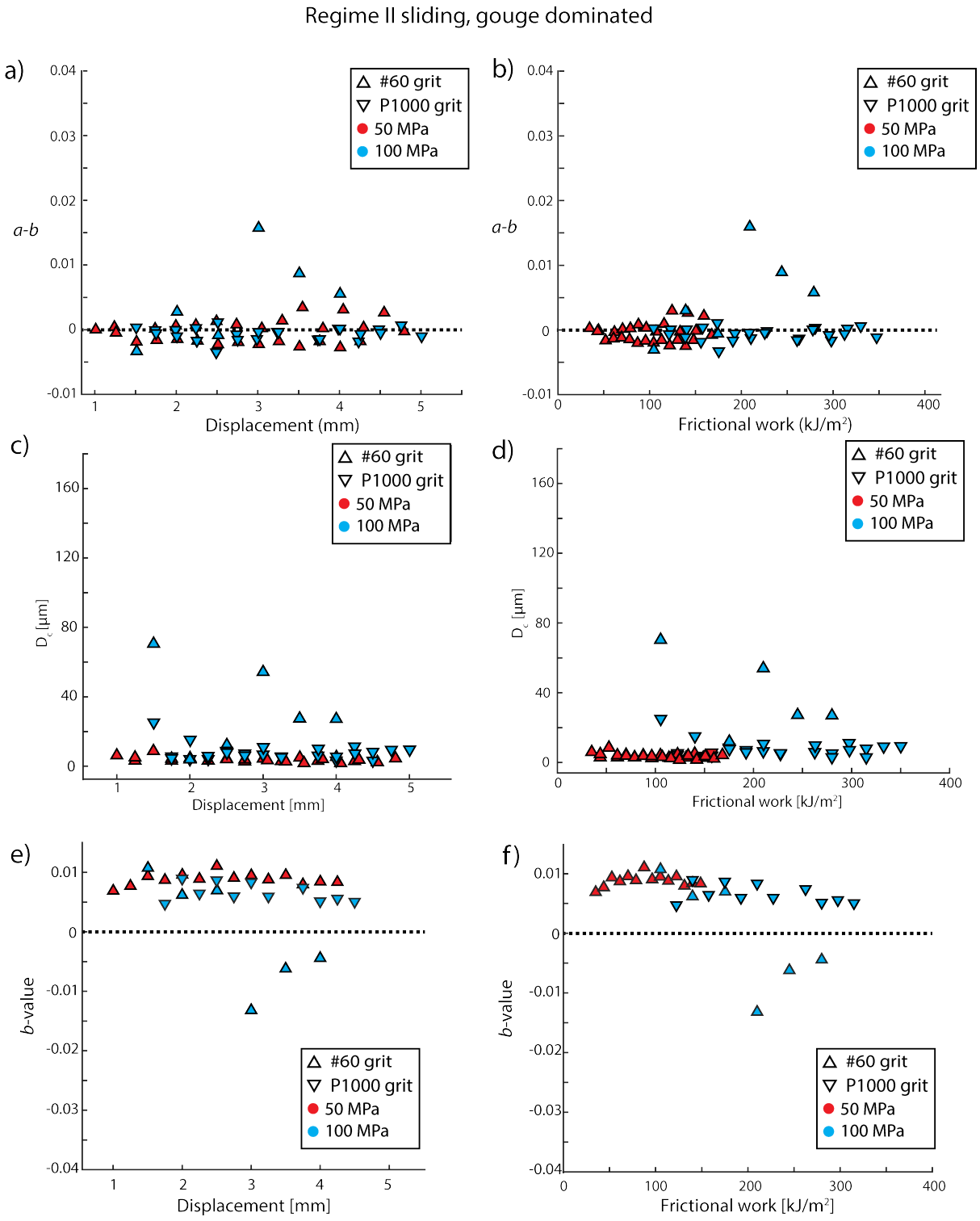

Figure 5.21 Mechanical characteristics of deformation on gouge dominated faults deforming in regime II. Both modelled a-b values (a and b), and values of D_c (c and d), are significantly lower than faults deforming under regime I. In a) a-b is plotted as a function of displacement, with little trend to remark of, in b) a similar lack of clear trend is observed when plotting a-b values as a function of frictional work. In c) and d) the critical slip distance is plotted as a function of displacement and frictional work respectively, D_c shows little systematic dependance on these variables.

In many frictional studies spanning conditions of semi-brittle to brittle gouge behaviour, observations of positive *b*-values and small D_c values are linked to brittle behaviour (Carpenter et al., 2016; Shimamoto, 1986; Noda and Shimamoto, 2010). Indeed, mechanical and microstructural results in regime II share many similarities to experiments conducted with simulated gouge as a starting material (e.g. Logan *et al.*, 1992; Beeler *et al.*, 1996). In previous interpretations progressive grain size reduction leads to the development of a localised slip zone within the gouge, often associated to the formation of R_1 and B-shears of angular material that progressively interlinks to form through going Y-shears (Logan et al., 1992; Beeler et al., 1996; Scuderi et al., 2017; Marone, 1998). These microstructural features are accompanied by a reduction in *a-b* values and small D_c values as deformation becomes less dilatant and increasingly localised (Scuderi et al., 2017; Beeler et al., 1996). Therefore, faults deforming in regime II are interpreted to slide through brittle deformation mechanisms (Figure 5.20). Generally this frictional behaviour seems to more prevalent at high normal stress conditions as shown in Figure 5.4 (#60 grit, 50 and 100 MPa curves) and Figure 5.7 (P1000 grit paper, 100 MPa curve), which is contrary to the observations of (Carpenter et al., 2016) who showed that increased normal stress promotes the appearance of semi-brittle deformation in gouge friction.

5.4.3 Microphysical modelling

In order to provide a preliminary test of the hypothesis that diffusion creep plays are role in the frictional sliding of faults in regime I, a diffusion creep law following (Schmid et al., 1977) was implemented into the (Niemeijer and Spiers, 2007) model. The Niemeijer-Spiers model has been shown to model the velocity dependant behaviour of calcite gouges (Verberne et al., 2014; Verberne, et al., 2013; Chen and Spiers, 2016), where a competition of compaction through diffusive mass transfer creep processes, $\dot{\varepsilon_c}$, (typically pressure solution) and granular compaction, $\dot{\varepsilon_g}$, is considered. The model provides a prediction of the steady state frictional strength as a function of a steady state porosity, ϕ_{ss}, which is obtained by balance of the two competing mechanisms:

$$\phi_{ss} \approx 0.5\left\{q - \left(\dot{\varepsilon}_c \frac{1}{\dot{\gamma}\varsigma}\right)^{\frac{1}{3}} f(\phi)\right\} \qquad 5.4$$

where $f(\phi) = \frac{2\phi}{(1-2\phi)^2} \approx 0.02$ with an estimated observed porosity of ≈0.01 in SEM images (Figure 5.13 f & h), $q \approx 2\phi_c$ (≈0.8-1), ϕ_c is the critical porosity, $\dot{\varepsilon}_c$ a compaction strain rate in s^{-1}, $\dot{\gamma}$ the shear strain rate and ς a geometric factor accounting for the orientation of grain boundaries, here $0.5\left(\frac{1}{\sqrt{3}} + \sqrt{3}\right)$ (Niemeijer and Spiers, 2007; Chen et al., 2017). The steady state porosity may then be utilised to obtain a granular dilatation angle, ψ, by the relation:-

$$\tan\psi = \varsigma(q - 2\phi_{ss})^l$$

5.5

Where l is constant, here taken to be 1 in accordance with (Verberne et al., 2014). The steady state coefficient of friction according to granular mechanics is therefore (Niemeijer and Spiers, 2007):-

$$\mu_{ss} = \frac{\varrho\pi C_0}{\varsigma\sigma_n}\left(\frac{tan\psi}{cos\psi - \mu_g sin\psi}\right) + \frac{sin\psi + \mu_g cos\psi}{cos\psi - \mu_g sin\psi}$$

5.6

Where ϱ is a geometric factor, C_0 the cohesion in Pa and μ_g the grain boundary coefficient of friction.

Experiments presented in this chapter are run under room humidity conditions, and microstructures show no evidence of flattened/truncated grains (Gratier et al., 2013), therefore, compaction by pressure solution seems unlikely at these conditions (Zhang et al., 2010). However, as previously discussed, the evidence of nanoparticles and mirror surfaces may be indicative of diffusion creep processes (Pozzi et al., 2018; De Paola et al., 2015).

In Schmid et al. (1977), a series of experiments were conducted at high temperature to investigate the flow strength of fine grain micritic limestones deforming in the diffusion creep regime. It was found that the strain rate, $\dot{\varepsilon}$, of limestone deforming by diffusion creep is given by:-

$$\dot{\varepsilon} = A^* D^{-m} e^{-\frac{\varpi}{RT}} \sigma^n$$

5.7

Where A^* is a pre-exponential constant in s^{-1} bar^{-n}, D the grain size in m, m a dimensionless grain size exponent, ϖ the activation enthalpy in kcal/Mol, R is the gas constant which is 1.987×10^{-3} kcal K mol^{-1}, T the temperature in K, σ the normal stress in bar and n is the dimensionless stress exponent. The parameters, $m = 3$, $n = 1.66$, $A^* = 9.55 \times 10^4$ and $\varpi = 51$ kcal/Mol, obtained for deformed calcite aggregates by Schmid et al. (1977). Equation 5.7 was implemented into the Niemeijer-Spiers model (equation 5.6) by setting $\dot{\varepsilon}_c = \dot{\varepsilon}$, and was then subsequently used to model the velocity dependant friction.

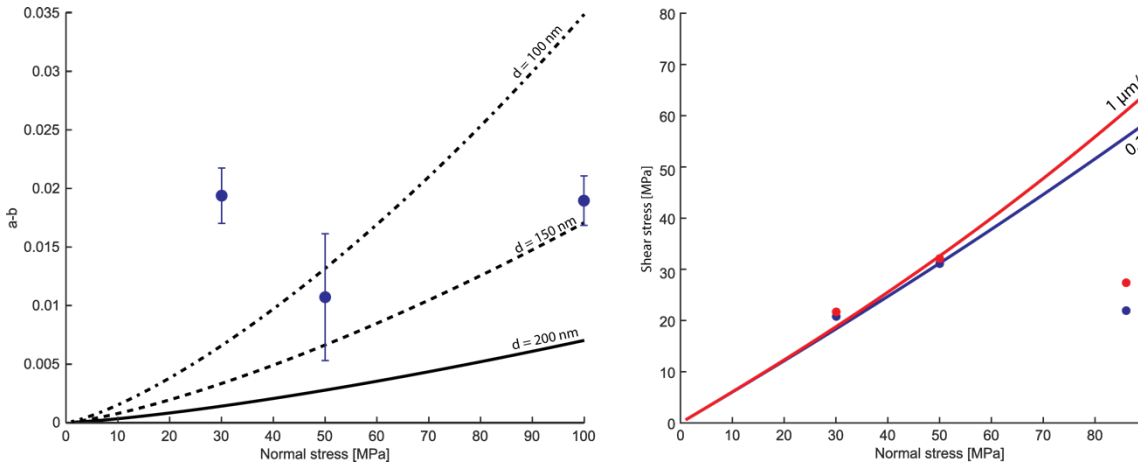

Figure 5.22 Results from preliminary implementation of diffusion creep laws into the model developed in Niemeijer and Spiers (2007) for samples prepared with #400 grit, where sliding is under regime I, and samples have well constrained microstructures. A) Shows predictions of a-b as a function of normal stress compared against experimental data and b) the absolute strength predictions for the parameters specified in the text.

The plots in Figure 5.22 show results from modelling the velocity dependence of friction (a) and the absolute strength of fault as a function of velocity (b). For the curve calculation the parameters, D = 100, 150 and 200 nm, h = 20 µm, $\mu_g = 0.6$ are estimated based on microstructural observations and mechanical data, q = 1 based on Verberne et al. (2014) and T = 298 K equivalent to a room temperature of 25°C .

Velocity dependence results are reasonably well fit by the modified model which fits well the *a-b* values at 50 and 100 MPa but fails to fit data at 30 MPa (Figure 5.22a). The absolute strength predicted by the model also has a similar success to the velocity dependence but does not completely predict the strength at low normal stress (Figure 5.22b). These modelling results therefore highlight that frictional sliding under regime I may occur through plastic mechanisms. The lack of fit obtained for the 30 MPa data could be explained by the fact that mirrors are observed not to be fully developed in Figure

5.17d, which suggests that the mirrors may need to extensively cover surfaces to allow the development of a completely interlinked boundary shear.

5.5 Conclusions

In conclusion several key observations are made:-

1. The changing conditions of experiments (roughness and normal stress) of initially bare faults in limestone results in two deformation regimes (I & II) dependant on the microstructural state and evolution of the fault surface.
2. For regime I- if fault mirrors are formed and retained throughout the duration of the experiment then friction is strongly velocity strengthening, with negative b and large D_c values. This may possibly be explained by a competition between diffusion facilitated compaction and granular compaction mechanisms.
3. For regime II- If fault mirrors are destroyed or not well formed then sliding is close to velocity neutral and sliding behaviour resembles that of gouges. Under this regime sliding is interpreted to be accommodated by brittle mechanisms.
4. The evolution of frictional parameters a-b and D_c both show a dependence on cumulative frictional work, and therefore wear, converging to a common value when sliding is under regime I.

These results highlight that the initial conditions of deformation, sliding history, roughness and normal stress, together governs the overall behaviour of faulting during frictional sliding. On calcite faults, smooth fault patches may evolve towards faulting that is characterised by velocity strengthening friction, and rougher patches towards cataclastic flow with velocity neutral to weakening frictional behaviour. These observations suggest that frictional sliding on natural carbonate built faults, like other studies (Tesei et al., 2013; Carpenter et al., 2014), is likely to be very heterogenous, raising important questions about the wide application of previous results to explain crustal seismicity (Verberne et al., 2014).

In these experiments the formation of pervasive fault mirror surfaces at slow velocities is accompanied by velocity strengthening friction, highlighting that in addition to other studies (Tesei et al., 2017; Verberne et al., 2013), fault mirrors are not reliable seismic markers. Fault mirrors may actually act to suppress instability in natural fault zones given their strongly velocity-strengthening nature. Results have also demonstrated that

diffusional creep mechanisms may be active in the shearing gouge which is rich in nanoparticles, which is normally active during high temperature creep of faults (Blanpied et al., 1998; Sibson, 1977; Scholz, 2002).

This is the first-time rate-and-state parameters have been documented to have a dependence on frictional work, and by extension frictional wear. However, in the future more work is required to directly understand the relationships between frictional wear mechanisms and fault friction. Further investigations of links between frictional wear and velocity dependant friction may provide an excellent opportunity to better understand the origins of rate-and-state friction.

5.6 Appendices

5.6.1 Pristine surface SEM images

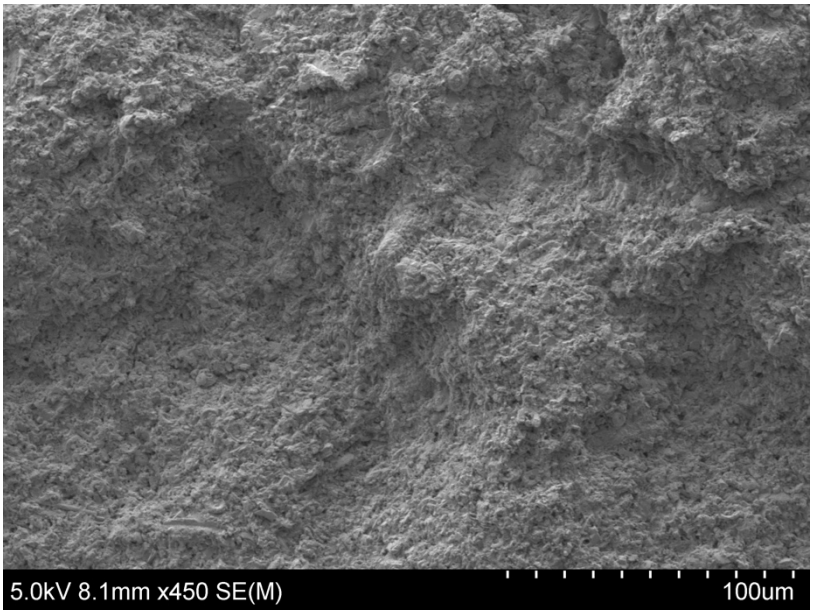

Figure 5.23 Secondary electron SEM image of a pristine Scaglia Rossa surface ground with #60 grit and ultrasonically cleaned in water.

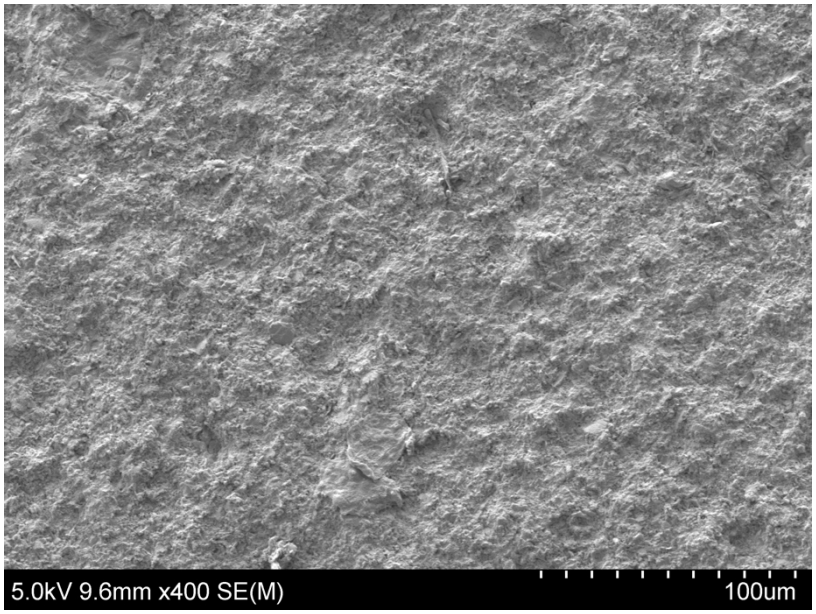

Figure 5.24 Secondary electron SEM image of a pristine Scaglia Rossa surface ground with #400 grit and ultrasonically cleaned in water.

5.6.2 Reflected light images of #220 surfaces

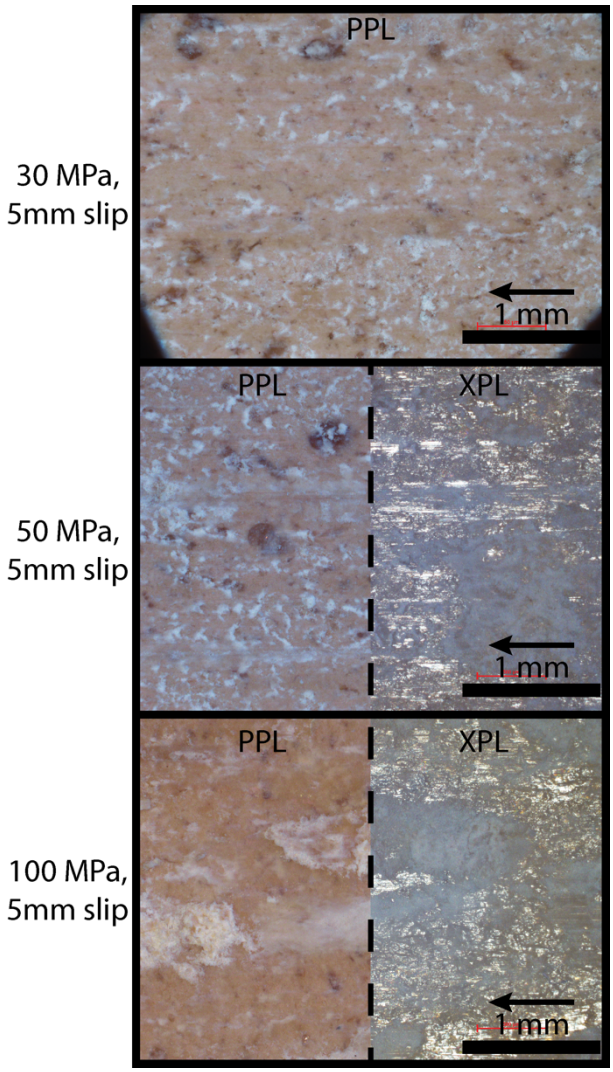

Figure 5.25 Reflected light images of #220 surfaces deformed at a range of normal stress conditions, all of these faults are categorised as deforming in regime I.

6 Thesis summary and suggestions for future work

The overall aim of the thesis was presented in chapter 1, and chapters 3, 4 and 5 have been presented as individual standalone pieces of work. This chapter aims to link back results together to address initial questions about the microphysics and energetics of earthquake nucleation and propagation on rough faults. Then results are placed in the context of wider research into the mechanics of faulting with suggestions to guide future research.

6.1 Summary of results

In chapter 1 it was stated that fault roughness is likely to play a key role in determining the frictional slip dynamics due to its influence on the nature and distribution of frictional asperity contacts. Additionally, the heterogeneity resulting from surface roughness was indicated to play a role in promoting nucleation of earthquake rupture. Contacting asperity characteristics are also strongly influenced by the normal stress acting on the plane, which serves to multiply asperities, and to a lesser extent grow them due to coalescence (Dieterich and Kilgore, 1994). Normal stress is also fundamental for the onset of instability as it reduces both the fault effective stiffness and the critical nucleation length (Passelègue et al., 2013).

In chapter 3 a series of experiments was conducted to investigate the effects of changing roughness and normal stress conditions upon the nucleation of earthquake rupture. Experiments revealed that roughness and normal stress interact in a complex manner, resulting in differing regimes of sliding stability. In general, smoother faults give rise to instability at low normal stress conditions (100-150 MPa), in comparison to rougher faults at similar normal stress conditions. Another key observations was that spontaneous ruptures can nucleate on faults that have a velocity strengthening friction dependence, which under rate-and-state friction is theoretically impossible (Marone, 1998; Gu and Wong, 1991b; Rice and Ruina, 1983). In addition to this, increases in normal stress stabilise slip, which is in direct contradiction to the stiffness criterion where a decrease in fault effective stiffness promotes frictional instability (Leeman et al., 2016; Scuderi et al., 2016). Finally, nucleation length calculations using rate-and-state parameters derived from experiments (Rubin and Ampuero, 2005; Uenishi and Rice, 2003) yields values typically 2 orders of magnitude larger than sample size used. These facts combined

indicates that rate-and-state does not fully capture the nucleation of instability on rough laboratory faults.

To address this issue, a new model of nucleation on rough faults was developed to explain the onset of instability in the experiments presented. The theory is rooted in Griffith's original theory of fracture, which posits that all materials contain small flaws or microcracks (Griffith, 1921). In the case of rough faults in bare rock, and some natural faults, not all of the wall rock is in contact which gives rise to pre-existing flaws between frictional asperities which can be equated to Griffith cracks. This led to a new microphysical interpretation of the parameters used to estimate the nucleation length. In the model the weakened stress between asperities is representative of the weak frictional state, and stress at asperities is equated to peak stress. The asperity length scale is then representative of the breakdown length and was estimated using numerical modelling. Estimates of the nucleation length scale derived from this approach yield values smaller than the sample size, and values that increase with roughness for a given normal stress.

In an extension of this model it was posited that if frictional bridges are larger than the nucleation length, then rupture would be expected to nucleate. A mathematical expression was derived from considerations of fault surface statistics to provide an estimate and scaling of the distance expected between asperities and was compared to numerical models of surface contact. It was found that λ_c decreases at a faster rate than L_c with normal stress, which leads to the suppression of instability at high normal stress conditions. These results highlight that roughness and the resulting heterogeneity play a crucial role in the nucleation of earthquake ruptures and raises some fundamental questions about the general applicability of rate-and-state friction to heterogenous fault systems.

In order to investigate the role of roughness and normal stress in frictional mechanics for other lithologies, in chapter 5 experiments were conducted using a micritic limestone Unit of the Scaglia Rossa formation from the Italian Appenines. The limestone was selected to be representative of faulting in sedimentary cover sequences, in contrast to the crystalline westerly granite used for chapter 3. Given the lower indentation hardness of limestone a greater degree of frictional wear was expected, which may also act to suppress instability (Byerlee and Summers, 1976) and remove stress heterogeneities which are fundamental to the model presented in chapter 3 and Harbord *et al.* (2017). Experimental results show that deformation mechanisms and the resulting frictional behaviour is vastly

different to that of westerly granite, being dominated by frictional wear and gouge build-up. Sliding behaviour can either be: Regime I- very strongly velocity strengthening (a-b ≈ +0.02), with negative b-values (≈-0.01) and large values of the critical slip distance (D_c ≈ 40-200 μm) or; Regime II- velocity neutral to weakening with a-b ≈ -0.005 to +0.005, with positive b-values and small values of D_c (≈5-10 μm). These sliding regimes are accompanied by differing microstructural behaviours, with fault mirrors dominating slip surfaces for regime I, and gouge dominated cataclastic faulting in regime II. Fault mirrors are interpreted to be formed through diffusive mechanisms, with a preliminary microphysical model predicting the observed velocity strengthening behaviour. In regime II the frictional behaviours are similar to that of simulated fault gouges, and is interpreted to result from brittle cataclastic deformation. In addition to these observations it is shown that faults deforming in regime II converge to common values of rate-and-state parameters with increasing frictional work. This shows for the first time that the velocity dependence of friction is linked to frictional wear processes that are widely observed on natural faults (Kirkpatrick and Brodsky, 2014; Sagy et al., 2007; Brodsky et al., 2016).

Taken together chapters 3 & 5 show that the effects of fault roughness are initially strongly pronounced, exhibiting a first order control on both frictional stability and frictional evolution of fault surfaces. The lack of fault gouge development on faults in chapter 3 results in a situation where the stress heterogeneity is high and promotes instability in a manner that differs from rate-and-state theories. Given subsequent frictional work and build-up of wear materials this stress heterogeneity is gradually suppressed, and frictional behaviour is stabilised as demonstrated by experiments in chapter 5. The two chapters show that the initial conditions (normal stress, roughness and lithology) exert a primary control on subsequent sliding behaviour.

Finally, chapter 4 addresses the nature of frictional sliding of bare granite surfaces under conditions of spontaneous dynamic rupture. Results serve to verify flash heating theories for spontaneous ruptures propagating at hypocentral conditions. Results show that granite is strongly velocity weakening during spontaneous rupture at slip velocities above 0.15 m/s, and the observed velocity weakening dependence during fault friction is well fit by a flash heating model of friction. Normalisation of events suggest that they are self-similar, with slip functions demonstrating similarity to the Yoffe function for a moving Griffith crack (Yoffe, 1951). The strong velocity weakening also lends support to the self-healing slip-pulse model of rupture (Beeler and Tullis, 1996; Heaton, 1990). Significantly

these results open up a toolbox to develop a direct quantification of the earthquake energy balance at a range of hypocentral conditions, whilst also providing verification of seismological source mechanisms.

6.2 On implications for crustal earthquakes

The model of nucleation presented in chapter 3 provides a new model to explain the nucleation of earthquake ruptures, which predicts that nucleation lengths on smoother fault surfaces are larger than those expected for rough faults. This directly agrees with previous experimental work (Ohnaka and Shen, 1999; Okubo and Dieterich, 1984) and results of numerical simulations with simulated fault roughness which have recently been published (Tal et al., 2018; Tal and Hager, 2018). In addition, it may be consistent with larger scale observations of subduction zone seismicity where smoother interfaces are associated with large earthquakes, and rougher subducted slabs with smaller earthquakes and possibly more slow slip events (Wang and Bilek, 2014; Bürgmann, 2018). In essence the model may also be extended to earthquakes induced by fluid injection, whereby the injection of fluids creates a stress relieved patch that can nucleate when energetically favourable.

Results may also contribute to the ongoing literature discussion about cascade-up vs. pre-slip models of earthquake nucleation. This highlighted by the recent publication of two papers, first Tape et al. (2018) favouring pre-slip models, and secondly Ellsworth and Bulut (2018) which favours a cascade-up model. Pre-slip is generally associated to rate-and-state frictional models, whereby a small patch of slow-slip grows over a long time period until it is big enough to propagate unstably (Kaneko et al., 2016; Rubin and Ampuero, 2005). Generally pre-slip is associated with large subduction zone earthquakes, where long periods of low frequency tremor indicative of slow slip have been observed (Bouchon et al., 2013; Socquet et al., 2017; Tape et al., 2018). Alternatively cascade-up seismicity, characterised by an abrupt onset seismicity and short nucleation time period is interpreted to result from the transfer of stress from individual failing seismic asperities (Dodge et al., 1995; Ellsworth and Beroza, 1995; Ellsworth and Bulut, 2018). This model is invoked to explain some smaller earthquakes on strike slip faults such as the San Andreas fault (Dodge et al., 1995; Bohnhoff et al., 2009) and the larger Izmit earthquake of 1999 (Tape et al., 2018; Aochi and Madariaga, 2003) although this is contested by Bouchon et al. (2011) due the nature of picking and filtering techniques used.

The characteristics of the Izmit foreshocks and dynamic rupture shows evidence for a heterogeneous fault structure (Aochi and Madariaga, 2003; Ellsworth and Bulut, 2018), which when combined with a short nucleation period may indicate similarity to the results presented in chapter 3 and Harbord et al. (2017). Alternatively pre-slip models may be more appropriate to gouge filled faults, where rate-and-state is successful (Scuderi et al., 2016; Leeman et al., 2016), in direct comparison to subduction faults which contain thick packages of gouge and wide fault cores (Fulton et al., 2013; Wang and Bilek, 2014).

The results presented in chapter 4 present a significant advance on previous studies investigating earthquake dynamic rupture in the laboratory. Being able to determine the slip-velocity function combined with the frictional strength evolution during earthquake rupture has provided the first direct verification of flash heating theory during dynamic rupture on rocks. The observations suggest that flash heating accurately captures the weakening of earthquake faults for earthquakes of magnitude $M < 5$. However, they have highlighted that flash heating cannot capture restrengthening behaviour, and therefore needs to be reformulated in future studies to account for microstructural and mechanical changes caused by melting of fault surfaces and frictional asperities. Results also directly support the notion of self-similar self-healing slip-pulses as an accurate representation of the seismic source (Nielsen and Madariaga, 2003; Brantut and Viesca, 2017; Beeler and Tullis, 1996). Finally, the ability to measure coseismic slip directly opens the door to fully constrain the earthquake energy balance in the laboratory, at a range of conditions previously inaccessible.

6.3 Implications for long term evolution of fault zones

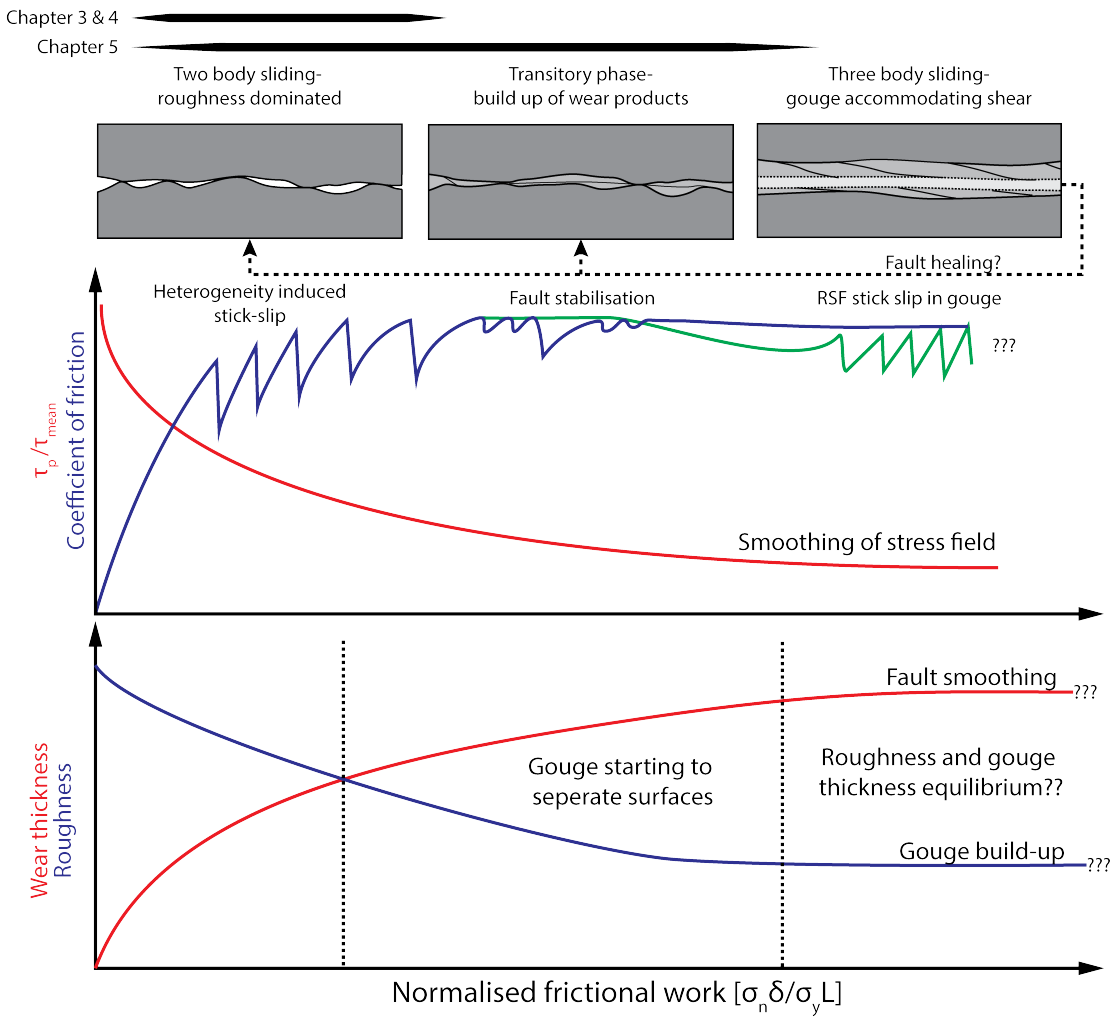

Figure 6.1 Coupled microstructural and mechanical evolution of initially bare faults in rock. Frictional work, which defines the wear of a fault, is normalised by the yield strength of a rock and linear fault length providing a dimensionless measure of fault 'maturity'. The schematic diagram provides a model linking the gradual smoothing of faults and build-up of wear products to the overall mechanical behaviour. The model shows initial wear on faults reduces stress heterogeneity (τ_p/τ_{mean}) by smoothing and build-up of gouge which suppresses instability mechanisms presented in chapter 3 and will modify the nature of flash heating presented in chapter 4. The continued wear and continued smoothing of fault walls lead to stable sliding and behaviour similar to that observed in chapter 5 which may be linked to delocalising slip. Finally, at some stage faults are expected to reach an equilibrium state between wear and gouge build up leading to a 'steady-state' roughness condition. In this regime thick gouge layers may result in localisation of slip within the fault core leading to rate-and-state instabilities observed in gouge sliding experiments (Leeman et al., 2016; Scuderi et al., 2016).

The schematic model presented in Figure 6.1 is intended to help summarise results by linking fault microstructure to mechanical behaviour of fault zones. The principal factor defining the evolution is the frictional work normalised by the product of the yield

strength and the linear fault dimension, which allows a dimensionless comparison of fault maturity across scales and rock types. The aim of this plot is to show that frictional wear exerts a fundamental control on the mechanical behaviour of faults by modifying stress distributions and more generally fault microstructure.

As was shown in chapter 3, faults that contain low volumes of gouge and are characterised primarily by contacting wall rock, are likely to be strongly dependant on the geometric heterogeneities imparted by roughness. This can lead to unstable slip with the nucleation of earthquake rupture due to flaws induced between asperities. During unstable slip, as was shown in chapter 4, faults may become dynamically weak and accelerate up to metres per second of velocity. These results highlight that immature faults, with little to no gouge volume, may be characterised by repeated earthquakes, with failure on fault jogs or bends. As slip continues in the schematic, wear produces gouges and breccias which begin to eliminate heterogeneity imparted by the roughness of the wall rock, as highlighted by the decreasing shear stress ratio $\left(\frac{\tau_p}{\tilde{\tau}}\right)$. Continued wear results in a smoothing (decreasing roughness) of the wall rock and a mechanical transition to stable sliding as heterogeneity is reduced. This process is best represented by the results presented in chapter 5, where wear is abundant, and the resulting slip is stable. Finally, as observed in some of the experiments in chapter 5, but more widely in the literature, localisation within the gouge layer may lead to the onset of velocity weakening behaviour and associated 'rate-and-state style instability'. In this region sliding is accommodated in a three-body manner, and instability is well described by rate-and-state friction. Based on these inferences it is suggested that results may provide a description of the mechanics of fault slip during immature faulting up to the early stages of fault maturity, perhaps equivalent to the running-in phase described by Power et al. (1988)

6.4 Suggestions for future work

Many avenues of work are possible, but I have a few suggestions for work that I think would be interesting to pursue. Further studies should look to investigate the role of frictional wear, with the aim to investigate fundamental connections between wear processes and frictional slip behaviours. Wear is a fundamental aspect of many natural fault systems, and understanding how the build-up of gouge, and natural fault structures may hold some important clues as to the origins of frictional sliding behaviours. There is a need to define wear and wear rates under confined conditions at slow loading rates

which may help to solve questions of understanding fault structure at depth. This is a relatively under explored domain in the modern experimental era, and could yield many important results.

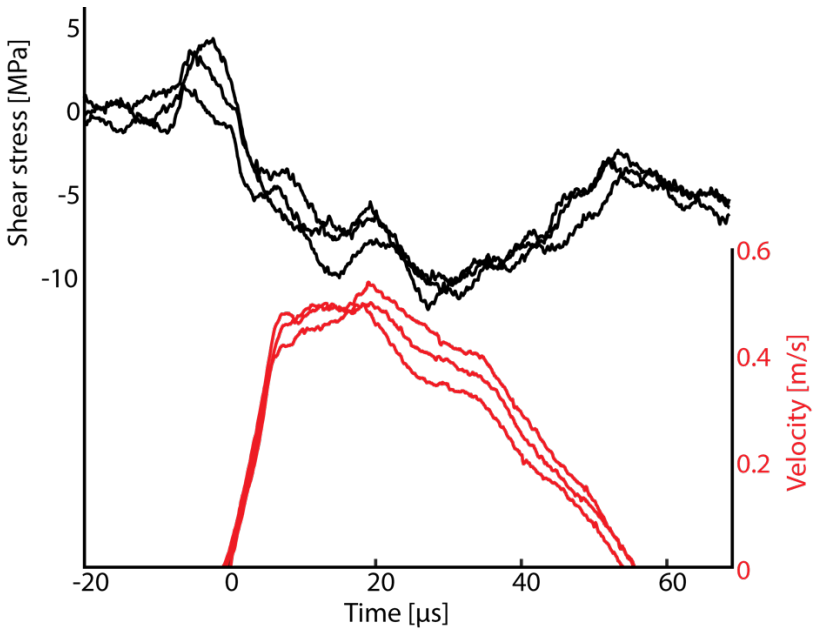

Figure 6.2 Preliminary results from stick-slip experiments in Quartzite showing velocity and stress as a function of time.

Another clear research aim is to extend the results of the strain gauge work to other lithologies to develop and test frictional sliding laws where rock physical properties are fundamentally different (provided that certain elusive aspects of experimental conditions proliferating instability are fully comprehended). Preliminary tests have been undertaken using quartzite and show some differences (the behaviour appears to be more slip weakening), of particular encouragement is the observation of peak stress preceding rupture arrival (Figure 6.2). Building on this, changes to ambient faulting conditions (roughness, normal stress, pore fluids etc.), may be introduced to establish constitutive properties of friction during earthquake rupture propagation and test literature theories e.g. thermal pressurisation, Weertman pulses in bimaterial faults etc. In this vein constraining the complete earthquake energy balance, which may be achieved by adding in a calibrated acoustic receiver array to stick-slip experiments (in addition to strain gauges), is an exciting prospect and one which certainly merits further investigation.

7 Appendices

7.1 Instrument calibrations and performance

7.1.1 Axial displacement LVDT

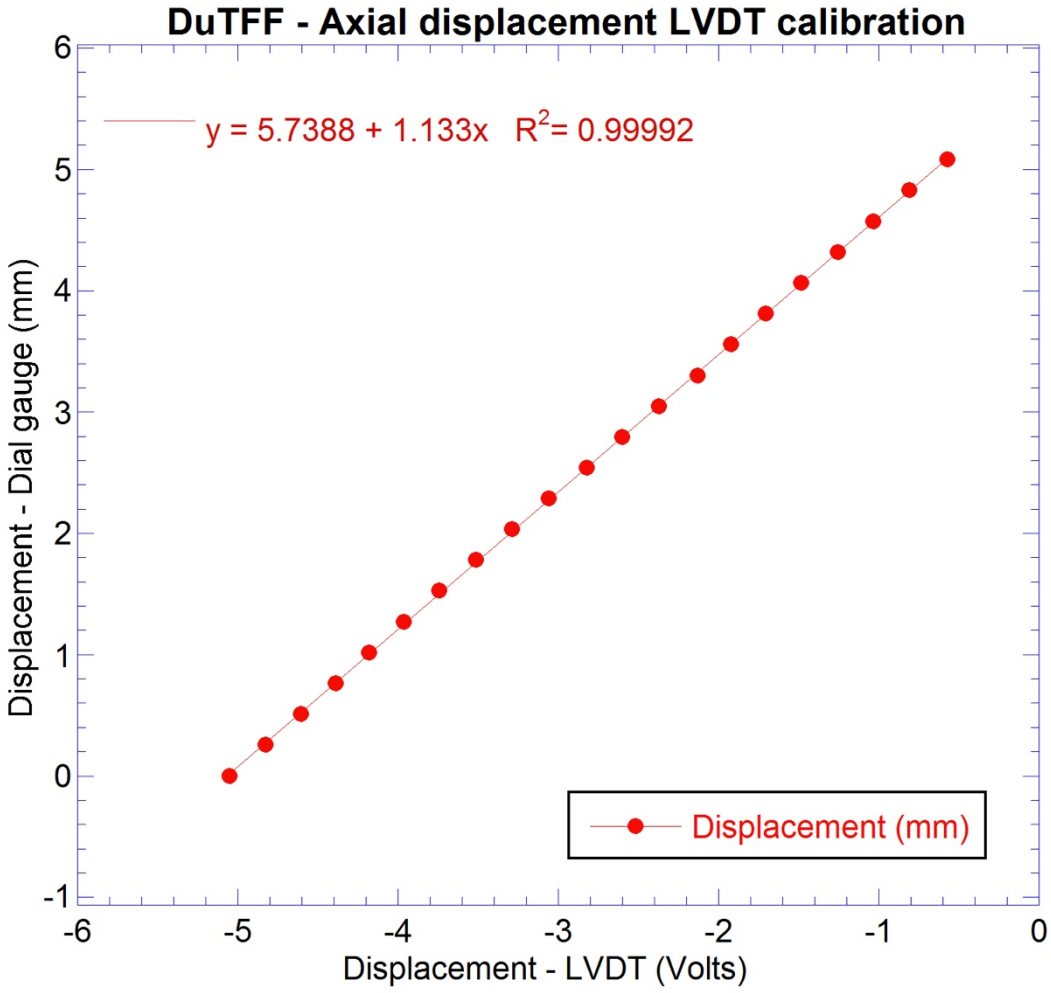

Figure 7.1 Axial displacement LVDT calibration plot. Performed by D. Faulkner, S. Nielsen & N. De Paola in February 2014.

7.1.2 Axial force calibration

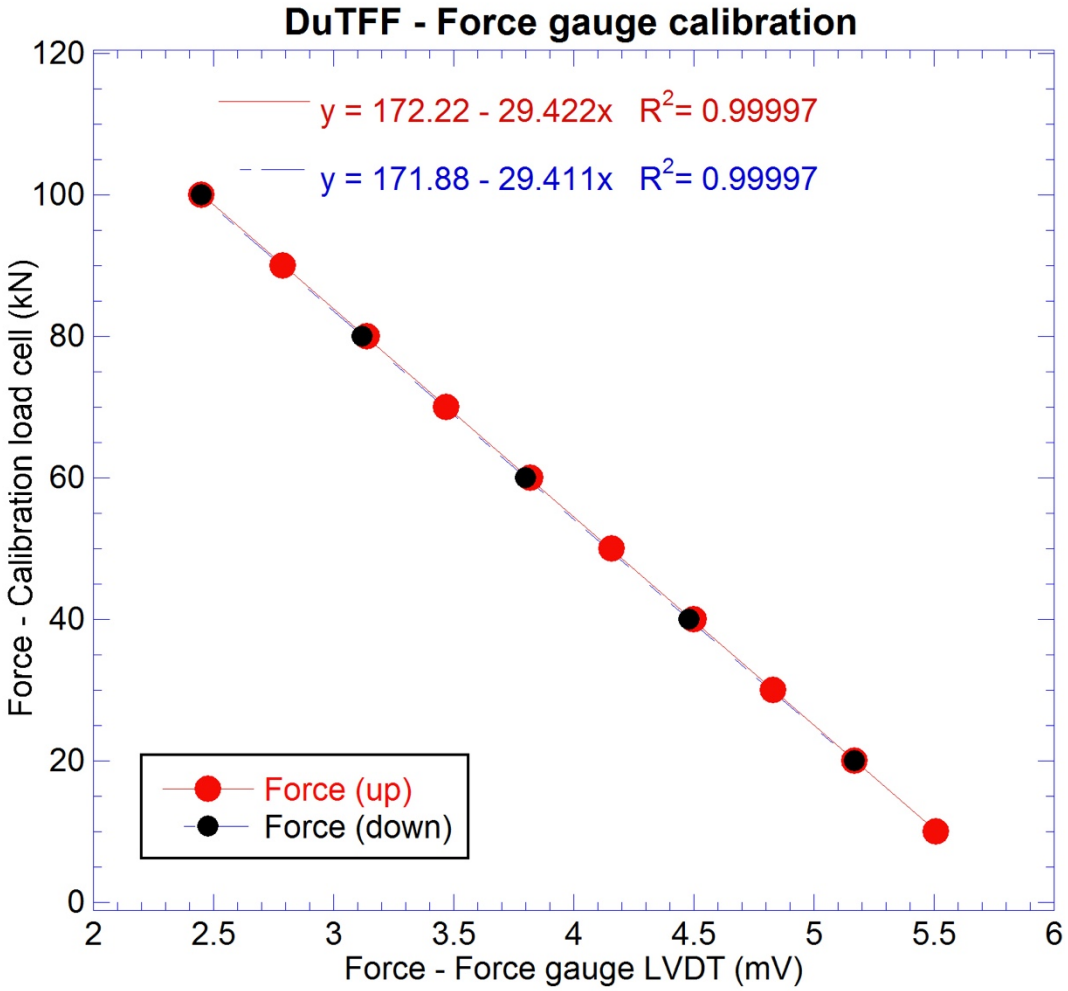

Figure 7.2 Force gauge calibration plot. Performed by D. Faulkner, S. Nielsen & N. De Paola in February 2014.

7.1.3 Confining pressure transducer

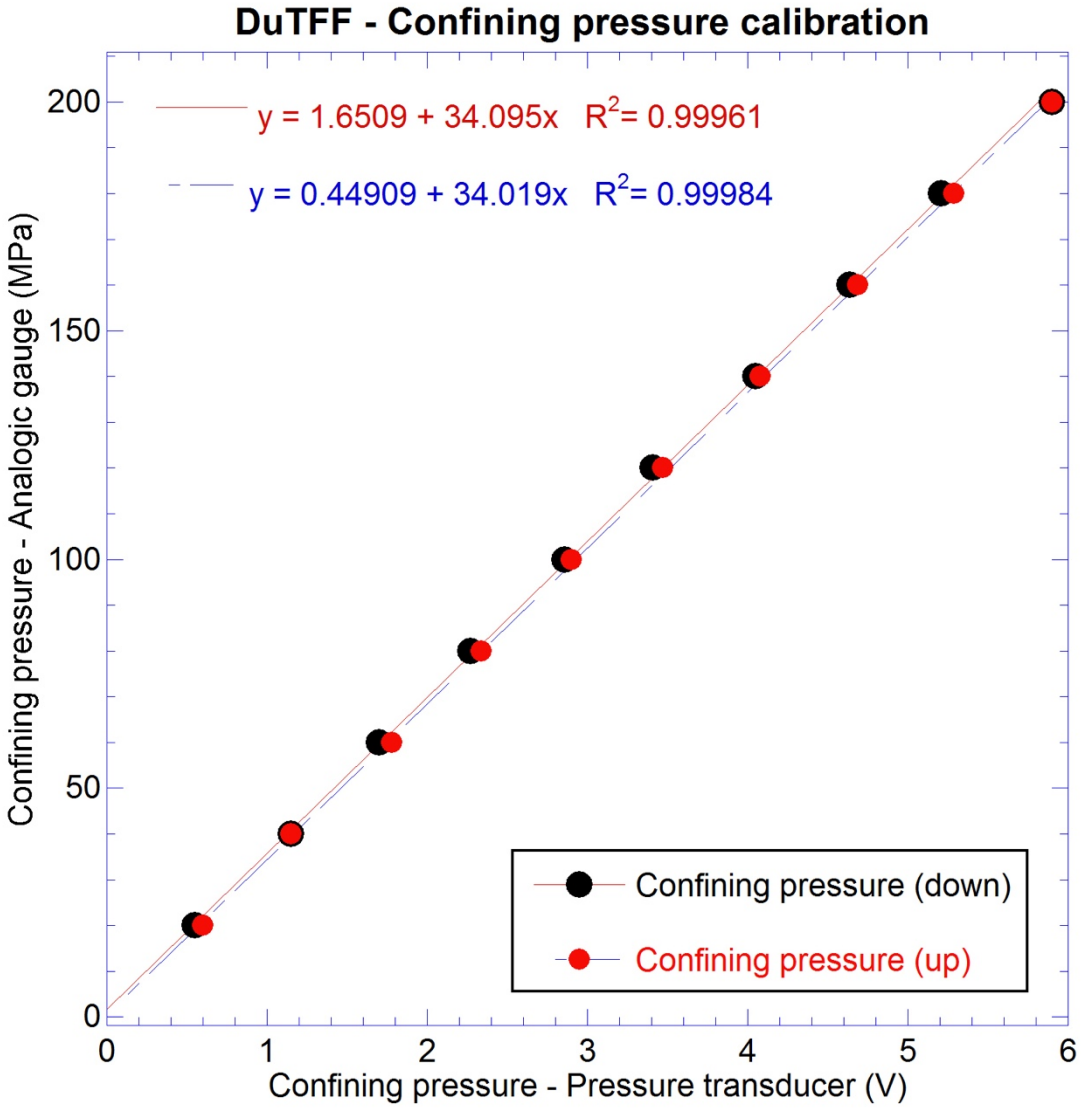

Figure 7.3 Confining pressure transducer calibration plot. Performed by D. Faulkner, S. Nielsen & N. De Paola in February 2014.

7.1.4 Porefluid pressure transducer

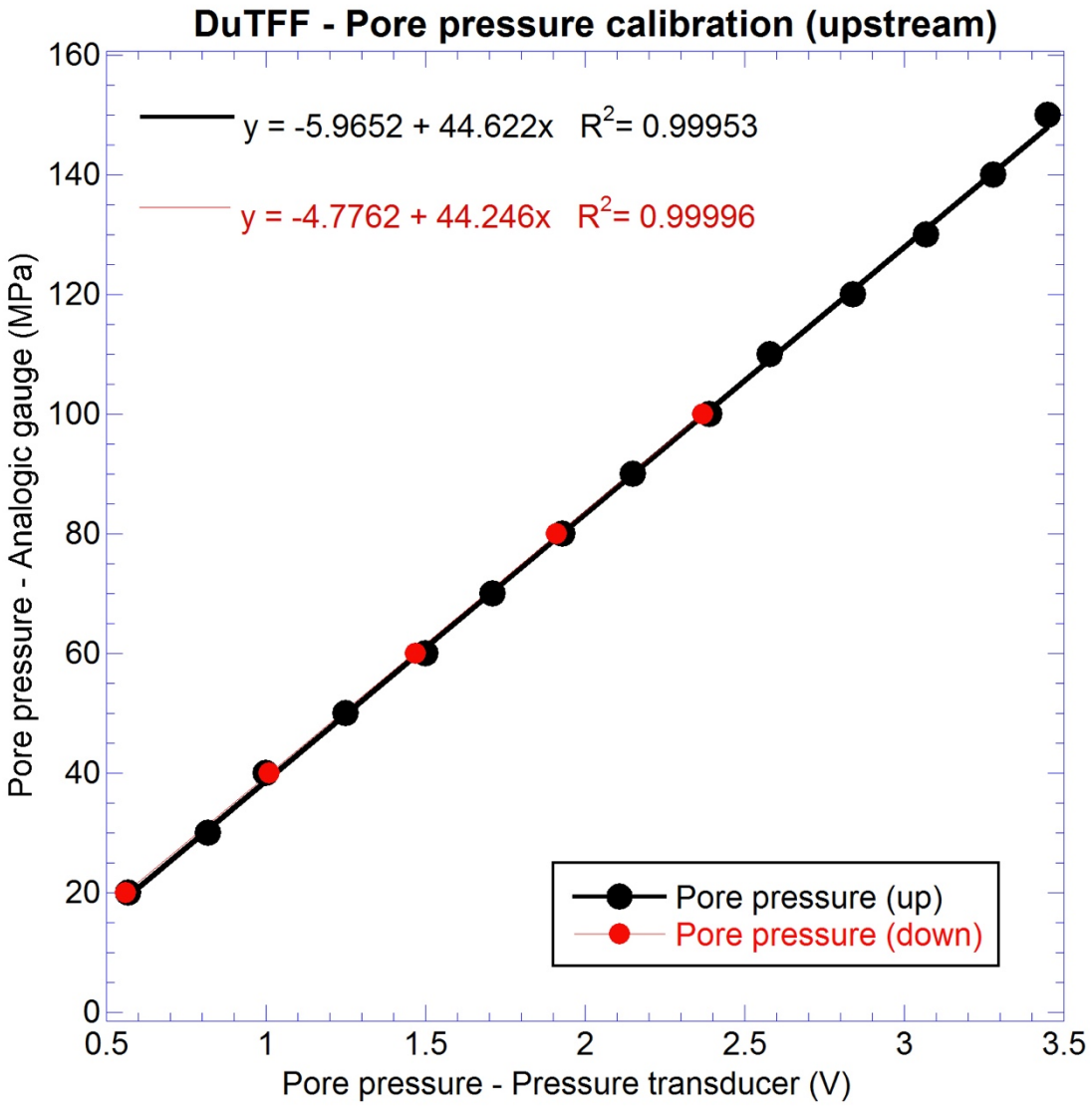

Figure 7.4 Up stream pore pressure transducer calibration. Performed by D. Faulkner, S. Nielsen & N. De Paola in February 2014.

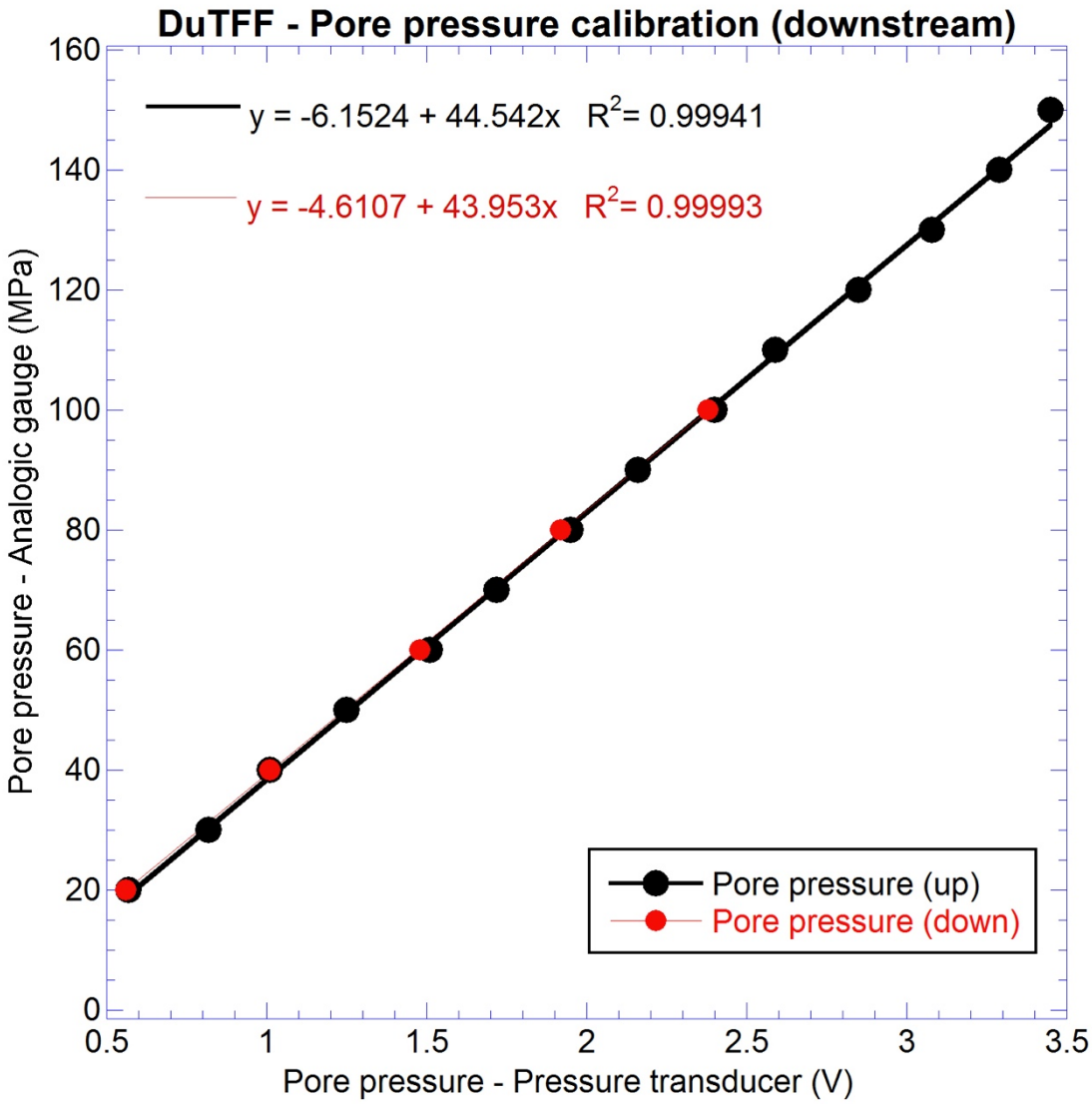

Figure 7.5 Downstream pore-fluid pressure calibration. Performed by D. Faulkner, S. Nielsen & N. De Paola in February 2014.

7.1.5 Porefluid volumometer LVDT

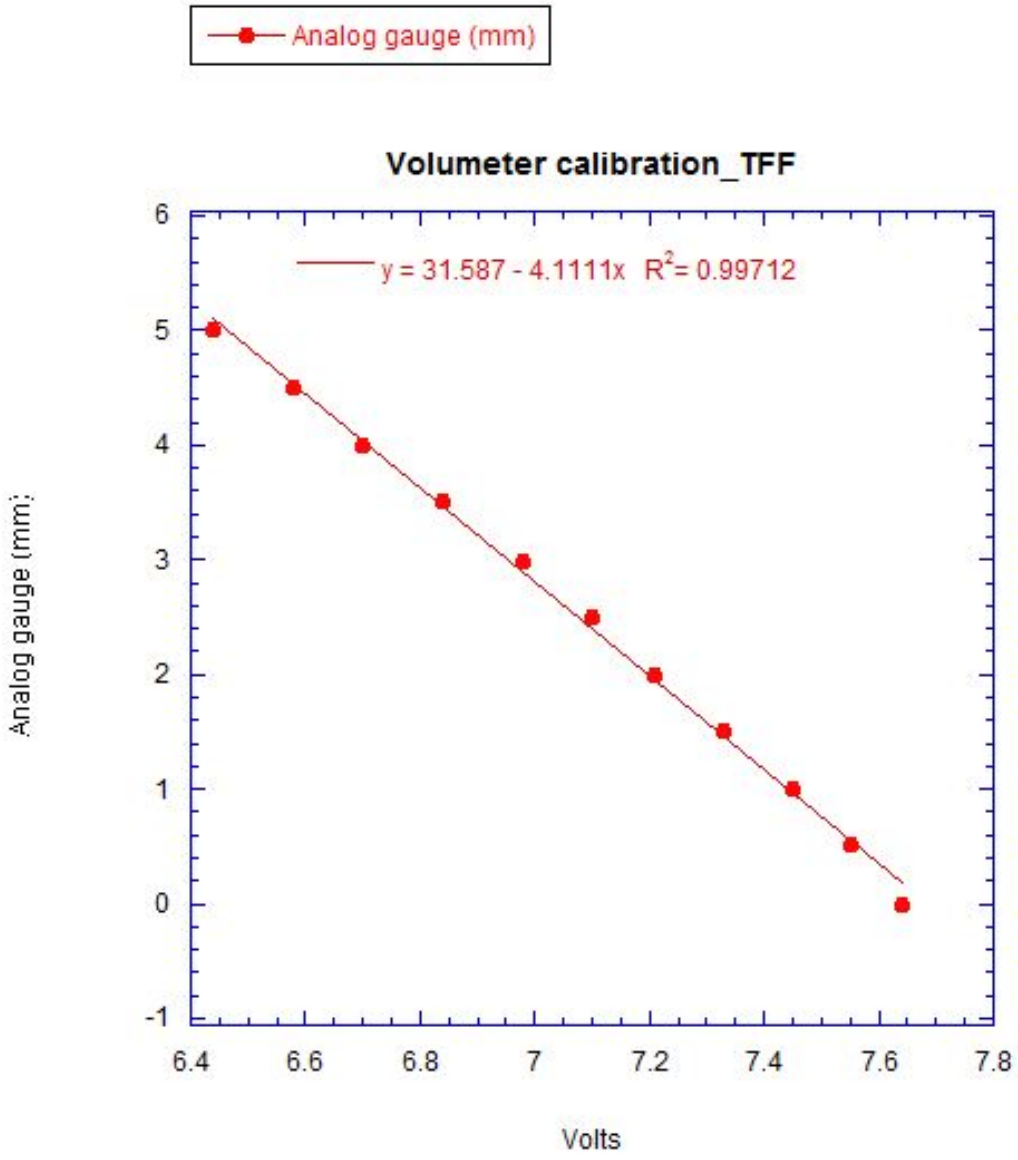

Figure 7.6 Pore fluid volumometer LVDT calibration plot. Performed by D. Faulkner, S. Nielsen & N. De Paola in February 2014.

7.1.6 Machine stiffness measurements

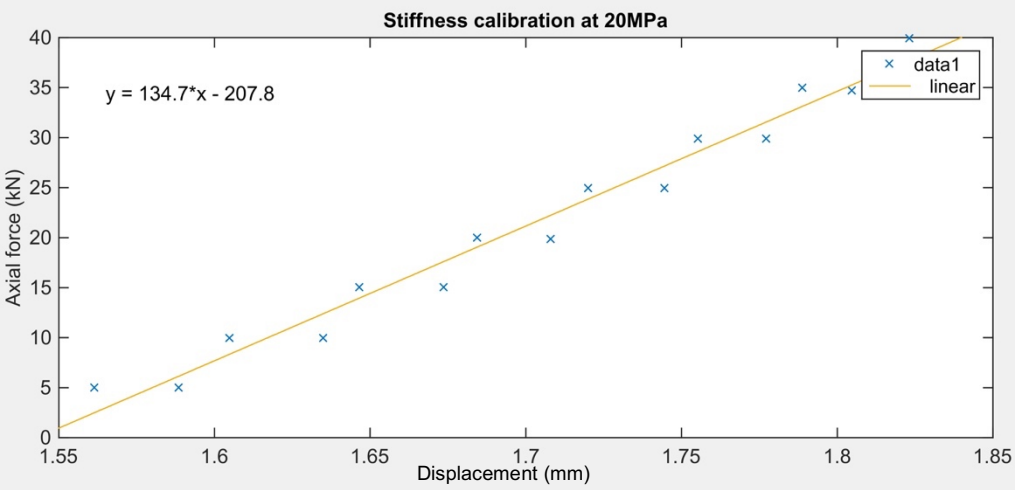

Figure 7.7 Stiffness calibration performed by C. Harbord at 20 MPa confining pressure and equilibrated force on 04/06/2015.

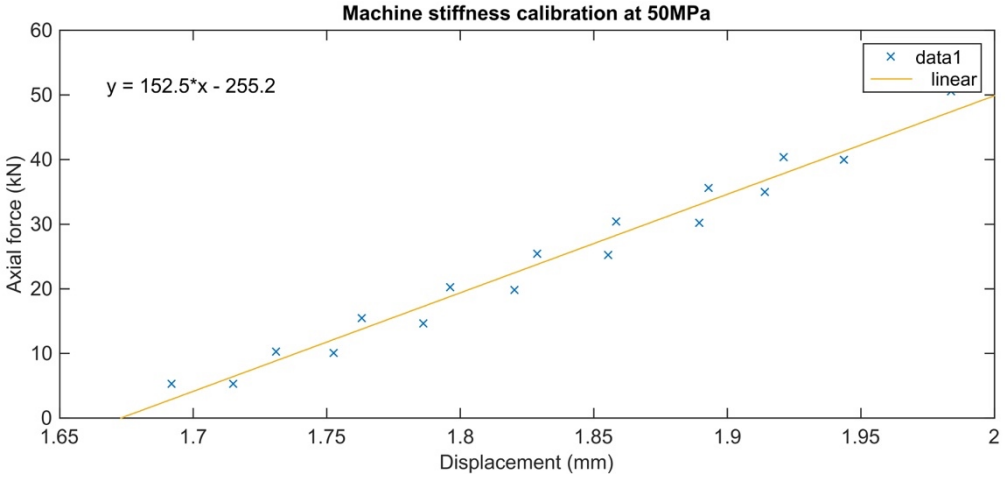

Figure 7.8 Stiffness calibration performed by C. Harbord at 50 MPa confining pressure and equilibrated force on 04/06/2015.

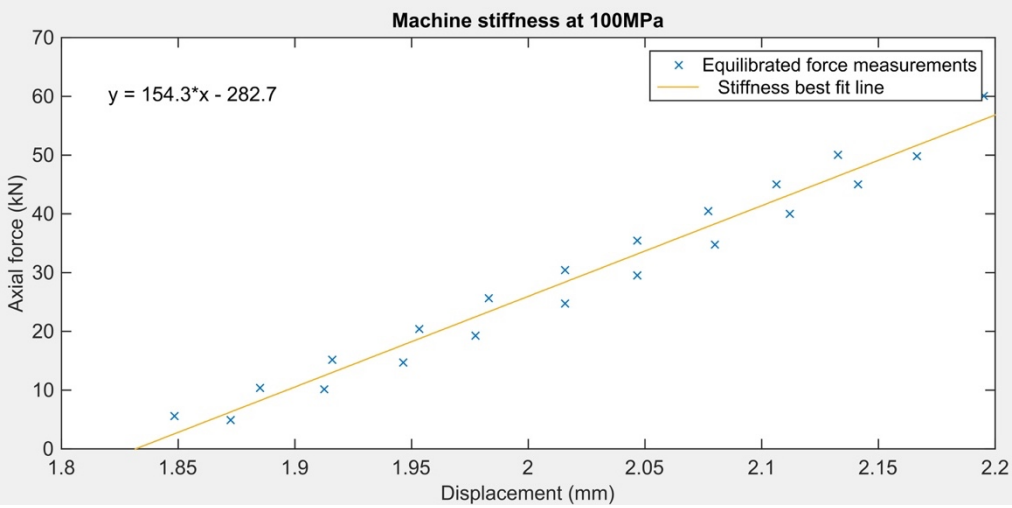

Figure 7.9 Stiffness calibration performed by C. Harbord at 50 MPa confining pressure and equilibrated force on 04/06/2015.

7.1.7 Voltage to velocity calibration

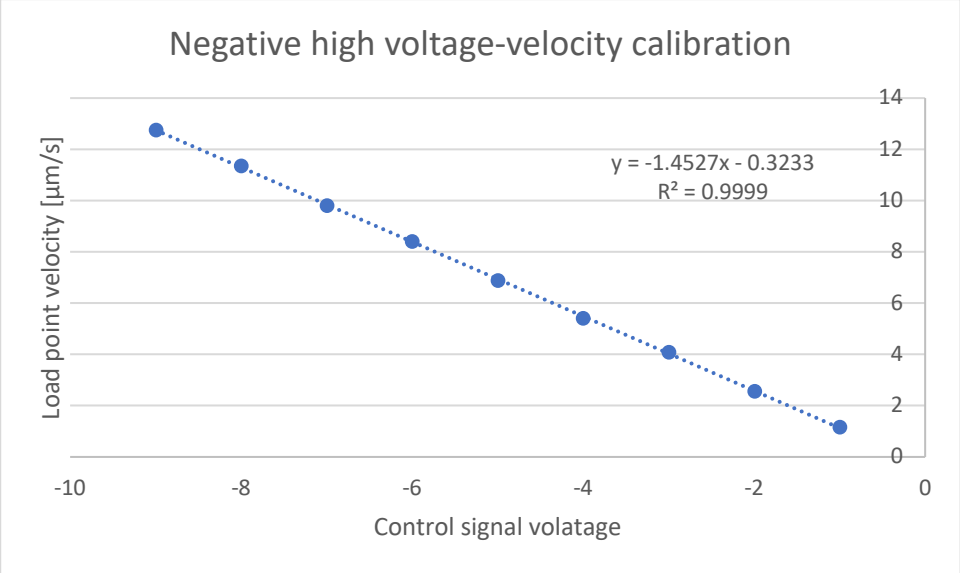

Figure 7.10 Load point velocity resulting from applying constant voltage (-9 to -1V) to servo control box, calibration performed by C. Harbord in 20/03/2015.

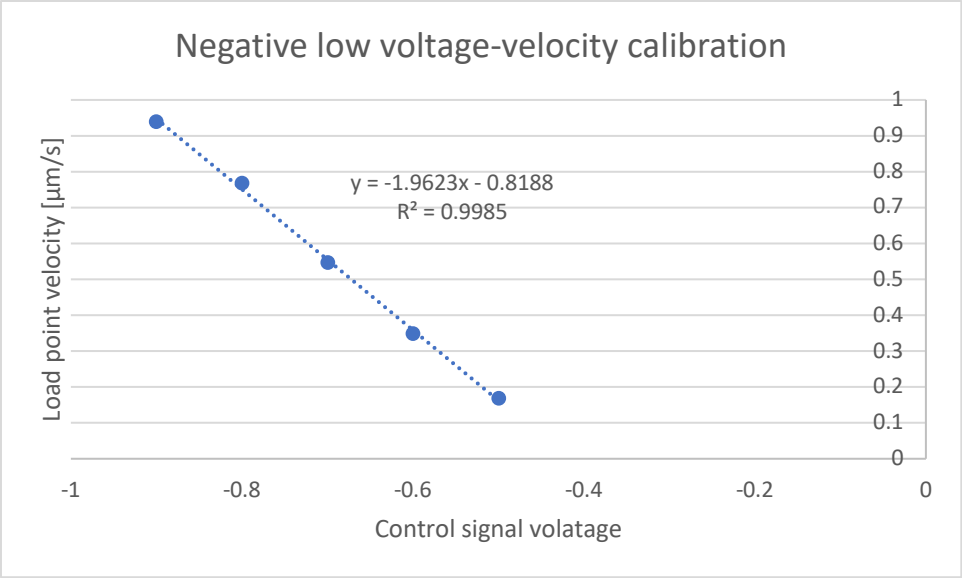

Figure 7.11 Load point velocity resulting from applying constant voltage (-0.9 to -0.5V) to servo control box, calibration performed by C. Harbord in 20/03/2015.

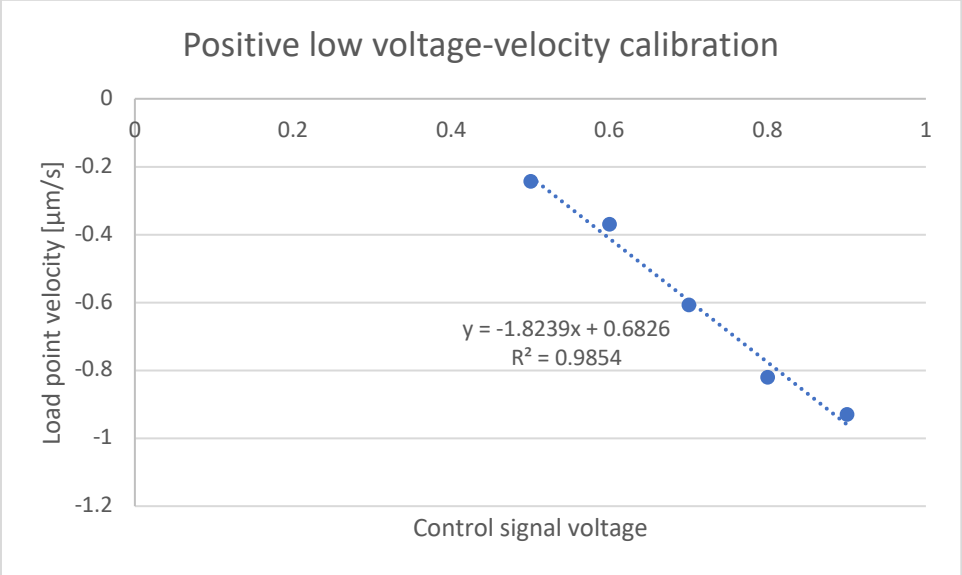

Figure 7.12 Load point velocity resulting from applying constant voltage (+0.5 to +0.9V) to servo control box, calibration performed by C. Harbord in 20/03/2015.

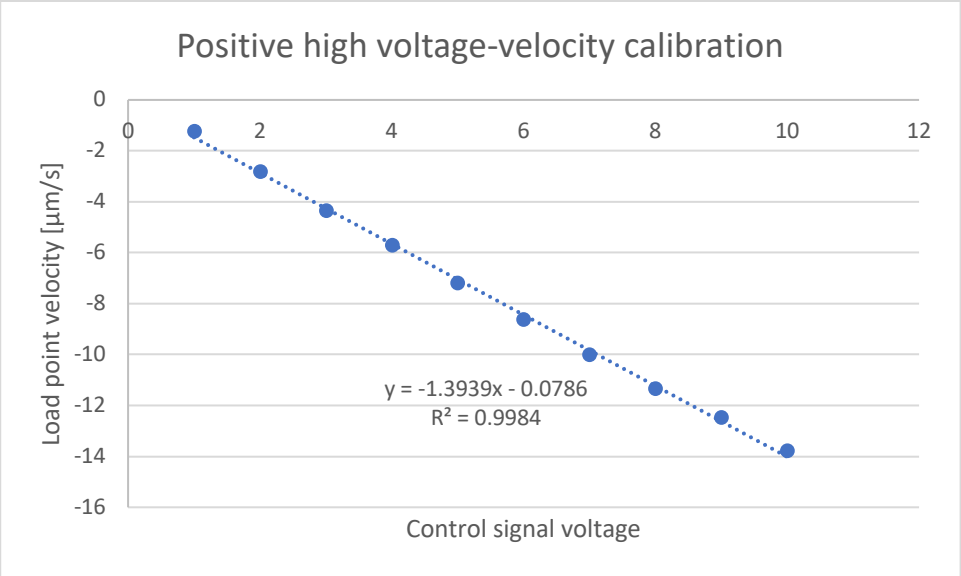

Figure 7.13 Load point velocity resulting from applying constant voltage (+1 to +10V) to servo control box, calibration performed by C. Harbord in 20/03/2015.

7.1.8 Stepwise velocity change from open loop servo control

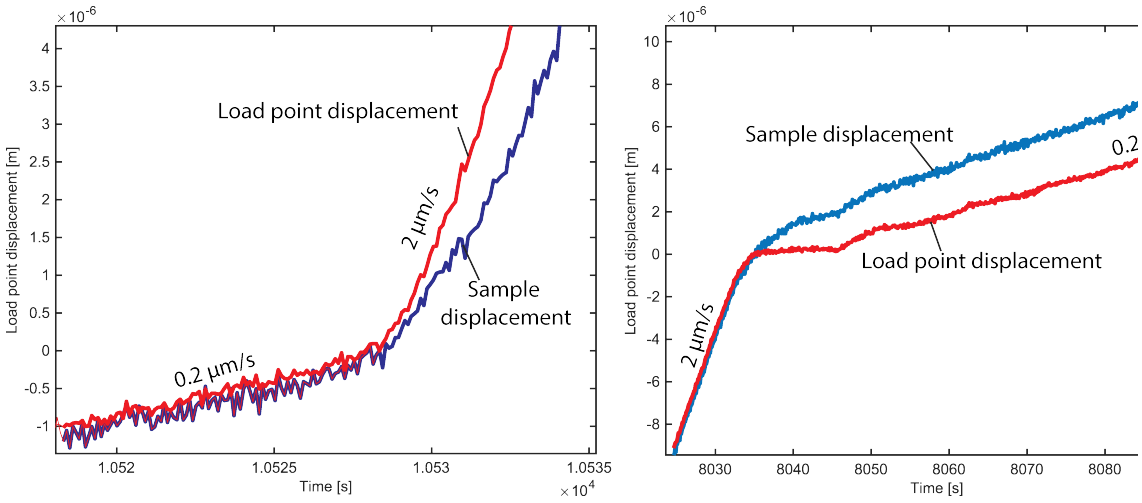

Figure 7.14 Control response of loading system and sample (obtained by removing stiffness) to step-wise change in sliding velocity for an experiment controlled using the PID loop in LabView, a) for a decrease in sliding velocity, b) for a decrease in sliding velocity.

7.1.9 Stepwise velocity change from closed loop control

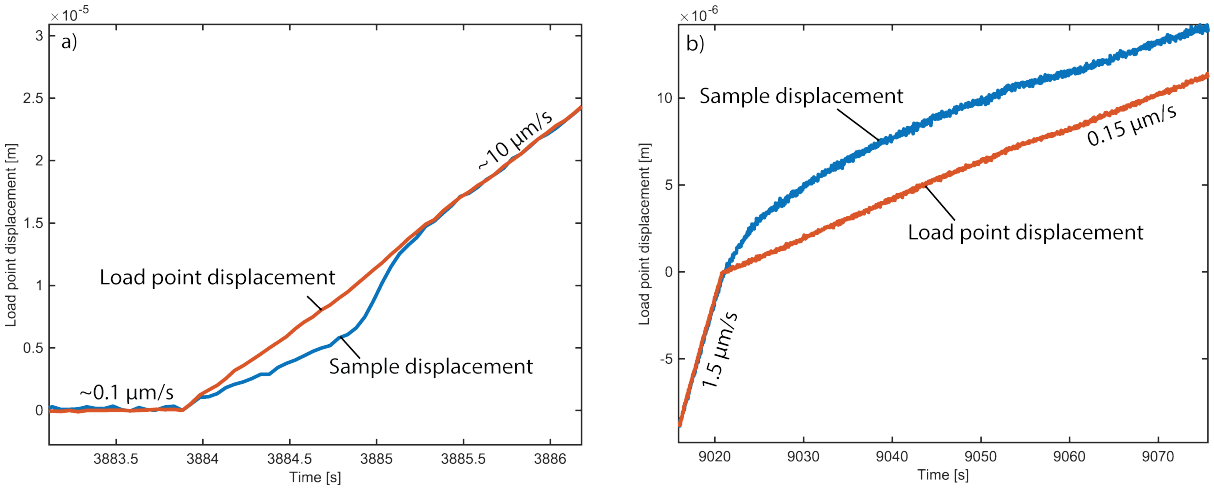

Figure 7.15 Control response of loading system and sample (obtained by removing stiffness) to step-wise change in sliding velocity for an experiment controlled using a constant voltage, a) for a decrease in sliding velocity, b) for a decrease in sliding velocity.

7.1.10 Choice and fit of state evolution laws

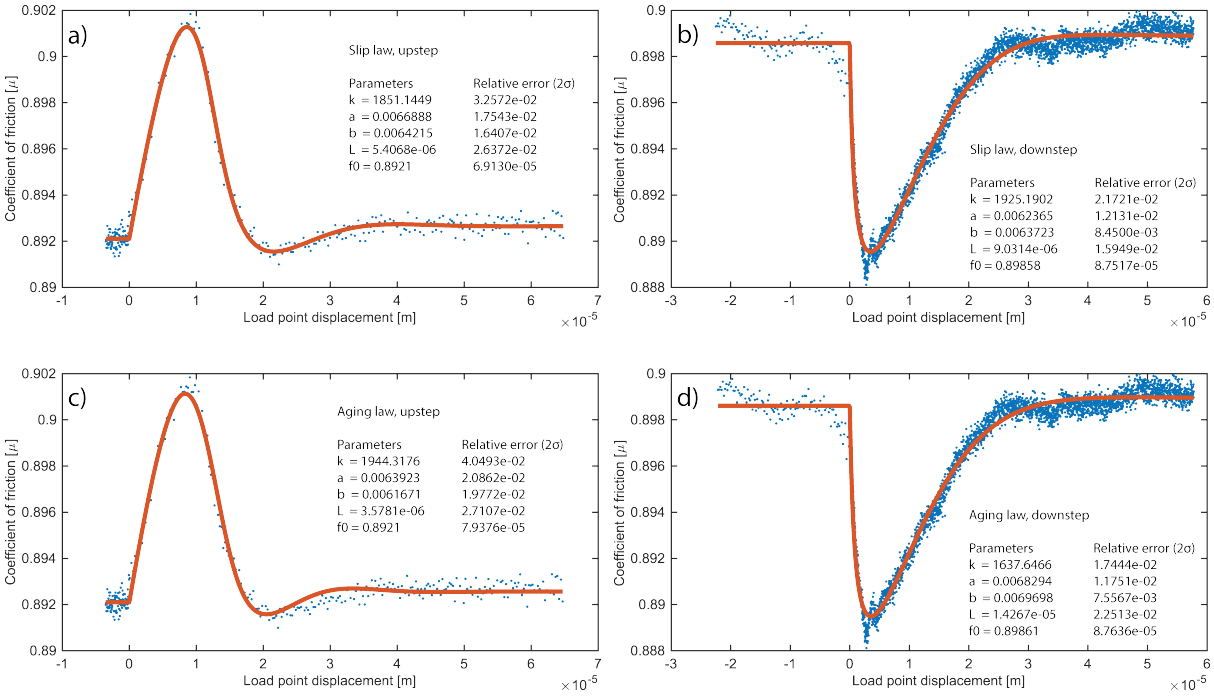

Figure 7.16 Comparison of velocity steps fitted with differing formulations of the state variable using FSS 7.0. The slip law is used to fit and upstep in a) and a downstep in b), whereas the aging is used to fit an upstep in c) and a downstep in d). Both show a good fit and low error; however, the slip law has a smaller upstep error, and is comparable on down stepping to the aging law. Therefore steps were fit with the slip law, in agreement with the results of (Bhattacharya et al., 2015).

7.1.11 Strain gauge calibration

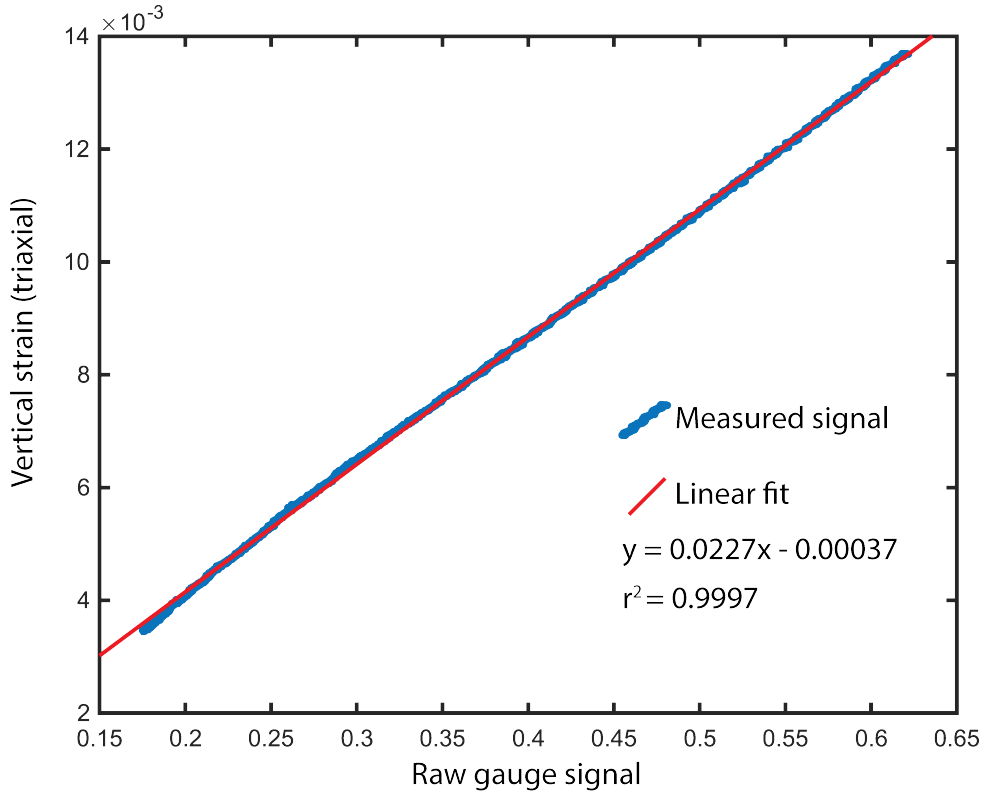

Figure 7.17 Strain gauge signal calibration against loading column in triaxial apparatus.

8 References

Abercrombie, R.E., and Rice, J.R., 2005, Can observations of earthquake scaling constrain slip weakening? Geophys. J. Int., v. 162, p. 406–424.

Alvarez, W., Lowrie, W., and Gimli, G., 1978, Upper Cretaceous palaeomagnetic stratigraphy at the mines of Moria (Umbrain Apennines, Italy): verification of the Gubbio section: v. 29.

Andrews, D.J., 1976, Rupture velocity of plane strain shear cracks: Journal of Geophysical Research, v. 81, p. 5679–5687, doi: 10.1029/JB081i032p05679.

Aochi, H., and Madariaga, R., 2003, The 1999 Izmit, Turkey, earthquake: Nonplanar fault structure, dynamic rupture process, and strong ground motion: Bulletin of the Seismological Society of America, v. 93, p. 1249–1266, doi: 10.1785/0120020167.

Archard, J.F., 1953, Contact and rubbing of flat surfaces: Journal of Applied Physics, v. 24, p. 981–988, doi: 10.1063/1.1721448.

Archard, J.F., 1959, The temperature of rubbing surfaces: Wear, v. 2, p. 438–455, doi: 10.1016/0043-1648(59)90159-0.

Barenblatt, G.I., 1962, The mathematical theory of equilibrium cracks in brittle fracture: Advances in applied mechanics, v. 7, p. 55–129.

Bedford, J.D., 2017, The kinetics and mechanics of a dehydrating system and the deformation of porous rock: PhD Thesis, University of Liverpool.

Beeler, N.M., and Tullis, T.E., 1996, Self-healing slip pulses in dynamic ruptures models due to velocity-dependent strength: Bull. Seismol. Soc. Am., v. 86, p. 1130–1148.

Beeler, N.M., Tullis, T.E., Blanpied, M.L., and Weeks, J.D., 1996, Frictional behavior of large displacement experimental faults: Journal of Geophysical Research: Solid Earth, v. 101, p. 8697–8715, doi: 10.1029/96JB00411.

Beeler, N.M., Tullis, T.E., and Goldsby, D.L., 2008, Constitutive relationships and physical basis of fault strength due to flash heating: Journal of Geophysical Research-Solid Earth, v. 113, p. 12, doi: 10.1029/2007jb004988.

Beeler, N.M., Tullis, T.E., and Weeks, J.D., 1994, The roles of time and displacement in the evolution effect in rock friction: Geophysical Research Letters, v. 21, p. 1987–1990, doi: 10.1029/94GL01599.

Bhattacharya, P., Rubin, A.M., Bayart, E., Savage, H.M., and Marone, C., 2015, Critical evaluation of state evolution laws in rate and state friction: Fitting large velocity steps in simulated fault gouge with time-, slip-, and stress-dependent constitutive laws: Journal of Geophysical Research: Solid Earth, v. 120, p. 6365–6385, doi: 10.1002/2015JB012437.

Bistacchi, A., Griffith, W.A., Smith, S.A.F., Di Toro, G., Jones, R., and Nielsen, S., 2011, Fault Roughness at Seismogenic Depths from LIDAR and Photogrammetric Analysis: Pure and Applied Geophysics, v. 168, p. 2345–2363, doi: 10.1007/s00024-011-0301-7.

Blanpied, M.L., Marone, C.J., Lockner, D.A., Byerlee, J.D., and King, D.P., 1998, Quantitative measure of the variation in fault rheology due to fluid-rock interactions: Journal of Geophysical Research: Solid Earth, v. 103, p. 9691–9712, doi: 10.1029/98JB00162.

Blenkinsop, T.G., 1991, Cataclasis and processes of particle size reduction: Pure and Applied Geophysics, v. 136, p. 59–86, doi: 10.1007/BF00878888.

Bohnhoff, M., Dresen, G., Ellsworth, W.L., and Ito, H., 2009, Passive Seismic Monitoring of Natural and Induced Earthquakes: Case Studies, Future Directions and Socio-Economic Relevance: New Frontiers in Integrated Solid Earth Sciences, p. 261–285, doi: 10.1007/978-90-481-2737-5_7.

Boneh, Y., and Reches, Z., 2018, Geotribology - Friction, wear, and lubrication of faults: Tectonophysics, p. 1–11, doi: 10.1016/j.tecto.2017.11.022.

Boneh, Y., Sagy, A., and Reches, Z., 2013, Frictional strength and wear-rate of carbonate faults during high-velocity, steady-state sliding: Earth and Planetary Science Letters, v. 381, p. 127–137, doi: 10.1016/j.epsl.2013.08.050.

Borri-Brunetto, M., Chiaia, B., and Ciavarella, M., 2001, Incipient sliding of rough surfaces in contact: A multiscale numerical analysis: Computer Methods in Applied Mechanics and Engineering, v. 190, p. 6053–6073, doi: 10.1016/S0045-

7825(01)00218-3.

Bos, B., Peach, C.J., and Spiers, C.J., 2000, Slip behavior of simulated gouge-bearing faults under conditions favoring pressure solution: Journal of Geophysical Research: Solid Earth, v. 105, p. 16699–16717, doi: 10.1029/2000JB900089.

Bouchon, M., Bouin, M.P., Karabulut, H., Toksoz, M.N., Dietrich, M., and Rosakis, A.J., 2001, How fast is rupture during an earthquake? New insights from the 1999 Turkey earthquakes: Geophysical Research Letters, v. 28, p. 2723–2726, doi: 10.1029/2001gl013112.

Bouchon, M., Durand, V., Marsan, D., Karabulut, H., and Schmittbuhl, J., 2013, The long precursory phase of most large interplate earthquakes: Nature Geoscience, v. 6, p. 299–302, doi: 10.1038/ngeo1770.

Bouchon, M., Karabulut, H., Aktar, M., Özalaybey, S., Schmittbuhl, J., and Bouin, M.-P., 2011, Extended Nucleation of the 1999 Mw 7.6 Izmit Earthquake: Science, v. 331, p. 877–880, doi: 10.1126/science.1197341.

Brace, W.F., and Byerlee, J.D., 1966, Stick-Slip as a Mechanism for Earthquakes: Science, v. 153, p. 990–992, doi: 10.1126/science.153.3739.990.

Brace, W.F., and Kohlstedt, D.L., 1980, Limits on lithospheric stress imposed by laboratory experiments: Journal of Geophysical Research: Solid Earth, v. 85, p. 6248–6252.

Brantut, N., Han, R., Shimamoto, T., Findling, N., and Schubnel, A., 2010, Fast slip with inhibited temperature rise due to mineral dehydration: Evidence from experiments on gypsum: Geology, v. 39, p. 59–62, doi: 10.1130/g31424.1.

Brantut, N., Passelègue, F.X., Deldicque, D., Rouzaud, J.-N., and Schubnel, A., 2016, Dynamic weakening and amorphization in serpentinite during laboratory earthquakes: Geology, v. 44, p. 607–610, doi: 10.1130/G37932.1.

Brantut, N., and Viesca, R.C., 2015, Earthquake nucleation in intact or healed rocks: Journal of Geophysical Research: Solid Earth, v. 120, p. 191–209, doi: 10.1002/2014JB011518.

Brantut, N., and Viesca, R.C., 2017, The fracture energy of ruptures driven by flash

heating: Geophysical Research Letters, v. 44, p. 6718–6725, doi: 10.1002/2017GL074110.

Brodsky, E.E., Gilchrist, J.J., Sagy, A., and Collettini, C., 2011, Faults smooth gradually as a function of slip: Earth and Planetary Science Letters, v. 302, p. 185–193, doi: 10.1016/j.epsl.2010.12.010.

Brodsky, E.E., Kirkpatrick, J.D., and Candela, T., 2016, Constraints from fault roughness on the scale-dependent strength of rocks: Geology, v. 44, p. 19–22, doi: 10.1130/G37206.1.

Broz, M.E., Cook, R.F., and Whitney, D.L., 2006, Microhardness, toughness, and modulus of Mohs scale minerals: American Mineralogist, v. 91, p. 135–142, doi: 10.2138/am.2006.1844.

Brune, J.N., 1991, Seismic source dynamics, radiation and stress: Reviews of geophysics, supplement, U.S. National Report to international union of geodesy and geophysics, p. 688–699.

Bullock, R.J., De Paola, N., Holdsworth, R.E., and Trabucho-Alexandre, J., 2014, Lithological controls on the deformation mechanisms operating within carbonate-hosted faults during the seismic cycle: Journal of Structural Geology, v. 58, p. 22–42, doi: 10.1016/j.jsg.2013.10.008.

Bürgmann, R., 2018, The geophysics, geology and mechanics of slow fault slip: Earth and Planetary Science Letters, v. 495, p. 112–134, doi: 10.1016/j.epsl.2018.04.062.

Burov, E.B., 2011, Rheology and strength of the lithosphere: Marine and Petroleum Geology, v. 28, p. 1402–1443, doi: 10.1016/j.marpetgeo.2011.05.008.

Byerlee, J.D., 1978, Friction of Rocks: Pure and Applied Geophysics, v. 116, p. 615–626.

Byerlee, J., Mjachkin, V., Summers, R., and Voevoda, O., 1978, Structures developed in fault gouge during stable sliding and stick-slip: Tectonophysics, v. 44, p. 161–171, doi: 10.1016/0040-1951(78)90068-9.

Byerlee, J., and Summers, R., 1976, A note on the effect of fault gouge thickness on fault stability: International Journal of Rock Mechanics and Mining Sciences and, v. 13, p. 35–36, doi: 10.1016/0148-9062(76)90226-6.

Campillo, M., and Ionescu, I.R., 1997, Initiation of antiplane shear instability under slip dependent friction: Journal of Geophysical Research: Solid Earth, v. 102, p. 20363–20371, doi: 10.1029/97JB01508.

Candela, T., and Brodsky, E.E., 2016, The minimum scale of grooving on faults: Geology, v. 44, p. 603–606.

Candela, T., Renard, F., Klinger, Y., Mair, K., Schmittbuhl, J., and Brodsky, E.E., 2012, Roughness of fault surfaces over nine decades of length scales: Journal of Geophysical Research: Solid Earth, v. 117, p. n/a–n/a, doi: 10.1029/2011JB009041.

Carpenter, B.M., Collettini, C., Viti, C., and Cavallo, A., 2016, The influence of normal stress and sliding velocity on the frictional behaviour of calcite at room temperature: Insights from laboratory experiments and microstructural observations: Geophysical Journal International, v. 205, p. 548–561, doi: 10.1093/gji/ggw038.

Carpenter, B.M., Scuderi, M.M., Collettini, C., and Marone, C., 2014, Frictional heterogeneities on carbonate-bearing normal faults: Insights from the Monte Maggio Fault, Italy: Journal of Geophysical Research: Solid Earth, p. n/a-n/a, doi: 10.1002/2014JB011337.

Chen, J., Niemeijer, A.R., and Spiers, C.J., 2017, Microphysically Derived Expressions for Rate-and-State Friction Parameters, a, b, and Dc: Journal of Geophysical Research: Solid Earth, v. 122, p. 9627–9657, doi: 10.1002/2017JB014226.

Chen, J., and Spiers, C.J., 2016, Rate and state frictional and healing behavior of carbonate fault gouge explained using microphysical model: Journal of Geophysical Research: Solid Earth, v. 121, p. 8642–8665, doi: 10.1002/2016JB013470.

Chester, J.S., Chester, F.M., and Kronenberg, A.K., 2005, Fracture surface energy of the Punchbowl fault, San Andreas system: Nature, v. 437, p. 133–136, doi: 10.1038/nature03942.

Chester, F.M., and Higgs, N.G., 1992, Multimechanism friction constitutive model for ultrafine quartz gouge at hypocentral conditions: Journal of Geophysical Research: Solid Earth, v. 97, p. 1859–1870, doi: 10.1029/91JB02349.

Cochard, A., and Madariaga, R., 1996, Complexity of seismicity due to highly rate-

dependent friction: Journal of Geophysical Research: Solid Earth, v. 101, p. 25,321-325,336.

Cochard, A., and Madariaga, R., 1994, Dynamic Faulting Under Rate-Dependent Friction: Pure and Applied Geophysics, v. 142, p. 419–445.

Cochard, A., and Rice, J., 1997, Mode of rupture, self-healing pulse versus enlarging shear crack, for a velocity weakening fault in a 3D solid: EOS Transactions, v. 78, p. F472.

Collettini, C., Barchi, M.R., Chiaraluce, L., Mirabella, F., and Pucci, S., 2003, The Gubbio fault: Can different methods give pictures of the same object? Journal of Geodynamics, v. 36, p. 51–66, doi: 10.1016/S0264-3707(03)00038-3.

Dieterich, J.H., 1992, Earthquake nucleation on faults with rate-and state-dependent strength: Tectonophysics, v. 211, p. 115–134, doi: 10.1016/0040-1951(92)90055-B.

Dieterich, J.H., 1979a, Modeling of rock friction. 2: Simulation of preseismic slip: Journal of Geophysical Research: Solid Earth, v. 84, p. 2169–2175, doi: 10.1029/JB084iB05p02169.

Dieterich, J.H., 1979b, Modeling of rock friction .1. Experimental results and constitutive equations: Journal of Geophysical Research, v. 84, p. 2161–2168, doi: 10.1029/JB084iB05p02161.

Dieterich, J.H., 1979c, Modeling of rock friction 1. Experimental results and constituve equations: Journal of Geophysical Research: Solid Earth, v. 84, p. 2161–2168, doi: 10.1007/BF00876539.

Dieterich, J.H., and Kilgore, B.D., 1994, Direct observation of frictional contacts - new insights for state-dependent properties: Pure and Applied Geophysics, v. 143, p. 283–302, doi: 10.1007/bf00874332.

Dieterich, J.H., and Kilgore, B.D., 1996a, Imaging surface contacts: power law contact distributions and contact stresses in quartz, calcite, glass and acrylic plastic: Tectonophysics, v. 256, p. 219–239, doi: 10.1016/0040-1951(95)00165-4.

Dieterich, J.H.H., and Kilgore, B., 1996b, Implications of fault constitutive properties for earthquake prediction: Proceedings of the National Academy of Sciences of the

United States of America, v. 93, p. 3787–3794, doi: 10.1073/pnas.93.9.3787.

Doan, M.L., and Gary, G., 2009, Rock pulverisation at high strain rate near the san andreas fault: Nature Geoscience, v. 2, p. 709–712.

Dodge, D.A., Beroza, G.C., and Ellsworth, W.L., 1995, Foreshock sequence of the 1992 Landers, California, earthquake and its implications for earthquake nucleation: Journal of Geophysical Research, v. 100, p. 9865–9880, doi: 10.1029/95JB00871.

Dor, O., Ben-Zion, Y., Rockwell, T.K., and Brune, J., 2006, Pulverized rocks in the Mojave section of the San Andreas Fault Zone: Earth and Planetary Science Letters, v. 245, p. 642–654, doi: 10.1016/j.epsl.2006.03.034.

Dunham, E.M., and Archuleta, R.J., 2004, Evidence for a supershear transient during the 2002 Denali Fault earthquake: Bulletin of the Seismological Society of America, v. 94, p. 256–268.

Dunham, E.M., Favreau, P., and Carlson, J.M., 2003, A supershear transition mechanism for cracks: Science, v. 299, p. 1557–1559, doi: 10.1126/science.1080650.

Ellsworth, W.L., and Beroza, G.C., 1995, Seismic evidence for an earthquake nucleation phase: Science, v. 268, p. 851–855.

Ellsworth, W.L., and Bulut, F., 2018, Nucleation of the 1999 Izmit earthquake by a triggered cascade of foreshocks: Nature Geoscience, v. 0, doi: 10.1038/s41561-018-0145-1.

Fang, Z., and Dunham, E.M., 2013, Additional shear resistance from fault roughness and stress levels on geometrically complex faults: Journal of Geophysical Research: Solid Earth, v. 118, p. 3642–3654, doi: 10.1002/jgrb.50262.

Faulkner, D.R., Jackson, C.A.L., Lunn, R.J., Schlische, R.W., Shipton, Z.K., Wibberley, C.A.J., and Withjack, M.O., 2010, A review of recent developments concerning the structure, mechanics and fluid flow properties of fault zones: Journal of Structural Geology, v. 32, p. 1557–1575, doi: 10.1016/j.jsg.2010.06.009.

Faulkner, D.R., Mitchell, T.M., Behnsen, J., Hirose, T., and Shimamoto, T., 2011, Stuck in the mud? Earthquake nucleation and propagation through accretionary forearcs: Geophys. Res. Lett., v. 38, p. L18303, doi: 10.1029/2011GL048552.

Fondriest, M., Smith, S.A.F.F., Candela, T., Nielsen, S.B., Mair, K., Toro, G. Di, and Di Toro, G., 2013, Mirror-like faults and power dissipation during earthquakes: Geology, v. 41, p. 1175–1178, doi: 10.1130/G34641.1.

Fredrich, J.T., Evans, B., and Wong, T.-F., 1989, Micromechanics of the brittle to plastic transition in Carrara marble: Journal of Geophysical Research: Solid Earth, v. 94, p. 4129–4145, doi: 10.1029/JB094iB04p04129.

Fulton, P.M., Brodsky, E.E., Kano, Y., Mori, J., Chester, F., Ishikawa, T., Harris, R.N., Lin, W., Eguchi, N., Toczko, S., Expedition 343 343T, and Scientists, K.-08, 2013, Low Coseismic Friction on the Tohoku-Oki Fault Determined from Temperature Measurements: Science, v. 342, p. 1214–1217, doi: 10.1126/science.1243641.

Goldsby, D.L., and Tullis, T.E., 2011, Flash Heating Leads to Low Frictional Strength of Crustal Rocks at Earthquake Slip Rates: Science, v. 334, p. 216–218, doi: 10.1126/science.1207902.

Goldsworthy, M., Jackson, J., and Haines, a J., 2002, The continuity of active fault systems in Greece: Geophysical Journal International, v. 148, p. 596–618.

Gratier, J., Dysthe, D.K., and Renard, F., 2013, The role of pressure solution creep in the ductility of the Earth's upper crust: Advances in Geophysics, v. 54, p. 1–112, doi: 10.1016/B978-0-12-380940-7.00002-0.

Griffith, A.A., 1921, The Phenomena of Rupture and Flow in Solids: Philosophical Transactions of the Royal Society of London Series A, v. 221, p. 163–198, doi: 10.1098/rsta.1921.0006.

Gu, Y., and Wong, T., 1991a, Effects of loading velocity, stiffness, and inertia on the dynamics of a single degree of freedom Spring-Slider System: Journal of Geophysical Research: Solid Earth, v. 96, p. 21677–21691, doi: 10.1029/91JB02271.

Gu, Y., and Wong, T.-F., 1991b, Effects of sliding velocity, stiffness, and inertia an the dynamics of a single degrees of freedom spring-slider system: Journal of Geophysical Research: Solid Earth, v. 96, p. 21,621-677,691.

Han, R., Hirose, T., and Shimamoto, T., 2010, Strong velocity weakening and powder

lubrication of simulated carbonate faults at seismic slip rates: Journal of Geophysical Research-Solid Earth, v. 115, p. 23, doi: 10.1029/2008jb006136.

Han, R., Shimamoto, T., Hirose, T., Ree, J.H., and Ando, J., 2007, Ultralow friction of carbonate faults caused by thermal decomposition: Science, v. 316, p. 878–881, doi: 10.1126/science.1139763.

Hansen, A., Schmittbuhl, J., Batrouni, G.G., and de Oliveira, F.A., 2000, Normal stress distribution of rough surfaces in contact: Geophys. Res. Lett., v. 27, p. 3639–3642, http://dx.doi.org/10.1029/2000GL011757.

Harbord, C.W.A., Nielsen, S.B., De Paola, N., and Holdsworth, R.E., 2017, Earthquake nucleation on rough faults: Geology, v. 45, p. 931–934, doi: 10.1130/G39181.1.

Hayward, K.S., Cox, S.F., Gerald, J.D.F., Slagmolen, B.J.J., Shaddock, D.A., Forsyth, P.W.F., Salmon, M.L., and Hawkins, R.P., 2016, Mechanical amorphization, flash heating, and frictional melting: Dramatic changes to fault surfaces during the first millisecond of earthquake slip: Geology, v. 44, p. 1043–1046, doi: 10.1130/G38242.1.

Heaton, T.H., 1990, Evidence for and implications of self-healing pulsed of slip in earthquake rupture: Physics of the Earth and Planetary Interiors, v. 64, p. 1–20, doi: 10.1016/0031-9201(90)90002-f.

Ida, Y., 1972, Cohesive force across the tip of a longitudinal-shear crack and Griffith's specific surface energy: Journal of Geophysical Research: Solid Earth, v. 77, p. 3796–3805.

Ikari, M.J., Marone, C., and Saffer, D.M., 2011, On the relation between fault strength and frictional stability: Geology, v. 39, p. 83–86, doi: 10.1130/G31416.1.

Ikari, M.J., Saffer, D.M., and Marone, C., 2009, Frictional and hydrologic properties of clay-rich fault gouge: Journal of Geophysical Research: Solid Earth, v. 114, p. 1–18, doi: 10.1029/2008JB006089.

Irwin, G.R., 1957, Analysis of stresses and strains near the end of a crack traversing a plate: Journal of Applied Mechanics, v. 24, p. 361–364.

Jackson, J., McKenzie, D., Priestley, K., and Emmerson, B., 2008, New views on the

structure and rheology of the lithosphere: Journal of the Geological Society, v. 165, p. 453–465, doi: 10.1144/0016-76492007-109.

Jaeger, J.C., Cook, N.G.W., and Zimmerman, R., 2009, Fundamentals of rock mechanics: John Wiley & Sons.

Johnson, T.L., and Scholz, C.H., 1976, Dynamic properties of stick-slip friction of rock: Journal of Geophysical Research, v. 81, p. 881–888, doi: 10.1029/JB081i005p00881.

Kanamori, H., and Anderson, D.L., 1975, Theoritical basis of some empirical relations in seismology: Bulletin of the Seismological Society of America, v. 65, p. 1073–1095.

Kanamori, H., and Brodsky, E.E., 2004, The physics of earthquakes: Reports on Progress in Physics, v. 67, p. 1429–1496, doi: 10.1088/0034-4885/67/8/r03.

Kaneko, Y., Nielsen, S.B., and Carpenter, B.M., 2016, The onset of laboratory earthquakes explained by nucleating rupture on a rate-and-state fault: Journal of Geophysical Research: Solid Earth, v. 121, doi: 10.1002/2016JB013143.

Karato, S.-I., 2008, Deformation of Earth Materials: An Introduction to the Rheology of Solid Earth: Cambridge University Press.

Kirkpatrick, J.D., and Brodsky, E.E., 2014, Slickenline orientations as a record of fault rock rheology: Earth and Planetary Science Letters, v. 408, p. 24–34, doi: 10.1016/j.epsl.2014.09.040.

Kostrov, B. V, 1964, Self-similar problems of propagation of shear cracks: J. Appl. Math. Mech., v. 28, p. 1077–1087, doi: http://dx.doi.org/10.1016/0021-8928(64)90010-3.

Latour, S., Schubnel, A., Nielsen, S., Madariaga, R., and Vinciguerra, S., 2013, Characterization of nucleation during laboratory earthquakes: Geophysical Research Letters, v. 40, p. 5064–5069, doi: 10.1002/grl.50974.

Lay, T., Kanamori, H., Ammon, C.J., Nettles, M., Ward, S.N., Aster, R.C., Beck, S.L., Bilek, S.L., Brudzinski, M.R., Butler, R., DeShon, H.R., Ekstrom, G., Satake, K., and Sipkin, S., 2005, The great Sumatra-Andaman earthquake of 26 December 2004: Science, v. 308, p. 1127–1133, doi: 10.1126/science.1112250.

Leclère, H., Faulkner, D., Wheeler, J., and Mariani, E., 2016, Permeability control on transient slip weakening during gypsum dehydration: Implications for earthquakes in subduction zones: Earth and Planetary Science Letters, v. 442, p. 1–12, doi: http://dx.doi.org/10.1016/j.epsl.2016.02.015.

Leeman, J.R., Saffer, D.M., Scuderi, M.M., and Marone, C., 2016, Laboratory observations of slow earthquakes and the spectrum of tectonic fault slip modes: Nature Communications, v. 7, http://dx.doi.org/10.1038/ncomms11104.

Logan, J.M., Dengo, C.A., Higgs, N.G., and Wang, Z.Z., 1992, Chapter 2: Fabrics of Experimental Fault Zones: Their Development and Relationship to Mechanical Behavior: v. 51, 33-67 p., doi: https://doi.org/10.1016/S0074-6142(08)62814-4.

Logan, J.M., and Rauenzahn, K.A., 1987, Frictional dependence of gouge mixtures of quartz and montmorillonite on velocity, composition and fabric: Tectonophysics, v. 144, p. 87–108, doi: 10.1016/0040-1951(87)90010-2.

Marone, C., 1998, Laboratory-derived friction laws and their application to seismic faulting: Annual Review of Earth and Planetary Sciences, v. 26, p. 643–696, doi: 10.1146/annurev.earth.26.1.643.

Marone, C.J., and Cox, S.J.D., 1994, Scaling of rock friction constitutive parameters: The effects of surface roughness and cumulative offset on friction of gabbro: Pure and Applied Geophysics, v. 143, p. 359–385, doi: 10.1007/BF00874335.

Marone, C., and Kilgore, B., 1993, Scaling of the critical slip distance for seismic faulting with shear strain in fault zones: Nature, v. 362, p. 618–621, doi: 10.1038/362618a0.

McLaskey, G.C., and Kilgore, B.D., 2013, Foreshocks during the nucleation of stick-slip instability: Journal of Geophysical Research: Solid Earth, v. 118, p. 2982–2997, doi: 10.1002/jgrb.50232.

McLaskey, G.C., and Lockner, D.A., 2014, Preslip and cascade processes initiating laboratory stick slip: Journal of Geophysical Research: Solid Earth, v. 119, p. 6323–6336, doi: 10.1002/2014JB011220.

Mello, M., Bhat, H.S., Rosakis, A.J., and Kanamori, H., 2011, Identifying the unique ground motion signatures of supershear earthquakes: Theory and experiments:

Tectonophysics Special Edition on Supershear Ruptures (Ed: S. Das and M. Bouchon), v. 493, p. 297–326, doi: 10.1016/j.tecto.2010.07.003.

Mitchell, T.M., and Faulkner, D.R., 2008, Experimental measurements of permeability evolution during triaxial compression of initially intact crystalline rocks and implications for fluid flow in fault zones: Journal of Geophysical Research, v. 113, p. B11412, doi: 10.1029/2008JB005588.

Mitchell, T.M., and Faulkner, D.R., 2009, The nature and origin of off-fault damage surrounding strike-slip fault zones with a wide range of displacements: A field study from the Atacama fault system, northern Chile: Journal of Structural Geology, v. 31, p. 802–816, doi: 10.1016/j.jsg.2009.05.002.

Nadeau, R.M., and Johnson, L.R., 1998, Seismological studies at Parkfield VI: moment release rates and estimates of source parameters for small repeating earthquakes: Bulletin of the Seismological Society of America, v. 88, p. 790–814.

Nagata, K., Nakatani, M., and Yoshida, S., 2012, A revised rate- and state-dependent friction law obtained by constraining constitutive and evolution laws separately with laboratory data: Journal of Geophysical Research: Solid Earth, v. 117, p. 1–17, doi: 10.1029/2011JB008818.

Nichols, G., 2009, Sedimentology and stratigraphy: v. 53, 419 p., doi: 10.1017/CBO9781107415324.004.

Nielsen, S., and Madariaga, R., 2003, On the self-healing fracture mode: Bulletin of the Seismological Society of America, v. 93, p. 2375–2388, doi: 10.1785/0120020090.

Nielsen, S., Spagnuolo, E., Smith, S.A.F., Violay, M., Di Toro, G., and Bistacchi, A., 2016, Scaling in natural and laboratory earthquakes: Geophysical Research Letters, v. 43, p. 1504–1510, doi: 10.1002/2015GL067490.

Nielsen, S., Taddeucci, J., and Vinciguerra, S., 2010, Experimental observation of stick-slip instability fronts: Geophysical Journal International, v. 180, p. 697–702, doi: 10.1111/j.1365-246X.2009.04444.x.

Niemeijer, A.R., and Spiers, C.J., 2007, A microphysical model for strong velocity weakening in phyllosilicate-bearing fault gouges: Journal of Geophysical Research:

Solid Earth, v. 112, p. 1–12, doi: 10.1029/2007JB005008.

Niemeijer, A., Di Toro, G., Nielsen, S., and Di Felice, F., 2011, Frictional melting of gabbro under extreme experimental conditions of normal stress, acceleration, and sliding velocity: Journal of Geophysical Research, v. 116, p. B07404, doi: 10.1029/2010JB008181.

Noda, H., and Lapusta, N., 2013, Stable creeping fault segments can become destructive as a result of dynamic weakening: Nature, v. 493, p. 518–521, doi: 10.1038/nature11703.

Noda, H., and Shimamoto, T., 2010, A rate- and state-dependent ductile flow law of polycrystalline halite under large shear strain and implications for transition to brittle deformation: Geophysical Research Letters, v. 37, p. n/a-n/a, doi: 10.1029/2010GL042512.

Noda, H., and Shimamoto, T., 2009, Constitutive properties of clayey fault gouge from the Hanaore fault zone, southwest Japan: Journal of Geophysical Research: Solid Earth, v. 114, p. B04409, doi: 10.1029/2008JB005683.

Ohnaka, M., 2003, A constitutive scaling law and a unified comprehension for frictional slip failure, shear fracture of intact rock, and earthquake rupture: Journal of Geophysical Research: Solid Earth, v. 108, p. 21, doi: 10.1029/2000JB000123.

Ohnaka, M., and Kuwahara, Y., 1990, Characteristic features of local breakdown near a crack-tip in the transition zone from nucleation to unstable rupture during stick-slip shear failure: Tectonophysics, v. 175, p. 197–220, doi: 10.1016/0040-1951(90)90138-X.

Ohnaka, M., and Shen, L.F., 1999, Scaling of the shear rupture process from nucleation to dynamic propagation: Implications of geometric irregularity of the rupturing surfaces: Journal of Geophysical Research: Solid Earth, v. 104, p. 817–844, doi: 10.1029/1998JB900007.

Okubo, P.G., and Dieterich, J.H., 1984, Effects of physical fault properties on frictional instabilities produced on simulated faults: Journal of Geophysical Research: Solid Earth, v. 89, p. 5817–5827, doi: 10.1029/JB089iB07p05817.

Palmer, A.C., and Rice, J., 1973, The growth of slip surfaces in the progressive failure of over-consolidated clay: Proc. Roy. Soc. Lond., v. 332, p. 527–548.

De Paola, N., Hirose, T., Mitchell, T., Di Toro, G., Viti, C., and Shimamoto, T., 2011, Fault lubrication and earthquake propagation in thermally unstable rocks: Geology, v. 39, p. 35–38, doi: 10.1130/G31398.1.

De Paola, N., Holdsworth, R.E., Viti, C., Collettini, C., and Bullock, R., 2015, Can grain size sensitive flow lubricate faults during the initial stages of earthquake propagation? Earth and Planetary Science Letters, v. 431, p. 48–58, doi: 10.1016/j.epsl.2015.09.002.

Passelègue, F.X., Schubnel, A., Nielsen, S., Bhat, H.S., Deldicque, D., and Madariaga, R., 2016, Dynamic rupture processes inferred from laboratory microearthquakes: Journal of Geophysical Research: Solid Earth, v. 121, p. 4343–4365, doi: 10.1002/2015JB012694.

Passelègue, F.X., Schubnel, A., Nielsen, S., Bhat, H.S., Madariaga, R.R., Passelegue, F.X., Schubnel, A., Nielsen, S., Bhat, H.S., and Madariaga, R.R., 2013, From sub-Rayleigh to supershear ruptures during stick-slip experiments on crustal rocks: Science, v. 340, p. 1208–1211, doi: 10.1126/science.1235637.

Paterson, M.S., and Wong, T.-F., 2005, Experimental Rock Deformation- The Brittle Field: 87 p.

Perrin, G., Rice, J.R., and Zheng, G., 1995, Self-healing slip pulse on a frictional surface: Journal of the Mechanics and Physics of Solids, v. 43, p. 1461–1495, doi: 10.1016/0022-5096(95)00036-I.

Persson, B., 2013, Sliding friction: physical principles and applications: Springer Science & Business Media.

Poirier, J.-P., 1985, Creep of Crystals: High-Temperature Deformation Processes in Metals, Ceramics and Minerals: Cambridge University Press.

Power, W.L., and Tullis, T.E., 1991, Euclidean and fractal models for the description of rock surface roughness: Journal of Geophysical Research, v. 96, p. 415, doi: 10.1029/90JB02107.

Power, W.L., Tullis, T.E., and Weeks, J.D., 1988, Roughness and wear during brittle faulting: Journal of Geophysical Research: Solid Earth, v. 93, p. 15268–15278, doi: 10.1029/JB093iB12p15268.

Pozzi, G., De Paola, N., Nielsen, S.B., Holdsworth, R.E., and Bowen, L., 2018, A new interpretation for the nature and significance of mirror-like surfaces in experimental carbonate-hosted seismic faults: Geology, p. 1–4, doi: 10.1130/G40197.1.

Price, R.A., 1988, The mechanical paradox of large overthrusts: Bulletin of the Geological Society of America, v. 100, p. 1898–1908, doi: 10.1130/0016-7606(1988)100<1898:TMPOLO>2.3.CO;2.

Proctor, B.P., Mitchell, T.M., Hirth, G., Goldsby, D., Zorzi, F., Platt, J.D., and Di Toro, G., 2014, Dynamic weakening of serpentinite gouges and bare surfaces at seismic slip rates: Journal of Geophysical Research: Solid Earth, v. 119, p. 8107–8131, doi: 10.1002/2014JB011057.

Queener, C.A., Smith, T.C., and Mitchell, W.L., 1965, Transient wear of machine parts: Wear, v. 8, p. 391–400, doi: 10.1016/0043-1648(65)90170-5.

Ranjith, K., and Rice, J.R., 1999, Stability of quasi-static slip in a single degree of freedom elastic system with rate and state dependent friction: Journal of the Mechanics and Physics of Solids, v. 47, p. 1207–1218, doi: 10.1016/S0022-5096(98)00113-6.

Reches, Z., and Lockner, D.A., 2010, Fault weakening and earthquake instability by powder lubrication: Nature, v. 467, p. 452–455, doi: 10.1038/nature09348.

Reinen, L.A., and Weeks, J.D., 1993, Determination of rock friction constitutive parameters using an iterative least squares inversion method: Journal of Geophysical Research, v. 98, p. 15937, doi: 10.1029/93JB00780.

Rempel, A.W., and Weaver, S.L., 2008, A model for flash weakening by asperity melting during high-speed earthquake slip: Journal of Geophysical Research, v. 113, p. B11308, doi: 10.1029/2008JB005649.

Rice, J.R., 2006, Heating and weakening of faults during earthquake slip: Journal of Geophysical Research: Solid Earth, v. 111, p. 1–29, doi: 10.1029/2005JB004006.

Rice, J.R., 1993, Spatio-temporal complexity of slip on a fault: Journal of Geophysical Research, v. 98, p. 9885, doi: 10.1029/93JB00191.

Rice, J.R., 1980, The mechanics of earthquake rupture: Physics of the Earth's Interior, p. 555–649, doi: 10.1.1.161.3251.

Rice, J.R., Lapusta, N., and Ranjith, K., 2001, Rate and state dependent friction and the stability of sliding between elastically deformable solids: Journal of the Mechanics and Physics of Solids, v. 49, p. 1865–1898, doi: 10.1016/s0022-5096(01)00042-4.

Rice, J.R., and Ruina, A.L., 1983, Stability of Steady Frictional Slipping: Journal of Applied Mechanics, v. 50, p. 343, doi: 10.1115/1.3167042.

Richards, P.G., 1973, The dynamic field of a growing plane elliptical shear crack: International Journal of Solids and Structures, v. 9, p. 843–861, doi: 10.1016/0020-7683(73)90007-3.

Rosakis, A.J., Kanamori, H., and Xia, K., 2006, Laboratory earthquakes: International Journal of Fracture, v. 138, p. 211–218, doi: 10.1007/s10704-006-0030-6.

Rubin, A.M., and Ampuero, J.-P., 2005, Earthquake nucleation on (aging) rate and state faults: Journal of Geophysical Research: Solid Earth, v. 110, p. B11312, doi: 10.1029/2005JB003686.

Rubino, V., Rosakis, A.J., and Lapusta, N., 2017, Understanding dynamic friction through spontaneously evolving laboratory earthquakes: Nature Communications, v. 8, p. 1–12, doi: 10.1038/ncomms15991.

Rubinstein, S.M., Cohen, G., and Fineberg, J., 2004, Detachment fronts and the onset of dynamic friction: Nature, v. 430, p. 1005–1009, doi: 10.1038/nature02830.

Ruina, A., 1983, Slip instability and state variable friction laws: Journal of Geophysical Research: Solid Earth, v. 88, p. 10359–10370, doi: 10.1029/JB088iB12p10359.

Rutter, E.H., 1974, The influence of temperature, strain rate and interstitial water in the experimental deformation of calcite rocks: Tectonophysics, v. 22, p. 311–334, doi: 10.1016/0040-1951(74)90089-4.

Sagy, A., and Brodsky, E.E., 2009, Geometric and rheological asperities in an exposed

fault zone: Journal of Geophysical Research, v. 114, p. B02301, doi: 10.1029/2008JB005701.

Sagy, A., Brodsky, E.E., and Axen, G.J., 2007, Evolution of fault-surface roughness with slip: Geology, v. 35, p. 283–286, doi: 10.1130/G23235A.1.

Sagy, A., Tesei, T., and Collettini, C., 2017, Fault-surface geometry controlled by faulting mechanisms: Experimental observations in limestone faults: Geology, v. 45, p. 851–854, doi: 10.1130/G39076.1.

Sammis, C.G., and Ben-Zion, Y., 2008, Mechanics of grain-size reduction in fault zones: Journal of Geophysical Research: Solid Earth, v. 113, p. 1–12, doi: 10.1029/2006JB004892.

Samuelson, J., and Spiers, C.J., 2012, Fault friction and slip stability not affected by Co2 storage: Evidence from short-term laboratory experiments on North Sea reservoir sandstones and caprocks: International Journal of Greenhouse Gas Control, v. 11, p. S78–S90, doi: 10.1016/j.ijggc.2012.09.018.

Schmid, S.M., Boland, J.N., and Paterson, M.S., 1977, Superplastic flow in finegrained limestone: Tectonophysics, v. 43, p. 257–291, doi: 10.1016/0040-1951(77)90120-2.

Scholz, C.H., 1998, Earthquakes and friction laws: Nature, v. 391, p. 37–42, doi: 10.1038/34097.

Scholz, C.H., 1988, The critical slip distance for seismic faulting: Nature, v. 336, p. 761–763, doi: 10.1038/336761a0.

Scholz, C.H., 2002, The mechanics of earthquakes and faulting: Cambridge university press.

Scholz, C.H., and Engelder, J.T., 1976, The role of asperity indentation and ploughing in rock friction - I. Asperity creep and stick-slip: International Journal of Rock Mechanics and Mining Sciences and, v. 13, p. 149–154, doi: 10.1016/0148-9062(76)90819-6.

Schubnel, A., Nielsen, S., Taddeucci, J., Vinciguerra, J., and Rao, S., 2011, Photo-acoustic study of subshear and supershear ruptures in the laboratory: Earth and Planetary Science Letters, v. 308, p. 424–432, doi: 10.1016/j.epsl.2011.06.013.

Schubnel, A., Walker, E., Thompson, B.D., Fortin, J., Guéguen, Y., and Young, R.P., 2006, Transient creep, aseismic damage and slow failure in Carrara marble deformed across the brittle-ductile transition: Geophysical Research Letters, v. 33, p. 1–6, doi: 10.1029/2006GL026619.

Scuderi, M.M., Collettini, C., Viti, C., Tinti, E., and Marone, C., 2017, Evolution of shear fabric in granular fault gouge from stable sliding to stick slip and implications for fault slip mode: Geology, v. 45, p. G39033.1, doi: 10.1130/G39033.1.

Scuderi, M.M., Marone, C., Tinti, E., Di Stefano, G., and Collettini, C., 2016, Precursory changes in seismic velocity for the spectrum of earthquake failure modes: Nature Geoscience, v. 9, p. 695–700, doi: 10.1038/ngeo2775.

Selvadurai, P.A., and Glaser, S.D., 2017, Asperity generation and its relationship to seismicity on a planar fault: A laboratory simulation: Geophysical Journal International, v. 208, p. 1009–1025, doi: 10.1093/gji/ggw439.

Sharland, P.R., Casey, D.M., Davies, R.B., Simmons, M.D., and Sutcliffe, O.E., 2004, Arabian Plate Sequence Stratigraphy revisions to SP2:

Shimamoto, T., 1986, Transition Between Frictional Slip and Ductile Flow for Halite Shear Zones at Room Temperature: Science, v. 231, p. 711–714.

Sibson, R.H., 1977, Fault rocks and fault mechanisms: Journal of the Geological Society, v. 133, p. 191–213, doi: 10.1144/gsjgs.133.3.0191.

Siman-Tov, S., Aharonov, E., Boneh, Y., and Reches, Z., 2015, Fault mirrors along carbonate faults: Formation and destruction during shear experiments: Earth and Planetary Science Letters, v. 430, p. 367–376, doi: 10.1016/j.epsl.2015.08.031.

Siman-Tov, S., Aharonov, E., Sagy, A., and Emmanuel, S., 2013, Nanograins form carbonate fault mirrors: Geology, v. 41, p. 703–706, doi: 10.1130/G34087.1.

Smith, S.A.F., Di Toro, G., Kim, S., Ree, J.H., Nielsen, S., Billi, A., and Spiess, R., 2013, Coseismic recrystallization during shallow earthquake slip: Geology, v. 41, p. 63–66, doi: 10.1130/g33588.1.

Socquet, A., Valdes, J.P., Jara, J., Cotton, F., Walpersdorf, A., Cotte, N., Specht, S., Ortega-Culaciati, F., Carrizo, D., and Norabuena, E., 2017, An 8 month slow slip

event triggers progressive nucleation of the 2014 Chile megathrust: Geophysical Research Letters, v. 44, p. 4046–4053, doi: 10.1002/2017GL073023.

Stanley, H.M., and Kato, T., 1997, An FFT-based method for rough surface contact: Journal of Tribology, v. 119, p. 481–485, doi: 10.1115/1.2833523.

Summers, R., and Byerlee, J., 1977, A note on the effect of fault gouge composition on the stability of frictional sliding: International Journal of Rock Mechanics and Mining Sciences and, v. 14, p. 155–160, doi: 10.1016/0148-9062(77)90007-9.

Svetlizky, I., and Fineberg, J., 2014, Classical shear cracks drive the onset of dry frictional motion: Nature, v. 509, p. 205–208, doi: 10.1038/nature13202.

Tal, Y., and Hager, B.H., 2018, The Slip Behavior and Source Parameters for Spontaneous Slip Events on Rough Faults Subjected to Slow Tectonic Loading: Journal of Geophysical Research: Solid Earth, p. 1–14, doi: 10.1002/2017JB014737.

Tal, Y., Hager, B.H., and Ampuero, J.P., 2018, The Effects of Fault Roughness on the Earthquake Nucleation Process: Journal of Geophysical Research: Solid Earth, doi: 10.1002/2017JB014746.

Tape, C., Holtkamp, S., Silwal, V., Hawthorne, J., Kaneko, Y., Ampuero, J.P., Ji, C., Ruppert, N., Smith, K., and West, M.E., 2018, Earthquake nucleation and fault slip complexity in the lower crust of central Alaska: Nature Geoscience, doi: 10.1038/s41561-018-0144-2.

Tesei, T., Carpenter, B.M., Giorgetti, C., Scuderi, M.M., Sagy, A., Scarlato, P., and Collettini, C., 2017, Friction and scale-dependent deformation processes of large experimental carbonate faults: Journal of Structural Geology, v. 100, p. 12–23, doi: 10.1016/j.jsg.2017.05.008.

Tesei, T., Collettini, C., Barchi, M.R., Carpenter, B.M., and Di Stefano, G., 2014, Heterogeneous strength and fault zone complexity of carbonate-bearing thrusts with possible implications for seismicity: Earth and Planetary Science Letters, v. 408, p. 307–318, doi: 10.1016/j.epsl.2014.10.021.

Tesei, T., Collettini, C., Viti, C., and Barchi, M.R., 2013, Fault architecture and deformation mechanisms in exhumed analogues of seismogenic carbonate-bearing

thrusts: Journal of Structural Geology, v. 55, p. 167–181, doi: 10.1016/j.jsg.2013.07.007.

Tinti, E., Fukuyama, E., Piatanesi, A., and Cocco, M., 2005, A kinematic source-time function compatible with earthquake dynamics: Bulletin of the Seismological Society of America, v. 95, p. 1211–1223, doi: 10.1785/0120040177.

Tinti, E., Scognamiglio, L., Michelini, A., and Cocco, M., 2016, Slip heterogeneity and directivity of the ML 6.0, 2016, Amatrice earthquake estimated with rapid finite-fault inversion: Geophysical Research Letters, v. 43, p. 10,745-10,752, doi: 10.1002/2016GL071263.

Tinti, E., Spudich, P., and Cocco, M., 2005, Earthquake fracture energy inferred from kinematic rupture models on extended faults: Journal of Geophysical Research: Solid Earth, v. 110, p. 1–25, doi: 10.1029/2005JB003644.

Di Toro, G., Goldsby, D.L., and Tullis, T.E., 2004, Friction falls towards zero in quartz rock as slip velocity approaches seismic rates: Nature, v. 427, p. 436–439, doi: 10.1038/nature02249.

Di Toro, G., Han, R., Hirose, T., De Paola, N., Nielsen, S., Mizoguchi, K., Ferri, F., Cocco, M., and Shimamoto, T., 2011, Fault lubrication during earthquakes: Nature, v. 471, p. 494–499, doi: 10.1038/nature09838.

Di Toro, G., Hirose, T., Nielsen, S., Pennacchioni, G., and Shimamoto, T., 2006, Natural and experimental evidence of melt lubrication of faults during earthquakes: Science, v. 311, p. 647–649, doi: 10.1126/science.1121012.

Di Toro, G., Nielsen, S., and Pennacchioni, G., 2005, Earthquake rupture dynamics frozen in exhumed ancient faults: Nature, v. 436, p. 1009–1012, doi: 10.1038/nature03910.

Uenishi, K., and Rice, J.R., 2003, Universal nucleation length for slip-weakening rupture instability under nonuniform fault loading: Journal of Geophysical Research: Solid Earth, v. 108, p. n/a-n/a, doi: 10.1029/2001JB001681.

Venkataraman, A., and Kanamori, H., 2004, Observational constraints on the fracture energy of subduction zone earthquakes: Journal of Geophysical Research: Solid Earth, v. 109, p. n/a--n/a, doi: 10.1029/2003JB002549.

Verberne, B.A., de Bresser, J.H.P., Niemeijer, A.R., Spiers, C.J., de Winter, D.A.M., and Plumper, O., 2013, Nanocrystalline slip zones in calcite fault gouge show intense crystallographic preferred orientation: Crystal plasticity at sub-seismic slip rates at 18-150 degrees C: Geology, v. 41, p. 863–866, doi: 10.1130/g34279.1.

Verberne, B.A., Plümper, O., De Winter, D.A.M., and Spiers, C.J., 2014, Superplastic nanofibrous slip zones control seismogenic fault friction: Science, v. 346, p. 1342–1344, doi: 10.1126/science.1259003.

Verberne, B.A., Spiers, C.J., Niemeijer, A.R., De Bresser, J.H.P., De Winter, D.A.M., and Plümper, O., 2013, Frictional Properties and Microstructure of Calcite-Rich Fault Gouges Sheared at Sub-Seismic Sliding Velocities: Pure and Applied Geophysics, v. 171, p. 2617–2640, doi: 10.1007/s00024-013-0760-0.

Viesca, R.C., and Garagash, D.I., 2015, Ubiquitous weakening of faults due to thermal pressurization: Nature Geoscience, v. 8, p. 875–879, doi: 10.1038/ngeo2554.

Wang, K., and Bilek, S.L., 2014, Invited review paper: Fault creep caused by subduction of rough seafloor relief: Tectonophysics, v. 610, p. 1–24, http://www.sciencedirect.com/science/article/pii/S0040195113006896.

Wang, W., and Scholz, C.H., 1994, Wear processes during frictional sliding of rock: a theoretical and experimental study: Journal of Geophysical Research, v. 99, p. 6789–6799, doi: 10.1029/93JB02875.

Weeks, J.D., and Tullis, T.E., 1985, Frictional sliding of dolomite: A variation in constitutive behavior: Journal of Geophysical Research, v. 90, p. 7821, doi: 10.1029/JB090iB09p07821.

Wong, T.-F., 1982, Shear fracture energy of Westerly granite from post-failure behavior: J. Geophys. Res., v. 87, p. 990–1000.

Xia, K.W., Rosakis, A.J., and Kanamori, H., 2004, Laboratory earthquakes: The sub-Rayleigh-to-supershear rupture transition: Science, v. 303, p. 1859–1861, doi: 10.1126/science.1094022.

Yoffe, E.H., 1951, LXXV. The moving griffith crack: The London, Edinburgh, and Dublin Philosophical Magazine and Journal of Science, v. 42, p. 739–750, doi:

10.1080/14786445108561302.

Yoshioka, N., and Scholz, C.H., 1989, Elastic properties of contacting surfaces under normal and shear loads: 1. Theory: Journal of Geophysical Research, v. 94, p. 17681, doi: 10.1029/JB094iB12p17681.

Zhang, X., Spiers, C.J., and Peach, C.J., 2010, Compaction creep of wet granular calcite by pressure solution at 28°C to 150°C: Journal of Geophysical Research: Solid Earth, v. 115, p. 1–18, doi: 10.1029/2008JB005853.

9 Publications associated to the PhD